Measurement of the CKM angle gamma in the B ->DK* decays using the Dalitz method in the LHCb experiment at CERN and photon reconstruction optimisation for the LHCb detector upgrade

Alexis Vallier

LAL 15-263

UNIVERSITÉ PARIS-SUD

École Doctorale : Particules, Noyaux et Cosmos - ED 517
Laboratoire de l'Accélérateur Linéaire - UMR 8607
Centre Scientifique d'Orsay, Bâtiment 200 - BP 34, 91898 Orsay CEDEX - France

THÈSE DE DOCTORAT

Discipline : PHYSIQUE
Spécialité : Physique des particules

soutenue le 10 septembre 2015

par

Alexis VALLIER

Measurement of the CKM angle γ in the $B^0 \to DK^{*0}$ decays using the Dalitz method in the LHCb experiment at CERN and photon reconstruction optimisation for the LHCb detector upgrade

Mesure de l'angle γ de la matrice CKM dans les désintégrations $B^0 \to DK^{*0}$ en utilisant la méthode de Dalitz dans l'expérience LHCb au CERN et optimisation de la reconstruction des photons pour l'upgrade du détecteur LHCb

Composition du jury :

Directeur de thèse	Frédéric MACHEFERT	Directeur de recherche (LAL)
Rapporteur	Fernando MARTÍNEZ VIDAL	Professeur (IFIC)
Rapporteur	Guy WILKINSON	Professeur (University of Oxford)
Président	Achille STOCCHI	Professeur (LAL)
Examinatrice	Isabelle WINGERTER-SEEZ	Directrice de recherche (LAPP)
Examinateur	Jure ZUPAN	Professeur (University of Cincinnati)

À Pépé, Mémé, Yvonne et Michel.

“il faut cultiver notre jardin”
Candide ou l’optimisme,
Voltaire.

Résumé

Le mélange des quarks est décrit dans le modèle standard de la physique des particules par le mécanisme de Cabibbo-Kobayashi-Maskawa (CKM). À ce jour, l'angle γ du triangle d'unitarité est un des paramètres de ce mécanisme mesuré avec la moins bonne précision. La mesure de cet angle sert de référence pour le modèle standard, puisqu'elle peut être réalisée sans contribution significative de nouvelle physique. La précision actuelle de la meilleure mesure directe de γ est d'environ 10°, alors que les ajustements globaux des paramètres CKM, potentiellement sujets à une contribution de nouvelle physique, déterminent cet angle à quelques degrés près. Par conséquent, une mesure directe précise de cette quantité est nécessaire pour contraindre d'avantage le triangle d'unitarité de la matrice CKM et ainsi tester la cohérence de ce modèle.

Cette thèse présente une mesure de γ par une analyse de Dalitz du canal $B^0 \to DK^{*0}$, avec une désintégration du méson D en $K^0_S\pi^+\pi^-$. Elle est basée sur les 3 fb^{-1} de données enregistrés par LHCb pendant le Run I du LHC, à une énergie de collision proton-proton dans le centre de masse de 7 et 8 TeV. Ce canal est sensible à γ par l'interférence entre les transitions $b \to u$ et $b \to c$. La mesure des observables de violation de *CP* réalisée est

$$\begin{aligned} x_- &= -0.09^{+0.13}_{-0.13} \pm 0.09 \pm 0.01 \,, \\ x_+ &= -0.10^{+0.27}_{-0.26} \pm 0.06 \pm 0.01 \,, \\ y_- &= 0.23^{+0.15}_{-0.16} \pm 0.04 \pm 0.01 \,, \\ y_+ &= -0.74^{+0.23}_{-0.26} \pm 0.07 \pm 0.01 \,, \end{aligned}$$

où le première incertitude est statistique, la deuxième est l'incertitude systématique expérimentale et la troisième est l'incertitude systématique venant du modèle de Dalitz. Une interprétation fréquentiste de ces observables donne

$$r_{B^0} = 0.39 \pm 0.13 \,, \qquad \delta_{B^0} = \left(186^{+24}_{-23}\right)^\circ \,, \qquad \gamma = \left(77^{+23}_{-24}\right)^\circ \,,$$

où r_{B^0} est le module du rapport des amplitudes des désintégrations supprimées et favorisées et δ_{B^0} la différence de phase forte entre ces deux désintégrations.

Par ailleurs, un travail sur l'optimisation de la reconstruction des photons pour la mise à niveau du détecteur LHCb est aussi présenté. Lors du Run III du LHC, la luminosité instantanée reçue par LHCb sera augmentée d'un facteur cinq, générant un plus grand recouvrement entre les cascades se développant dans le calorimètre électromagnétique. L'étude montre que l'effet de ce recouvrement entre les gerbes est limité en réduisant la taille des clusters utilisés pour la détection des photons, tout en évitant une diminution significative de l'énergie reconstruite. Avec des corrections adaptées, la nouvelle reconstruction développée améliore la résolution en masse de 7 à 12%, suivant la région du calorimètre considérée.

Mots-clés : Physique des particules, Physique des saveurs, Modèle standard, Violation de *CP*, CKM, Triangle d'unitarité, LHC, LHCb, LHCb upgrade, Calorimètre électromagnétique.

Abstract

Quark mixing is described in the standard model of particle physics with the Cabibbo-Kobayashi-Maskawa mecanism. The angle γ of the unitarity triangle is one of the parameters of this mecanism that is still determined with a large uncertainty. It can be measured without significant contribution of new physics, making it a standard model key measurement. The current precision of the best direct measurement of γ is approximately 10°, whereas the global fits of the CKM parameters determine this angle up to a few degrees. Therefore precise measurement of this quantity is needed to further constrain the Unitarity Triangle of the CKM matrix, and check the consistency of the theory.

This thesis reports a measurement of γ with a Dalitz analysis of the $B^0 \to DK^{*0}$ channel where the D meson decays into $K^0_S\pi^+\pi^-$, based on the $3\,\text{fb}^{-1}$ of proton-proton collision data collected by LHCb during the LHC Run I, at the centre-of-mass energy of 7 and 8 TeV. This channel is sensitive to γ through the interference between the $b\to u$ and $b\to c$ transitions. The *CP* violation observables are measured to be

$$\begin{aligned} x_- &= -0.09^{+0.13}_{-0.13} \pm 0.09 \pm 0.01\,, \\ x_+ &= -0.10^{+0.27}_{-0.26} \pm 0.06 \pm 0.01\,, \\ y_- &= 0.23^{+0.15}_{-0.16} \pm 0.04 \pm 0.01\,, \\ y_+ &= -0.74^{+0.23}_{-0.26} \pm 0.07 \pm 0.01\,, \end{aligned}$$

where the first uncertainty is statistical, the second is the experimental systematic uncertainty and the third is the systematic uncertainty due to the Dalitz model. A frequentist interpretation of these observables leads to

$$r_{B^0} = 0.39 \pm 0.13\,, \qquad \delta_{B^0} = \left(186^{+24}_{-23}\right)^\circ\,, \qquad \gamma = \left(77^{+23}_{-24}\right)^\circ\,,$$

where r_{B^0} is the magnitude of the ratio between the suppressed and favoured decays and δ_{B^0} the strong phase difference between these two decays.

In addition, the work performed on the optimisation of the photon reconstruction for the upgraded LHCb detector is reported. During LHC Run III, the LHCb instantaneous luminosity will be increased by a factor five, implying a larger shower overlap in the electromagnetic calorimeter. The study shows that reducing the cluster size used in the photon reconstruction limits the effect of the overlap between the showers, without inducing a significant energy leakage. With some dedicated corrections, the new cluster reconstruction improves the $B^0_s \to \phi\gamma$ mass resolution by 7 to 12%, depending on the calorimeter region.

Key words: Particle physics, Flavour physics, Standard model, *CP* violation, CKM, Unitarity triangle, LHC, LHCb, LHCb upgrade, Electromagnetic calorimeter.

Synthèse

Le mélange des quarks est décrit dans le modèle standard de la physique des particules par le mécanisme de Cabibbo-Kobayashi-Maskawa (CKM). Il relie les états propres de masse des quarks à leurs états propres de l'interaction faible grâce à une matrice de rotation, la matrice CKM :

$$V_{CKM} \equiv \begin{pmatrix} V_{ud} & V_{us} & V_{ub} \\ V_{cd} & V_{cs} & V_{cb} \\ V_{td} & V_{ts} & V_{tb} \end{pmatrix} . \tag{1}$$

Chaque terme V_{ij} de la matrice correspond au couplage entre les quarks de saveur i et j. En adoptant la paramétrisation de Wolfenstein [1], qui se base sur une expansion en puissance de $\lambda \equiv V_{us} \approx 0.22$, l'ordre de grandeur de ces couplages apparaît clairement.

$$V_{CKM} = \begin{pmatrix} 1-\frac{\lambda^2}{2} & \lambda & A\lambda^3(\rho - i\eta) \\ -\lambda & 1-\frac{\lambda^2}{2} & A\lambda^2 \\ A\lambda^3(1-\rho-i\eta) & -A\lambda^2 & 1 \end{pmatrix} + \mathcal{O}\left(\lambda^4\right) . \tag{2}$$

Ainsi, les transitions au sein d'une même génération de quark sont favorisées. Avec un paramètre η différent de zéro, la matrice CKM possède une phase complexe non nulle, qui explique la violation de la symétrie *CP* dans le modèle standard.

La matrice CKM étant une matrice de rotation, elle doit être unitaire. Cette condition peut, entre autre, se représenter dans un plan complexe par un triangle d'unitarité (Fig.1). Le sujet principal de cette thèse porte sur la mesure de l'angle γ de ce triangle d'unitarité, défini comme

$$\gamma = \arg\left(-\frac{V_{ud}V_{ub}{}^*}{V_{cd}V_{cb}{}^*}\right) . \tag{3}$$

À ce jour, l'angle γ du triangle d'unitarité est un des paramètres du mécanisme CKM mesuré avec la moins bonne précision. La mesure de cet angle sert de référence pour le modèle standard, puisqu'elle peut être réalisée sans effet significatif de nouvelle physique. En effet, la contribution de processus d'ordre supérieur aux diagrammes à l'arbre est négligeable. La précision actuelle de la meilleure mesure directe de γ est d'environ 10°, alors que les ajustements globaux des paramètres CKM, potentiellement sujets à une contribution de nouvelle physique, déterminent cet angle à quelques degrés près. Par conséquent, une mesure directe précise de cette quantité est nécessaire pour contraindre d'avantage le triangle d'unitarité de la matrice CKM et ainsi tester la cohérence de ce modèle.

Comme γ correspond à la différence de phase entre les termes V_{ub} et V_{cb} de la matrice CKM, sa mesure s'effectue en réalisant une interférence entre les transitions $b \to u$ et $b \to c$. Le canal classiquement étudié est $B^{\pm} \to DK^{\pm}$. Dans cette thèse, c'est la transition neutre $B^0 \to DK^{*0}$ qui

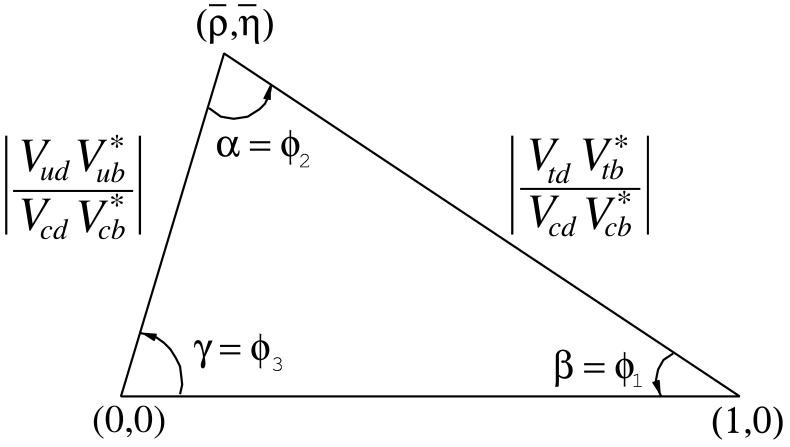

FIGURE 1 – Le triangle d'unitarité de la matrice CKM

est étudiée. Elle présente un rapport d'embranchement inférieure à la transition $B^{\pm} \to DK^{\pm}$, mais l'interférence entre les désintégrations $b \to u$ et $b \to c$ y est plus grande. Donc le canal $B^0 \to DK^{*0}$ a intrinsèquement une meilleure sensibilité à γ. Les diagrammes de Feynman impliqués dans ce canal sont illustrés Fig. 2. Pour réaliser une interférence entre les diagrammes V_{ub} et V_{cb}, les mésons D^0 et $\overline{D}^0$ doivent être reconstruits dans le même état final. Suivant les méthode d'analyse adoptées, plusieurs états finaux sont utilisés. Les méthodes GLW [2,3] et ADS [4,5] sont basées sur des désintégrations à deux corps des mésons D. La méthode GGSZ [6,7] utilise quant à elle une désintégration à trois corps, comme par exemple $D \to K^0_S\pi^+\pi^-$. Dans ce cas, la distribution sur le plan de Dalitz, construit à partir des masses invariantes carrées $m^2_{\pm} \equiv m^2(K^0_S\pi^{\pm})$, est fonction de l'angle γ. Cette distribution peut s'écrire

$$\mathscr{P}_- \propto |A_D|^2 + r^2_{B^0}|A_{\overline{D}}|^2 + 2\kappa r_{B^0}\mathscr{R}e\left[A^*_D A_{\overline{D}} e^{i(\delta_{B^0}-\gamma)}\right], \tag{4}$$

$$\mathscr{P}_+ \propto |A_{\overline{D}}|^2 + r^2_{B^0}|A_D|^2 + 2\kappa r_{B^0}\mathscr{R}e\left[A_D A^*_{\overline{D}} e^{i(\delta_{B^0}+\gamma)}\right]. \tag{5}$$

pour les désintégrations $\overline{B}^0 \to D\overline{K}^{*0}$ et $B^0 \to DK^{*0}$ respectivement. r_{B^0} est la norme du rapport entre les amplitudes $b \to u$ et $b \to c$ et δ_{B^0} la différence de phase forte entre ces transitions. Le facteur de cohérence κ prend en compte l'effet des contributions non résonantes $B^0 \to DK\pi$. Il est évalué dans cette thèse à $\kappa = 0.93 \pm 0.04$. Les amplitudes A_D et $A_{\overline{D}}$ des désintégrations $D^0 \to K^0_S\pi^+\pi^-$ et $\overline{D}^0 \to K^0_S\pi^+\pi^-$ sont ici décrites grâce à un modèle déterminé par l'expérience BaBar. À partir d'un ajustement sur la distribution des événements dans le plan de Dalitz, les paramètres cartésiens

$$x_{\pm} \equiv r_{B^0}\cos(\delta_{B^0} \pm \gamma), \tag{6}$$

$$y_{\pm} \equiv r_{B^0}\sin(\delta_{B^0} \pm \gamma), \tag{7}$$

sont évalués. Ce qui permet dans déduire des contraintes sur r_{B^0}, δ_{B^0} et surtout γ.

Le détecteur LHCb (Fig. 3) est particulièrement bien adapté pour réaliser des mesures de précisions relatives au secteur des saveurs lourdes. D'abord il profite de la grande section efficace de production de paires $b\overline{b}$ au LHC, le collisionneur de hadrons installé au CERN (Genève, Suisse). Et par sa conception, il offre d'excellentes performances en reconstruction de vertex déplacés, en mesure d'impulsion et de paramètre d'impact, et en identification de

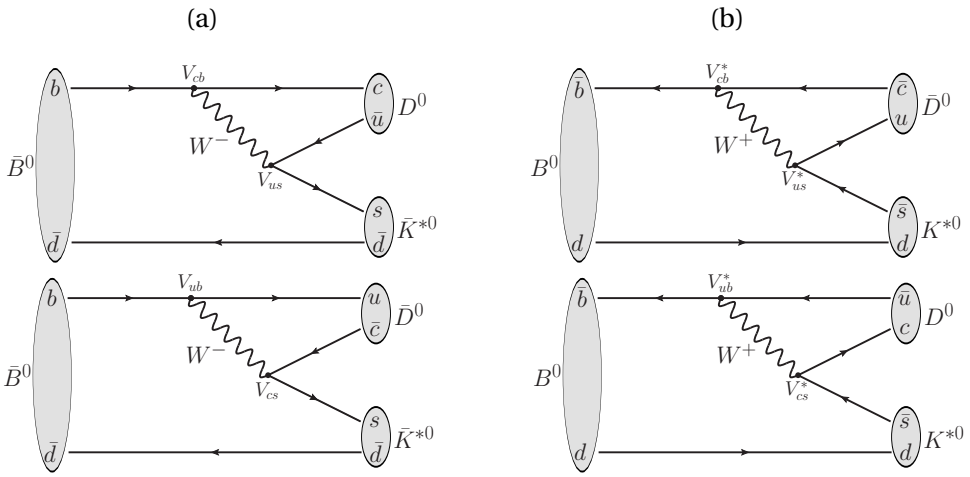

FIGURE 2 – Diagrammes de Feynman impliqués dans les désintégrations $\overline{B}^0 \to D\overline{K}^{*0}$ (a) et $B^0 \to DK^{*0}$ (b). Les transitions proportionnelles au terme $|V_{cb}|^2$ figurent en haut et les transitions proportionnelles au terme $|V_{ub}|^2$ figurent au bas. Tous les diagrammes sont supprimés de couleur.

particules. Il est constitué d'un détecteur de vertex (Vertex Locator), de trajectographes placés en amont et aval de l'aimant, de deux détecteurs à effet Cherenkov (RICH1 et RICH2), d'un calorimètre électromagnétique et hadronique et de chambres à muons.

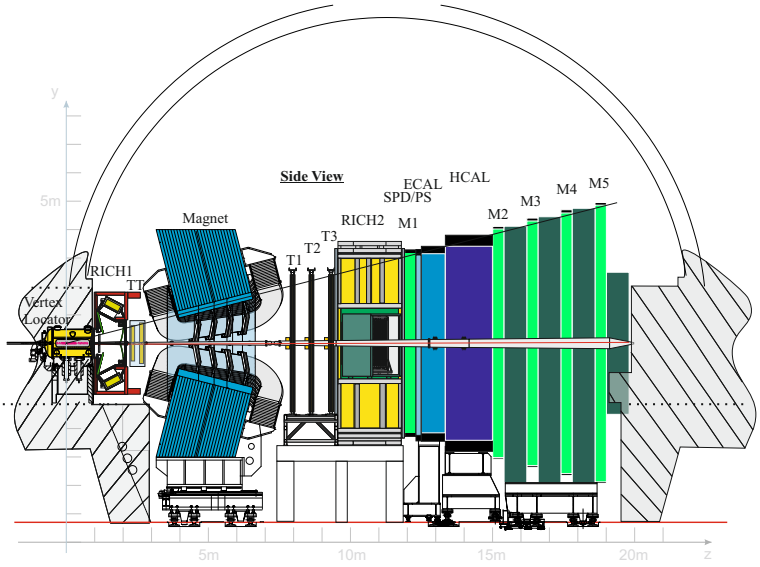

FIGURE 3 – Coupe du détecteur LHCb.

Cette thèse présente une mesure de γ par une analyse de Dalitz du canal $B^0 \to DK^{*0}$, avec une désintégration du méson D en $K^0_S\pi^+\pi^-$. Elle est basée sur les 3 fb^{-1} de données enregistrés par LHCb pendant le Run I du LHC, à une énergie de collision proton-proton dans le centre de masse de 7 et 8 TeV. Une sélection basée sur un algorithme d'arbre de décision

boosté (BDT) est appliquée pour sélectionner les événements de signal $B^0 \to D(K^0_S\pi^+\pi^-)K^{*0}$ et rejeter efficacement les bruits de fond. Les variables discriminantes utilisées par le BDT sont des impulsions transverses, des critères de bonne reconstruction des vertex et des chaînes de désintégration ainsi que des significances de distances de vol. Les efficacités d'acceptance, de reconstruction et de sélection sont déterminées à partir de la simulation, en utilisant des corrections évaluées à partir d'échantillons de calibration issus de données réelles, pour les efficacité dues au système de déclenchement et d'identification des particules. Un premier ajustement de la distribution de la masse invariante du méson B^0 reconstruite est réalisé (Fig. 4). Il permet de déterminer les niveaux de signal $B^0 \to DK^{*0}$, du bruit de fond combinatoire et des bruits de fond issus des désintégrations $B^0_s \to D\overline{K}^{*0}$, $B^0_{(s)} \to D^{*0}K^{*0}$ et $B^0 \to D\rho^0$.

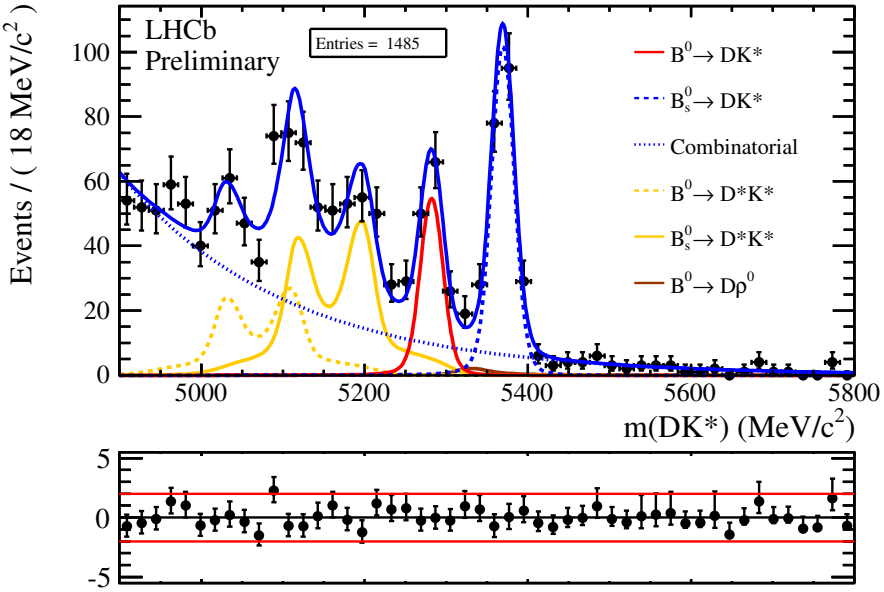

FIGURE 4 – Ajustement de la distribution de la masse du méson B^0 des événements $B^0 \to DK^{*0}$.

Une fois ces niveaux fixés, un ajustement de la distribution des événements sur le plan de Dalitz est fait (Fig. 5. Il permet la mesure des observables de violation de *CP*

$$\begin{aligned} x_- &= -0.09^{+0.13}_{-0.13} \pm 0.09 \pm 0.01\,, \\ x_+ &= -0.10^{+0.27}_{-0.26} \pm 0.06 \pm 0.01\,, \\ y_- &= 0.23^{+0.15}_{-0.16} \pm 0.04 \pm 0.01\,, \\ y_+ &= -0.74^{+0.23}_{-0.26} \pm 0.07 \pm 0.01\,, \end{aligned}$$

où le première incertitude est statistique, la deuxième est l'incertitude systématique expérimentale et la troisième est l'incertitude systématique venant du modèle utilisé pour décrire la désintégration $D \to K^0_S\pi^+\pi^-$.

Pour déduire une contrainte sur r_{B^0}, δ_{B^0} et γ à partir des mesures de $(x_\pm, y_\pm)$, une interpréta-

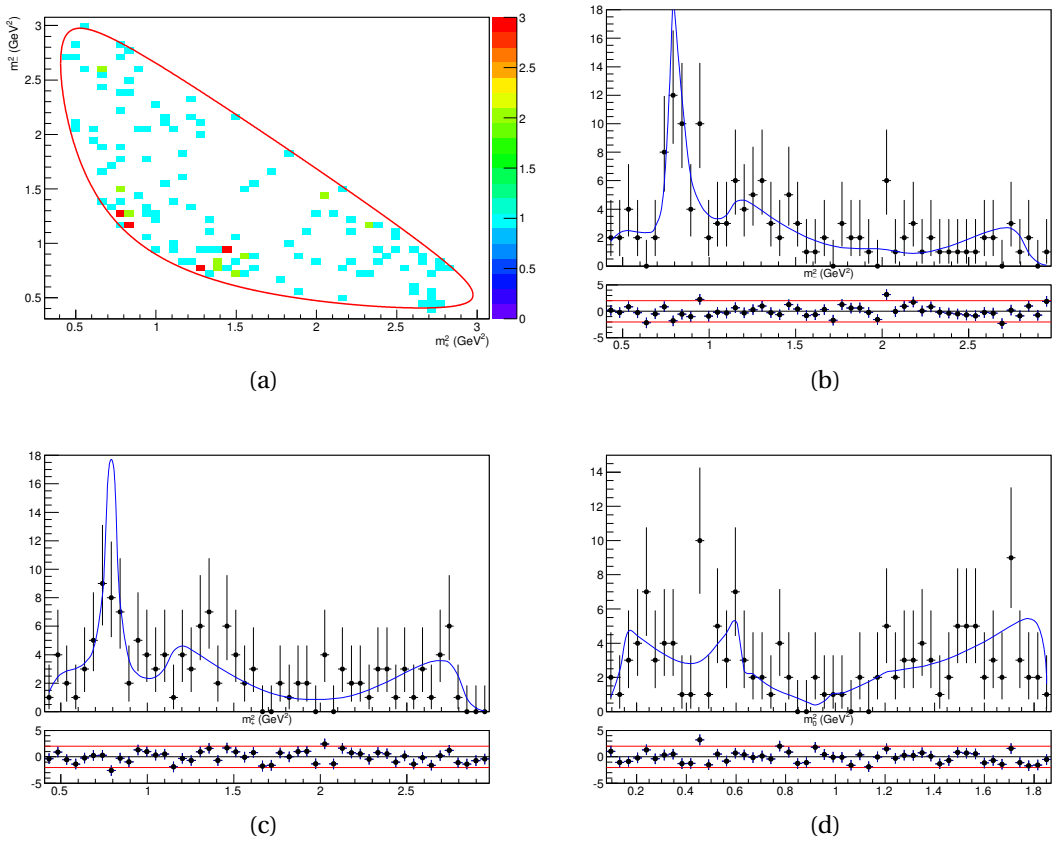

FIGURE 5 – Diagramme de Dalitz (a) et ses projections sur m_-^2 (b), m_+^2 (c) and m_0^2 (d) faits à partir des événements $B^0 \to DK^{*0}$ sélectionnés dans les données. La ligne bleue superposée aux projections correspond au résultat de l'ajustement.

tion statistique fréquentiste de ces observables est menée. Elle donne

$$\begin{aligned} r_{B^0} = &\quad 0.39 \pm 0.13\,, \\ \delta_{B^0} = &\quad \left(186^{+24}_{-23}\right)^\circ\,, \\ \gamma = &\quad \left(77^{+23}_{-24}\right)^\circ\,. \end{aligned}$$

Les courbes correspondantes de niveaux de confiance sont illustrées Fig. 6 et 7. Les contraintes obtenues dans les plans à deux dimensions (γ, r_{B^0}) et (γ, δ_{B^0}) sont aussi illustrées Fig. 8 et 9. La mesure de γ réalisée dans cette thèse avec le canal $B^0 \to D(K^0_S\pi^+\pi^-)K^{*0}$ est comparée sur la Fig. 10 avec les combinaisons des mesures directes faites par BaBar, Belle et LHCb, les moyennes faites par les collaborations CKMfitter et UTFit et la mesure individuelle la plus précise, obtenue avec des désintégration $B^\pm \to DK^\pm$. Malgré une statistique réduite par rapport au canal $B^\pm \to DK^\pm$, le résultat de cette thèse montre la grande sensibilité à γ de la désintégration $B^0 \to DK^{*0}$. Ce canal est donc très prometteur pour réaliser une mesure précise de γ avec les données collectées lors du Run II du LHC.

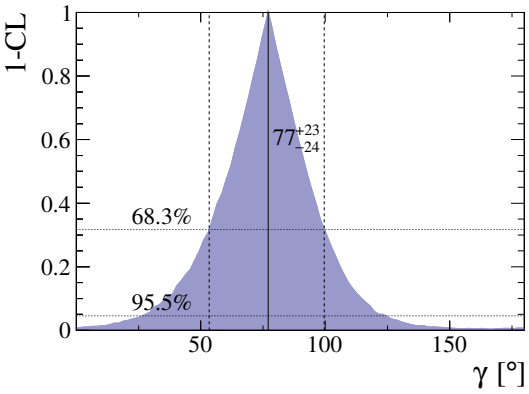

(a)

FIGURE 6 – Courbe de niveau de confiance sur l'angle γ.

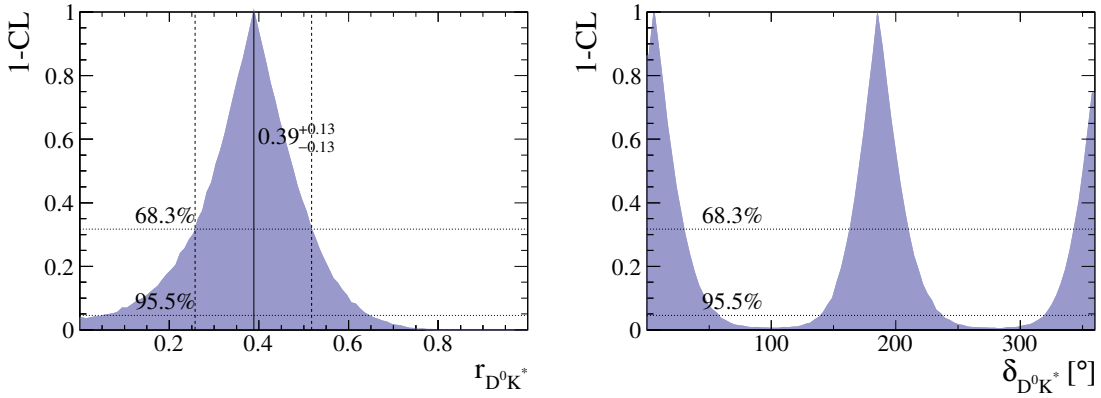

(a) (b)

FIGURE 7 – Courbes de niveau de confiance sur les paramètres r_{B^0} (a) et δ_{B^0} (b).

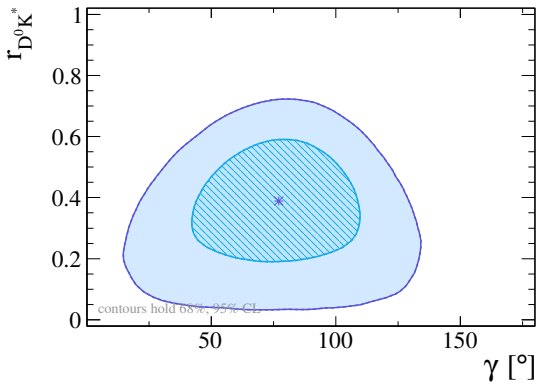

FIGURE 8 – Niveau de confiance de r_{B^0} en fonction de γ. Les contours correspondent à 1σ et 2σ de déviation standard. L'étoile représente le résultat de l'ajustement, correspondant au maximum de vraisemblance.

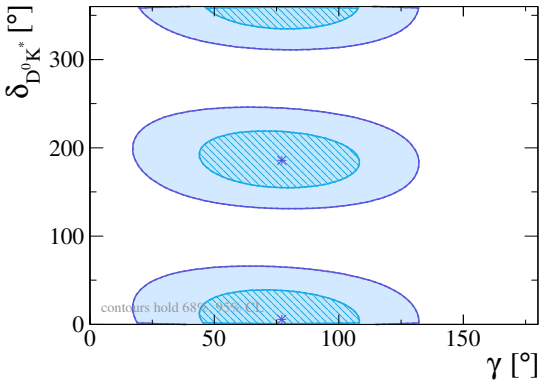

(a)

FIGURE 9 – Niveau de confiance de δ_{B^0} en fonction de γ. Les contours correspondent à 1σ et 2σ de déviation standard. L'étoile représente le résultat de l'ajustement, correspondant au maximum de vraisemblance.

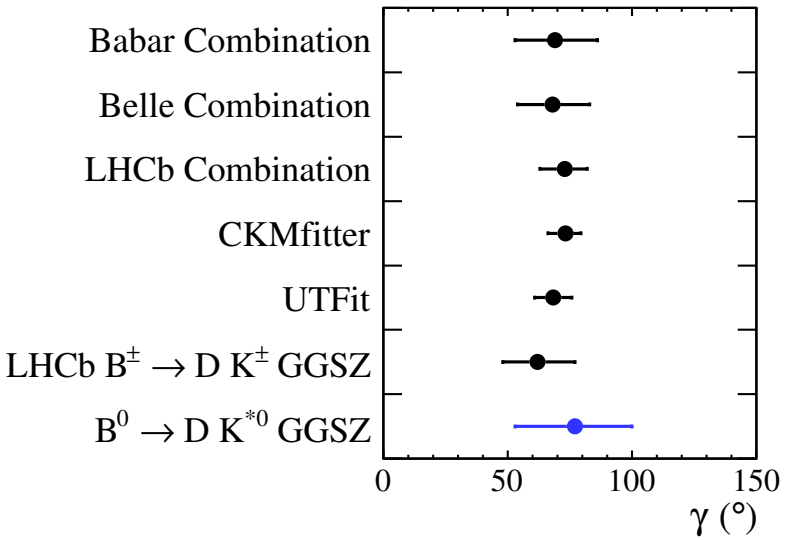

FIGURE 10 – Comparaison entre la mesure de γ reportée dans cette thèse (en bleue) avec les combinaisons des mesures directes faite par BaBar [8], Belle [9] et LHCb [10] ; les moyennes obtenues par les collaborations CKMfitter [11] et UTFit [12] ; et la mesure seule actuellement la plus précise, obtenue avec des désintégrations $B^{\pm} \to DK^{\pm}$ [13].

Par ailleurs, un travail sur l'optimisation de la reconstruction des photons pour la mise à niveau du détecteur LHCb est aussi présenté. Il est basé sur la simulation d'événements $B_s^0 \to \phi\gamma$ dans les conditions prévues pour le Run III du LHC. Lors du Run III, la luminosité instantanée reçue par LHCb sera augmentée d'un facteur cinq, générant un plus grand recouvrement entre les cascades se développant dans le calorimètre électromagnétique. Ce recouvrement crée un empilement des énergies déposées dans les cellules. Ainsi, comme le montre la Fig. 11, la distribution de la résolution en énergie $(E_{\text{true}} - E_{\text{rec}})/E_{\text{true}}$, où E_{true} est la vraie énergie du photon et E_{rec} son énergie reconstruite, présente une importante queue non gaussienne quand $E_{\text{rec}} > E_{\text{true}}$ (empilement). Cette queue non gaussienne est plus petite pour des clusters 2×2 et croix, qui sont plus petits que les clusters 3×3 actuels. La taille de cette queue non gaussienne est mesurée par un ajustement des distributions de la résolution en énergie par une fonction Crystal Ball

$$f(x;\alpha,n,\mu,\sigma) \equiv N \cdot \begin{cases} e^{-\frac{(x-\mu)^2}{2\sigma^2}} & \text{for } \frac{x-\mu}{\sigma} > -\alpha, \\ A\left(B - \frac{x-\mu}{\sigma}\right)^{-n} & \text{otherwise.} \end{cases} \tag{8}$$

On remarque (Fig. 12) que les clusters à taille réduite ont toujours un paramètre α de la Crystal Ball bien supérieur à ceux obtenus avec le clusters 3×3. Cela signifie que la queue non gaussienne du à l'empilement est plus petite avec les clusters de taille réduite. Ainsi l'effet du recouvrement entre les gerbes électromagnétiques est limité en réduisant la taille des clusters utilisés pour la mesure de l'énergie des photons. Malgré une taille réduite, les clusters 2×2 ont même une résolution gaussienne (paramètre σ de la Crystal Ball) similaire au clusters 3×3 (Fig. 12).

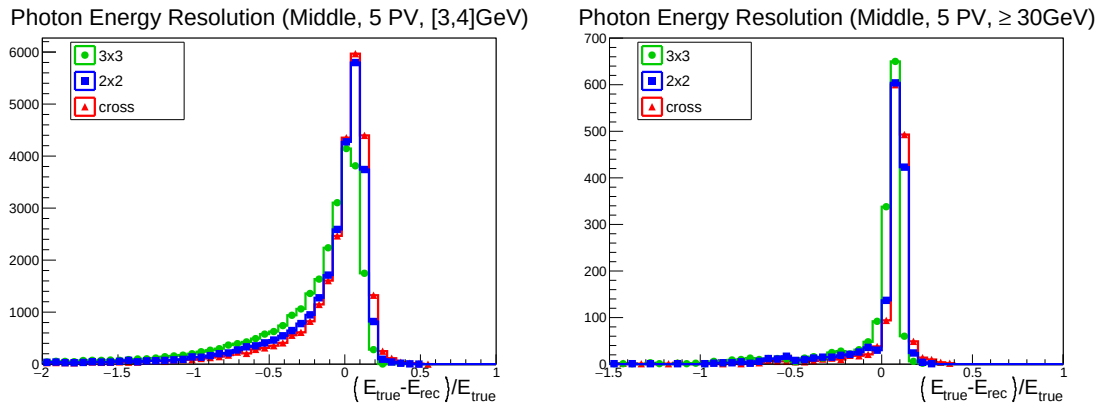

FIGURE 11 – Résolution en énergie dans la zone "middle" du calorimètre électromagnétique, pour deux intervalles d'énergie [3,4] GeV (gauche) et ≥ 30 GeV (droite) pour 5 vertex primaires et pour les clusters 3×3 (vert), 2×2 (bleu) et croix (rouge). L'effet de l'empilement est particulièrement visible à basse énergie.

Pour la mesure de la position des photons, les clusters 2×2 ne sont pas adaptés. En revanche, les clusters en croix fonctionnent très bien, et avec les corrections adaptées, la nouvelle reconstruction développée améliore la résolution en position de 15 à 20% (Fig. 13) et en masse de 7 à 12%, suivant la région du calorimètre considérée et pour des photons issus d'une désintégration $B_s^0 \to \phi\gamma$.

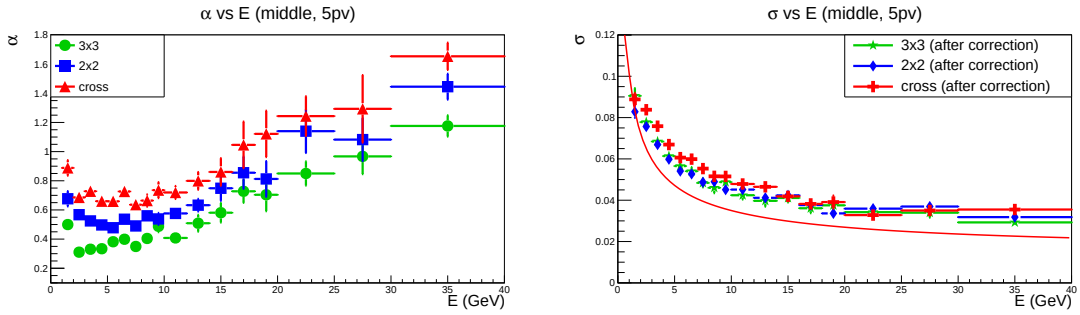

FIGURE 12 – Valeurs ajustées des paramètres α (gauche) et σ (droite) de la fonction Crystal Ball décrivant la résolution en énergie des photons, en fonction de l'énergie du photon, dans la zone "middle" de l'ECAL, pour 5 vertex primaires et pour les clusters 3×3 (vert), 2×2 (bleu) et croix (rouge). La courbe rouge est une approximation de la résolution du calorimètre $\sigma(E) = \frac{10\%}{\sqrt{E}} \oplus 1.5\%$.

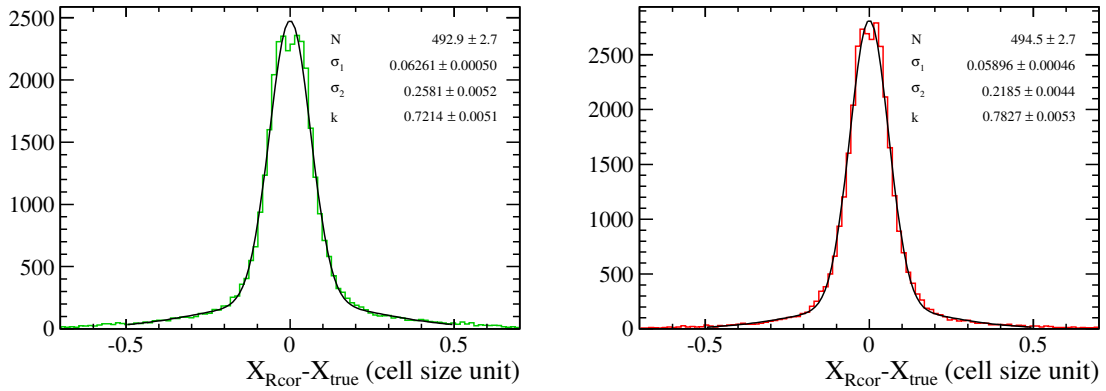

(a) 3×3 clusters (b) cross clusters

FIGURE 13 – Résolution sur la position reconstruite du photons pour des clusters 3×3 (a) et croix (b), dans la region "outer" de l'ECAL.

Contents

Introduction

The standard model (SM) of particle physics describes with an excellent accuracy the elementary particles constituting the matter of our universe and their fundamental interactions. The theory has been extensively tested over the past decades, especially in the electroweak sector, at the LEP, Tevatron and LHC accelerators, and in the heavy flavour sector, at the SLAC, KEK and LHC accelerators. Despite its numerous successes, the SM has some remaining challenges. For instance, it does not include a description of the gravity and cannot explain the matter-antimatter asymmetry observed in the universe. That is why particle physicists look for evidence of new physics, in particular with the consistency check of the CKM model, which describes quark flavour mixing. The SM and the CKM model are presented in Chapter 1.

This thesis focuses on the γ angle of the unitarity triangle, which is one of the least known CKM parameters. It can be measured without significant contribution of new physics, making it a SM key measurement. The current precision of the best direct measurement of γ is approximately 10°, whereas the global fits of the CKM parameters can determine this angle up to a few degrees. That is why, to further constrain the heavy quark sector and check the consistency of the CKM model, more precise direct measurements of γ are needed. This is not an easy task, since it involves the study of hadronic B meson decays with low rates. The experimental status on γ and its measurement principle are presented in Chapter 2.

The LHCb detector is well suited to measure γ, and for flavour physics measurements in general. For instance, with its silicon vertex detector, it efficiently reconstructs secondary vertices, specific to B meson decay topologies. It can also separate kaons and pions thanks to its Cherenkov detectors. In addition, the luminosity conditions are adjusted to limit the occupancy of the detector, in order to efficiently reconstruct the whole decay chain of the signals. A description of the LHCb detector is made in Chapter 3.

During the LHC Long Shutdown 2, the LHCb detector will be upgraded to cope with an increase of the instantaneous luminosity. The operating conditions will be harsher, with a larger detector occupancy, making the neutral objects such as neutral pions and photons more difficult to measure. Thus, an optimisation of the calorimeter reconstruction for the upgrade should be done. Chapter 4 reports the study of a new photon reconstruction, adapted to the upgrade conditions.

Finally, the $B^0 \to DK^{*0}$ decays are a promising channel to measure γ. The sensitivity to this weak phase arises from the interference between $b \to u$ and $b \to c$ transitions, which is particularly high in the $B^0 \to DK^{*0}$ decays. Chapter 5 presents the measurement of γ using a Dalitz analysis of these decays, using the so-called GGSZ method, and is the main work of this thesis.

Chapter 1

The standard model of particle physics

Contents

The theory describing the structure of the matter that constitutes our universe is called the *standard model* of particle physics (SM). It explains with a tremendous accuracy how the elementary particles interact, at a subatomic scale, with three fundamental interactions (gravity is not considered in the SM). In this chapter, a brief overview of the standard model is made. Particular attention is given to quark flavour mixing, described by the CKM mechanism. The remaining standard model challenges are also mentioned, as well as the reasons why the test of the CKM paradigm can bring a valuable insight to the search of physics beyond the standard model. A more detailed introduction to the standard model can be found for instance in Ref. [14], to quantum field theory in Ref. [15] and to the flavour physics in Ref. [16].

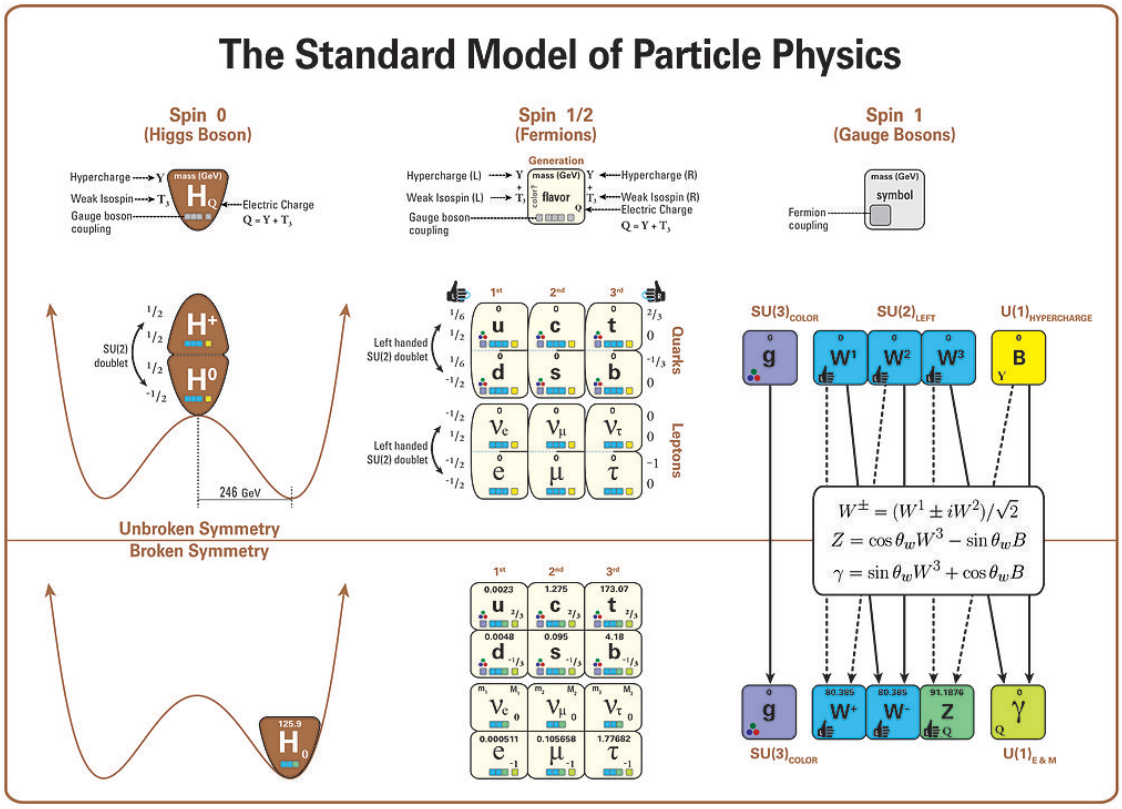

Figure 1.1 – Illustration of the standard model of particle physics, taken from [17].

1.1 Particles, interactions and symmetries

The standard model is based on Quantum Field Theory, and describes matter as made of elementary particles which are fermions (with spin 1/2), interacting through exchange of virtual particles which are vector bosons (with spin 1). These particles are massive if they couple to the Higgs field, mediated by the Higgs boson (with spin 0). This structure is illustrated in Fig. 1.1. Before describing the SM Lagrangian, a quick overview of the constituents and the symmetries included in this theory is presented, following roughly Fig. 1.1 from the right to the left.

1.1.1 The elementary particles

Currently, the behaviour of matter is described with four fundamental interactions: gravity, the strong force, the electromagnetic force and the weak interaction; out of which only the last three are in the SM. A fully satisfactory quantum theory of gravity has yet to be formulated. However at the elementary particle scale, the effect of gravity is so weak that it can be neglected (see Table 1.1). The three SM interactions are mediated through vector bosons, which exchange the three fundamental charges: colour, weak isospin (T_3) and hypercharge (Y).

The strong interaction is mediated by gluons (g) and takes place between particles carrying a *colour* charge, which can take six values: (anti)red, (anti)green and (anti)blue. Only quarks and gluons carry a colour and therefore feel the strong force. In nature, only strong colourless bound states of quarks are observed, which are called *hadrons*. Among the hadrons, two types can be

Table 1.1 – Relative strengths of the four fundamental interactions observed in nature [14]. Notice that their couplings, therefore the relative strengths quoted here, depend on the energy or the distance scales considered.

Interaction	Strength
Strong	10
Electromagnetic	10^{-2}
Weak	10^{-13}
Gravitational	10^{-42}

made: the *mesons*, bound states of one quark and one antiquark ($q\overline{q}$); and the *baryons*, bound states of three quarks or three antiquarks (qqq or $\bar{q}\bar{q}\bar{q}$). There are some experimental evidence of more exotic hadrons such as tetraquark and pentaquarks (see for instance Ref. [18]and [19]).

Even though the gluons are massless, the strong interaction does not have an infinite range, because of the way in which the strong coupling constant α_s varies with the spatial (or energy) scale considered. At large distance, or low energy, the effective coupling increases, making the proton a bound states of quarks. Whereas at short distance, smaller than the size of a proton, the coupling becomes smaller and reaches the quark *asymptotic freedom*. That is why at high energy the strong interaction can be described perturbatively.

The residual effects of the strong interaction inside the nucleons are the origin of the nuclear force, analogous to the Van der Waals force between neutral objects which has its origin from the electromagnetic interaction.

The electromagnetic interaction is mediated by photons (γ) and takes place between particles which have an electric *charge* ($Q = Y + T_3$). Since the photon is massless, the interaction has an infinite range and is the only "Standard Model" force which can have direct macroscopic effects, such as electromagnetic waves or Coulomb interaction.

The weak interaction is mediated by three vector bosons, two electrically charged, the W^+ and W^-, and one neutral, the Z. Because of their high masses (see Table 1.2) the interaction has a very short range, making it *weak*. Unlike the strong and electromagnetic interactions, the weak interaction violates a large number of the SM symmetries(see Sec.1.1.2), and couples to all the fermions: the quarks, the charged leptons (electron e, muon μ and tau τ) and the neutral leptons (neutrinos ν_e,ν_μ and ν_τ).

In the top of Fig. 1.1, there are only massless fermions and gauge bosons (g, W^1, W^2, W^3 and B). The theory of Glashow Weinberg and Salam unifies the electromagnetic and weak interactions into the electroweak interaction with the $\mathrm{SU}(2)_L \times \mathrm{U}(1)_Y$ gauge symmetry, which would be spoiled if the bosons and fermions were massive. In order to describe the observed massive $W^\pm$ and Z bosons, the $\mathrm{SU}(2)_L \times \mathrm{U}(1)_Y$ symmetry is spontaneously broken into $\mathrm{U}(1)_{em}$ by the Brout-Englert-Higgs mechanism (see Sec. 1.2.3). Thanks to this mechanism, the fermions (see Sec. 1.2.4) and the electroweak bosons get dynamically a mass. The resulting mass eigenstates $W^\pm$, Z and γ are a mixture of W^1, W^2, W^3 and B, as illustrated in Fig. 1.1, and the weak isospin and the hypercharge are not conserved, only their sum $Q = Y + T_3$.

Finally, as this is related to the subject of this thesis, it is important to notice that the quarks and leptons follow a particular mass hierarchy (see Table. 1.2), with three generations which are poorly coupled between each other, as explained in Sec. 1.3).

Table 1.2 – Masses of the elementary particles of the standard model [20]

Quarks		Leptons		Gauge bosons		Higgs boson	
u	2.3 MeV	e	0.511 MeV	g	0	H^0	125.7 GeV
d	4.8 MeV	ν_e	< 2 eV	γ	0		
s	95 MeV	μ	105.66 MeV	W	80.385 GeV		
c	1.275 GeV	ν_μ	< 0.19 MeV	Z	91.1876 GeV		
b	4.18 GeV	τ	1776.82 MeV				
t	173.21 GeV	ν_τ	< 18.2 MeV				

1.1.2 Symmetries

Physics tries to describe the evolution of the phenomena observed in nature. Often, the starting point of any description of these phenomena uses a conservation law (like the energy one). That is why symmetries in particle physics play a fundamental role. Emmy Noether's theorem demonstrates that a continuous symmetry is equivalent to a conservation law [21]. Hence, a translation in time corresponds to the energy conservation, a translation in space corresponds to the momentum conservation, rotations correspond to the angular momentum conservation and a gauge symmetry corresponds to the conservation of the associated charge. As a consequence, symmetries are a useful tool to build a theoretical model (a Lagrangian) which describes the conservation laws observed in nature.

In quantum field theory a symmetry is related to an operator O, which transforms the states in such a way that the physical observables are unchanged. In particular, two conditions are needed [16]:

1. The vacuum must be invariant : $O|0\rangle = |0\rangle$.
2. The action (*i.e.* the Lagrangian) must be invariant: $S \equiv \int d^4x\, \mathscr{L}(t,\vec{x}) \overset{\text{symmetry}}{\longrightarrow} S$.

A symmetry is not always exact. It can be conserved by one interaction and not by another. There are two ways for breaking a symmetry:

1. Explicitly: the Lagrangian is not invariant under the symmetry operation. This is the case of parity violation for the weak interaction for instance.
2. Spontaneously: the ground state is not invariant under the symmetry operation. But the Lagrangian still conserves the symmetry. This is the case of the $\mathrm{SU}(2)_L \times \mathrm{U}(1)_Y$ electroweak symmetry, which is broken into $\mathrm{U}(1)_{em}$ because of a non zero vacuum expectation value of the Higgs field.

In addition to continuous symmetries, there are the discrete space-time symmetries C, P and T and the number conservation laws of leptons, baryons and quark flavour.

Parity

The parity operation P transforms a space coordinate $\vec{x}$ into $-\vec{x}$. It corresponds to a mirror reflection followed by a 180° rotation. For instance, it transforms a left-handed particle into a right-handed particle. The strong and electromagnetic interactions conserve parity, whereas the weak interaction maximally violates parity [22]. Indeed, it couples only left-handed fermions (or right-handed antifermions). An illustration is the $\pi^+ \to \mu^+ \nu_\mu$ decay, where the antimuon and the neutrino are emitted almost always with a left-handed helicity (*i.e.* a spin projection in the opposite direction of their momentum, closely related to the chirality), to conserve the spin.

Charge conjugation

The charge conjugation C transforms a particle into its antiparticle, which has the same mass, momentum and spin but opposite internal quantum numbers such as electric charge. C is again conserved by the strong and electromagnetic interactions and maximally violated by weak interaction. For instance, the electromagnetic decay of a C eigenstate π^0, of eigenvalue +1 and spin 0, can only produce two photons and not three (photons have a C eigenvalue of −1, and charge conjugation is a multiplicative number). And the weak decay $\pi^- \to \mu^- \overline{\nu}_\mu$, charged conjugate of $\pi^+ \to \mu^+ \nu_\mu$, almost never happens since it produces a left-handed antineutrino.

Time reversal

The time reversal symmetry T reflects the time coordinate t into $-t$, while leaving the spatial coordinates unchanged. Assuming CPT invariance, it is equivalent to CP symmetry. Again, only the weak interaction is not invariant under a T transformation. This phenomenon has been directly observed for the first time by the BaBar collaboration [23].

CP

The CP transformation is the conjugation of C and P operators. Since it transforms a left-handed fermion into a right-handed fermion, is an approximate symmetry of the weak interaction. For instance the decays $\pi^+ \to \mu^+ \nu_\mu$ with a left-handed neutrino, occurs with the same rate as its CP conjugate $\pi^- \to \mu^- \overline{\nu}_\mu$, with a right-handed antineutrino. However, CP violation appears with the presence of the second and third generation of quarks. It was experimentally observed for the first time in 1964 by Cronin and Fitch [24], extensively studied by the B-factories BaBar and Belle, and the LHCb collaboration is pursuing the work. The current CP violation measurements are in good agreement with the Cabbibo-Kobayashi-Maskawa (CKM) model, presented in Sec. 1.3.

CPT

The CPT symmetry is required to be exact for any interaction [25]. This is due to the so-called CPT theorem [25–28], proving that any quantum field theory must be CPT invariant. The consequence of this theorem is that particles and antiparticles have the same masses and lifetimes. For now, no evidence of CPT violation has been found, see for instance the dedicated section in Ref. [20].

Lepton number

Lepton number (1 for lepton, -1 for antilepton, in a same generation) is always strictly conserved by electromagnetic interaction. The weak interaction also appears to conserve the absolute value

of the three separate lepton numbers L_e, L_μ and L_τ, apart from the neutrino in the phenomenon of oscillations.

Baryon number

Baryon number (1 for baryon, -1 for antibaryon, 0 for anything else) is also found to be conserved. Its violation could allow the proton to decay, like in the $p \rightarrow e^+\pi^0$ transition, as predicted by some Grand Unification Theory [29].

Quark flavour

Quark flavour is conserved by the strong and electromagnetic interactions, however the weak interaction does not. An up-quark can turn into a down-quark, a bottom-quark can turn into a charm or a up-quark. This flavour change, described with the CKM model, occurs only with charged currents. Hence, flavour-changing neutral currents (FCNC) are only second order effects in the SM.

1.2 The standard model Lagrangian

The standard model is based on quantum field theory. In this approach, particles are seen as quanta of excitation of different fields with regards to a ground state, called "vacuum". These fields are encoded in a Lagrangian, which gives the propagation equation of a given particle thanks to the Euler-Lagrange formula. According to the particle nature, scalar, spinor or vector, the Lagrangian has an appropriate structure, leading to the Klein-Gordon, Dirac and Proca equation respectively [14].

Quarks and leptons, which are fermions, are described by spinor fields. To explain the presence of the gluons, photons, $W^\pm$ and Z vector bosons, the Lagrangian of the standard model is supposed to follow the $\mathrm{SU(3)}_C \times \mathrm{SU(2)}_L \times \mathrm{U(1)}_Y$ local gauge symmetry. To conserve this local symmetry, in addition to the quark and lepton free fields, new fields are required in the Lagrangian. These additional fields are the vector bosons of the three fundamental interactions. $\mathrm{SU(3)}_C$ is the "colour" symmetry and is at the origin of the Quantum ChromoDynamics Lagrangian ($\mathscr{L}_{\mathrm{QCD}}$), responsible for the strong interaction (Sec. 1.2.1). $\mathrm{SU(2)}_L \times \mathrm{U(1)}_Y$ is the weak isospin and hypercharge (Y) symmetry ($\mathscr{L}_{\mathrm{EW}}$), describing the electroweak interaction (Sec. 1.2.2).

The standard model Lagrangian can be written in a general way as

$$\begin{aligned} \mathscr{L} = & \underbrace{\mathscr{L}_{\mathrm{QCD}}}_{\text{Strong interaction (gluons)}} + \underbrace{\mathscr{L}_{\mathrm{EW}}}_{\text{Electroweak interaction } (\gamma,\ \mathrm{W}^\pm \text{ and Z})} \\ & + \underbrace{\mathscr{L}_{\mathrm{Higgs}}}_{\text{Higgs mechanism (masses of } \mathrm{W}^\pm, \mathrm{Z} \text{ and } \mathrm{H}^0)} + \underbrace{\mathscr{L}_{\mathrm{Yukawa}}}_{\text{Yukawa coupling (fermion masses)}} . \end{aligned} \tag{1.1}$$

The third term corresponds to the Higgs mechanism responsible for the $W^\pm$, Z, H^0 boson masses, and their interactions (Sec. 1.2.3). The last term is the Yukawa interaction between the fermions and the Higgs field, which creates the fermion masses and their flavour mixing (Sec. 1.2.4).

In this Lagrangian, some terms describe the propagation of the fields, free from any interaction, and lead to the propagators in the Feynman diagrams. The other terms correspond to the

interactions. For a given interaction, the transition probability from an initial state $|i\rangle$ to a final state $\langle f|$ is deduced from the squared amplitude of the S matrix element

$$S_{fi} = \langle f|S|i\rangle \,. \tag{1.2}$$

It can be shown that the S matrix depends on the exponential of the interaction Lagrangian $\mathscr{L}_{\text{int}}$ [15],

$$S \sim e^{i\int d^4x\, \mathscr{L}_{\text{int}}} \,. \tag{1.3}$$

If the coupling constant of the corresponding interaction is small enough, this exponential can be perturbatively expanded, leading to the vertices in the Feynman diagrams description, widely used in particle physics.

The next sections briefly describe the four terms of the standard model Lagrangian, with a particular emphasise on the origin of the CKM matrix.

1.2.1 Quantum ChromoDynamics

The QCD Lagrangian describes the strong interaction between the quarks and gluons with

$$\mathscr{L}_{\text{QCD}} = -\frac{1}{4} Tr\left[G_{\mu\nu}G^{\mu\nu}\right] - \sum_{f=1}^{n_f} \overline{\psi}_f (\not{D} + m_f)\psi_f \,. \tag{1.4}$$

The trace on the $G^a_{\mu\nu}$ gluon field tensor corresponds to a sum over the colour states $a \in \{1,...,8\}$. It is expressed as

$$G^a_{\mu\nu} = \partial_\mu A^a_\nu - \partial\nu A^a_\mu + g_S f^{abc} A^b_\mu A^c_\nu, \tag{1.5}$$

where g_S denotes the strong coupling constant, A^a_μ the gluon fields and f^{abc} the structure constant of SU(3).
The D_μ covariant derivative is, with t^a the SU(3) generators,

$$D_\mu = \partial_\mu - i g_S t^a A^a_\mu \,. \tag{1.6}$$

The quark fields, for a given flavour f, are represented by the column vector ψ_f, which includes the three colour states. In this form, the QCD Lagrangian is invariant under a *CP* transformation. However another gauge-invariant term can be also added:

$$\mathscr{L}_{\not{CP}} = \theta\, Tr\left[G_{\mu\nu}G_{\alpha\beta}\right]\varepsilon^{\mu\nu\alpha\beta} \,. \tag{1.7}$$

This term in not invariant under a *CP* transformation. Hence, for a non vanishing value of the θ parameter, the strong interaction could violate *CP* symmetry. At present, no evidence of such effect has been measured. Experimental limits on the electric dipole moment of the neutron imply that $|\theta| \lesssim 10^{-10}$ [20]. This absence of *CP* violation in QCD is called the *strong CP problem*.

1.2.2 Electroweak Lagrangian

To account for the maximal parity violation observed in the weak interaction, the fermions are described with left-handed doublets and right-handed singlets

$$Q_L = \begin{pmatrix} U \\ D \end{pmatrix}_L \,, \qquad E_L = \begin{pmatrix} \nu_l \\ l^- \end{pmatrix}_L \,, \qquad U_R,\ D_R,\ l^-_R, \tag{1.8}$$

where U, D, ν_l and l^- represent the flavour eigenstates of the up-type quarks, down-type quarks, neutral leptons and charged leptons, respectively. With the three generations of the standard model they are

$$U = \begin{pmatrix} u \\ c \\ t \end{pmatrix}, \qquad D = \begin{pmatrix} d \\ s \\ b \end{pmatrix}, \qquad \nu_l = \begin{pmatrix} \nu_e \\ \nu_\mu \\ \nu_\tau \end{pmatrix}, \qquad \text{and } l^- = \begin{pmatrix} e^- \\ \mu^- \\ \tau^- \end{pmatrix}. \tag{1.9}$$

And the chiral fields are obtained by projection: $\psi_{L/R} = \frac{1}{2}(1 \mp \gamma_5)\psi$.

The interaction between the fermion fields and the gauge bosons of the electroweak force is based on three types of currents:

- Charged current:
$$J_\mu^+ = \overline{U}_L \gamma_\mu D_L + \overline{l}_L \gamma_\mu \nu_L \text{ , and h.c. ,} \tag{1.10}$$
- Neutral current:
$$J_\mu^3 = \frac{1}{2}\left(\overline{U}_L \gamma_\mu U_L - \overline{D}_L \gamma_\mu D_L + \overline{\nu}_L \gamma_\mu \nu_L - \overline{l}_L \gamma_\mu l_L\right), \tag{1.11}$$
- Electromagnetic current:
$$\begin{aligned} J_\mu^{em} = &\frac{2}{3}\overline{U}_L \gamma_\mu U_L - \frac{1}{3}\overline{D}_L \gamma_\mu D_L - \overline{l}_L \gamma_\mu l_L \\ &+ \frac{2}{3}\overline{U}_R \gamma_\mu U_R - \frac{1}{3}\overline{D}_R \gamma_\mu D_R - \overline{l}_R \gamma_\mu l_R \,. \end{aligned} \tag{1.12}$$

These currents couple to the vector bosons $W^\pm$, Z and γ, and give the electroweak interaction Lagrangian

$$\mathscr{L}_{EW}^{int} = \frac{g}{\sqrt{2}}\left(J_\mu^+ W^{-\,\mu} + J_\mu^- W^{+\,\mu}\right) + \frac{g}{\cos\theta_W}\left(J_\mu^3 - \sin^2\theta_W J_\mu^{em}\right) Z^\mu + e J_\mu^{em} A^\mu \,, \tag{1.13}$$

where the first term corresponds to the $W^\pm$ exchange, the second to the Z exchange and the third to the photon exchange; g and e are the constants of the weak and electromagnetic interaction respectively. The angle θ_W defines the mixing between the isospin and hypercharge eigenstates W_μ^3 and B_μ of the $\mathrm{SU}(2)_L$ and $\mathrm{U}(1)_Y$ groups respectively, into the mass eigenstates Z and γ. At this point, there is no mass term for the electroweak bosons included in the Lagrangian. Indeed, a simple mass term would spoil the local symmetry $\mathrm{SU}(2)_L \times \mathrm{U}(1)_Y$. Instead, the masses of the gauge bosons are generated dynamically thanks to the Higgs mechanism.

1.2.3 Higgs mechanism

The electromagnetic and weak interactions are unified in the electroweak interaction under the $\mathrm{SU}(2)_L \times \mathrm{U}(1)_Y$ gauge symmetry. $\mathrm{SU}(2)_L$ is the weak isospin symmetry and $\mathrm{U}(1)_Y$ is the hypercharge symmetry. However, these gauge symmetries must be broken, since experimentally isospin and hypercharge are not observed to be conserved. The relevant quantity which is conserved is the electric charged, given by the operator

$$Q = \tau_3 + Y, \tag{1.14}$$

where $\tau_3 = \frac{\sigma_3}{2}$ is the third generator of the SU(2) group (σ_3 is the third Pauli matrix), and Y the generator of the U(1) group. Thus, the $\mathrm{SU}(2)_L \times \mathrm{U}(1)_Y \rightarrow \mathrm{U}(1)_{em}$ symmetry breaking is expected.

This breaking is obtained spontaneously thanks to the Higgs mechanism, with the introduction of a complex doublet H, whose corresponding Lagrangian is

$$\mathscr{L}_{\text{Higgs}} = \left(D_\mu H\right)^\dagger \left(D_\mu H\right) + m^2 H^\dagger H - \lambda (H^\dagger H)^2 \,. \tag{1.15}$$

Written in this form the Lagrangian is invariant under the $\mathrm{SU}(2)_L \times \mathrm{U}(1)_Y$ symmetry. The covariant derivative is

$$D_\mu H = \partial_\mu H - i g W_\mu^a \tau^a H - \frac{1}{2} i g' B_\mu H, \tag{1.16}$$

where B_μ is the hypercharge gauge boson and W_μ^a are the SU(2) gauge bosons. g and g' are the $\mathrm{SU}(2)_L$ and $\mathrm{U}(1)_Y$ couplings. The potential in the Lagrangian (1.15) $V(H) = -m^2|H|^2 + \lambda|H|^4$ induces a non zero vacuum expectation value (vev). Hence, the complex doublet can be written as

$$H = \begin{pmatrix} 0 \\ \frac{v+h}{\sqrt{2}} \end{pmatrix}, \tag{1.17}$$

with h an excitation from the ground state v. In this formulation, the interaction term between the gauge bosons and the Higgs doublet becomes (considering only the term with v)

$$|D_\mu H|^2 = g^2 \frac{v^2}{8} \left[\left(W_\mu^1\right)^2 + \left(W_\mu^2\right)^2 + \left(\frac{g'}{g} B_\mu - W_\mu^3\right)^2 \right]. \tag{1.18}$$

To make appear the massive Z_μ boson and the massless A_μ photon, the neutral bosons B_μ and W_μ^3 are rotated with the weak mixing angle θ_W such that

$$\begin{aligned} B_\mu &= \cos\theta_{\mathrm{W}} A_\mu - \sin\theta_{\mathrm{W}} Z_\mu \,, \\ W_\mu^3 &= \sin\theta_{\mathrm{W}} A_\mu + \cos\theta_{\mathrm{W}} Z_\mu \,. \end{aligned} \tag{1.19}$$

Hence, the $\left(\frac{g'}{g} B_\mu - W_\mu^3\right)^2$ term becomes equal to the Z boson mass term $\frac{1}{2} m_Z^2 Z_\mu Z^\mu$ with $m_z = \frac{g v}{2\cos\theta_{\mathrm{W}}}$. Furthermore, the A_μ field does not get a mass term, leading to the correct description of the photon. The charged bosons $W^\pm$ correspond to the linear combination

$$W_\mu^\pm = \frac{1}{\sqrt{2}} \left(W_\mu^1 \mp i W_\mu^2\right), \tag{1.20}$$

and have the mass $m_W = \frac{g v}{2} = m_Z \cos\theta_{\mathrm{W}}$.

Eventually, from a Lagrangian invariant under a $\mathrm{SU}(2)_L \times \mathrm{U}(1)_Y$ transformation, a new formulation is obtained, which hides this symmetry. Indeed, the symmetry does not leave invariant the ground state. Thanks to this spontaneous symmetry breaking, the weak bosons get masses and a new neutral boson appears, as the excitation h of the Higgs field H. This mechanism was predicted in 1964 by three independent groups of physicists: F. Englert and R. Brout [30]; P. Higgs [31, 32]; G. Guralnik, C. Hagen and T. Kibble [33]. The Higgs boson was discovered in July 2012 by the ATLAS and CMS collaborations using the data recorded at the CERN Large Hadron Collider [34, 35].

The Higgs field does not only provide masses to the gauge bosons, but also generates the fermion masses through Yukawa interaction (see next section).

1.2.4 Yukawa interaction and quark masses

As for the gauge bosons, explicit fermion mass terms cannot be included in the SM Lagrangian without breaking the $SU(2)_L$ symmetry. Therefore to describe massive fermions, a Yukawa interaction term between the fermions and the Higgs field is added. Only the quark sector will be developed here, since it is directly relevant to the analysis presented in this thesis [1] (see Chap. 5). The Lagrangian related to the quark sector is

$$\mathscr{L}_{\text{Yukawa}} = \quad -Y^d_{ij}\,\overline{Q}^i_L\,H\,d^j_R \quad -Y^u_{ij}\,\overline{Q}^i_L\,\tilde{H}\,u^j_R \quad + h.c. \tag{1.21}$$

The indices i and j represent the sum over all the fermion generations, $Q^i_L = \begin{pmatrix} U_i \\ D_i \end{pmatrix}$ is the component of the quark doublet defined in Eq. (1.8) corresponding to the i^{th} generation , the Y_{ij} are the Yukawa matrix elements and the Higgs field conjugate is defined as

$$\tilde{H} \equiv i\sigma_2 H^* = i\begin{pmatrix} 0 & -i \\ i & 0 \end{pmatrix}\begin{pmatrix} \phi^+ \\ \phi^0 \end{pmatrix}^* = \begin{pmatrix} \phi^0 \\ -\phi^- \end{pmatrix}. \tag{1.22}$$

With the electroweak spontaneous symmetry breaking, the Higgs field gets a vev with

$$H = \begin{pmatrix} \phi^+ \\ \phi^0 \end{pmatrix} \rightarrow \begin{pmatrix} 0 \\ \frac{v}{\sqrt{2}} \end{pmatrix} \qquad \text{and} \qquad \tilde{H} = \begin{pmatrix} \phi^0 \\ -\phi^- \end{pmatrix} \rightarrow \begin{pmatrix} \frac{v}{\sqrt{2}} \\ 0 \end{pmatrix}. \tag{1.23}$$

Thus the Yukawa Lagrangian can be simplified as

$$\begin{aligned} \mathscr{L}_{\text{Yukawa}} &= -\frac{v}{\sqrt{2}} Y^d_{ij}\,\overline{d}^i_L d^j_R - \frac{v}{\sqrt{2}} Y^u_{ij}\,\overline{u}^i_L u^j_R \quad + \quad h.c. \\ &= -\frac{v}{\sqrt{2}}\left[Y^d \overline{D}_L d_R + Y^u \overline{U}_L u_R\right] \quad + \quad h.c.\,, \end{aligned} \tag{1.24}$$

where in the last line the matrix notation is adopted. The quark mass matrices can be now defined from the Yukawa matrices

$$M^u = \frac{v}{\sqrt{2}} Y^u \qquad \text{and} \qquad M^d = \frac{v}{\sqrt{2}} Y^d\,. \tag{1.25}$$

The values of the Yukawa couplings are arbitrary, that is why the masses of the quarks are free parameters of the SM. Moreover, these couplings can be complex and therefore lead to *CP* violation (see next section).

1.3 The Cabbibo-Kobayashi-Maskawa paradigm

The weak interaction is experimentally observed not to conserve the quark flavours. A quark b for instance can decay into a quark c or a quark u. Moreover the flavour transition is always accompanied by a charge exchange [2]. To describe quark flavour mixing, Cabbibo's idea [38] was extended to multiple quark generations by Kobayashi and Maskawa [39]. The fundamental principle is that the quark eigenstates of the weak interaction differ from their mass eigenstates.

[1] A similar Yukawa interaction can be adopted for the leptons. It leads also to a flavour mixing matrix, describing the neutrino oscillation, called PMNS [36,37]

[2] At least, at the tree level.

1.3.1 The CKM matrix

Since the weak interaction mixes the quark flavour, in the weak basis the mass matrices M^u and M^d defined in Eq. (1.25) are not diagonal. In order to diagonalise them, a basis change is performed with four unitary matrices $V_{u,L}$, $V_{d,L}$, $V_{u,R}$, and $V_{d,R}$, such that

$$\mathscr{M}^u = V_{u,L} M^u V_{u,R}^\dagger \qquad \text{and} \qquad \mathscr{M}^d = V_{d,L} M^d V_{d,R}^\dagger \tag{1.26}$$

are the diagonal mass matrices. As a result, the quark mass eigenstates are obtained from the weak basis made of the states U_L, D_L, u_R and d_R, with

$$\begin{aligned} U_L^m &= V_{u,L} U_L \quad , \quad u_R^m = V_{u,R} u_R \, , \\ D_L^m &= V_{d,L} D_L \quad , \quad d_R^m = V_{d,R} d_R \, . \end{aligned} \tag{1.27}$$

Thus, the Yukawa Lagrangian (1.24) in the mass eigenstates basis is simplified into

$$\mathscr{L}_{\text{Yukawa}} = -\overline{D}_L^m \mathscr{M}^d d_R^m - \overline{U}_L^m \mathscr{M}^d u_R^m + h.c. \tag{1.28}$$

The basis change on the electroweak Lagrangian (1.13) has two consequences:

- The neutral currents are unchanged. For instance the term $\overline{U}_L \gamma_\mu U_L$ is invariant,

$$\overline{U}_L \gamma_\mu U_L \quad = \quad \overline{U}_L^m V_{u,L} \gamma_\mu V^\dagger{}_{u,L} U_L^m \quad = \quad \overline{U}_L^m \gamma_\mu U_L^m \, . \tag{1.29}$$

  Hence, only identical flavours of quarks can interact through neutral current. This corresponds to the absence of *flavour neutral changing currents* (FCNC) at the tree level in the SM, and is known as the GIM mechanism [40].

- The behaviour of the charged currents is different. They are not identical if they are written in the *mass* or *weak* basis. For instance, the term $\overline{U}_L \gamma_\mu D_L$ is transformed according to

$$\overline{U}_L \gamma_\mu D_L \quad = \quad \overline{U}_L^m V_{u,L} \gamma_\mu V^\dagger{}_{d,L} D_L^m \quad = \quad \overline{U}_L^m \gamma_\mu V_{CKM} D_L^m, \tag{1.30}$$

  with the CKM matrix defined as

$$V_{CKM} \equiv V_{u,L} V^\dagger{}_{d,L} = \begin{pmatrix} V_{ud} & V_{us} & V_{ub} \\ V_{cd} & V_{cs} & V_{cb} \\ V_{td} & V_{ts} & V_{tb} \end{pmatrix} . \tag{1.31}$$

  As a consequence, a given down-type quark in a mass eigenstate d_i^m can couple to an up-type quark with a different flavour u_j^m (and the opposite). The probability of the flavour changing transitions are directly related to the squared module of the V_{ij} elements of the CKM matrix. That is why, for instance, the $b \to c$ and $b \to u$ transitions are observed, and with different probabilities.

1.3.2 *CP* violation phase

To describe the *CP* violation observed in charged weak interaction, a complex phase must be present in the charged current, and appears in the CKM matrix. A $n \times n$ unitary matrix has a total of n^2 independent real parameters. Since the quark fields can be freely rotated with arbitrary phases, $(2n-1)$ relative phases vanish among the n^2 parameters (one global phase

remains). Hence, at the end, the CKM matrix has $(n-1)^2$ independent real parameters, among them $N_{\text{angles}} = \frac{1}{2}n(n-1)$ angles and $N_{\text{phases}} = \frac{1}{2}(n-1)(n-2)$ phases.

This implies that for two generations of quarks, only one angle is needed (the Cabbibo angle θ_c) and no phase appears. Therefore, no *CP* violation can occur with only two families. For three generations, there are three angles and one phase which are irreducible. This is illustrated by the standard parameterisation of the CKM matrix

$$V_{CKM} = \begin{pmatrix} c_{12}c_{13} & s_{12}c_{13} & s_{13}e^{-i\delta} \\ -s_{12}c_{23} - c_{12}s_{23}s_{13}e^{i\delta} & c_{12}c_{23} - s_{12}s_{23}s_{13}e^{i\delta} & s_{23}c_{13} \\ s_{12}s_{23} - c_{12}c_{23}s_{13}e^{i\delta} & -c_{12}s_{23} - s_{12}c_{23}s_{13}e^{i\delta} & c_{23}c_{13} \end{pmatrix}, \tag{1.32}$$

where $c_{ij} = \cos\theta_{ij}$ and $s_{ij} = \sin\theta_{ij}$ are the cosine and the sine of the three mixing angles. The phase δ is the only *CP* violation source in the SM. Additional sources of *CP* violation would require, for instance, a more complex Higgs sector, new quark generations, or *CP* violation in the leptonic sector.

1.3.3 Wolfenstein parameterisation

To highlight the hierarchy encoded in the CKM matrix, Wolfenstein developed a parametrisation through an expansion in powers of $\lambda \equiv \sin\theta_c \approx 0.22$ [1]. Using the convention [41]

$$\begin{aligned} s_{12} &\equiv \lambda\,, \\ s_{23} &\equiv A\lambda^2\,, \\ s_{13}e^{-i\delta} &\equiv A\lambda^3(\rho - i\eta), \end{aligned} \tag{1.33}$$

resulting in

$$V_{CKM} = \begin{pmatrix} 1 - \frac{\lambda^2}{2} & \lambda & A\lambda^3(\rho - i\eta) \\ -\lambda & 1 - \frac{\lambda^2}{2} & A\lambda^2 \\ A\lambda^3(1 - \rho - i\eta) & -A\lambda^2 & 1 \end{pmatrix} + \mathcal{O}\left(\lambda^4\right). \tag{1.34}$$

From this development a clear pattern is unveiled: the matrix is almost diagonal and symmetric, and its elements are smaller the farther away from the diagonal. Hence, transitions inside a family are favoured, and transitions between two different families are suppressed. Furthermore, this suppression becomes larger when it involves the third quark generation. By increasing order of suppression we have the $2 \to 1$, $3 \to 2$ and $3 \to 1$ generation transitions.

1.3.4 Unitarity triangle

The CKM matrix is unitary, and this implies the relations

$$\sum_{i=1}^{3} V_{ij}V_{ik}^* = \delta_{jk} \qquad \text{and} \qquad \sum_{j=1}^{3} V_{ij}V_{kj}^* = \delta_{ik}. \tag{1.35}$$

The six vanishing relations can be graphically represented by triangles in the complex plane. It can be shown that all the triangles have the same area [42]. However, among the six triangles only two are not "squashed" [16], and the most commonly used is derived from the relation

$$V_{ud}{V_{ub}}^* + V_{cd}{V_{cb}}^* + V_{td}{V_{tb}}^* = 0\,, \tag{1.36}$$

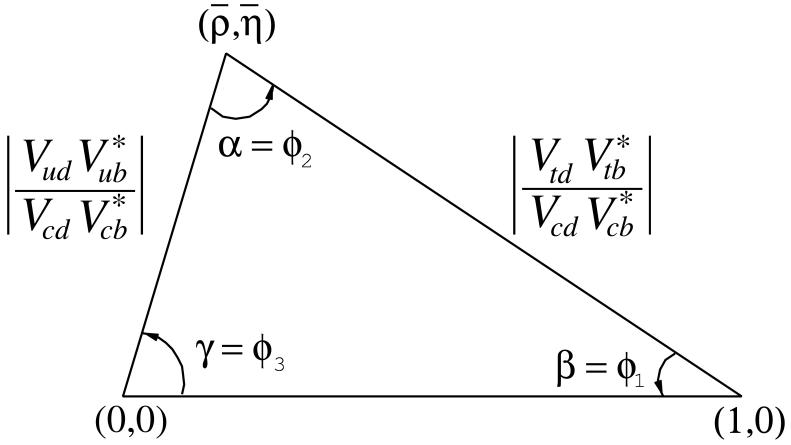

Figure 1.2 – The unitarity triangle of the CKM matrix.

which can be normalised by the best known term $V_{cd}V_{cb}{}^*$, leading to

$$\frac{V_{ud}V_{ub}{}^*}{V_{cd}V_{cb}{}^*}+1+\frac{V_{td}V_{tb}{}^*}{V_{cd}V_{cb}{}^*}=0\,. \tag{1.37}$$

Eq. (1.37) is the definition of *the* unitarity triangle (UT) of the CKM matrix, and is illustrated on Fig. 1.2. The triangle apex is the complex number $(\overline{\rho},\overline{\eta})$, which is by definition [41]

$$\overline{\rho}+i\overline{\eta}\equiv\frac{V_{ud}V_{ub}{}^*}{V_{cd}V_{cb}{}^*}\,, \tag{1.38}$$

and leads to the relation

$$\rho+i\eta=\frac{\sqrt{1-A^2\lambda^4}(\overline{\rho}+i\overline{\eta})}{\sqrt{1-\lambda^2}[1-A^2\lambda^4(\overline{\rho}+i\overline{\eta})]}\,. \tag{1.39}$$

The two sides of the UT which are not normalised to unity are, to all orders of the Wolfenstein expansion,

$$\begin{aligned}R_u&=\left|\frac{V_{ud}V_{ub}{}^*}{V_{cd}V_{cb}{}^*}\right|=\sqrt{\overline{\rho}^2+\overline{\eta}^2}\,,\\ R_t&=\left|\frac{V_{td}V_{tb}{}^*}{V_{cd}V_{cb}{}^*}\right|=\sqrt{(1-\overline{\rho})^2+\overline{\eta}^2}\,.\end{aligned} \tag{1.40}$$

And the three angles are

$$\alpha=\arg\left(-\frac{V_{td}V_{tb}{}^*}{V_{ud}V_{ub}{}^*}\right),\quad \beta=\arg\left(-\frac{V_{cd}V_{cb}{}^*}{V_{td}V_{tb}{}^*}\right),\quad \gamma=\arg\left(-\frac{V_{ud}V_{ub}{}^*}{V_{cd}V_{cb}{}^*}\right)\,. \tag{1.41}$$

It can be noted that, according to the Wolfenstein expansion, only the V_{ub} and V_{td} terms have a significant imaginary part. Furthermore, the *CP* violation phase can be expressed as [41]

$$\delta=\gamma+A^2\lambda^4\eta+\mathcal{O}\left(\lambda^6\right)\,. \tag{1.42}$$

Therefore, the γ angle can be well approximated as the complex phase of V_{ub}. The subject of this thesis is the measurement of γ with the $B^0\to DK^{*0}$ decay. The measurement principle is detailed in the next chapter. As further explained in Sec. 1.4, an important goal of the flavour physics is to precisely measure the CKM matrix elements to test the consistency of the resulting R_u, R_t, α, β and γ UT parameters. Any significant tension preventing the UT to be closed at its $(\overline{\rho},\overline{\eta})$ apex could be an evidence of new physics.

1.4 Testing the CKM model as a probe of new physics

The standard model describes with a tremendous precision the elementary particles found in nature, up to the electroweak scale ($\sim 100\,\text{GeV}$). However, there are several good reasons to believe that this theory is inaccurate to higher energy. These reasons are briefly mentioned in Sec. 1.4.1. Thus, particle physicists intensively look for experimental evidences of physics beyond the standard model (BSM), also known as *new physics*. Flavour physics is an excellent tool for hunting this new physics, with the consistency test of the CKM paradigm (Sec. 1.4.2).

1.4.1 The standard model is not the complete answer

As already mentioned, the standard model describes successfully all the current experimental observations (cross-sections, branching ratios, asymmetries, angular distributions...). But it cannot properly explain, for instance, the following points:

- Gravitation is well described by general relativity, which is incompatible with the actual SM. There is no satisfactory quantum theory of gravitation yet, and therefore the SM is expected to fail, if not before, at the Planck scale ($\sim 10^{19}\,\text{GeV}$).
- The Higgs boson mass seems *unnatural*, in a sense that the quantum correction needed to stabilise its mass at higher energy than the electroweak scale, are much larger than its on-shell mass. This implies a *fine tuning*, which could be avoided by the introduction of new particles which compensate the SM Higgs mass radiative corrections. The theory of supersymmetry (SUSY) proposes such new particle candidates.
- Cosmological observations indicate that the particles described in the SM can account only for approximately 5% of the total energy of the universe [43]. The rest is composed of dark matter (about 25%) and dark energy (about 70%). The dark matter explains, for instance, the velocities in the galaxy rotations. Some extensions of the SM provide good candidates of weakly interacting particle (WIMP), which could be dark matter objects.
- The current theory of Big Bang assumes that matter and antimatter were created in exactly equal amounts. However, in our universe we are only surrounded by matter. To explain this Matter/Antimatter asymmetry, Sakharov identified some necessary conditions, including *CP* violation [44]. Nevertheless, the required amount of *CP* violation is far greater than the one induced by the CKM phase δ. That is why there may be some other sources of *CP* violation, in the lepton sector for instance.

Hence, it is commonly assumed that the SM is not a complete description of the high energy physics, and can be seen as an effective theory valid only at energies below a scale Λ (just as the Fermi model of β decay is an effective theory of the weak interaction). In this scope, the effective Lagrangian can be expressed through an operator product expansion [16]

$$\mathscr{L}_{\text{eff}}(\phi_{\text{SM}}) = \mathscr{L}_{\text{SM}}(\phi_{\text{SM}}) + \sum_{n=1}^{+\infty} \frac{1}{\Lambda^n} \mathscr{O}^{(n)}(\phi_{\text{SM}}) \,, \tag{1.43}$$

where $\mathscr{L}_{\text{SM}}$ and ϕ_{SM} are the SM Lagrangian and fields. The $\mathscr{O}^{(n)}(\phi_{\text{SM}})$ denote all polynomials in the SM fields of operator of dimension $4+n$, that are consistent with the gauge symmetries of the SM and Lorentz invariant. The scale Λ tunes the probability to observe new physics at an energy E lower than Λ, with the expansion in power of E/Λ. If no new physics effect is observed at the energy E this means either that the new physics energy scale is much larger than E, or that the couplings involved in the operators are low.

1.4.2 Looking for new physics in inconsistencies

Finding BSM physics implies the detection of new and heavier particle effects. This can be done in two ways with particle colliders:

- New particles are produced from pp or e^+e^- collisions, and then directly detected. This "relativistic" method can probe new physics scale only close to the collision energy, but can show unambiguous direct evidence of new physics.
- New particles can have virtual effects in processes including loop diagrams (like in $B^0\overline{B}^0$ mixing or $B_s^0 \to \mu^+\mu^-$ transition). Precise measurement of some observables could highlight deviations from the SM predictions, due to these new particle virtual effects. This "quantum" method can probe new physics well beyond the collision energy (depending on the new physics coupling involved), but requires collecting a sufficiently large data sample to allow precise measurements to be performed.

The test of the CKM paradigm falls into the scope of the indirect constraint on new physics. Indeed, one of the main goals of the flavour physics is to measure precisely all the CKM parameters and perform a consistency test of the unitarity triangle. If the CKM description is valid, all the measurements of the matrix parameters must lead to a "closed" triangle. This test is performed by two collaborations, CKMfitter [11] and UTFit [12], with a global fit of the CKM parameter measurements. Fig. 1.3 shows the current result of the global fit performed by CKMfitter, and a good overall consistency is found. Yet, the uncertainties on V_{ub}, γ, Δm_d and Δm_s still leave some room for future and hypothetical tension, which could be revealed with an improved precision on these parameters. Fig. 1.4, taken from Ref. [45], illustrates this potential tension by hypothesising an improved precision on the CKM parameter measurements while keeping the central values the same as they were in 2011.

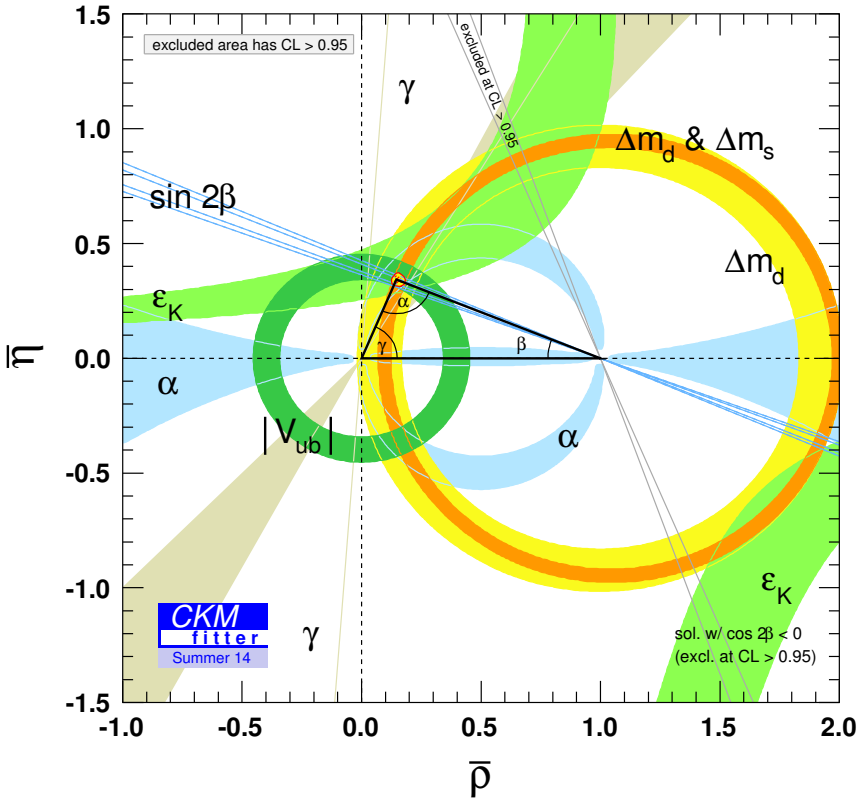

Figure 1.3 – Current global fit of the unitarity triangle performed by the CKMfitter group [11].

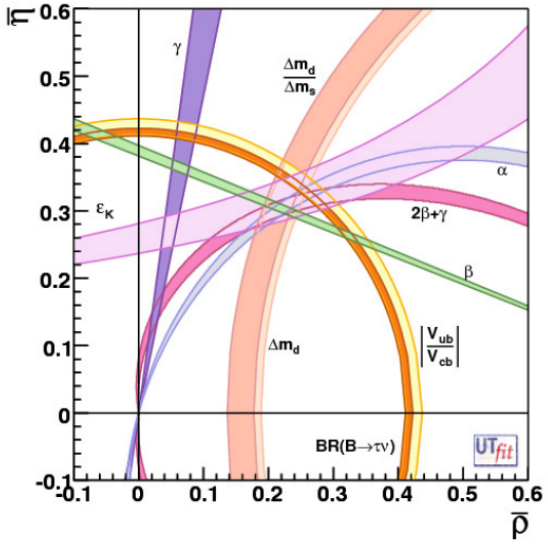

Figure 1.4 – Extrapolation of the UTFit group to illustrate a potential tension in the CKM model, with an improved precision on the CKM parameters and using the central values as of 2011 [45].

Chapter 2

Measurement principle of the CKM angle γ with $B^0 \to DK^{*0}$ decays

Contents

The angle γ is the least known CKM parameter, but is considered as a standard model key measurement. Since it does not depend on CKM elements involving the top quark, the contributions of loop diagrams are negligible in this angle measurement and the associated relative theoretical error is $\delta\gamma/\gamma \lesssim \mathcal{O}\left(10^{-7}\right)$ [46]. Therefore it is a valuable input for the consistency check of the CKM model. The measurement of this weak phase is based on the interference between the $b \to u$ and $b \to c$ quark transitions, involving the V_{ub} and V_{cb} elements of the CKM matrix respectively. Because the $b \to u$ transition is highly suppressed, a large size B meson sample is needed in order to have a good statistical sensitivity on γ.

B factories performed the first measurements of γ, and the LHCb experiment, described in the next chapter, is well suited to perform a precise measurement of this angle, which is one its the main goal. The present thesis reports a measurement of γ, made with the data collected by LHCb, using a Dalitz analysis of the $B^0 \to DK^{*0}$ decay (see Chap. 5).

This chapter presents an experimental status of the CKM parameters, especially of γ. The different measurement methods are described, with a detailed explanation of the $B^0 \to D(K^0_S\pi^+\pi^-)K^{*0}$ analysis principle.

2.1 Overview of the unitarity triangle parameter measurements

The CKM matrix elements, defined in the previous chapter, are determined through different measurements. A brief overview is made in Table 2.1 and more details can be found in Ref. [20].

Table 2.1 – Overview of the CKM matrix element measurements [20].

CKM matrix element	Measurement channel
Magnitudes	
$\lvert V_{ud}\rvert = 0.97425 \pm 0.00022$	superallowed $0^+ \to 0^+$ nuclear β decays
$\lvert V_{us}\rvert = 0.2253 \pm 0.0008$	$K^0_{\rm L} \to \pi\ell\nu$, $K^\pm \to \pi^0\ell\nu$, $K^0_{\rm S} \to \pi e\nu$ and $K/\pi \to \mu\nu(\gamma)$ decays
$\lvert V_{cd}\rvert = 0.225 \pm 0.008$	semileptonic charmed decays $D \to \pi\ell\nu$
$\lvert V_{cs}\rvert = 0.986 \pm 0.016$	semileptonic decays $D \to K\ell\nu$, $D_s^+ \to \mu^+\nu$ and $D_s^+ \to \tau^+\nu$
$\lvert V_{cb}\rvert = (41.1 \pm 1.3) \times 10^{-3}$	inclusive and exclusive semileptonic B decays to charm
$\lvert V_{ub}\rvert = (4.13 \pm 0.49) \times^{-3}$	inclusive and exclusive decays of the type $B \to X_u\ell\overline{\nu}$
$\lvert V_{td}\rvert = (8.4 \pm 0.6) \times 10^{-3}$	B^0 mixing measurements
$\lvert V_{ts}\rvert = (40.0 \pm 2.7) \times 10^{-3}$	B_s^0 mixing measurements
$\lvert V_{tb}\rvert = 1.021 \pm 0.032$	single top-quark production cross section
Phases	
$\alpha = \left(85.4^{+3.9}_{-3.8}\right)^\circ$	time dependent *CP* asymmetries in $B \to \pi\pi, \rho\pi$ and $\rho\rho$
$\sin 2\beta = 0.682 \pm 0.019$	time dependent *CP* asymmetries with $b \to c\bar{c}s$ decays
$\gamma = \left(68.0^{+8.0}_{-8.5}\right)^\circ$	$b \to c\bar{u}s$ and $b \to u\bar{c}s$ interference (see Sec. 2.3 for latest values)

2.2 Status of the γ angle measurement

As illustrated in Fig. 1.3 of the previous chapter, the γ angle is by far the least well constrained CKM angle. The most precise direct measurements to date have been obtained by the B-factories, BaBar [8] and Belle [9], and by the LHCb collaboration [10],

$$\begin{aligned} \gamma^{\rm BaBar} &= \left(69^{+17}_{-16}\right)^\circ , \\ \gamma^{\rm Belle} &= \left(68^{+15}_{-14}\right)^\circ , \\ \gamma^{\rm LHCb} &= \left(73^{+9}_{-10}\right)^\circ . \end{aligned} \tag{2.1}$$

The combination of these direct measurements has been made by the CKMfitter and UTfit collaborations, and results in [11, 12]

$$\begin{aligned} \gamma^{\rm CKMfitter}_{\rm comb} &= \left(73.2^{+6.3}_{-7.0}\right)^\circ , \\ \gamma^{\rm UTFit}_{\rm comb} &= (68.3 \pm 7.5)^\circ . \end{aligned} \tag{2.2}$$

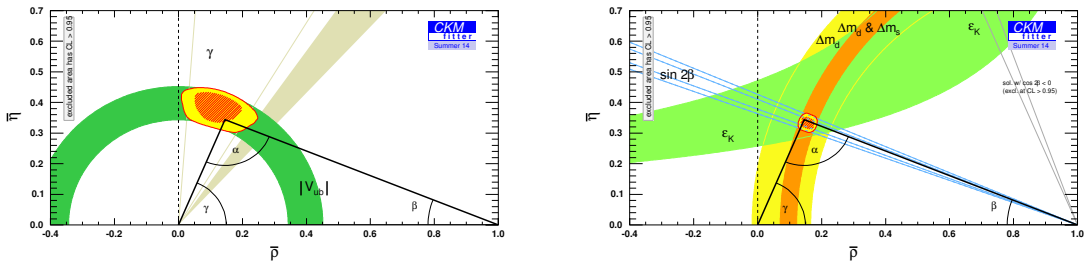

(a) (b)

Figure 2.1 – Global fit of the unitarity triangle, using only "tree" level constraints (a) and only "loop" quantities (b), made by CKMfitter [11].

The direct measurements uncertainty is larger than the one resulting from the global fit outputs [11, 12]:

$$\begin{aligned} \gamma_{\text{fit}}^{\text{CKMfitter}} &= \left(67.08^{+0.97}_{-2.17}\right)^\circ \ , \\ \gamma_{\text{fit}}^{\text{UTFit}} &= (69.2 \pm 3.4)^\circ \ . \end{aligned} \tag{2.3}$$

Thus, the global fits manage to constraint the angle γ to a few degrees precision, whereas the most precise direct measurement made by LHCb has a 10° precision. As a consequence, to further constraint new physics from the UT description, significant reduction of the uncertainty on the direct γ measurements is needed. This is also illustrated in Fig. 2.1, where the constraints obtained with quantities related to tree level diagrams only are compared to constraints obtained with quantities including significant loop contributions. The constraint on the apex is much weaker with the combination of the γ and $|V_{ub}|$ measurements, than with Δm_d, Δm_s, $\sin 2\beta$ and ε_K.

As further explained in Sec. 2.3.1, γ is essentially measured with $B^\pm \to DK^\pm$ decays. Its extraction is always done along with two other (nuisance) parameters r_B and δ_B, respectively the magnitude of the amplitude ratio and the strong phase difference between the suppressed and favoured decays. The measured values of r_B and δ_B corresponding to the quoted γ values in Eq. (2.1) are summarised in Table 2.2.

Table 2.2 – Summary of the latest direct measurements of γ, with the related values of the nuisance parameters r_B and δ_B corresponding to the $B^\pm \to DK^\pm$ decays.

	r_B	δ_B (°)	γ (°)	Ref.
BaBar	$0.092^{+0.013}_{-0.012}$	105^{+16}_{-17}	69^{+17}_{-16}	[8]
Belle	$0.112^{+0.014}_{-0.015}$	116^{+18}_{-21}	68^{+15}_{-14}	[9]
LHCb	$0.091^{+0.008}_{-0.009}$	127^{+10}_{-12}	73^{+9}_{-10}	[10]

2.3 Measurement of γ from tree processes

The angle $\gamma \equiv \arg\left(-\frac{V_{ud}V_{ub}^*}{V_{cd}V_{cb}^*}\right)$ corresponds to the phase difference between the V_{ub} and V_{cb} element of the CKM matrix. Therefore this angle is the weak phase difference between the $b \to c\bar{u}s$ and $b \to u\bar{c}s$ transitions. That is why the γ measurement are based on the interference of these two tree-level only decays. Two types of method can be distinguished, the time independent one, with $B^\pm \to DK^\pm$-like decays (Sec. 2.3.1), and the time dependent one with $B_s^0 \to D_s^\mp K^\pm$ decays (Sec. 2.3.2)

2.3.1 Time independent methods

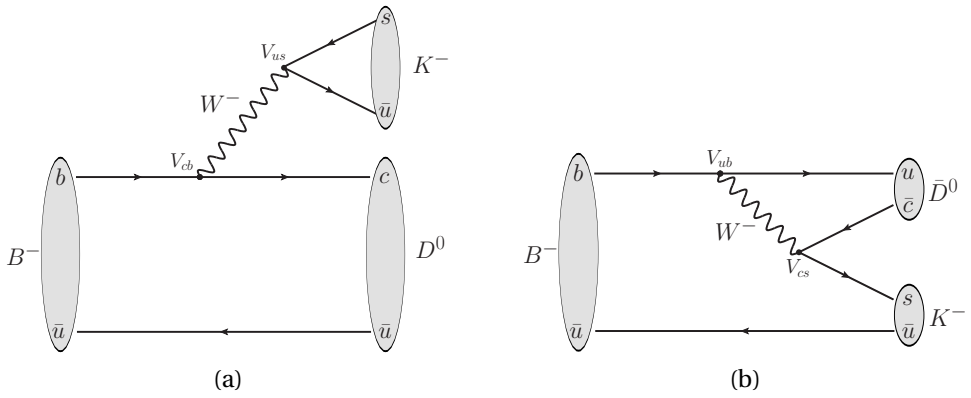

Figure 2.2 – Feynman diagrams of the $B^- \to D^0 K^-$ (a) and $B^- \to \bar{D}^0 K^-$ (b) decays.

A measurement of γ can be made through *CP* violation observables in the decays of the type $B^- \to DK^-$, where D stands either for a D^0, when a $b \to c$ favoured transition occurs, involving V_{cb}; or for a $\bar{D}^0$, when a $b \to u$ suppressed transition occurs, involving V_{ub}. The corresponding Feynman diagrams are illustrated on Fig. 2.2. The weak phase difference between these two diagrams is γ, therefore the sensitivity to this angle arises when the final state of the D mesons is accessible both for D^0 and $\bar{D}^0$, allowing for quantum interference. The strong phase difference is denoted δ_B, and the magnitude of the amplitude ratio between the suppressed and the favoured diagrams is called r_B.

It can be noticed on Fig. 2.2 that the favoured V_{cb} diagram is not colour suppressed, because of the presence of an external W^- emission. Therefore the ratio between the two interfering amplitudes can be approximated as $r_B \sim \frac{1}{3}\left|\frac{V_{ub}V_{cs}}{V_{cb}V_{us}}\right| \sim 0.1$. This parameter is important, since it drives the sensitivity to γ in the interference. The larger the interference, the higher the sensitivity to γ. More precisely, the uncertainty on γ scales as $1/r_B$.

Depending on the D decay mode used, several methods have been proposed to measure γ with $B^\pm \to DK^\pm$ decays. They are named with the initials of their respective proponents. In this section, only the most common $B^\pm \to DK^\pm$ decays are mentioned. The specific case of the $B^0 \to DK^{*0}$ neutral counterpart is further described in Sec. 2.6.

GLW method

In the Gronau-London-Wyler (GLW) approach, two-body D decays into *CP* eigenstates are used [2, 3]. Such *CP* eigenstates are both accessible for D^0 and $\bar{D}^0$ mesons, with the same

amplitudes (neglecting any *CP* violation in the charm sector). The *CP* eigenstates can be *CP*-even, such as K^+K^- and $\pi^+\pi^-$, or *CP*-odd, such as $K^0_S\pi^0$, $K^0_S\,\omega$, $K^0_S\,\eta$. The widths of the $B^\pm \to DK^\pm$ decays in the GLW modes can be expressed as

$$\begin{aligned}\Gamma\left(B^+ \to f_D^{CP^\pm} K^+\right) &\propto 1 + r_B^2 + \pm 2 r_B \cos(\delta_B + \gamma)\,,\\ \Gamma\left(B^- \to f_D^{CP^\pm} K^-\right) &\propto 1 + r_B^2 + \pm 2 r_B \cos(\delta_B - \gamma)\,,\end{aligned} \tag{2.4}$$

where $f_D^{CP^+}$ ($f_D^{CP^-}$) denotes a D meson CP-even (*CP*-odd) final state. From these widths, two types of observables sensitive to γ can be built: the *CP* asymmetries

$$A_{CP^\pm} \equiv \frac{\Gamma\left(B^- \to f_D^{CP^\pm} K^-\right) - \Gamma\left(B^+ \to f_D^{CP^\pm} K^+\right)}{\Gamma\left(B^- \to f_D^{CP^\pm} K^-\right) + \Gamma\left(B^+ \to f_D^{CP^\pm} K^+\right)} = \pm \frac{2 r_B \sin\delta_B \sin\gamma}{1 + r_B^2 \pm 2 r_B \cos\delta_B \cos\gamma}\,, \tag{2.5}$$

which measure the amount of *CP* violation in these decays; and the ratios of charge averaged partial rates using D decays to *CP* and specific flavour states

$$R_{CP^\pm} \equiv \frac{\Gamma\left(B^- \to f_D^{CP^\pm} K^-\right) + \Gamma\left(B^+ \to f_D^{CP^\pm} K^+\right)}{\Gamma\left(B^- \to D^0 K^-\right) + \Gamma\left(B^+ \to \overline{D}^0 K^+\right)} = 1 + r_B^2 \pm 2 r_B \cos\delta_B \cos\gamma\,, \tag{2.6}$$

which provide an indication of the sensitivity of the method.

ADS method

The Atwood-Dunietz-Soni (ADS) method is based on flavour specific D final states, such as $K\pi$ or $K\pi\pi\pi$ [4, 5]. Compared to the GLW approach, the amplitudes of the decay $D^0 \to f_D$ and $\overline{D}^0 \to f_D$ are not anymore equivalent. The use of the doubly Cabbibo-suppressed decay $D^0 \to K^+\pi^-$ allows for a large interference between the $B^- \to D^0 K^-$ and $B^- \to \overline{D}^0 K^-$ transitions. The difference in the magnitude of the amplitude $A(B^- \to \overline{D}^0 K^-) \ll A(B^- \to D^0 K^-)$ is compensated with $A(D^0 \to K^+\pi^-) \ll A(\overline{D}^0 \to K^+\pi^-)$. Therefore, this method has a better intrinsic sensitivity to γ than the GLW one, but suffers from smaller signal yields. Furthermore, two additional parameters are needed to describe the difference between the $D^0 \to f_D$ and $\overline{D}^0 \to f_D$ decays: the magnitude amplitude ratio r_D and the strong phase δ_D. These two parameters are already well constrained by some measurements performed in the charm sector [47]. As a result, the $B^\pm \to DK^\pm$ widths can be expressed as

$$\begin{aligned}\Gamma\left(B^+ \to f_D K^+\right) &\propto 1 + r_B^2 r_D^2 + 2 r_B r_D \cos(\delta_B + \delta_D + \gamma)\,,\\ \Gamma\left(B^- \to \bar{f}_D K^-\right) &\propto 1 + r_B^2 r_D^2 + 2 r_B r_D \cos(\delta_B + \delta_D - \gamma)\,,\\ \Gamma\left(B^+ \to \bar{f}_D K^+\right) &\propto r_B^2 + r_D^2 + 2 r_B r_D \cos(\delta_B - \delta_D + \gamma)\,,\\ \Gamma\left(B^- \to f_D K^-\right) &\propto r_B^2 + r_D^2 + 2 r_B r_D \cos(\delta_B - \delta_D - \gamma)\,,\end{aligned} \tag{2.7}$$

where f_D denotes the Cabbibo-favoured $D^0 \to f_D$ decay. The resulting *CP* observables are

$$\begin{aligned}A_{\mathrm{ADS}} &\equiv \frac{\Gamma\left(B^- \to f_D K^-\right) - \Gamma\left(B^+ \to \bar{f}_D K^+\right)}{\Gamma\left(B^- \to f_D K^-\right) + \Gamma\left(B^+ \to \bar{f}_D K^+\right)} = \frac{2 r_B r_D \sin(\delta_B - \delta_D)\sin\gamma}{r_B^2 + r_D^2 + 2 r_B r_D \cos(\delta_B - \delta_D)\cos\gamma}\,,\\ R_{\mathrm{ADS}} &\equiv \frac{\Gamma\left(B^- \to f_D K^-\right) + \Gamma\left(B^+ \to \bar{f}_D K^+\right)}{\Gamma\left(B^- \to \bar{f}_D K^-\right) + \Gamma\left(B^+ \to f_D K^+\right)} = \frac{r_B^2 + r_D^2 + 2 r_B r_D \cos(\delta_B - \delta_D)\cos\gamma}{1 + r_B^2 r_D^2 + 2 r_B r_D \cos(\delta_B + \delta_D)\cos\gamma}\,.\end{aligned} \tag{2.8}$$

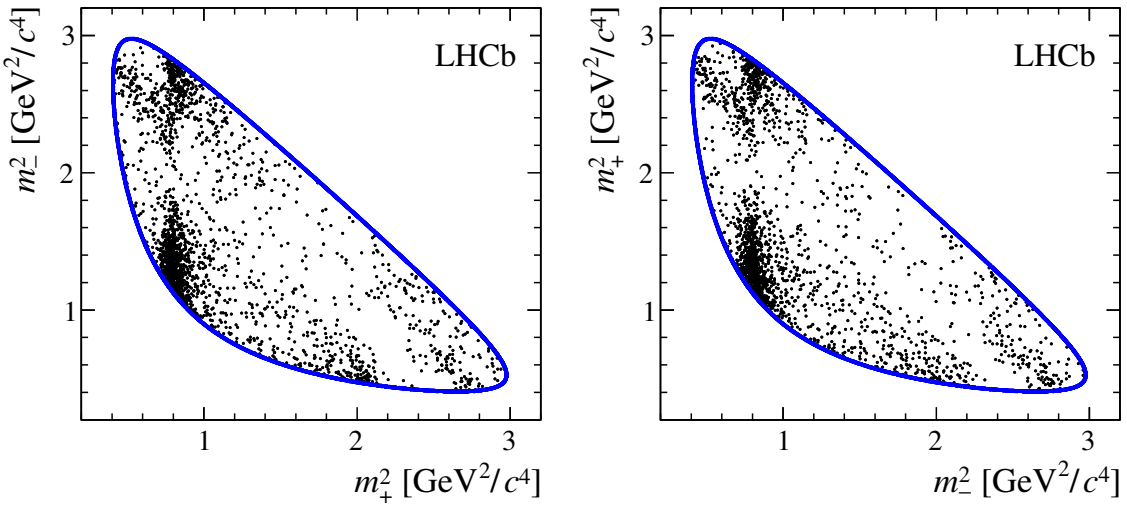

Figure 2.3 – Dalitz plots of $B^\pm \to D(K^0_S\pi^+\pi^-)K^\pm$ candidates from B^+ (a) and B^- decays (b), of the model independent GGSZ analysis of LHCb [13].

GLS method

The Grossman-Ligeti-Soffer (GLS) method adapts the ADS approach to singly Cabbibo suppressed D decays with specific flavour states, such as $D^0 \to K^0_S K^+\pi^-$ [48]. Because of the three-body final state, some measurements of the average strong phase variation across the D Dalitz are needed to constrain γ. A first GLS measurement has been performed by LHCb, and shows a better sensitivity to γ in the phase-space region around the K^{*+} resonance [49].

GGSZ method

One of the most sensitive methods to measure γ is the Giri-Grossman-Soffer-Zupan method (GGSZ) [6, 7]. It is based on self-conjugate three-body D final states, such as $D \to K^0_S\pi^+\pi^-$ or $D \to K^0_S K^+K^-$. The Dalitz plot resulting of these decays is analysed, and the sensitivity to γ arises in some particular region of the phase-space, depending on the resonance structure. This approach follows in a way, the ADS and GLW methods in different areas of the Dalitz plot. The $D \to K^0_S h^+h^-$ Dalitz plot is made from the two invariant masses $m^2_\pm \equiv m^2(K^0_S h^\pm)$, with h standing for either K or π. The decay widths giving the Dalitz plot distributions are

$$\begin{aligned}\Gamma\left(B^+ \to D(K^0_S h^+h^-)K^+\right) &\propto \left|A_{\overline{D}}(m^2_-, m^2_+) + r_B e^{i(\delta_B+\gamma)} A_D(m^2_-, m^2_+)\right|^2 ,\\ \Gamma\left(B^- \to D(K^0_S h^+h^-)K^-\right) &\propto \left|A_D(m^2_-, m^2_+) + r_B e^{i(\delta_B-\gamma)} A_{\overline{D}}(m^2_-, m^2_+)\right|^2 ,\end{aligned} \tag{2.9}$$

where A_D and $A_{\overline{D}}$ denote the $D^0 \to K^0_S h^+h^-$ and $\overline{D}^0 \to K^0_S h^+h^-$ amplitudes, respectively. The $B^\pm \to D^0K^\pm / B^\pm \to \overline{D}^0K^\pm$ interference is clearly visible, and a fit performed on the Dalitz distributions enables to evaluate the phase γ. In order to describe the A_D and $A_{\overline{D}}$ amplitudes, two methods can be used:

- The model independent (MI) approach is based on a binned Dalitz plot, and relies on the CLEO-c measurement of the average strong phase in each bin [50].

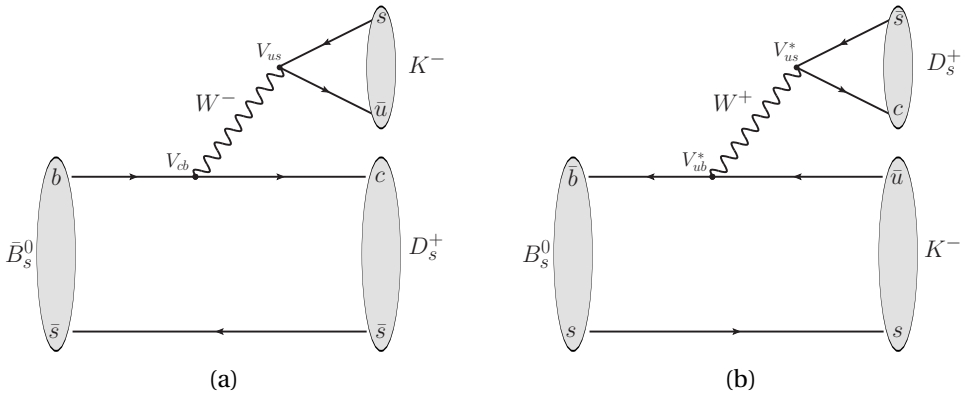

Figure 2.4 – Feynman diagrams of the $\overline{B}_s^0 \to D_s^+ K^-$ (a) and $B_s^0 \to D_s^+ K^-$ (b) decays.

- The model dependent (MD) approach uses an amplitude model determined by the BaBar collaboration [51].

Both methods are competitive. Whereas the MI approach looses some statistical precision through the binning and is dependent on the uncertainty of the CLEO-c measurement, the MD method is subject to the uncertainty coming from the choice of the model. In LHCb, the two methods have been used in GGSZ analyses of the $B^\pm \to DK^\pm$ mode [13,52]. Fig. 2.3 illustrates the Dalitz plot obtained in the LHCb MI analysis, which led to the most precise single measurement of γ to date, with $\gamma = \left(62^{+15}_{-14}\right)^\circ$ [13]. In Chap. 5 a MD analysis of the $B^0 \to D(K^0_S\pi^+\pi^-)K^{*0}$ decay is reported.

The *CP* observables used in the GGSZ analyses are the *cartesian parameters* defined as

$$\begin{aligned} x_\pm &\equiv r_B \cos(\delta_B \pm \gamma) \,, \\ y_\pm &\equiv r_B \sin(\delta_B \pm \gamma) \,. \end{aligned} \tag{2.10}$$

They are preferred to the *polar* coordinates (r_B, δ_B, γ) because they show a better Gaussian behaviour.

2.3.2 Time dependent method

The $B^\pm \to DK^\pm$ and $B^0 \to DK^{*0}$ decays are not the only modes which provide a measurement of γ at the tree level. The same $b \to c\overline{u}s$ and $b \to u\overline{c}s$ transitions can interfere in the $B_s^0 \to D_s^\mp K^\pm$ decays [53] (the corresponding diagrams are illustrated in Fig. 2.4). However, this time the interference takes place between the direct decay $\overline{B}_s^0 \to D_s^+ K^-$ and the decay $B_s^0 \to D_s^+ K^-$ after a $\overline{B}_s^0 \to B_s^0$ mixing. Therefore, a time dependent analysis using some flavour tagging methods is necessary. Moreover, the phase difference between the two interfering contributions is not only γ, but $\gamma - 2\beta_s$, where β_s is the *CP* violating B_s^0 mixing phase. The study of $B_s^0 \to J/\psi\,\phi$ decays provides a good constraint on $-2\beta_s$ [54], and can therefore be used as an external input to measure γ from $B_s^0 \to D_s^\mp K^\pm$.

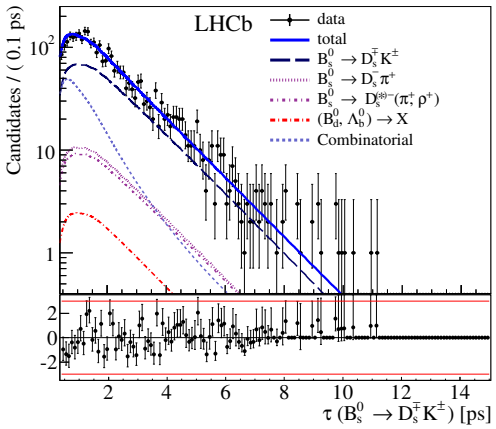

Figure 2.5 – Decay time distribution of $B_s^0 \to D_s^\mp K^\pm$ events observed in LHCb, with the fit result superimposed [55].

The time dependent decay rate of this decay can be expressed as

$$\begin{aligned}\Gamma_{B_s^0(\bar{B}_s^0)\to f}(t) = &\frac{e^{-\Gamma_s t}}{2}|A_f|^2\left(1+|\lambda_f|^2\right)\\ &\times\left[\cosh\left(\frac{\Delta\Gamma_s t}{2}\right) - D_f \sinh\left(\frac{\Delta\Gamma_s t}{2}\right) \pm C_f\cos(\Delta m_s t) \mp S_f \sin(\Delta m_s t)\right],\end{aligned} \tag{2.11}$$

where Γ_s, $\Delta\Gamma_s$ and Δm_s are the mixing parameters of the B_s^0 meson. The terms D_f, C_f and S_f depend on the amplitude ratio λ_f, defined as

$$\lambda_f \equiv \frac{\bar{A}_f}{A_f} = |\lambda_f| e^{i(\Delta - (\gamma - 2\beta_s))}, \tag{2.12}$$

with A_f ($\bar{A}_f$) the decay amplitude of the B_s^0 ($\bar{B}_s^0$) meson into the final state f. Δ is the relative strong phase, and $(\gamma - 2\beta_s)$ the relative weak phase. Hence, the D_f, C_f and S_f parameters depend on $(\gamma - 2\beta_s)$.

LHCb has made the first measurement of γ with the $B_s^0 \to D_s^\mp K^\pm$ decays [55]. The resulting decay time distribution is illustrated on Fig. 2.5, and led to $\gamma = \left(115^{+28}_{-43}\right)^\circ$.

In a similar way, a γ measurement can be obtained with $B^0 \to D^\pm \pi^\mp$ decays, with this time a direct dependence on $2\beta + \gamma$ [56]. However, in this case the interference amplitude is reduced.

2.4 LHCb γ combination

All the decays involved in the γ from tree measurements have a small decay rates. For instance, the combined branching ratio involved in the $B^\pm \to DK^\pm$ ADS mode is approximately $\mathscr{B}(B^- \to D^0 K^-, D^0 \to K^+\pi^-) \sim 5 \cdot 10^{-8}$. That is why the measurement of γ relies on the combination of all the available measurements.

The latest LHCb γ combination, as of September 2014 [10], includes *CP* violation measurements of the $B^\pm \to D(h^+h^-)K^\pm$ [57], $B^\pm \to D(\pi^\pm K^\mp \pi^+\pi^-)K^\pm$ [58], $B^\pm \to D(K_S^0 h^+h^-)K^\pm$ [13], $B^\pm \to D(K_S^0 K^+\pi^-)K^\pm$ [49], $B^0 \to D(h^+h^-)K^{*0}$ [59] and $B_s^0 \to D_s^\mp K^\pm$ [55] decays, where h stands

either for a pion or a kaon. The combination uses a Frequentist approach. It takes into account the D^0 mixing and includes some auxiliary inputs for hadronic parameters coming from the Heavy Flavor Averaging Group [47] or the CLEO experiment. The result of this combination is $\gamma = \left(73^{+9}_{-10}\right)^\circ$ at 68% confidence level. The corresponding confidence level curve is shown in Fig. 2.6. This is the first time that a single experiment has reached 10° precision on γ. A bayesian crosscheck has been also performed and is in good agreement.

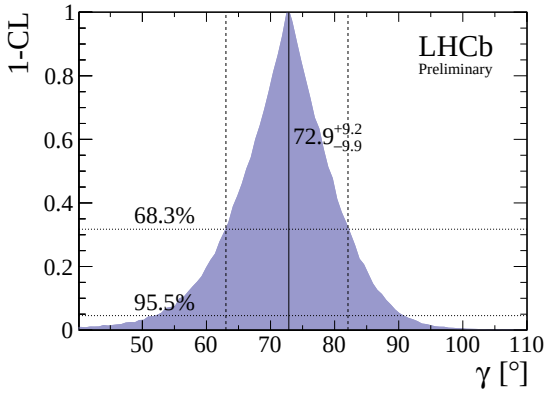

Figure 2.6 – Confidence level curve for the LHCb γ combination presented at the CKM 2014 conference. The dotted lines indicate the 1σ and 2σ bounds. [10].

The perspective to reach a precise measurement of γ, with the LHCb experiment is promising. During the LHC Run II, LHCb is expected to collect an integrated luminosity of 5 fb^{-1} at the centre-of-mass energy of 13 TeV, and the precision on γ is expected to reduce to 4°. After the long shutdown 2 (LS2), the detector will be upgraded to cope with a large increase of the delivered instantaneous luminosity. Ultimately, the LHCb collaboration foresees to collect a data sample of 50 fb^{-1}. With the combination of all the sensitive channels, the final uncertainty on γ should be around 1°. This would be a major improvement compared to the current precision on γ, and would be an important milestone for the consistency check of the CKM model.

2.5 Measurement of γ from loop processes

In addition to the measurements with open-charm final states, γ can be determined from charmless B decays. The sensitivity to γ is obtained by combining CP violation measurements from $B^0 \to \pi^+\pi^-$, $B^0_s \to K^+K^-$, $B^0 \to \pi^0\pi^0$ and $B^+ \to \pi^+\pi^0$ decays [60–64]. The contribution of diagrams with loops, illustrated in Fig. 2.7, is non negligible in these decays. Therefore, a precise extraction of γ with this method is difficult. Nevertheless, it is interesting to compare this measurement, potentially affected by new physics contribution, to the γ measurement made with tree only diagrams. The sensitivity to γ arises in the decay amplitudes, for instance for $B^0 \to \pi^+\pi^-$ decay [65]

$$A\left(B^0 \to \pi^+\pi^-\right) \propto e^{i\gamma} - d e^{i\delta}, \tag{2.13}$$

where $e^{i\delta}$ roughly corresponds to the ratio of penguin to tree amplitudes.

LHCb significantly contributed to the measurements of the $B^0 \to \pi^+\pi^-$ and $B^0_s \to K^+K^-$ decays, whereas the $B^0 \to \pi^0\pi^0$ and $B^+ \to \pi^+\pi^0$ decays have been studied by BaBar, Belle or CDF. LHCb performed a combination of all these measurements in order to set a constraint on

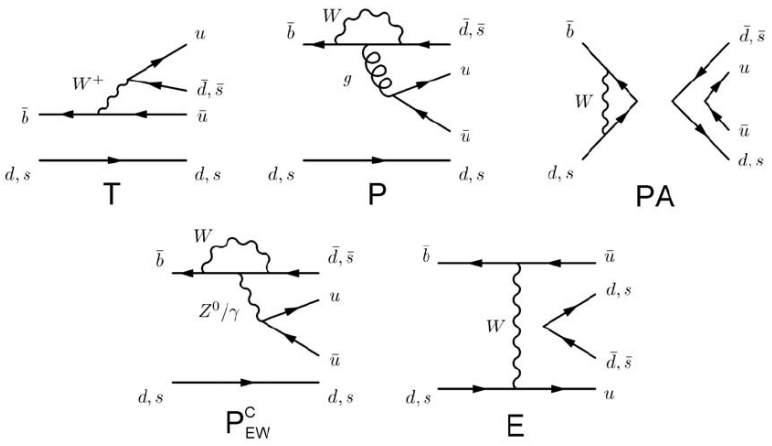

Figure 2.7 – Diagrams contributing to the amplitudes of charmless $B^0_{(s)}$ decays. The topologies involved are: Tree (T), Penguin (P), Penguin Annihilation (PA), Colour-suppressed Electroweak Penguin (P^C_{EW}) and Exchange (E) [65].

γ [66]. To reduce the number of free parameters in the global fit, the combination exploits the isospin and U-spin (exchange of d and s quarks) symmetries.

A Bayesian analysis is performed to determine the probability density function (PDF) of γ, while assuming the world average value of $\sin 2\beta$ compiled by the HFAG collaboration [47]. The dependence of the PDF on U-spin breaking is estimated by letting vary the maximum allowed amount of U-spin breaking. This amount is described with a parameter κ: $\kappa = 0$ corresponds to no U-spin breaking, $\kappa = 1$ corresponds to maximal breaking. The resulting probability intervals of γ as a function of κ is shown in Fig. 2.8. They depend strongly on the amount of U-spin breaking. If the breaking is assumed to be at most 50%, the global fit provides $\gamma = \left(63.5^{+7.2}_{-6.7}\right)^\circ$. This measurement is compatible and competitive with the one obtained from tree-level decays (see Sec.2.4). However, a better theoretical understanding of the U-spin breaking is needed to assess a reliable determination of γ from charmless B decays.

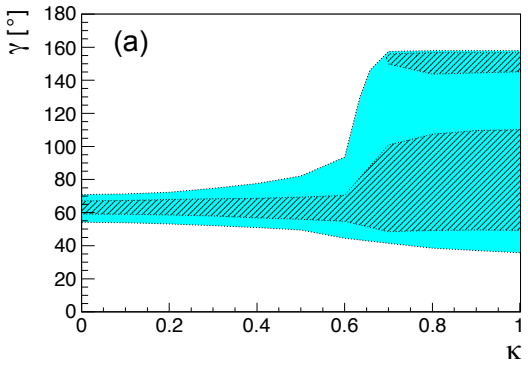

Figure 2.8 – Dependence of the 68% (hatched area) and 95% (filled area) probability intervals on the allowed amount of non-factorizable U-spin breaking for γ (κ parameter).

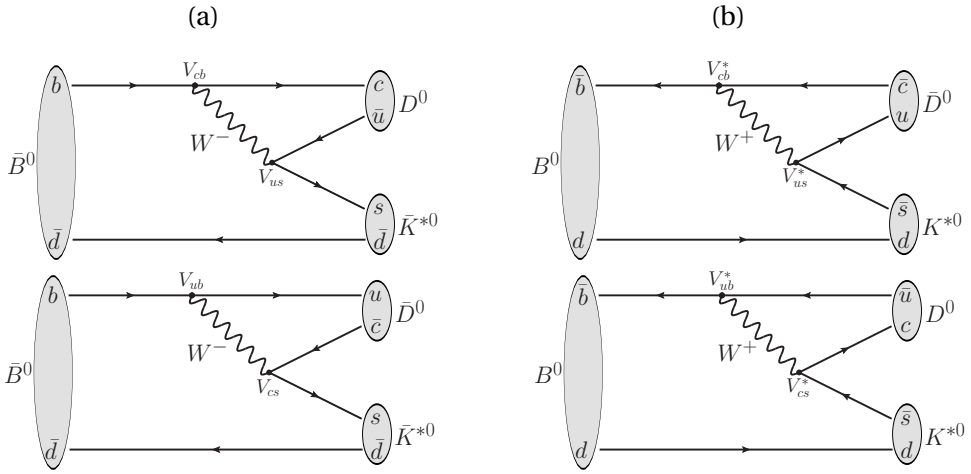

Figure 2.9 – Feynman diagrams involved in the $\overline{B}^0 \to D\overline{K}^{*0}$ (a) and $B^0 \to DK^{*0}$ (b) decays. Transitions proportional to $|V_{cb}|^2$ are at the top and transitions proportional to $|V_{ub}|^2$ are at the bottom. All diagrams are colour-suppressed.

2.6 Measurement of γ with $B^0 \to D(K^0_S\pi^+\pi^-)K^{*0}$

Fig. 2.9 shows the diagrams involved in the $B^0 \to DK^{*0}$ process (*CP* conjugation is implicit unless stated otherwise). Compared to the charged mode $B^\pm \to DK^\pm$, the neutral mode does not include any diagram with an external $W^\pm$ boson (see Fig. 2.2). Hence all $B^0 \to DK^{*0}$ diagrams are colour-suppressed and the $B^\pm \to DK^\pm$ is a more frequent process. According to the PDG [20], the branching fractions are $\mathscr{B}(B^+ \to \overline{D}^0 K^+) = (3.70 \pm 0.17) \times 10^{-4}$ and $\mathscr{B}(B^0 \to \overline{D}^0 K^{*0}) = (4.2 \pm 0.6) \times 10^{-5}$. However, the interference magnitude in the neutral mode is expected to be approximately three times larger, therefore this mode is about three times more sensitive to γ. Furthermore, the neutral channel is *self-tagged* thanks to the $K^{*0} \to K^+\pi^-$ decay. The flavour of the B meson at the decay time is known thanks to the charge of the kaon in the final state. Therefore, a time independent measurement can be performed, without relying on flavour tagging methods. The $B^0 \to DK^{*0}$ and $B^\pm \to DK^\pm$ decays share only the weak phase γ, since the strong phase δ_{B^0} and the interference magnitude r_{B^0} of the $B^0 \to DK^{*0}$ decays are different parameters to those that apply in $B^\pm \to DK^\pm$ decays.

An ADS/GLW analysis of the $B^0 \to DK^{*0}$ decay has been already published by LHCb [59]. The $B^0 \to DK^{*0}$ analysis described in this thesis follows the GGSZ MD method with the three body $D \to K^0_S\pi^+\pi^-$ decay. This method based on the Dalitz plot study has two advantages:

- flavour specific and *CP* eigenstates are used simultaneously thanks to the amplitude analysis of the $D \to K^0_S\pi^+\pi^-$ Dalitz plane,
- there is only a $(\delta_{B^0}, \gamma) \to (\delta_{B^0} + \pi, \gamma + \pi)$ ambiguity (in the ADS method there is a 4-fold ambiguity [5]).

First the $B^0 \to DK^{*0}$ event distribution across the Dalitz plane is developed, then the experimental status on the measurement of γ made from this neutral mode is summarised.

2.6.1 Dalitz PDF

Compared to the $B^\pm \to DK^\pm$ decay, the $B^0 \to DK^{*0}$ decay description must take into account the interference with any $B^0 \to DK^+\pi^-$ decay, since the K^{*0} resonance is broad [67,68]. In the following we write X_s^0 to represent any two body state composed by a $K^+\pi^-$ pair.

The favoured B^0 decays amplitudes can be expressed as

$$A\left(B^0 \to \overline{D}^0 X_s^0; p\right) = A_c(p) e^{i\delta_c(p)} \propto {V_{cb}}^* {V_{us}}^*, \tag{2.14}$$

$$A\left(\overline{B}^0 \to D^0 \overline{X}_s^0; p\right) = A_c(p) e^{i\delta_c(p)} \propto V_{cb} V_{us}, \tag{2.15}$$

and the suppressed as

$$A\left(B^0 \to D^0 X_s^0; p\right) = A_u(p) e^{i[\delta_u(p)+\Delta_{weak}]} \propto {V_{ub}}^* {V_{cs}}^*,$$

$$A\left(\overline{B}^0 \to \overline{D}^0 \overline{X}_s^0; p\right) = A_u(p) e^{i[\delta_u(p)-\Delta_{weak}]} \propto V_{ub} V_{cs},$$

where p is a position on the B Dalitz plane, δ represents the strong phase and Δ_{weak} the weak phase. We have $\Delta_{weak} \equiv \arg({V_{ub}}^* {V_{cs}}^*) - \arg({V_{cb}}^* {V_{us}}^*) \simeq \arg({V_{ub}}^*) - \arg({V_{cb}}^*)$ and $\gamma \equiv \arg\left(-\frac{V_{ud}V_{ub}^*}{V_{cd}{V_{cb}}^*}\right) \simeq \arg(-{V_{ub}}^*) - \arg({V_{cb}}^*) = \pi + \arg(V_{ub}^*) - \arg({V_{cb}}^*)$, therefore $\Delta_{weak} = \gamma - \pi$. With the variable change $\delta_u(p) - \pi \to \delta_u(p)$, the suppressed decays amplitudes are expressed as

$$A\left(B^0 \to D^0 X_s^0; p\right) = A_u(p) e^{i[\delta_u(p)+\gamma]}, \tag{2.16}$$

$$A\left(\overline{B}^0 \to \overline{D}^0 \overline{X}_s^0; p\right) = A_u(p) e^{i[\delta_u(p)-\gamma]}. \tag{2.17}$$

The decay amplitude of $D \to K_S^0\pi^+\pi^-$ is denoted A_D and depends on the position on the D meson Dalitz plane, described with any two of the three squared invariant masses $m_+^2 = m^2(K_S^0\pi^+)$, $m_-^2 = m^2(K_S^0\pi^-)$ and $m_0^2 = m^2(\pi^+\pi^-)$. The amplitude A_D is determined from the model developed by the BaBar collaboration [51], and is presented in Sec 5.6 of Chap. 5.

$$A\left(D^0 \to K_S^0\pi^+\pi^-; m_-^2, m_+^2\right) = A_D(m_-^2, m_+^2), \tag{2.18}$$

$$A\left(\overline{D}^0 \to K_S^0\pi^-\pi^+; m_-^2, m_+^2\right) = A_{\overline{D}}(m_-^2, m_+^2). \tag{2.19}$$

Since we neglect CP violation in the charm sector,

$$A_{\overline{D}}(m_-^2, m_+^2) = A_D(m_+^2, m_-^2). \tag{2.20}$$

The partial width resulting from the $B^0 \to D^0 X_s^0$ / $B^0 \to \overline{D}^0 X_s^0$ interference is noted $\mathrm{d}\Gamma_+(p, m_-^2, m_+^2) \equiv \mathrm{d}\Gamma\left(B^0 \to D(K_S^0\pi^+\pi^-)X_s^0; p, m_-^2, m_+^2\right)$ and from the $\overline{B}^0 \to D^0 \overline{X}_s^0$ / $\overline{B}^0 \to \overline{D}^0 \overline{X}_s^0$ interference $\mathrm{d}\Gamma_-(p, m_-^2, m_+^2) \equiv \mathrm{d}\Gamma\left(\overline{B}^0 \to D(K_S^0\pi^+\pi^-)\overline{X}_s^0; p, m_-^2, m_+^2\right)$. They can be expressed as

$$\mathrm{d}\Gamma_-(p, m_-^2, m_+^2) \propto \left| A\left(\overline{B}^0 \to D^0 \overline{X}_s^0; p\right) A_D + A\left(\overline{B}^0 \to \overline{D}^0 \overline{X}_s^0; p\right) A_{\overline{D}} \right|^2, \tag{2.21}$$

and

$$\mathrm{d}\Gamma_+(p, m_-^2, m_+^2) \propto \left| A\left(B^0 \to \overline{D}^0 X_s^0; p\right) A_{\overline{D}} + A\left(B^0 \to D^0 X_s^0; p\right) A_D \right|^2. \tag{2.22}$$

This gives

$$\mathrm{d}\Gamma_-(p, m_-^2, m_+^2) \propto \left| A_c(p) e^{i\delta_c(p)} A_D + A_u(p) e^{i[\delta_u(p)-\gamma]} A_{\overline{D}} \right|^2, \tag{2.23}$$

$$\mathrm{d}\Gamma_+(p, m_-^2, m_+^2) \propto \left| A_c(p) e^{i\delta_c(p)} A_{\overline{D}} + A_u(p) e^{i[\delta_u(p)+\gamma]} A_D \right|^2. \tag{2.24}$$

Then it can be expanded to

$$\begin{aligned} \mathrm{d}\Gamma_-(p, m_-^2, m_+^2) \propto\ & A_c^2(p)|A_D|^2 + A_u^2(p)|A_{\overline{D}}|^2 + \\ & 2A_c(p)A_u(p)\,\mathscr{R}e\left[A_D^* A_{\overline{D}}\, e^{i[\delta_u(p)-\delta_c(p)-\gamma]}\right], \end{aligned} \tag{2.25}$$

$$\begin{aligned} \mathrm{d}\Gamma_+(p, m_-^2, m_+^2) \propto\ & A_c^2(p)|A_{\overline{D}}|^2 + A_u^2(p)|A_D|^2 + \\ & 2A_c(p)A_u(p)\,\mathscr{R}e\left[A_D A_{\overline{D}}^*\, e^{i[\delta_u(p)-\delta_c(p)+\gamma]}\right]. \end{aligned} \tag{2.26}$$

If we consider only the K^{*0} region $\phi_{K^{*0}}$ in the $B^0 \to DX_s^0$ phase space (*i.e.* we integrate over $\phi_{K^{*0}}$):

$$\begin{aligned} d\Gamma_-^{K^{*0}}(m_-^2, m_+^2) \propto\ & |A_D|^2 \int_{\phi_{K^{*0}}} A_c^2(p)\,\mathrm{d}p + |A_{\overline{D}}|^2 \int_{\phi_{K^{*0}}} A_u^2(p)\,\mathrm{d}p + \\ & 2\mathscr{R}e\left[A_D^* A_{\overline{D}} e^{-i\gamma} \int_{\phi_{K^{*0}}} A_c(p)A_u(p) e^{i[\delta_u(p)-\delta_c(p)]}\,\mathrm{d}p\right], \end{aligned} \tag{2.27}$$

$$\begin{aligned} d\Gamma_+^{K^{*0}}(m_-^2, m_+^2) \propto\ & |A_{\overline{D}}|^2 \int_{\phi_{K^{*0}}} A_c^2(p)\,\mathrm{d}p + |A_D|^2 \int_{\phi_{K^{*0}}} A_u^2(p)\,\mathrm{d}p + \\ & 2\mathscr{R}e\left[A_D A_{\overline{D}}^* e^{+i\gamma} \int_{\phi_{K^{*0}}} A_c(p)A_u(p) e^{i[\delta_u(p)-\delta_c(p)]}\,\mathrm{d}p\right]. \end{aligned} \tag{2.28}$$

We define now the D Dalitz PDF $\mathscr{P}_\pm$ such that

$$\mathrm{d}\Gamma_\pm^{K^{*0}}(m_-^2, m_+^2) \equiv \mathscr{P}_\pm(m_-^2, m_+^2)\,\mathrm{d}m_-^2\,\mathrm{d}m_+^2 \cdot \int_{\phi_{K^{*0}}} A_c^2(p)\,\mathrm{d}p.$$

If we define

$$r_{B^0}^2 \equiv \frac{\int_{\phi_{K^{*0}}} A_u^2(p)\,\mathrm{d}p}{\int_{\phi_{K^{*0}}} A_c^2(p)\,\mathrm{d}p}, \tag{2.29}$$

$$\kappa e^{i\delta_{B^0}} \equiv \frac{\int_{\phi_{K^{*0}}} A_c(p)A_u(p) e^{i[\delta_u(p)-\delta_c(p)]}\,\mathrm{d}p}{\sqrt{\int_{\phi_{K^{*0}}} A_c^2(p)\,\mathrm{d}p \int_{\phi_{K^{*0}}} A_u^2(p)\,\mathrm{d}p}}, \tag{2.30}$$

then

$$\mathscr{P}_- \propto |A_D|^2 + r_{B^0}^2|A_{\overline{D}}|^2 + 2\kappa r_{B^0}\mathscr{R}e\left[A_D^* A_{\overline{D}} e^{i(\delta_{B^0}-\gamma)}\right], \tag{2.31}$$

$$\mathscr{P}_+ \propto |A_{\overline{D}}|^2 + r_{B^0}^2|A_D|^2 + 2\kappa r_{B^0}\mathscr{R}e\left[A_D A_{\overline{D}}^* e^{i(\delta_{B^0}+\gamma)}\right]. \tag{2.32}$$

From the Schwartz inequality [1] we can deduce that

$$0 \le \kappa \le 1. \tag{2.33}$$

r_{B^0} is the ratio between the amplitudes of the $B^0 \to D^0K^{*0}$ decay ($b \to u$ suppressed transition) over the $B^0 \to \overline{D}^0K^{*0}$ decay ($b \to c$ favoured transition). δ_{B^0} is the average strong phase between $B^0 \to D^0K^{*0}$ and $B^0 \to \overline{D}^0K^{*0}$. κ is the K^{*0} coherence factor, and measures the non-resonant pollution in the $K\pi$ pair. Indeed, the Dalitz PDF of Eq. (2.31) and (2.32) can be rewritten as

$$\mathscr{P}_- \propto \kappa|A_D + r_{B^0}e^{i(\delta_B-\gamma)}A_{\overline{D}}|^2 + (1-\kappa)\left(|A_D|^2 + r_{B^0}^2|A_{\overline{D}}|^2\right), \tag{2.34}$$

$$\mathscr{P}_+ \propto \kappa|A_{\overline{D}} + r_{B^0}e^{i(\delta_B+\gamma)}A_D|^2 + (1-\kappa)\left(|A_{\overline{D}}|^2 + r_{B^0}^2|A_D|^2\right). \tag{2.35}$$

[1] $\left|\int f(x)g(x)^* dx\right| \le \sqrt{\int |f(x)|^2 dx \int |g(x)|^2 dx}$ for two squared-integrable complex-valued functions g and f.

The first term, proportional to κ, corresponds to a coherent sum of the two amplitudes. The second term is an incoherent sum, where no interference appears. If the $K^+\pi^-$ pair were only coming from the K^{*0}, κ would be equal to unity.

It is convenient to define the CP violation observables

$$z_\pm \equiv r_{B^0} e^{i(\delta_{B^0} \pm \gamma)}, \tag{2.36}$$

and the function

$$\mathscr{P}(A, z, \kappa) \equiv \left|A\right|^2 + |z|^2 \left|\bar{A}\right|^2 + 2\kappa \mathscr{R}e\left[zA^* \bar{A}\right]. \tag{2.37}$$

The Cartesian coordinates are defined as

$$x_\pm \equiv \mathscr{R}e(z_\pm), \tag{2.38}$$

$$y_\pm \equiv \mathscr{I}m(z_\pm), \tag{2.39}$$

so we have

$$r_{B^0} = |z_\pm| = \sqrt{x_\pm^2 + y_\pm^2}. \tag{2.40}$$

Expressions (2.31) and (2.32) can be expressed as

$$\mathscr{P}_- \propto \mathscr{P}(A_D, z_-, \kappa) \tag{2.41}$$

$$\mathscr{P}_+ \propto \mathscr{P}(A_{\bar{D}}, z_+, \kappa) \tag{2.42}$$

These are the expressions of the PDFs used to describe the mixture of amplitudes in the analysis reported in Chap. 5. Equations (2.41-2.42) suggest that five parameters are needed to describe the PDFs, namely the Cartesian parameters and the coherence factor κ. Because of the relation (2.40), over these five degrees of freedom, only four are physical, which correspond to $\kappa, r_{B^0}, \delta_{B^0}$ and γ. As mentioned before, the use of the cartesian coordinates $(x_\pm, y_\pm)$ is preferred over the polar coordinates $(r_{B^0}, \gamma, \delta_{B^0})$ because they are expected to have a better Gaussian behaviour.

2.6.2 Experimental status of the γ measurement with $B^0 \to DK^{*0}$

The experimental status of the measurement of γ with the $B^0 \to DK^{*0}$ decay is summarised in Table 2.3. Both B-factories published an ADS/GLW $B^0 \to DK^{*0}$ analysis [69, 70], whereas only BaBar published a GGSZ analysis of this channel [71].

Table 2.3 – Summary of the direct measurements of γ, with the related values of the nuisance parameters r_{B^0} and δ_{B^0} corresponding to the $B^0 \to DK^{*0}$ decays. A hyphen is used when no constraint has been made on a parameter.

	Analysis type	r_{B^0}	δ_{B^0} (°)	γ (°)	Ref.
BaBar	ADS/GLW	$[0.07, 0.41]$ @ 95% CL	–	–	[69]
Belle	ADS/GLW	< 0.4 @ 95% CL	–	–	[70]
BaBar	GGSZ	< 0.55 @ 95% CL	$[-23, 147] \cup$ $[157, 327]$ @ 95% CL	$[77, 247] \cup$ $[257, 426]$ @ 95% CL	[71]
LHCb	ADS/GLW	$0.240^{+0.055}_{-0.048}$	–	–	[59]

Chapter 3

The LHCb detector at the LHC

Contents

The LHCb experiment [72] is located on the Large Hadron Collider (LHC) of the European Organisation for Nuclear Research (CERN). It is dedicated to precision measurements in heavy flavour physics. Its main goal is to look for indirect evidence of physics beyond the Standard Model in *CP* violation effects and rare b and c-hadron decays. Precise measurements can be sensitive to the effect of new particles in processes well predicted by the Standard Model. This chapter presents an overview of the LHCb detector.

3.1 The Large Hadron Collider

The LHC is a proton and heavy ions collider of 27 km of circumference. It is the biggest machine of the CERN accelerator complex (Fig. 3.1) and is composed of two rings. Inside, protons or ions circulate in opposite directions and can collide in four distinct interaction points, where the detectors ATLAS, CMS, LHCb and ALICE are installed. ATLAS and CMS are general purpose detectors mainly dedicated to Higgs physics and direct search for physics beyond the Standard Model. The ALICE detector is designed for heavy ion physics and to study strongly interacting matter at high energy densities. Three smaller experiments are also installed at the LHC, namely TOTEM, LHCf and MoEDAL. The TOTEM experiment (Total cross-section, elastic scattering and diffraction dissociation), located around CMS interaction point, is dedicated to the total proton-proton (pp) cross-section measurement and to proton structure studies with elastic and diffractive scattering processes. The Large Hadron Collider Forward (LHCf) experiment,

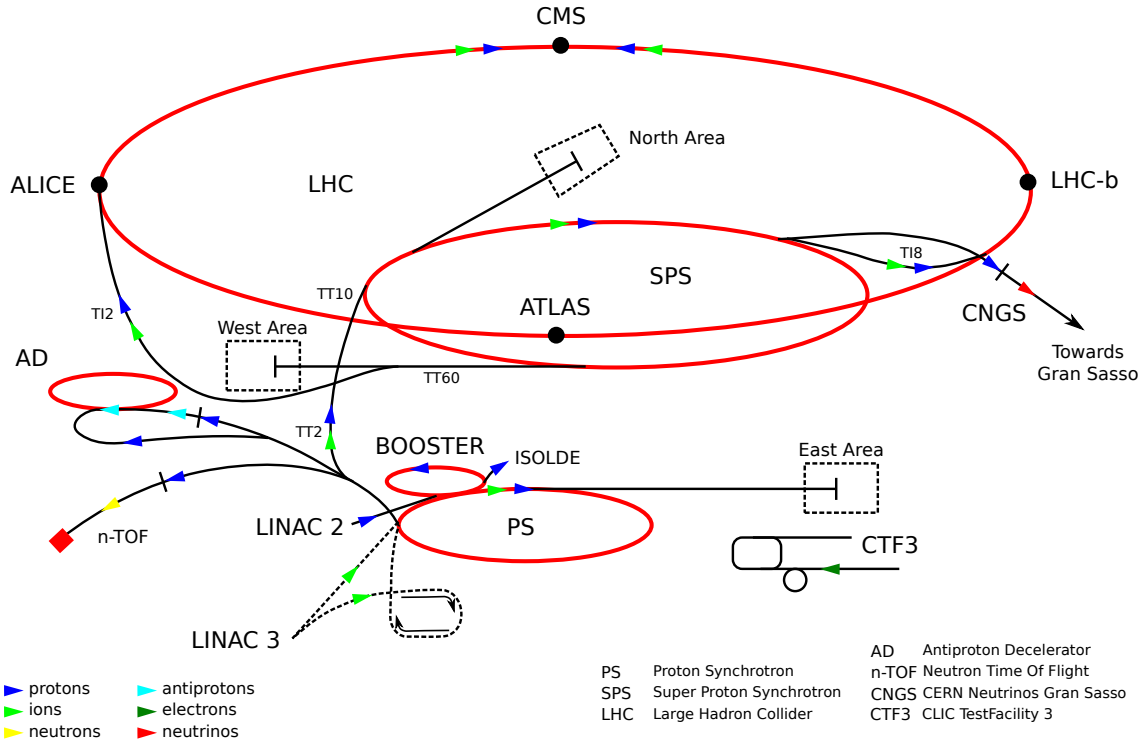

Figure 3.1 – Accelerator complex at CERN [73].

located around the ATLAS collision point, aims to emulate particle cascades similar to cosmic rays. It helps to understand the development of atmospheric showers, studied by astrophysical experiments. Finally, the Monopole and Exotics Detector at the LHC (MoEDAL), deployed around the LHCb interaction region, searches for magnetic monopole and for highly ionising stable massive particles.

The design energy of the proton collision in the centre of mass is $\sqrt{s} = 14\,\text{TeV}$. However in years 2010 and 2011, data were collected at $\sqrt{s} = 7\,\text{TeV}$ and in 2012 at $\sqrt{s} = 8\,\text{TeV}$. During Run II, the LHC runs at $\sqrt{s} = 13\,\text{TeV}$. To produce such high energetic beams, the most energetic to date, the LHC is fed by a complex chain of smaller accelerators (Fig. 3.1). The protons originate from a bottle of hydrogen gas which is ionised through an electric field. Thanks to the radiofrequency cavities of the linear accelerator 2 (LINAC 2) protons reach an energy of 50 MeV. Then they are injected into the Proton Synchrotron Booster (PSB) to be accelerated to 1.4 GeV. Next the Proton Synchrotron (PS) and the Super Proton Synchroton (SPS) boost the beam respectively to 25 GeV and 450 GeV. From this step the protons are separated in two beams and injected into the LHC, which ramps them up to the desired collision energy. The protons are gathered in packets, called bunches. The LHC nominal collision frequency is 40 MHz, which corresponds to a bunch spacing of 25 ns. This bunch spacing should be used during the second operating run (Run II). During Run I, between years 2010 and 2012, milder operating conditions were used with a bunch spacing of 50 ns instead.

The design instantaneous luminosity of LHCb is $2\times10^{32}\,\text{cm}^{-2}\,\text{s}^{-1}$, in contrast to $10^{34}\,\text{cm}^{-2}\,\text{s}^{-1}$ for the general purpose detector ATLAS and CMS. Indeed, the beam focusing at the interaction point is not the same. The amplitude function β^* is set to 3 m for LHCb whereas in ATLAS and CMS it is set to 1 m in 2011 and 60 cm in 2012. This lower luminosity makes a reduced average

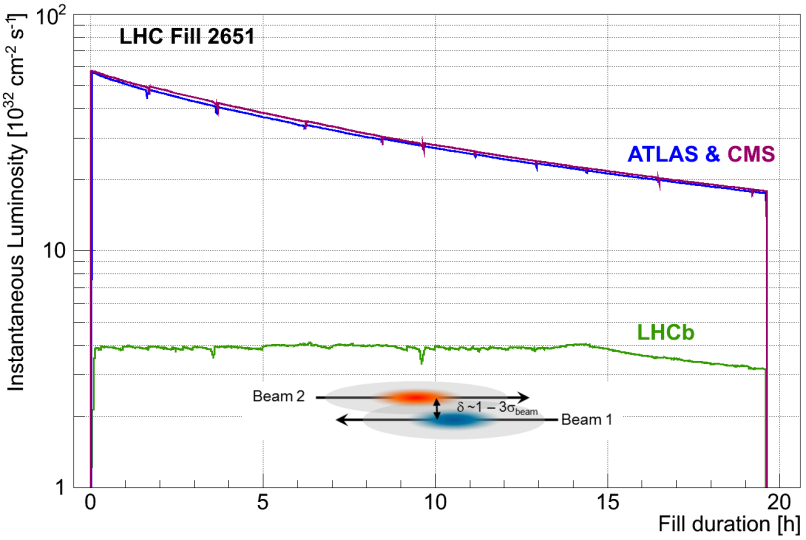

Figure 3.2 – Instantaneous luminosity for ATLAS, CMS and LHCb experiment during LHC fill 2651. By adjusting the transversal beam overlap, the luminosity for LHCb is kept a the desired value of $4 \times 10^{32}\,\mathrm{cm}^{-2}\,\mathrm{s}^{-1}$ for almost 15 hours.

number of visible pp interactions per bunch crossing, also known as pile-up. The design pile-up value of LHCb is $\mu_{vis} = 0.7$. It is a critical parameter since it drives the detector ability to identify the primary and secondary vertices and to reconstruct the whole decay chain. Another benefit of working at a modest luminosity is the reduced radiation damage. In 2011 the majority of the data were collected with an instantaneous luminosity of $3.5 \times 10^{32}\,\mathrm{cm}^{-2}\,\mathrm{s}^{-1}$, with $\mu_{vis} \approx 1.4$. In 2012 the data were collected at $4 \times 10^{32}\,\mathrm{cm}^{-2}\,\mathrm{s}^{-1}$, with $\mu_{vis} \approx 1.7$. Although these operating conditions were harsher than the design conditions, the detector showed excellent performances [74]. Since 2011, the peak luminosity has been kept stable to within about 5% during a LHC fill. This procedure is called "luminosity levelling" and consists of adjusting the transverse overlap of the beams at LHCb. Figure 3.2 highlights this feature for the LHC fill 2651 in 2012. At the beginning of the fill the two beams are transversely separated, and are then progressively brought closer as the beam intensity decays until they are head-on (after almost 15 hours of operation for this fill). Thanks to the luminosity levelling, the data taking conditions – like the trigger parameters and the detector occupancy – are stable throughout the fill. The integrated luminosity recorded by LHCb was $38\,\mathrm{pb}^{-1}$ in 2010, $1.11\,\mathrm{fb}^{-1}$ in 2011 and $2.08\,\mathrm{fb}^{-1}$ in 2012 (Fig. 3.3).

The $b\bar{b}$ production cross-section at a center-of-mass energy of $\sqrt{s}$ =7 TeV has been measured to be $\sigma(pp \to b\bar{b}X) = (284 \pm 20 \pm 49)\,\mu\mathrm{b}$ by LHCb [75]. This value corresponds to about 10^{11} $b\bar{b}$ pairs produced in the LHCb acceptance during Run I. To compare with e^+e^- B factories, the cross-section production of a $b\bar{b}$ pair at the $\Upsilon(4S)$ resonance is $\sigma(e^+e^- \to b\bar{b}) = 1.05\,\mathrm{nb}$ [76]. Therefore studying B physics at a hadronic collider has the advantage of a larger production cross-section, hence a larger number of b-hadrons produced per unit of luminosity. Moreover in a pp collision the $b\bar{b}$ pairs are mainly produced through a gluon fusion process, leading to a significant boost along the beam axis. Thus the typical flight distance of a B meson in LHCb is of the order of 1 cm. It makes possible the topological discrimination of "flying" b or c-like signals against light quarks background. At e^+e^- colliders such as PEP-II and KEK-B the boost was much

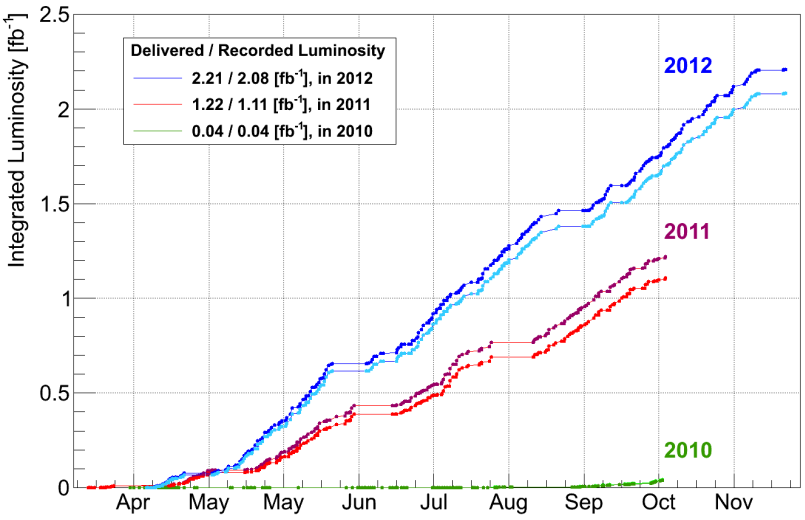

Figure 3.3 – Delivered (dark colour) and recorded (light colour) integrated luminosity in the LHCb experiment during the three years of LHC Run I.

smaller, with a resulting typical B flight distance of the order of $200-250\,\mu$m. Another benefit of a hadronic machine compared to e^+e^- colliders is the production of all types of b-hadrons. In addition of the $B^\pm$, B^0, $D^\pm$ and D^0 mesons produced at B factories, LHCb can study also B_s^0, $D_s^\pm$ and $B_c^\pm$ mesons as well as baryons like Ω_b^-, Λ_b^0 or Ξ_b^0.

However working at the LHC does not provide only advantages. Because of the hadronic environment, the background is significantly increased. It makes more difficult to trigger on signal events, to tag the b flavour states produced (there is no B^0–$\overline{B}^0$ coherence) and to reconstruct final states with missing or neutral particles. In addition, the collision energy at the parton level is unknown. Therefore the constraint of the beam energy cannot be used to discriminate signal and background as in B factories.

3.2 The LHCb detector

The LHCb detector is designed for indirect measurements of new physics in CP violating processes and rare decays of beauty and charm hadrons. Many models of physics beyond the Standard Model predict new sources of CP violating phases or enhancement of branching ratios in the heavy quark sector (see for instance Ref. [77–79]).

Among the main LHCb physics results we can cite: the first measurement of branching fraction of the rare decay $B_s^0 \to \mu^+\mu^-$ [80, 81], the angular analysis of the $B^0 \to K^{*0}\mu^+\mu^-$ decay [82–84], the ϕ_s CP violating phase measurement with the decays $B_s^0 \to J/\psi\, h^+h^-$ (h stands either for a pion or a kaon) [85, 86], the CKM angle γ measurement with $B \to DK$ decays [10, 87], CP asymmetry studies in the charm sector with $D^0 \to h^+h^-$ decays [88], measurement of electroweak gauge bosons production in the forward region [89, 90], the measurements of the properties of the exotic hadrons $X(3872)$ and $Z(4430)$ [18, 91], the searches for lepton number and lepton flavour violation [92, 93] and the heavy quarkonia measurements in proton-lead collisions [94, 95].

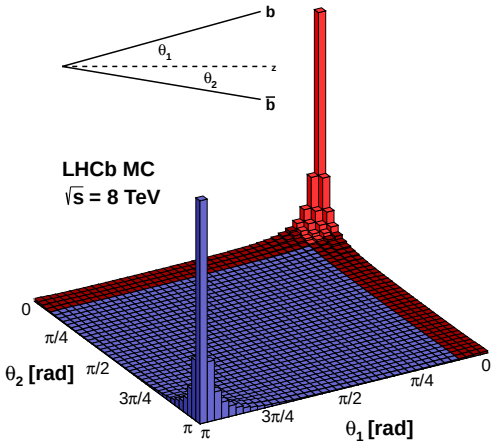

Figure 3.4 – Polar angles between the beam axis and the b and $\overline{b}$ quarks, produced from a proton-proton collision at a centre of mass energy $\sqrt{s} = 8$ TeV. Simulation performed with the PYTHIA event generator.

The LHCb detector is a single-arm spectrometer with a forward angular coverage from approximately 15 mrad to 300 (250) mrad in the bending (non-bending) plane. This corresponds to a pseudorapidity range of $2 < \eta < 5$. This particular acceptance is driven by the angular correlation of the $b\overline{b}$ pair produced in a pp collision at high energy. As can be seen in Fig. 3.4, the b and $\overline{b}$ quarks are mostly produced in the same forward or backward cone.

The main performance requirements for the precision measurements made at LHCb are a good vertexing and decay time resolution, an efficient track reconstruction, a good particle identification and the ability to trigger on interesting events, containing beauty or charmed hadrons. To fulfil these requirements, the LHCb detector is composed of several subdetectors, shown in Fig. 3.5. The tracks made by charged particles are measured with the Vertex Locator (VELO), the Tracker Turicensis (TT) and the Tracking Stations (T1,T2 and T3). The identification of charged hadrons (pions, kaons and protons) is realised by two Ring Imaging Cherenkov detectors (RICH1 and RICH2). Neutral particles, such as photons or π^0, are measured with the electromagnetic calorimeter (ECAL). The hadronic calorimeter (HCAL) is mainly used to trigger on hadronic signals. Finally muons are identified thanks to dedicated chambers (M1 to M5). Two system of coordinates are used to describe the detector: a right-handed Cartesian system, with z along the beam axis toward the detector, y vertical and x horizontal; and a cylindrical system with (r, ϕ, z).

This section briefly presents each subdetectors, the trigger system and the software. More details can be found in [72].

3.2.1 The tracking system

The tracking system measures the trajectories of the charged particles produced by the proton collisions. It determines the particle flight distances by reconstructing their production and decay vertices, and their momentum via magnetic deflection. The system is composed of three subdetectors: the Vertex Locator (VELO), located around the interaction point; the Tracker Turicensis (TT) located upstream of the magnet; and the tracking stations T1–T3 which are

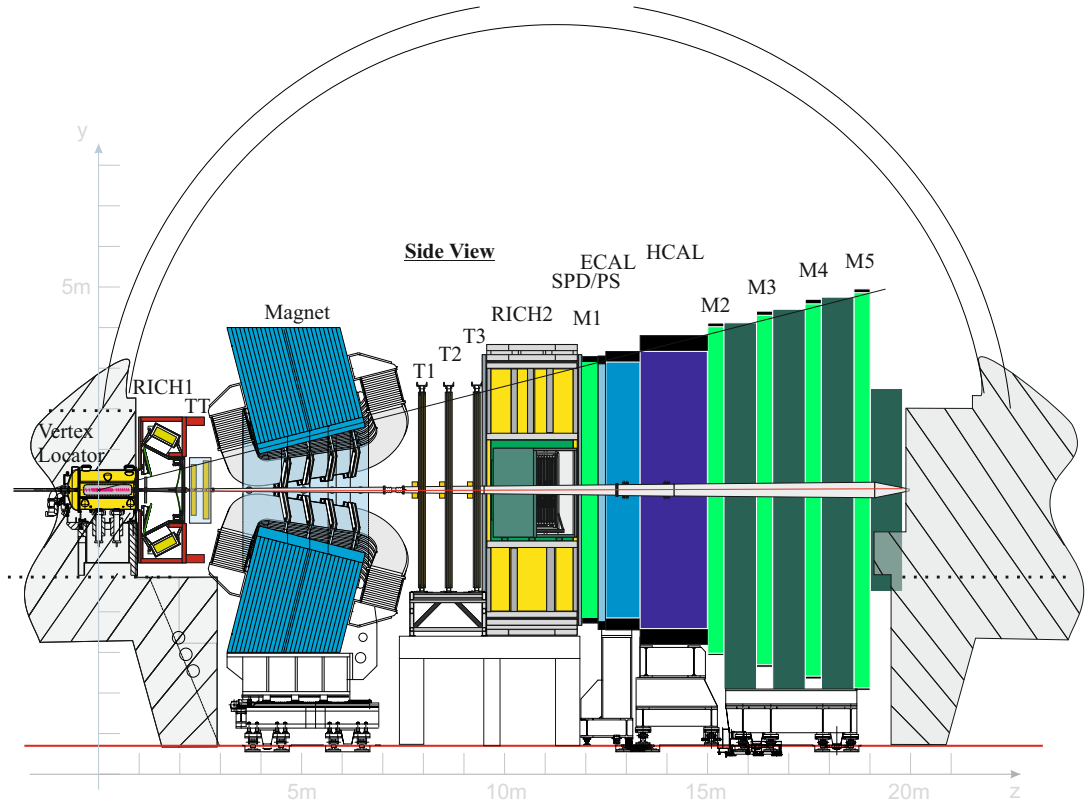

Figure 3.5 – The LHCb detector in the (y, z) plane (z is the beam axis).

downstream of the magnet. In order to go through all the tracking system, a charged particle must have a minimum momentum of 1.5 GeV.

The Vertex Locator

The VELO is crucial to precisely reconstruct vertices, and separate primary vertices from secondary ones. Since B and D mesons have a mean lifetime between 0.5 and 1.6 ps, and because of the large boost resulting from the pp collision, their typical flight distance in the detector is about 1 cm. Therefore the interesting signals contain reconstructed particle candidates with large flight distances and impact parameters. Thanks to the high spatial resolution of the VELO, it is possible to distinguish such b and c-like topologies from light quark flavour background. This topology criteria is the base of the High Level Trigger algorithm (see Sec.3.2.6). The other benefit from the high spatial resolution is the precision on the proper time measurement, essential for time-dependent analyses studying neutral meson mixing.

The VELO is separated in half along the beam axis, as represented in Fig. 3.6. Each half is composed of 21 circular silicon modules, perpendicular to the beam. The module outer radius is of 42 mm and the inner radius of 8.2 mm. Since this inner radius is too small compared to the safety aperture required during the LHC injection, each VELO half is automatically retracted by 29 mm in the horizontal direction when the accelerator is not in stable beam conditions. There are two types of modules: those measuring the r coordinates, called R-sensors, and those

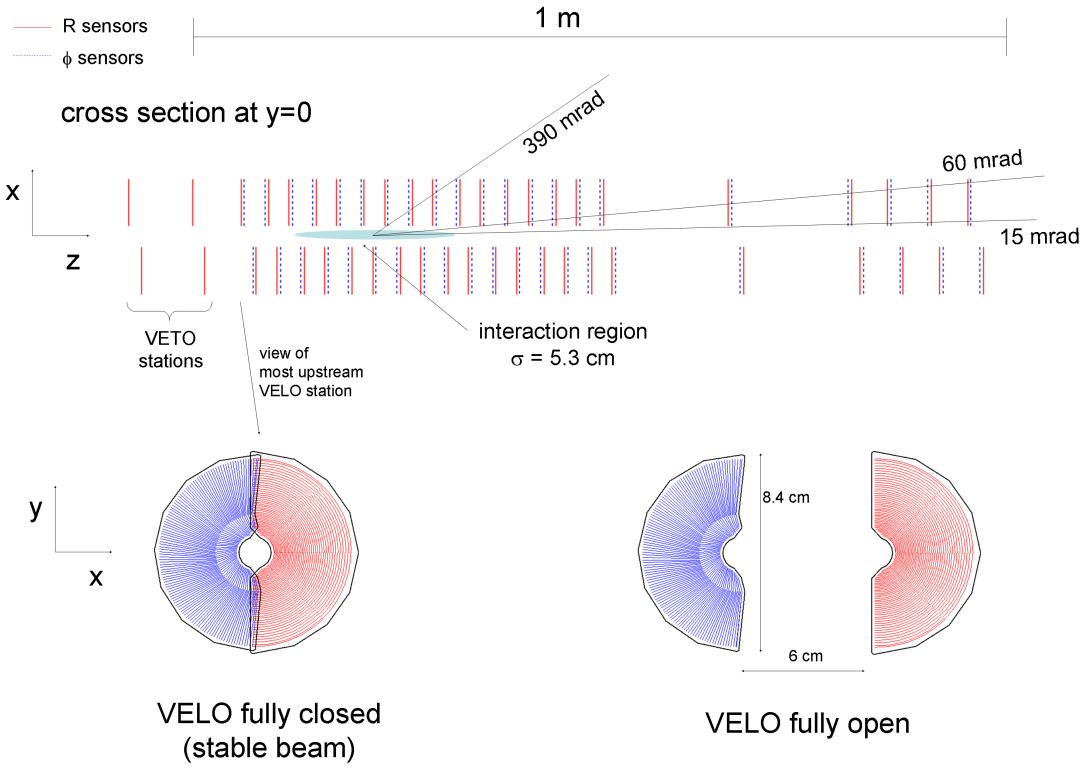

Figure 3.6 – Cross-section of the VELO in the horizontal (top) and vertical (bottom) planes. The R-sensors are in red and the ϕ-sensors in blue.

measuring the azimuthal angle ϕ, called ϕ-sensors. These sensors are made of silicon strips, with a pitch varying from 38 µm in the innermost region to 102 µm in the outermost region. To minimise the material length traversed by the particles between the sensors, the latter are placed in a vessel maintaining a secondary vacuum. The two halves are shifted along z by 1.5 cm to permit a complete overlap of the sensors once the detector is closed. Hence the azimuthal coverage is perfect. Along the z-axis, the sensors are placed with a 3.5 cm pitch to guarantee that at least three of them are traversed by a particle flying in the LHCb acceptance. In addition, four sensors are placed upstream the regular VELO sensors. They form the *pile-up veto system*, which aims to identify and reject events with multiple pp interactions. These additional planes help to measure the z position of the primary vertices and the total backward charged multiplicity.

Thanks to this layout, the VELO has a precision of 20 µm on the impact parameters (IP) of high transverse momentum (p_{T}) tracks. The decay time resolution reaches 45 fs. Such a time resolution makes possible for instance the most precise measurement of the B_s^0 oscillation frequency using the decay $B_s^0 \to D_s^- \pi^+$ [96]. With such a resolution, the oscillations in the flavour tagged decay time distribution can be clearly observed (Fig.3.7).

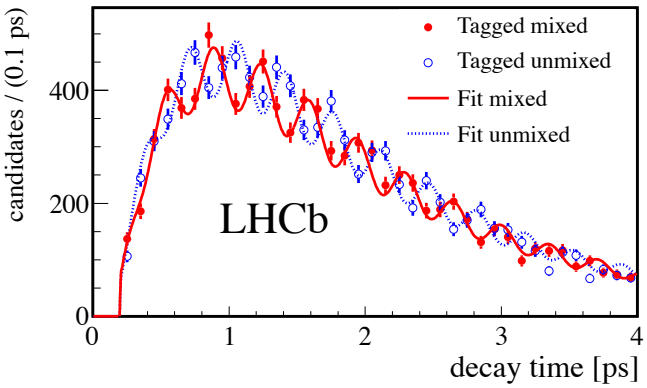

Figure 3.7 – Decay time distribution of $B_s^0 \to D_s^- \pi^+$ candidates tagged as mixed (different flavour at decay and production; red solid line) or unmixed (same flavour at decay and production; blue dotted line) [96].

The magnet

In order to measure their momentum, the trajectory of the charged particles is bent in the field produced by a warm dipole magnet. This magnet is composed of two identical coils of conical saddle shape, placed mirror-symmetrically to each other in the magnet yoke (Fig. 3.8). The resulting integrated magnetic field is about 4 Tm. The non-uniformity of the field magnitude is below 1%. This non-uniformity coupled with a slight detector asymmetry can provoke artificial asymmetries between negatively and positively charged particles. As a consequence, it may create systematic effects for *CP* violation measurements, which can be non negligible in a high statistics regime. In order to reduce them, the polarity of the magnetic field is periodically inverted. The two corresponding configurations are called *MagUp* and *MagDown*.

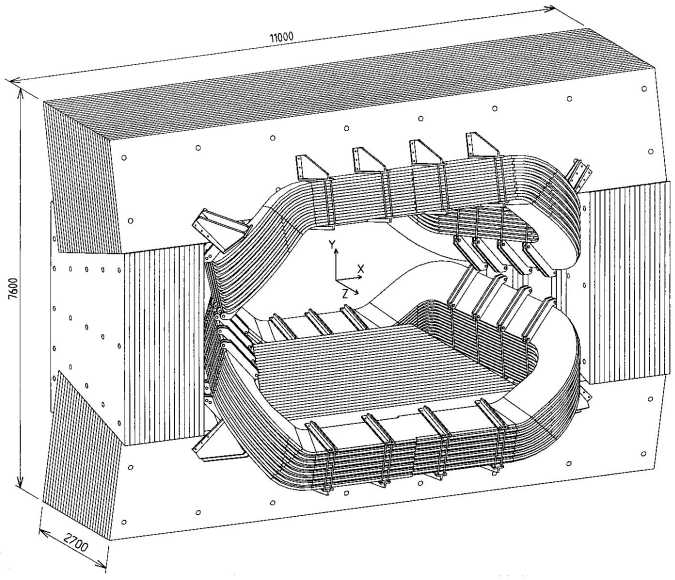

Figure 3.8 – Perspective view of the LHCb dipole magnet.

The Silicon Tracker

The Silicon Tracker (ST) system is designed to perform well in an environment of high particle densities. It is composed of one station upstream of the magnet, namely the Tracker Turicensis (TT), and three stations downstream of the magnet forming the inner part of the tracking station T1–T3, called the Inner Tracker (IT). These detectors are made of p^+-on-n silicon microstrips, with a strip pitch of 183 µm and 198 µm for the TT and the IT respectively. They are placed in boxes which are opaque, thermally and electrically insulated. These boxes keep them also at a temperature of 5°C to reduce the damage caused by radiation. To avoid condensation on the cold surfaces, they are continuously flushed with nitrogen.

The TT is about 150 cm wide and 130 cm high for a total active area around 8 m^2 (Fig. 3.9a), corresponding to the full LHCb detector angular coverage. Its sensors are 9.64 cm wide and 9.44 cm high, for a thickness of 500 µm. The IT is about 120 cm wide and 40 cm high for a total active area around 4 m^2 (Fig. 3.9b). It covers the region of the tracking stations T1–T3 located closest to the beam pipe, where the particles flux is the higher. Its sensors are 7.6 cm wide, 11 cm high and either 320 µm or 410 µm thick. They are placed in a cross shape around the beam pipe. There is some overlap between the modules to have a full coverage and allow an easier alignment. To guarantee an efficient track reconstruction algorithm, with low ghost rates[1], the ST modules are arranged in $x-u-v-x$ layers. The strips in x layers are vertical and rotated by a stereo angle of $-5°$ and $+5°$ in u and v layers, respectively.

In the years 2011 and 2012, the hit efficiency of both TT and IT was well above 99%, for a hit resolution below 55 µm.

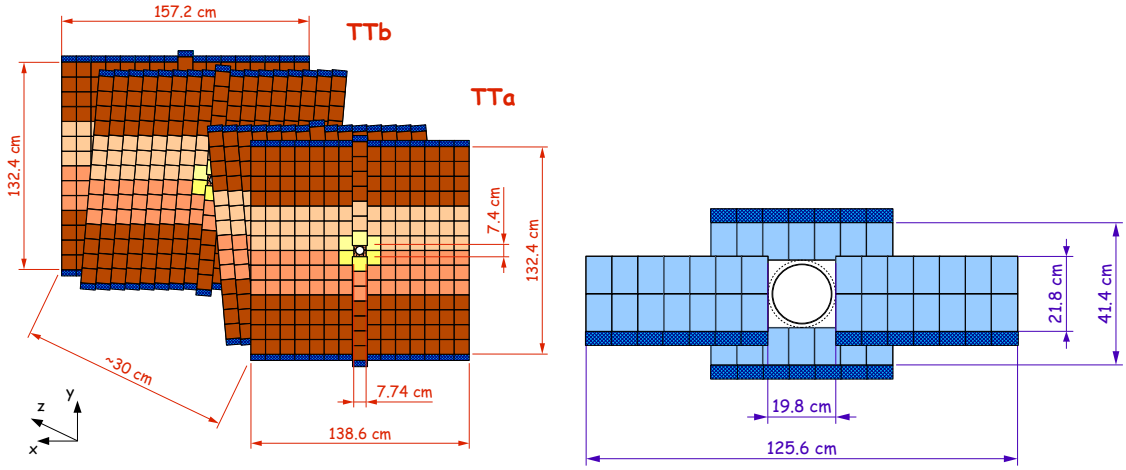

(a) TT (b) IT

Figure 3.9 – The Silicon Tracker layout, including the TT (a) and IT (b) stations.

The Outer Tracker

The tracking stations T1 to T3 are hybrid detectors. The central region, with a higher occupancy, is measured by the Inner Tracker. To cover the full LHCb detector angular acceptance, the

[1] A ghost track is made by a random combination of hits, faking a real track.

surrounding area is handled by the Outer Tracker (OT). This is a drift-time detector, consisting of an array of about 200 gas-tight straw tube modules. Each modules is composed of two staggered layers of drift-tubes, with an inner diameter of 4.9 mm. The counting gas is a mixture of Argon (70%), CO_2 (28.5%) and O_2 (1.5%) to have a drift-time below 50 ns and a spatial resolution of 200 µm. As for the ST, the OT layers are in a $x-u-v-x$ arrangement. The total active area covered is 597 cm × 483 cm.

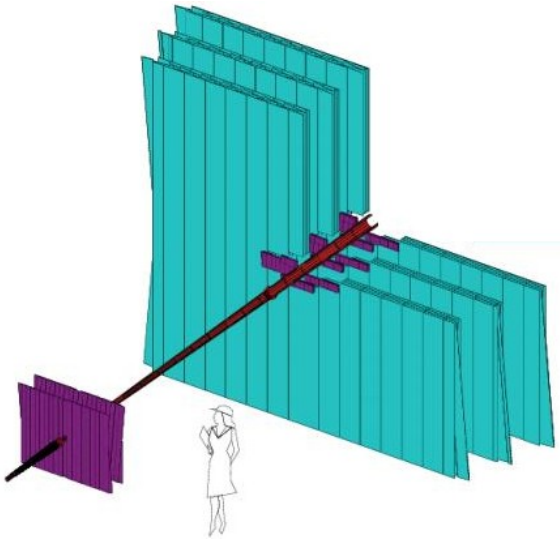

Figure 3.10 – The LHCb tracking stations. The Silicon Tracker is in purple, the Outer Tracker in blue.

The trajectories of the charged particles are reconstructed from the hits measured in the VELO, TT, IT and OT. Depending on their path through the subdetectors several track types are defined (Fig. 3.11). The two most important ones are the Long and Downstream tracks :

Long tracks traverse the full tracking system. They have hits at least in the VELO and the T stations, and optionally in the TT. Since in this case the particle trajectories are reconstructed with hits located across the whole magnetic field, they have the most accurate momentum determination.

Downstream tracks pass only through the TT and T stations. They mainly correspond to long-lived particles, such as K^0_S mesons and Λ baryons, which decay outside the VELO acceptance.

During Run I, the tracking efficiency was larger than 96% for Long tracks. The momentum resolution was of $\Delta p/p \sim 0.4\%$ at 5 GeV to 0.6% at 100 GeV. This performance corresponds to a mass resolution of about 8 MeV for $B \to J/\psi\, X$ decays (with a constraint on the J/ψ mass), 22 MeV for two body B decays and 100 MeV for $B^0_s \to \phi\gamma$ decays (dominated by the photon momentum resolution).

3.2.2 The Ring Imaging Cherenkov detectors

The ability to identify charged hadrons, such as pions, kaons and protons, is crucial for an experiment dedicated to flavour physics. For instance the following measurements are impossible without the ability to distinguish between pions and kaons:

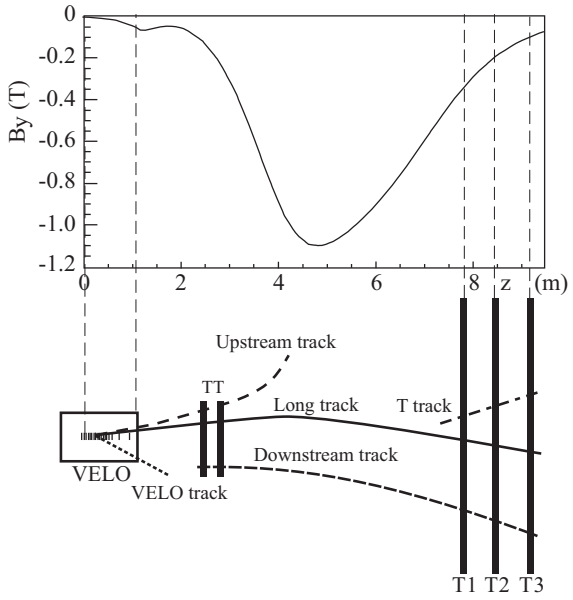

Figure 3.11 – Illustration of the different track types reconstructed by the tracking system. The magnetic field component on the y-axis, as a function of the z coordinate, is plotted above.

- measurement of the CP asymmetry $A_{CP} \equiv \frac{\Gamma(B^0 \to K^+\pi^-) - \Gamma(\overline{B}^0 \to K^-\pi^+)}{\Gamma(B^0 \to K^+\pi^-) + \Gamma(\overline{B}^0 \to K^-\pi^+)}$,
- B^0 meson flavour tagging in $B^0 \to DK^{*0}$ and $\overline{B}^0 \to D\overline{K}^{*0}$ decays (the $K^{*0} \to K^+\pi^-$ and $\overline{K}^{*0} \to K^-\pi^+$ must be disentangled),
- distinction of the suppressed $D^0 \to \pi^+K^-$ decay mode from the favoured $D^0 \to K^+\pi^-$ channel.

This charged hadron identification is possible thanks to the Cherenkov effect. A charge particle which goes through a medium faster than the speed of light in this medium, emits a cone of light. The cone angle depends directly on the particle velocity. Hence combining the measurement of its velocity and momentum, the particle mass, therefore its type, can be determined. In LHCb this identification is realised by two Ring Imaging Cherenkov detectors (RICHs). They are designed to cover the momentum range of B and D daughters studied in LHCb, which is typically from 2 to 100 GeV. A schematic description of the two detectors is provided in Fig. 3.12. RICH1, located upstream of the magnet, is dedicated to momentum from 2 to 60 GeV. Its radiators are a combination of aerogel and C_4F_{10} gas. The full LHCb acceptance is covered, from 25 to 300 (250) mrad in the bending (non-bending) plane. RICH2 is placed downstream of the magnet, just after the tracking stations. Its momentum range extends from 15 to 100 GeV, with CF_4 gas as a radiator. Its angular acceptance is limited from 15 to 120 (100) mrad and corresponds to the angular distribution of the highest momentum particles. The momentum coverage of both detectors is illustrated in Fig. 3.13.

The Cherenkov photons are detected with Hybrid Photon Detectors (HPD). They are located outside the spectrometer acceptance, in order to limit the material budget and protect them from high radiation levels. The light is guided and focused thanks to a combination of spherical and flat mirrors. The HPDs are put in iron shield boxes to reduce the magnetic field effect inside the detectors. They measure the spatial position of the Cherenkov photons. Each photon

reaching the photocathode of an HPD can produce a photo-electron. This electron is accelerated in the detector vacuum chamber, thanks to a high voltage. The electron is then detected with a silicon sensor. The major characteristic of an HPD is its large area coverage, high active-to-total area ratio, high granularity and high speed. Simulated typical Cherenkov rings measured by the HPDs can be seen on Fig. 3.14.

In 2012, the RICHs performance resulted in a kaon identification efficiency of 95% (probability to detect a kaon as a kaon) for a pion mis-identification probability of 10% (probability to identify a pion as a kaon).

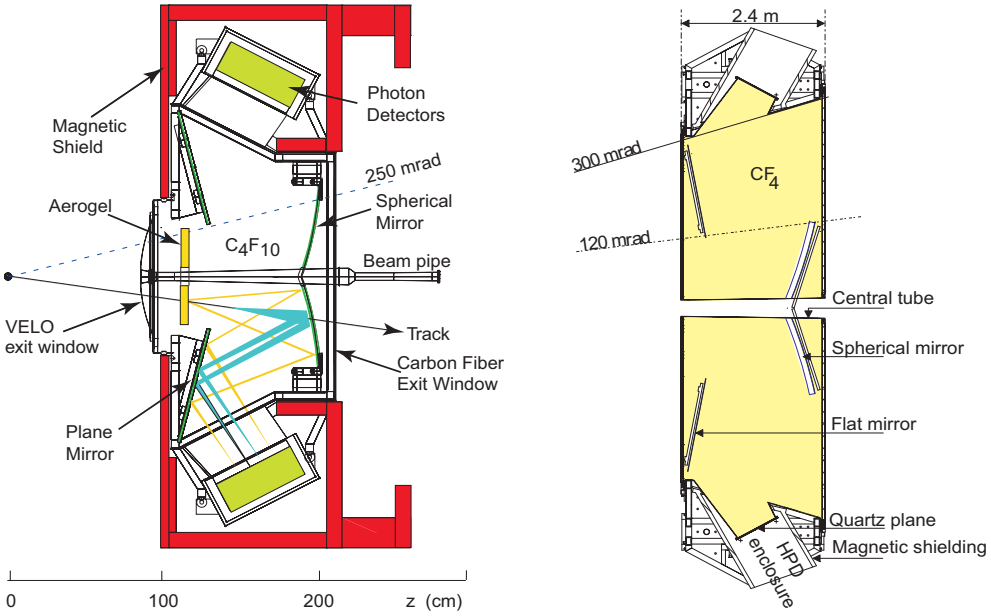

(a) RICH1 (b) RICH2

Figure 3.12 – The two Ring Imaging Cherenkov detectors: RICH1 side view (a) and RICH2 top view (b).

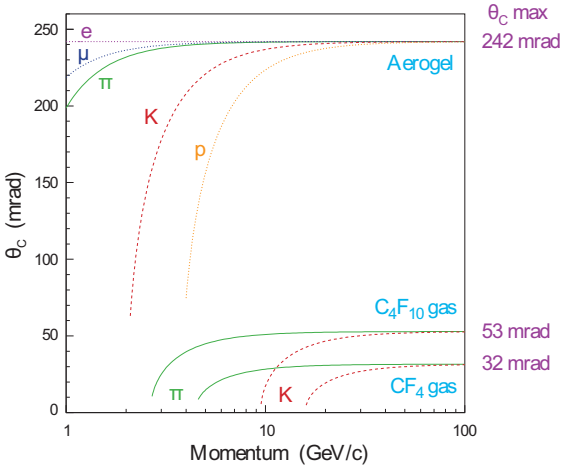

Figure 3.13 – Cherenkov angle as a function of the particle momentum for the RICH detector.

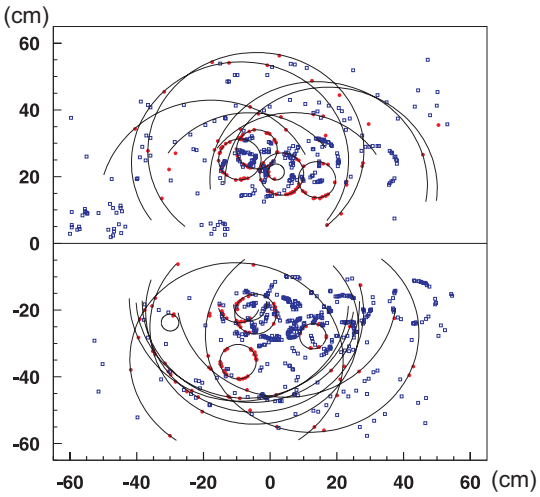

Figure 3.14 – Display of a simulated typical LHCb event in RICH1.

3.2.3 The calorimeters

The LHCb calorimeters have three purposes. First, they identify electrons, photons and neutral pions. They also provide useful information, in addition to the RICH, for charged hadrons identification. Then, they measure the energy and position for the electrons, photons and neutral pions. Such measurements are crucial for the study of radiative decays like $B^0 \to K^{*0}\gamma$ or $B_s^0 \to \phi\gamma$ and electronic decays like $B^0 \to K^{*0}e^+e^-$. Finally, the hardware trigger (see Sec. 3.2.6) needs a fast measurement of the particles transverse energy, to detect candidates from beauty and charmed decays and take its decision in less than 4 µs. The calorimeters provide such a measurement, and make possible to trigger on electromagnetic and hadronic signals.

The calorimeters system is located between 12.3 and 15 m after the pp interaction point. It is composed of a Scintillating Pad Detector (SPD), a Preshower (PS), an electromagnetic calorimeter (ECAL) and a hadronic calorimeter (HCAL). The whole follows a projective geometry to cover the full LHCb angular acceptance. The same principle is used for the four detectors: the scintillation light produced by the charged particles is collected by wavelength shifting (WLS) fibres and transmitted to photomultiplier tubes (PMT). The longitudinal structure of the calorimeters is shown in Fig. 3.15. The particle identification principle is also illustrated. The charged particles produce scintillation light in the SPD and PS detectors. Electromagnetic showers are initiated just before the PS, within the lead layer, and develop in the ECAL, whereas hadronic showers develop later in the HCAL (with a potential energy deposit at the end of the ECAL). The particle flux varies by two orders of magnitude between the region close to the beam pipe and those more distant. Thus to have a high granularity, at reduced-cost, a lateral segmentation is made. As illustrated in Fig. 3.16a, the SPD, PS and ECAL are divided into three areas: the inner, middle and outer regions (listed by decreasing granularity). The HCAL needs only to be divided in two areas: the inner and outer regions (Fig.3.16b). The following sections focus on each calorimeter subsystem.

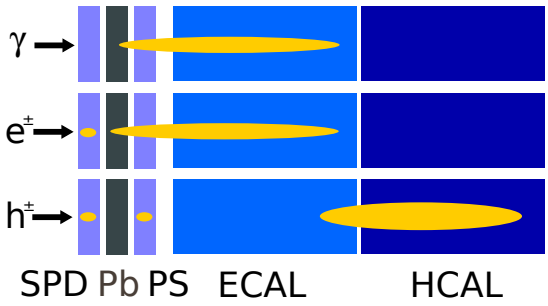

Figure 3.15 – Schematic illustration of shower development in the LHCb calorimeter system for the photons, electrons and charged hadrons.

The scintillating pad and preshower detectors

The SPD/PS detectors consist of two layers of scintillator pads 15 mm thick. Between them is placed 15 mm of lead, which corresponds to $2.5X_0$ radiation length and $0.1\lambda_{int}$ nuclear interaction length. The lead serves to initiate the electromagnetic cascades. The SPD is used to discriminate between the electrons and the photons. The number of hits in the SPD also provides some information about the charged particle multiplicity in an event. The PS, coupled

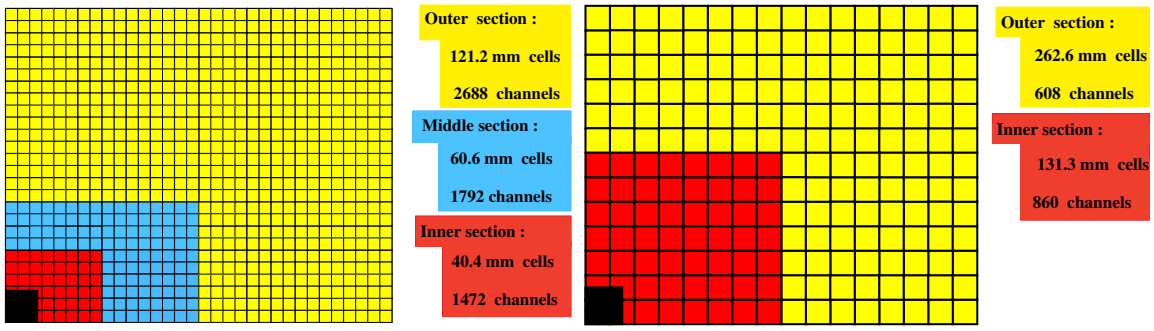

(a) ECAL (b) HCAL

Figure 3.16 – The electromagnetic (a) and hadronic (b) calorimeters segmentation.

to the ECAL, provides a longitudinal segmentation of the electromagnetic calorimeter. This is used to separate pure electromagnetic showers from charged pion background. The active area of the PS is 7.6 m wide and 6.2 m high.

The electromagnetic calorimeter

The electromagnetic calorimeter is based on the shashlik technology. It is composed of alternating layers of sampling plastic scintillator and lead converter tiles, transversely crossed by wavelength shifting fibres. The measurement principle relies on the energy conversion of incoming photons or electrons into electromagnetic cascades. These cascades develop through a large number of the lead layers. When the charged particles composing the showers cross the scintillator layers, the plastic emits scintillation light. In first approximation, the amount of light produced by an electromagnetic shower is proportional to the energy of the incoming particle. The scintillation light is collected thanks to the WLS fibres. These fibres are doped in such a way that the scintillation light crossing a fibre is absorbed and re-emitted in wave lengths which propagate inside the fibres.

The structure of an ECAL module is illustrated in Fig. 3.17a. One module is made of 66 lead plates 2 mm thick and 67 scintillator layers 4 mm thick. Between each layer a light reflecting TYVEK paper, 120 µm thick, is inserted to improve the scintillation light collection. The whole is assembled in a 42 cm deep stack, corresponding to $25X_0$ and $1.1\lambda_{int}$. The Molière radius of this stack is 3.5 cm. To ensure light tightness and have modules isolated from each others, they are individually wrapped in black paper. As already mentioned and illustrated in Fig. 3.16a, a variable lateral segmentation is made. The modules of the outer part of the ECAL are made with one cell 121.2 mm wide. Those of the middle part are divided in 4 cells 60.4 mm wide, while in the inner modules there are 9 cells 40.20 mm wide. In each module the cells share the same lead plate, but are made of distinct scintillator tiles. These tiles are chemically treated at the edges to ensure an efficient light collection, a good lateral uniformity and a reduce tile-to-tile light cross talk. The fibre density is also adapted to the variable granularity. In the outer area the modules are crossed by 64 fibres, whereas in the middle and inner area there are 144 fibres. In each area there is one PMT connected to one cell.

The energy resolution of a calorimeter can be expressed as

$$\frac{\sigma_E}{E} = \frac{a}{\sqrt{E}} \oplus B \oplus \frac{c}{E} \text{ (GeV)}. \tag{3.1}$$

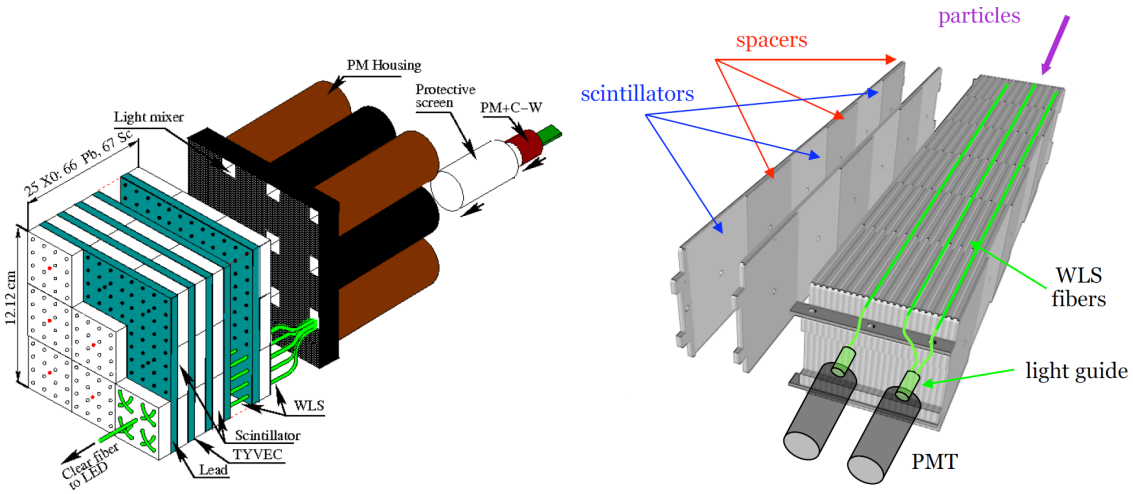

(a) ECAL module (b) HCAL module

Figure 3.17 – Structure of the electromagnetic (a) and hadronic (b) inner calorimeter cells.

The first term, namely the *stochastic* term, arises from the light collection fluctuation for a shower at a given energy. The second is the *constant* term, linked to the calorimeter non uniformity. The third is the *noise* term, corresponding to the electronic noise effect. The design ECAL resolution is

$$\frac{\sigma_E}{E} = \frac{10\%}{\sqrt{E}} \oplus 1\% \text{ (GeV)}. \tag{3.2}$$

A measurement of this resolution has been performed with a test beam [97] and is in good agreement with the design value:

$$\frac{\sigma_E}{E} = \frac{(9.4 \pm 0.2)\%}{\sqrt{E}} \oplus (0.83 \pm 0.02)\% \oplus \frac{(0.11 \pm 0.03)}{E} \text{ (GeV)}. \tag{3.3}$$

Due to the dynamic range imposed by the physics, the maximal transverse energy measurable by the ECAL is 10 GeV. The neutral energy deposit reconstruction is discussed further in chapter 4. The photon energy and position measurement made by the ECAL drives directly the mass resolution for the radiative decay channel, such as $B^0 \to K^{*0}\gamma$. For this channel the mass resolution is found to be 93 MeV [98].

The hadronic calorimeter

The hadronic calorimeter is located at 13.33 m from the interaction point, just after the ECAL. It is also a sampling device, based on the Tilecal technology. Scintillating tiles parallel to the beam axis are assembled between iron absorbers (Fig. 3.17b). The scintillating light is collected by WLS fibers, placed along the tiles, and guided to the PMTs at the back of the HCAL. The cells are 131.3 mm and 262.3 mm wide in the inner and outer part, respectively. The calorimeter is 1.65 m deep, which correspond to $5.6\lambda_{int}$. This results in an energy resolution of

$$\frac{\sigma_E}{E} = \frac{(69 \pm 5)\%}{\sqrt{E}} \oplus (9 \pm 2)\% \text{ (GeV)}, \tag{3.4}$$

filling the requirements imposed by the trigger system.

The HCAL embeddes a self-calibration system based on a ^{137}Cs source. This source travels through all the HCAL modules, thanks to steel tubes at the center of each tiles and a water pumping system. This system enables ageing effects to be monitored, and to adjust accordingly the gains to keep a constant trigger rate.

3.2.4 The muon system

The muon system has two purposes: triggering on high transverse momentum muons and providing offline muon identification. These are essential requirements to study properly, for instance, *CP* violation in $B^0 \to J/\psi\, K^0_S$ or $B^0_s \to J/\psi\, \phi$ decays, or to search for rare decays such as $B^0_s \to \mu^+\mu^-$. One component of the flavour tagging of neutral B mesons relies also on the good performances of the muon system. Indeed, muons from semi-leptonic b decays tag the flavour at the production time of the accompanying neutral B meson.

Five rectangular stations, M1 to M5, are installed in a projective geometry to have an angular coverage from 20 (16) mrad to 306 (258) mrad in the bending (non-bending) plane. All the stations are composed of Multi Wire Proportional Chambers (MWPC), except the inner region of M1, which is made of triple Gas Electron Multiplier (GEM) detectors to ensure a better ageing in this high radiation area. There is a total of 1380 chambers. As illustrated in Fig. 3.18, the chamber M1 is placed in front of the calorimeters to provide a better p_{T} measurement to the hardware first level trigger (L0). The chambers M2 to M5 are downstream of the calorimeters, and separated by iron absorbers 80 cm thick. In this way, only muons can penetrate the totality of the chambers and reach M5. Indeed, the total interaction length including the calorimeters is around $20\lambda_{int}$. Thus, to cross all the stations a muon must have a minimal momentum of 6 GeV.

The stations M1–M3 have a high spatial resolution on x (the bending plane) to efficiently determine the track direction and measure the p_{T} with a 20% resolution, sufficient for the L0. The last stations M4 and M5 have a more limited spatial resolution. They are mainly designed to select the penetrating muons. The layout of the stations is shown in Fig. 3.18. Each station is divided into four regions, R1–R4, whose segmentation scales with the ratio 1:2:4:8. Thanks to this adapted granularity, the channel occupancy is approximately constant between each region.

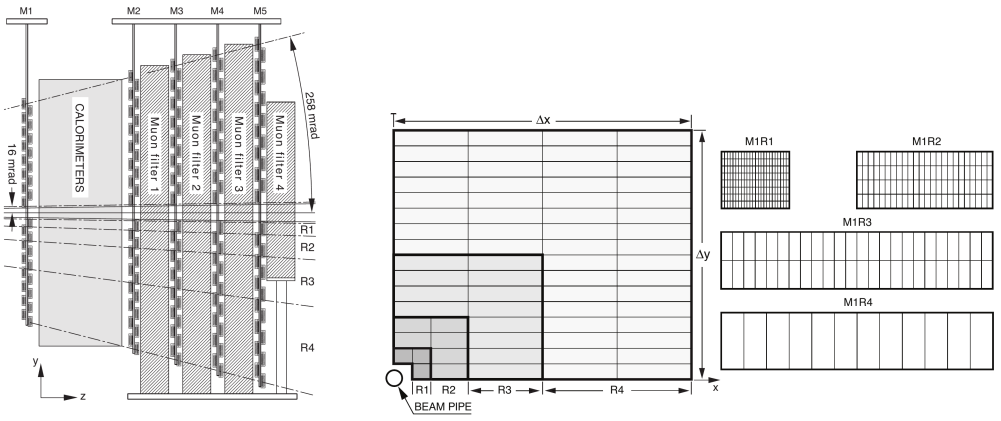

Figure 3.18 – Sideview of the muon sytem (left), front view of a quadrant of one muon station where each square represents a muon chamber (middle) and segmentation layout of the chambers in the different region of M1 (right).

To provide a muonic trigger at the 40 MHz LHC collision rate, a good hit efficiency, a good time resolution, a high rate capability, a fast electronics and a strong ageing resistance are required features. During Run I operation, the muon identification efficiency was of 97% for a pion to muon mis-identification probability of 1 to 3% (depending on the particle energy).

3.2.5 Charged hadron identification

The analysis presented in chapter 5 uses the charged hadron identification ability of the LHCb detector. This section briefly explains how the *particle identification* (PID) information given by the RICH, calorimeters and muon sub-detectors is combined to provide a powerful set of discriminating variables. Two different methods are used. The first is based on the separate likelihoods provided by each sub-system, $L^{\text{subsyst}}(h)$. These likelihoods give the probability, according to a given sub-system, that a given track is from a particle of type h. The global likelihood is simply obtained by multiplication:

$$L_{\text{comb}}(h) = L^{\text{RICH}}(h) \cdot L^{\text{CALO}}(\text{non } e) \cdot L^{\text{MUON}}(\text{non } \mu). \tag{3.5}$$

To discriminate one particle hypothesis against one another, the delta-log likelihood is computed. It gives for instance the kaon-pion separation variable

$$\text{DLL}_{K\pi} \equiv \ln \frac{L_{\text{comb}}(K)}{L_{\text{comb}}(\pi)}. \tag{3.6}$$

The second method available is based on a multivariate technique. It combines directly the different information provided by the RICH, calorimeters and muons sub-systems, into a single estimator for each particle hypothesis. In this technique, the correlation between the sub-detectors is taken into account. The likelihood and the multivariate methods show different performances depending on the momentum range of the particles. Their usage depends on the characteristics of each analysis.

3.2.6 The trigger system

At the design LHC bunch crossing rate and a luminosity of 2×10^{32}, the rate of visible interaction in the LHCb detector is about 10 MHz. Among these interactions, only 100 kHz correspond to a $b\bar{b}$ pair production. And only 15% of these events produce a B meson with all his decay products in the detector acceptance. Hence, it is essential for LHCb to trigger on b and c signals while rejecting a large amount of uninteresting light flavour events.

To fulfil this requirement, the trigger system is divided in two levels: the Level-0 (L0) and the High Level Trigger (HLT). This scheme, illustrated in Fig. 3.19, reduces to 5 kHz the rate at which the selected events are stored for further offline analysis. The L0 consists of a custom made electronics, capable of a fast reading of the information provided by the calorimeters and the muon system. It reduces the event rate to 1 MHz. At this frequency all the detector can be read out, and the HLT takes over. The HLT is a software application running on the Event Filter Farm (EFF), containing around 29000 logical CPU cores. In 2012, a fraction of events accepted by the L0 were deferred to disk, to be processed by the HLT during the time between LHC fills. This deferral enables a more efficient use of available EFF resources. The deferred trigger scheme is illustrated in Fig. 3.19b.

The trigger efficiency during Run I was about 90% for dimuon channels and 30% for multi-body hadronic final states.

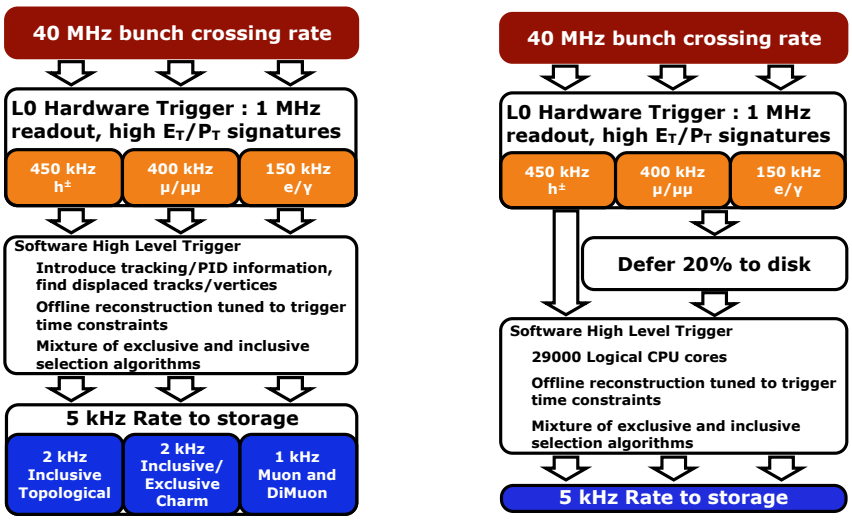

Figure 3.19 – (a) Scheme of the LHCb trigger system used during the 2011–2012 data taking period. (b) Scheme of the LHCb deferred trigger used during 2012 data taking period.

The Level-0 trigger

The L0 trigger runs synchronously with the 40 MHz bunch crossing rate of the LHC. Its latency is fixed and independent of the occupancy and the bench crossing history. As already mentioned, the purpose of this hardware trigger is to reduce the event rate from 40 MHz to 1 MHz, while keeping a maximum of interesting events. Hence, it relies on the fact that, due to the high mass of the B mesons, their decay products have in average a higher transverse momentum (p_{T}) and transverse energy (E_{T}) than more common decay products. Three independent units form the L0 trigger: the L0-calorimeter, the L0-muon and the L0-PileUp.

The L0-PileUp is used for the determination of the luminosity [99]. It aims to veto events with multiple interactions, by using the information provided by the four VELO sensors placed most upstream of the collision point (see Sec. 3.2.1). This unit is also used for triggers dedicated to Central Exclusive Production signal.

The L0-calorimeter unit gathers the information collected by the SPD, PS, ECAL and HCAL to compute the E_{T} in clusters of 2×2 cells. Three kinds of candidates are built: `L0Hadron`, `L0Photon` and `L0Electron`. A `L0Hadron` candidate corresponds to a highest E_{T} HCAL cluster, taking into account also the residual energy deposit in the corresponding ECAL cluster. A `L0Photon` candidate is a highest E_{T} ECAL cluster with 1 or 2 PS hits in front of the matching ECAL cluster. In addition, no hit in the corresponding SPD cells has to be found. `L0Electron` candidates must fulfil the same criteria as `L0Photon`, except that they must have at least one SPD hit in front of the PS cluster. To fire the trigger, these candidates must have an E_{T} larger than a fixed threshold. The typical threshold used during Run I are listed in Table 3.1. Besides E_{T} cuts, events are required to have a total number of SPD hits lower than a particular limit (listed in Table 3.1). This criterion prevents the HLT from spending a disproportionately large fraction of the available processing time on events with a too high multiplicity.

The L0-Muon unit takes the two highest p_{T} tracks in each quadrant of the muon chambers. The resulting eight candidates are considered and compared to a single threshold on either the

Table 3.1 – Typical L0 thresholds used in Run I. More details are in Ref. [100]

	p_T or E_T		SPD hits
	2011	2012	2011 and 2012
Single muon	1.48 GeV	1.76 GeV	600
Dimuon $p_{T1} \times p_{T2}$	$(1.30\,\text{GeV})^2$	$(1.60\,\text{GeV})^2$	900
Hadron	3.50 GeV	3.70 GeV	600
Electron	2.50 GeV	3.00 GeV	600
Photon	2.50 GeV	3.00 GeV	600

largest p_T, or the product of the two highest transverse momentum ${p_T}^{\text{largest}} \times {p_T}^{2^{\text{nd}}\text{ largest}}$.

The L0 Decision Unit (DU) collects information from the L0-PileUp, the L0-Calorimeter and the L0-Muon and combines it in a logical OR to make the global L0 trigger decision. The time for the L0 trigger decision to reach the front end electronics is fixed to 4 µs after the corresponding pp interaction occurred. This time includes the particle time-of-flights and the delays arising from the cables and the front end electronics. It means that approximately 2 µs are left for the L0 data processing.

The High Level Trigger

The HLT runs asynchronously with the LHC collision rate and is a C++ application running on each CPU of the Event Filter Farm (EFF). It reduces the 1 MHz data flow at the L0 output to 5 kHz, at which rate the data can be stored on disk. Each HLT application has access to the whole detector information and could, in principle, perform the full offline reconstruction. However, given the EFF resources, the time per event available is around fifty times smaller than in the offline processing and some simplification are adopted. The HLT is divided into two steps, namely HLT1 and HLT2. Since it is a software trigger, the HLT is very flexible and can easily be adjusted to follow the experimental needs and the development of the reconstruction and selection software. Its selection principle relies on high p_T tracks, but also on topological properties – b and c-hadrons produce displaced vertices – and PID information.

The HLT1 performs a partial event reconstruction on the L0 candidates, by adding some information coming from the tracking system. The tracks in the VELO are reconstructed, and PVs are formed with at least 5 intersecting tracks. A vertex is considered as a PV if it lies within a radius of 300 µm of the mean position of the pp interaction. Then the VELO tracks are passed to the forward tracking algorithm, performed in a simplified way. Only a subset of the VELO tracks are selected. They must have either a significant Impact Parameter (IP) with respect to all PVs, or be associated to a muon track. Several inclusive and exclusive lines are developed with their appropriate selection requirements. For instance, the inclusive beauty and charm trigger asks for a track of good quality with a minimal transverse momentum (with a typical value of $p_T > 1.6 - 1.7\,\text{GeV}$) and displacement from the primary vertex (with a typical value of $IP > 0.1\,\text{mm}$). At the end, the HLT1 output rate is about 80 kHz, low enough to apply the full pattern recognition in HLT2.

The HLT2 performs a complete event reconstruction, close to the offline algorithm. Because of CPU constraints, only long tracks with $p > 3\,\text{GeV}$ and $p_\text{T} > 0.3\,\text{GeV}$ are considered. HLT2 includes both a mixture of exclusive lines, such as a prompt c-hadron decays line, a $B \to hh$ decay line (with h standing either for a pion or a kaon), and inclusive lines, such as a dimuon trigger, a $\phi \to KK$ line and a topological trigger. The topological trigger is the one used in the analysis presented in Chap. 5. It is designed to trigger on partially reconstructed b-hadron decays, with at least two charged particles in the final state and a displaced decay vertex. The considered tracks are preselected on track fit χ^2/ndf, IP, and electronic and muonic ID criteria. From these tracks, two-, three- and four-body vertices are made, with a requirement on the distance to closest approach of the tracks (DOCA). Then the n-body candidates are selected with a dedicated Boosted Decision Tree (BDT) [101] based on the following discriminating variables: $\sum |p_\text{T}|$, ${p_\text{T}}^\text{min}$, n-body invariant mass, DOCA, IP significance, flight distance (FD) significance and the corrected mass m_corr. The corrected mass is defined as $m_\text{corr} \equiv \sqrt{m^2 + |p_{\text{T}_\text{miss}}'|^2} + |p_{\text{T}_\text{miss}}'|$, where $|p_{\text{T}_\text{miss}}'|$ is the missing momentum transverse to the line of flight between the n-body vertex and the PV to which it has the smallest IP.

The deferred trigger

The LHC delivers stable beams – beams producing collisions used for the physics analyses – only 30% of its operating time, on average. This would imply that about 70% of the time the EFF would be idle. To optimise the CPU usage, a system of deferred trigger has been set up for data taking in 2012 [102]. Its architecture is illustrated in Fig. 3.19b. Around 20% of the events at the output of the L0 is buffered on disks. The events temporarily stored are processed by the HLT during the inter-fill period (*e.g.* when the fill is prepared or when some machine development is done). This results in an effective increase of the available CPU time to filter the events. Hence, the p_T threshold on the tracks can be relaxed and the Downstream tracks (see Sec. 3.2.1) have been also included in the HLT. Another advantage of this deferring is the reduction of dead-time in the farm. If a problem occurs downstream the L0, for instance preventing the HLT from running correctly, the fraction of deferred events increases until the problem is fixed.

For Run II, the trigger scheme has evolved to allow a run-time calibration and alignment on the HLT1 output, which is buffered. This enables a better online event reconstruction, and therefore a better quality of the trigger decisions.

TIS and TOS categories

Depending on the source of a positive trigger decision, an event is classified with two categories TOS and TIS:

TOS means Trigger On Signal event, in this case the trigger objects associated to the considered signal candidate are sufficient to trigger the event,

TIS means Trigger Independent of Signal event, in this case the trigger objects which have triggered the event are not associated to the considered signal.

The two categories are not mutually exclusive, some events can be classified as TIS and TOS (TIS & TOS). Thanks to these TIS & TOS events, the trigger efficiency relative to the offline reconstructed events can be evaluate from data alone [103]. The efficiency to trigger an event independently of the signal is determined with

$$\varepsilon^\text{TIS} = N^\text{TIS\&TOS} / N^\text{TOS}, \tag{3.7}$$

where N^{TOS} ($N^{\text{TIS\&TOS}}$) is the number of events classified as TOS (TIS & TOS). In the same way, the efficiency to trigger an event on the signal alone is determined with

$$\varepsilon^{\text{TOS}} = N^{\text{TIS\&TOS}} / N^{\text{TIS}}. \tag{3.8}$$

3.2.7 The LHCb software: data processing, event filtering and simulation

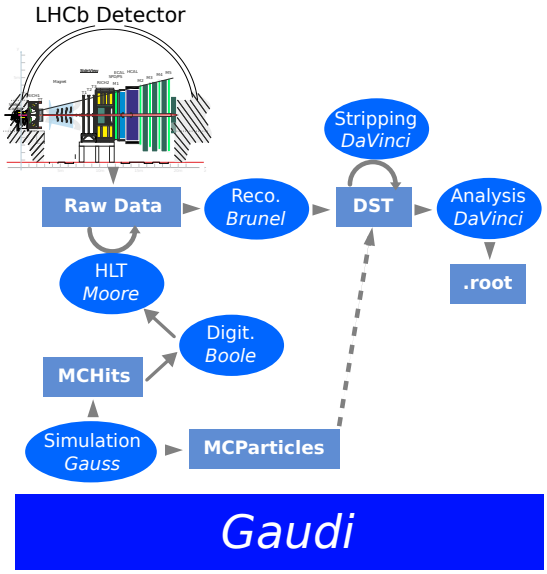

Figure 3.20 – Software framework of the data processing in LHCb.

The LHCb software is based on the C++ `Gaudi` framework [104]. All the applications handling the data processing in LHCb use this framework. Figure 3.20 illustrates this architecture. The raw data produced by the detector are first processed with the `Moore` application, which runs the HLT algorithm. The full offline reconstruction is performed by the Brunel application, which stores the events in "data summary tape" (dst) files format. Running every single analysis on the whole data set at the output of the offline reconstruction would take an unthinkable processing time. As a consequence, a loose pre-selection of the events is set up to distribute the data into several streams adapted to a particular topology, such as hadronic B decays, semileptonic B decays or charm decays. Each stream includes several lines dedicated to the selection of specific decay channel. This event filtering is called *Stripping* and is implemented in the `DaVinci` application. The physics analysis are performed on *stripped* data. `DaVinci` is used to gather the events passing a given stripping line and collect their measured physical properties into a `ROOT` tree [105].

The Monte-Carlo (MC) simulation of the signals measured with the LHCb detector are generated with the `Gauss` application [106]. It relies on the `Pythia` generator [107, 108] to simulate pp collisions, the `EvtGen` package [109] to simulate the B meson decays and the `GEANT4` package [110, 111] to simulate the passage of the particles through the detector material. This passage produces simulated hits (MCHits) in the different sub-detectors. These hits are digitised with the `Boole` application. The output of this digitisation is similar to the raw data produced by the detector.

3.3 The LHCb detector upgrade

After the LHC Long Shutdown 2 (LS2), at the time of writing planned for the end of 2018, a major upgrade of the LHCb Detector will take place. During Run II, LHCb is expected to take around $5\,\text{fb}^{-1}$ of data. After the first two runs, it is not feasible to operate long enough with the current detector to double the collected statistics, which is required to produce results with a more significant scientific impact. That is why the goal of the upgraded experiment is to take a total sample of $50\,\text{fb}^{-1}$ with an improved detector. The general upgrade scheme is detailed in Ref. [112] and Ref. [113].

The luminosity will be increased from 4×10^{32} to a maximum of $2\times10^{33}\,\text{cm}^{-2}\,\text{s}^{-1}$, with an average number of (visible) interactions per bunch crossing $\nu = 7.6$ ($\mu_{\text{vis}} = 5.2$). To benefit from such an increase of data rate, the trigger efficiency must be significantly improved. In particular, E_{T} thresholds used to trigger on the hadronic decays constitute a bottleneck. If the current trigger scheme were kept, the thresholds would have to be raised to keep a 1 MHz L0 output rate. This would lead to a unacceptable loss of signal efficiency. As illustrated in Fig. 3.21, the trigger yields of hadronic B decays saturate with an increase of the luminosity. The saturation is not present for the muon channels, because the thresholds can be tuned to milder values.

To solve this issue, the detector readout will be performed at the 40 MHz rate, instead of 1 MHz. Thus a fully software-based trigger can be installed. Using a full software trigger provides flexibility and the ability to use more information than simply E_{T} to discriminate signals against backgrounds. The resulting gain in trigger efficiency will lead to an increase of the signal yields by a factor 10 in muonic channels and 20 in hadronic channels. In addition, it will be possible to trigger on long-lived particles. To follow this strategy, the front-end electronics of the sub-systems will be replaced to allow the 40 MHz readout. The sub-detectors have also to be adapted to operate at a higher luminosity and to record $50\,\text{fb}^{-1}$ of data.

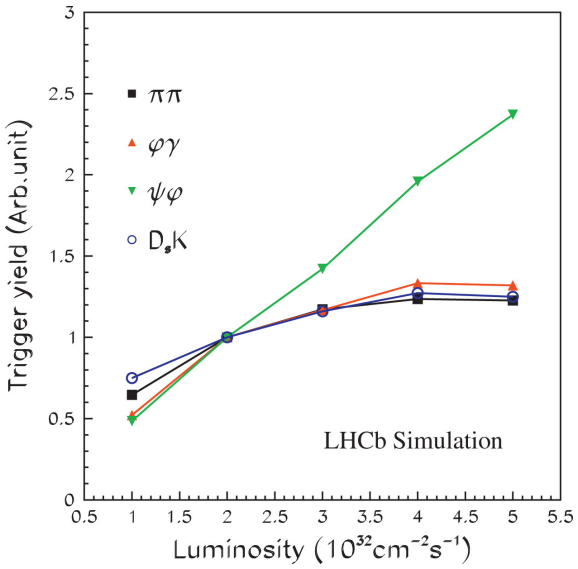

Figure 3.21 – L0 trigger yields for $B^0 \to \pi^+\pi^-$, $B_s^0 \to \phi\gamma$, $B_s^0 \to J/\psi\,\phi$ and $B_s^0 \to D_s^{\mp}K^{\pm}$ decays, normalised to the yields at the design luminosity of $2\times10^{32}\,\text{cm}^{-2}\,\text{s}^{-1}$. Taken from [114].

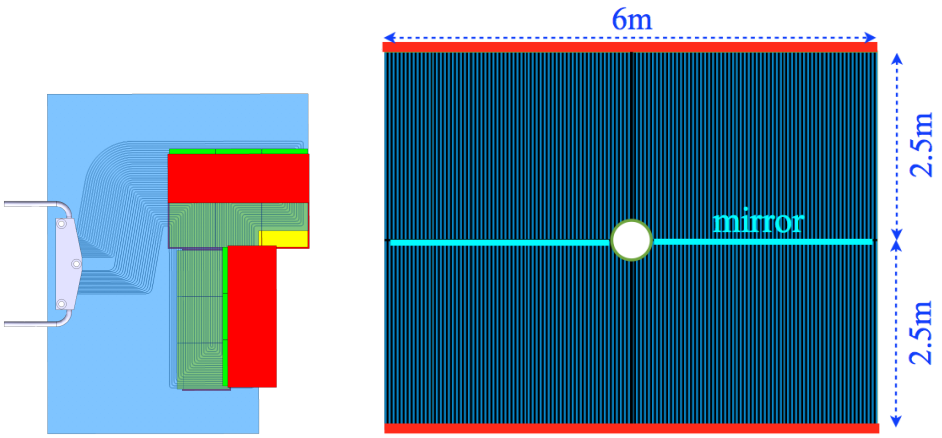

(a) (b)

Figure 3.22 – Front view of a module of the upgraded VELO (a) and layout of the scintillating fibre tracker (b). The red lines represent the SiPMs position.

The tracking system will be completely changed. Thanks to the new design of the VELO [115], the speed and the precision of the track reconstruction will be improved, even with a higher detector occupancy. The silicon strip R–Φ geometry of the VELO will be replaced by a square pixel geometry, as illustrated Fig. 3.22a. The sensors will be also closer to the beam axis, with a distance of 5.1 mm. In total, there will be 41 million of 55 µm × 55 µm pixels. The current TT cannot survive the radiation damage foreseen after LS2, and its strip geometry is not suited to the high occupancy. It will be replaced by the Upstream Tracker (UT), similar to the TT in its design, but with thinner silicon sensors, finer segmentation and larger coverage [113]. The T1–T3 stations are also not adapted to the expected occupancy, especially the OT. They will be changed for the Scintillating Fibre tracker (SciFi) [113], composed of 2.5 m long fibres with a diameter of 250 µm, read out by silicon photomultipliers (SiPMs). This layout is illustrated in Fig. 3.22b.

The RICH will keep its overall structure largely unchanged [116]. The aerogel in RICH1 will be removed, since it performs not efficiently at high luminosity [112]. The HPDs enclose the current 1 MHz read-out electronics. They will be replaced by multianode photomultipliers (MaPMTs). The optics of RICH1 will also be re-optimised.

The calorimeters will not be radically changed [116]. The PS and SPD will be removed since they are mainly used for the L0 trigger. This will simplify the calibration of the ECAL. Moreover, the PMT gains will be lowered in order to ensure a longer lifetime at a high luminosity operation. Chapter 4 presents a study made to optimise the photon reconstruction with the ECAL, after the upgrade.

The muon chambers will suffer much less from the luminosity increase, since they are shielded by the other subdetectors. The particle rates will be tolerable, therefore the stations will be unchanged, except M1 which will be removed [116]. To reduce the particle rate in the innermost region of M2, additional shielding will be installed around the beam pipe, behind HCAL.

The expected sensitivity on key measurements, at the end of the Upgrade era, are summarised in Table 3.2, reproduced from [117] (with an update on the γ current precision).

Table 3.2 – Statistical sensitivities of the LHCb upgrade to key observables. Reproduced from [117], with an update on the γ current precision. For each observable the current sensitivity is compared to that which will be achieved by LHCb before the upgrade, and that which will be achieved with 50 fb^{-1} by the upgraded experiment. Systematic uncertainties are expected to be non-negligible for the most precisely measured quantities (such as $a^s_{\rm sl}$, A_Γ and $\Delta\mathscr{A}^{CP}$).

Type	Observable	Current precision	LHCb 2018	**Upgrade** (50 fb^{-1})	Theory uncertainty
B^0_s mixing	$2\beta_s\ (B^0_s \to J/\psi\,\phi)$	0.10 [118]	0.025	0.008	~ 0.003
	$2\beta_s\ (B^0_s \to J/\psi\,f_0(980))$	0.17 [119]	0.045	0.014	~ 0.01
	$a^s_{\rm sl}$	6.4×10^{-3} [47]	0.6×10^{-3}	0.2×10^{-3}	0.03×10^{-3}
Gluonic penguins	$2\beta^{\rm eff}_s(B^0_s \to \phi\phi)$	–	0.17	0.03	0.02
	$2\beta^{\rm eff}_s(B^0_s \to K^{*0}\bar{K}^{*0})$	–	0.13	0.02	< 0.02
	$2\beta^{\rm eff}(B^0 \to \phi K^0_S)$	0.17 [47]	0.30	0.05	0.02
Right-handed currents	$2\beta^{\rm eff}_s(B^0_s \to \phi\gamma)$	–	0.09	0.02	< 0.01
	$\tau^{\rm eff}(B^0_s \to \phi\gamma)/\tau_{B^0_s}$	–	5%	1%	0.2%
Electroweak penguins	$S_3(B^0 \to K^{*0}\mu^+\mu^-; 1 < q^2 < 6\,{\rm GeV}^2/c^4)$	0.08 [120]	0.025	0.008	0.02
	$s_0\,A_{\rm FB}(B^0 \to K^{*0}\mu^+\mu^-)$	25% [120]	6%	2%	7%
	$A_{\rm I}(K\mu^+\mu^-; 1 < q^2 < 6\,{\rm GeV}^2/c^4)$	0.25 [121]	0.08	0.025	~ 0.02
	$\mathscr{B}(B^+ \to \pi^+\mu^+\mu^-)/\mathscr{B}(B^+ \to K^+\mu^+\mu^-)$	25% [122]	8%	2.5%	$\sim 10\%$
Higgs penguins	$\mathscr{B}(B^0_s \to \mu^+\mu^-)$	1.5×10^{-9} [123]	0.5×10^{-9}	0.15×10^{-9}	0.3×10^{-9}
	$\mathscr{B}(B^0 \to \mu^+\mu^-)/\mathscr{B}(B^0_s \to \mu^+\mu^-)$	–	$\sim 100\%$	$\sim 35\%$	$\sim 5\%$
Unitarity triangle angles	$\gamma\ (B \to D^{(*)}K^{(*)})$	~ 7–7.5° [11, 12]	4°	0.9°	negligible
	$\gamma\ (B^0_s \to D_s K)$	~ 30–40° [55]	11°	2.0°	negligible
	$\beta\ (B^0 \to J/\psi\,K^0_S)$	0.8° [47]	0.6°	0.2°	negligible
Charm *CP* violation	A_Γ	2.3×10^{-3} [47]	0.40×10^{-3}	0.07×10^{-3}	–
	$\Delta\mathscr{A}^{CP}$	2.1×10^{-3} [124]	0.65×10^{-3}	0.12×10^{-3}	–

Chapter 4

Photon reconstruction optimisation with the upgraded LHCb detector

Contents

Neutral objects like photons or neutral pions do not leave hits in the tracking system. Therefore they can only be measured with the electromagnetic calorimeter (ECAL). Reconstructing neutrals is not an easy task in an hadronic environment with high multiplicity. However the performance of the LHCb electromagnetic calorimeter makes possible the study of radiative decays such as $B^0 \to K^{*0}\gamma$ [98], or decays with π^0 mesons in the final state such as $B^\pm \to D(K^\mp\pi^\pm\pi^0)K^\pm$ [125]. After the Long Shutdown 2 (LS2) of the LHC, the delivered luminosity will be increased by one order of magnitude above the LHCb design value (see Sec. 3.3). Thus, the occupancy of the detector will significantly grow. This chapter presents a work performed in order to optimise the photon reconstruction under LHCb upgrade conditions. The first section summarised the current photon measurement method. Then the study for the upgrade is developed in the second section.

4.1 Photon measurement with the LHCb Detector

Photon energy and momentum are measured by detecting the development of electromagnetic cascades in the ECAL absorber material (for a presentation of the ECAL layout, see Sec. 3.2.3). The energy is directly measured from the energy deposit in the ECAL cells. The 3-vector momentum is deduced from the particle impact on the calorimeter surface, itself obtained from the

measurement of the position of the cascade. This section summarised the characteristics of an electromagnetic shower and its current reconstruction in LHCb.

4.1.1 Electromagnetic Shower

When a high-energy electron or photon, with an energy of at least few MeV, crosses the lead tiles, an electromagnetic shower is produced. An incoming electron radiates a bremsstrahlung photon and an incoming photon makes an electron-positron pair. These created photons and electrons produce additional photons and electrons with lower energy, making a cascade. This mechanism is illustrated in Fig. 4.1. The cascade stops when the electron energies fall below the critical energy. In this case they dissipate their energy not any more by bremsstrahlung, but by ionisation or excitation. Eventually, all the energy of the incoming photon or electron is absorbed in the ECAL material.

The longitudinal development of an electromagnetic cascade can be well described with [20, 126]

$$\frac{\mathrm{d}E}{\mathrm{d}t} = E_0 b \frac{(bt)^{a-1} e^{-bt}}{\Gamma(a)}, \tag{4.1}$$

where E_0 is the energy of the incoming particle, and a and b are parameters depending on the absorber material. The longitudinal distance z is described in units of radiation length with the scale variable

$$t \equiv z / X_0. \tag{4.2}$$

The maximal development of a shower is at $t_{\max} = (a-1)/b$, and can be expressed as [20]

$$t_{\max} = \ln \frac{E_0}{E_\mathrm{c}} + C, \tag{4.3}$$

where $C_e = -0.5$ for electron-induced showers and $C_\gamma = +0.5$ for photon-induced showers. E_c is the critical energy, the energy at which the electron looses energy by ionisation and bremsstrahlung at the same rates. Another definition of the critical energy, formulated by Rossi [127], is the energy at which the ionisation loss per radiation length is equal to the electron energy.

The transverse development of an electromagnetic shower is characterised by the *Molière radius* R_M, defined as [128, 129]

$$R_\mathrm{M} \equiv X_0 \frac{E_\mathrm{s}}{E_\mathrm{c}}, \tag{4.4}$$

where the Rossi critical energy is used and E_s is the scale energy defined as

$$E_\mathrm{s} \equiv \sqrt{4\pi/\alpha}\, m_e c^2 \approx 21\,\mathrm{MeV}. \tag{4.5}$$

The Molière radius determines a cylinder in which 90% of the energy shower lies. The Molière radius of the LHCb ECAL is 3.5 cm. The energy transverse distribution is described with different shapes in the literature, either with a sum of two exponentials [130, 131], or a sum of two Gaussians [132], or a sum of two Bessel functions [133]. Alternatively, Grindhammer uses a sum of two functions of the form [134, 135]

$$f(r) \equiv \frac{2rR^2}{(r^2+R^2)^2}, \tag{4.6}$$

with the average radial profile R depending on the energy and the shower depth t. For each description, the use of the sum of two functions describes better the measured shower profile, with a core and a tail shape.

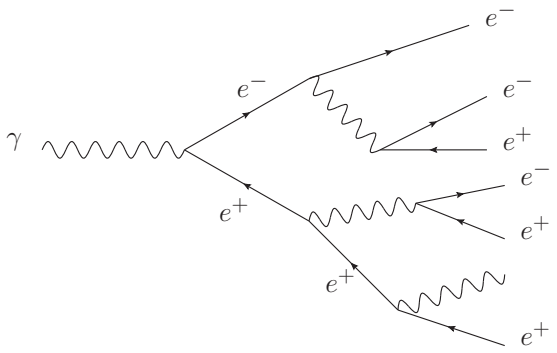

Figure 4.1 – Illustration of the creation an electromagnetic cascade.

4.1.2 Energy measurement in a calorimetric cell

As described in Sec.3.2.3, the calorimeter cells collect the scintillation light produced by the charged particles making the cascade and transmit it to their corresponding photomultiplier tube (PMT). The analog signals at the PMTs output is processed by a dedicated electronics and converted in numerical signals with analog-to-digital converters (ADC). The number of recorded ADC counts is proportional to the amount of scintillation light collected. This amount of light may vary between two different cells even with incident particles of same energy. This variation has multiple origins. For instance, the calorimeter is slightly non homogeneous, the fibres are not exactly identical and they even do not age at the same speed, depending on their location in the ECAL. Therefore, the calorimeter needs to be finely calibrated in order to provide a precise measurement of neutral particles. The calibration of the ECAL is made in three steps. First, an initial calibration has been made at the beginning of LHCb commissioning by using the test-beam measurements. This calibration resulted in a 10% resolution on the π^0 mass, for the first collisions in 2009 [74]. During the Run I operations, the calibration was monitored with a LED system. As can be seen in Fig. 3.17a, a fibre at the centre of each cell is linked to a LED. With this system a monitored amount of light can be sent to the PMTs, and their response stability is measured. It provides a calibration with a 8–10% accuracy. The second step of the calibration is based on the measurement of the energy flow over the ECAL surface [136]. After a large number of collisions, the accumulated energy deposit should be continuous across cell boundaries. This constraint enables the calibration parameters to be refined and an inter-cell energy scale to be established. Finally, the absolute energy scale (and an improved inter-calibration) is determined with fits to the neutral pion mass distribution in the decay $\pi^0 \to \gamma\gamma$ [137]. The calibration constant of a given cell is refined by combining a photon hitting the cell with another photon over a large statistics. The resulting π^0 mass distribution is fitted and the calibration constant adjusted to obtain the correct π^0 mass. The process is repeated as many times as needed to get stable parameters. At the end, the cell-to-cell intercalibration is estimated to be approximately 2% [74].

4.1.3 Energy and position measurement of a calorimetric cluster

Once the energy is correctly measured in the calorimeter cells, they can be grouped in clusters to reconstruct neutral particles. The recontruction of neutral particles in LHCb is detailed in Ref. [138]. The following sections summarise the main points.

To realise the clusterisation, local energy deposition maxima are first searched for. They are required to have a transverse energy larger than 50 MeV. A cell corresponding to one local maximum is called a *seed*. Then a 3×3 cell pattern is applied around every seeds to build all the clusters. Consequently, the seeds are always separated by at least one cell. If one cell is shared by several clusters, the energy of the cell is shared between these clusters proportionally to the total clusters energies. This sharing algorithm is iterative and quickly converges since the Molière radius of the ECAL (3.5 cm) is smaller than the cell sizes (4.04 cm, 6.06 cm and 12.12 cm in the inner, middle and outer regions respectively, see Sec.3.2.3). To each cluster can be associated an energy E_{cl} and a position x_{b}, y_{b} defined as

$$E_{\text{cl}} \equiv \sum_{i=0}^{8} E_i, \qquad x_{\text{b}} \equiv \frac{1}{E_{\text{cl}}} \sum_{i=0}^{8} x_i E_i, \qquad y_{\text{b}} \equiv \frac{1}{E_{\text{cl}}} \sum_{i=0}^{8} y_i E_i, \tag{4.7}$$

where E_i, x_i and y_i are the energy, the x- and y-positions of the nine cells corresponding to the 3×3 cluster, respectively. The index b on x_{b} and y_{b} denotes the *barycentre* position. This cell energy barycentre provides a biased position measurement [130], which must be corrected for by the so-called *S-shape* correction (see Sec. 4.1.4). The cluster energy spread is also encoded in a 2×2 symmetric matrix with the elements

$$\begin{aligned} S_{xx} &\equiv \frac{1}{E'_{\text{cl}}} \sum_{E_i>0} x_i^2 E_i - {x'_{\text{b}}}^2, \\ S_{xy} &\equiv \frac{1}{E'_{\text{cl}}} \sum_{E_i>0} x_i y_i E_i - x'_{\text{b}} y'_{\text{b}}, \\ S_{yy} &\equiv \frac{1}{E'_{\text{cl}}} \sum_{E_i>0} y_i^2 E_i - {y'_{\text{b}}}^2, \end{aligned} \tag{4.8}$$

where the primed quantities E'_{cl}, x'_{b} and y'_{b} are evaluated with only positive cell energies (a cell energy can be measured to be negative because of the electronic pedestal suppression).

Photon candidates are reconstructed from *neutral* clusters. A cluster is considered as neutral if it cannot be associated to a charged track. This decision is obtained by extrapolating all the charged tracks – provided by the tracking system – to the calorimeter. Then the extrapolated tracks are combined with the reconstructed cluster to build the χ^2_{2D} estimator:

$$\chi^2_{\text{2D}} \equiv (\vec{r}_{\text{tr}} - \vec{r}_{\text{cl}})^T (C_{\text{tr}} + S_{\text{cl}})^{-1} (\vec{r}_{\text{tr}} - \vec{r}_{\text{cl}}), \tag{4.9}$$

where $\vec{r}_{\text{tr}}$ is the 2D position of the track extrapolated at the z_{cl} cluster longitudinal position, $\vec{r}_{\text{cl}} = (x_{\text{b}}, y_{\text{b}})$ is the barycentre position, C_{tr} is the covariance matrix of $\vec{r}_{\text{tr}}$ and S_{cl} the cluster energy spread matrix defined in Eq. 4.8.

The longitudinal cluster position is set at the z-position of the maximal shower development. It is evaluated from the ECAL front-face z-position z_{ecal}, with a logarithmic energy dependence (see Eq. 4.3),

$$z_{\text{cl}} = z_{\text{ecal}} + a \ln E_{\text{cl}} + b(E_{\text{PRS}}). \tag{4.10}$$

The b parameter takes into account the information provided by the energy deposit in the preshower E_{PRS}.

A cluster is considered as originating from a photon if it has a minimum value of χ^2_{2D} larger than 4, with respect to any extrapolated track.

4.1.4 Making a photon from a cluster

The reconstructed photon candidates are made from the neutral clusters described in the previous section. The energy and direction of the photons are obtained from the clusters energies and positions, after applying dedicated corrections.

The photon energy is measured from the cluster energy E_{cl} with a correction taking into account the leakage induced by the finite size of a 3×3 cluster. This correction is expressed as

$$E_\gamma = \alpha\left(\vec{r}_{\text{b|cluster}}, \vec{r}_{\text{b|module}}\right) E_{\text{cl}} + \beta\, E_{\text{PRS}} + \delta, \tag{4.11}$$

where the α and β parameters correct the energy leakage in the ECAL and PRS respectively, and δ corresponds to a global offset. All these parameters depend on the ECAL region. And α depends also on the photon barycentre position inside the cluster $\vec{r}_{\text{b|cluster}}$, and inside the module $\vec{r}_{\text{b|module}}$ (to take into account the dead material between the modules). The values of these corrections have been determined from simulation. Moreover, the case of converted photons – photons converting into an electron-positron pair before reaching the calorimeter – is treated separately.

The photon momentum is deduced directly from its direction. The photon is first assumed to come from the interaction point origin (some corrections are applied offline to take into account the vertex position reconstruction). Therefore, as a first approximation, the photon direction corresponds to the barycentre $\vec{r}_{\text{b}} = (x_{\text{b}}, y_{\text{b}}, z_{\text{cl}})$, where z_{cl} is the cluster z-position defined in Eq. (4.10). In this chapter, the lower case letters (x, y, z) correspond to position in the standard LHCb frame, whereas capital letters (X, Y, Z) correspond to position inside a cell, with the origin placed at the cell centre (Fig. 4.2).

As explained in Ref. [130], the energy barycentre is a biased estimator of the position. Because of the non linearity of the transverse profile of the shower, the energy barycentre along the (X, Y) direction tends to be closer to the centre of the cell than the true photon impact. This bias is highlighted in Sec. 4.2.2. The transverse profile of the shower can be assumed to approximately follow a single exponential distribution $E(X) \sim E_0\, e^{-|X - X_\gamma|/b}$ (see Sec. 4.1.1), with X_γ the true

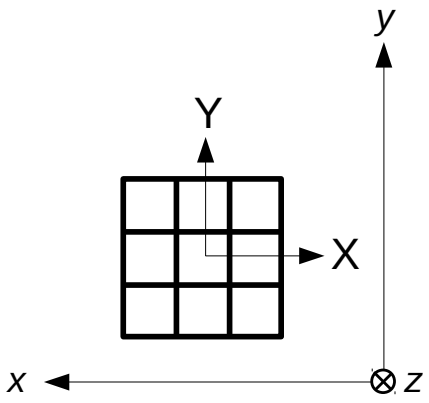

Figure 4.2 – Coordinates convention used in this chapter. Capital letters refer to local positions relative to the centre of a given cell. Lower case letters refer to absolute positions with the standard LHCb system.

photon position and b the decay constant of the exponential profile. Under this assumption, the relation between the barycentre position X_b and the true position can be expressed as [130]

$$X_\gamma = S(X_\mathrm{b}, b) \equiv b \,\mathrm{asinh}\left(\frac{X_b}{\Delta}\sinh\frac{\Delta}{b}\right), \tag{4.12}$$

where Δ is the cell half size. This non linear relation is a correction applied to the barycentre in order to recover an unbiased position measurement. It is the so-called *S-shape* correction. The larger the cell size compared to the Molière radius, the larger the correction. In LHCb, the S-shape correction is slightly modified with [138]

$$S_0(X_\mathrm{b}, b) \equiv b \,\mathrm{asinh}\left(\frac{X_b}{\Delta}\cosh\frac{\Delta}{b}\right). \tag{4.13}$$

The parameter b is adjusted from simulation, and found to be around 14%, 17% and 18% of the cell size in the outer, middle and inner region respectively. And since the transverse shower profile is not perfectly described with a simple exponential, an additional correction is applied. The residuals remaining after the S-shape correction are corrected with a 4^{th}-order polynomial.

4.1.5 Photon identification

Two different estimators have been developed to check the compatibility between the reconstructed electromagnetic cluster and the photon hypothesis. One is mainly built to separate photons from electrons or charged hadrons. The other is made for distinguishing photons from high E_T merged π^0 mesons. Indeed, energetic neutral pions decay into two photons that are almost collinear in the laboratory frame and eventually produce a single cluster in the ECAL.

The first photon identification estimator treats separately the converted photons (with hits in the matching SPD cluster) and the non-converted ones (without hits in the matching SPD cluster). A photon hypothesis likelihood is based on three variables: the track matching χ^2_{2D}, the energy deposit in the preshower cluster facing the ECAL cluster and the ratio between the energy of the seed and the total energy of the cluster. The dependence on the photon energy and its location in the three ECAL regions are taken into account. The resulting estimator consists of a delta-log likelihood between the photon and background hypothesis.

The estimator which aims to reject mis-identification of merged π^0 with photons is based on the difference in cluster shape expected. A Neural Network is trained to look for this difference.

4.2 Photon reconstruction with the upgraded LHCb detector

Starting from LHC Run III, the luminosity for LHCb operation will increase from $4\times10^{32}\,\mathrm{cm^{-2}\,s^{-1}}$ (end of Run I instantaneous luminosity) to $2\times10^{33}\,\mathrm{cm^{-2}\,s^{-1}}$. This will result in a large increase in the particle multiplicity and the average number of interactions per bunch crossing will be $\nu = 7.6$. As for the number of *visible* interactions per bunch crossing, it will increase to $\mu_{\mathrm{vis}} = 5.2$ (instead of 1.7 during 2012 operations). As explained in Sec. 3.3, no major upgrade of the calorimeters is planned. The SPD and PRS will be removed, which will only simplify the calibration, and the electronics will be changed to allow a 40 MHz readout. As a result, the ECAL modules will have no hardware upgrade to cope with a higher occupancy. Nevertheless, the software may be optimised in order to avoid a degradation of the performances. The work presented in the following sections has been made to adapt the photon reconstruction to the upgrade luminosity conditions.

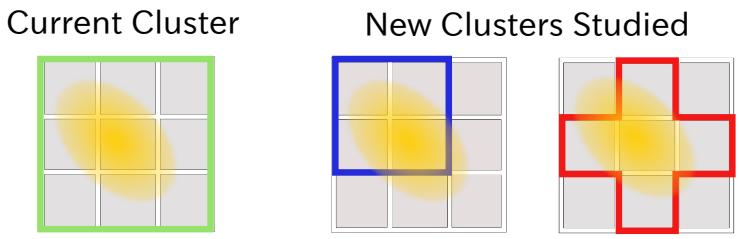

Figure 4.3 – Shapes of the three types of clusters considered: 3 × 3 (left), 2 × 2 (middle) and cross (right).

At higher luminosity, the showers produced in the ECAL will overlap more frequently. This will lead to a degradation of the energy and position measurements for the calorimetric objects, as other particles can contribute to the shower of the object to be measured. In the following, this overlap effect is called "pile-up". In order to reduce the resolution degradation due to the pile-up, the size of the clusters used to reconstruct the neutral particles may be reduced with respect to those formed at present. Two new shapes of smaller clusters have been studied, to investigate whether they do mitigate the effects of pile-up without degrading the overall resolution. These new shapes are 2 × 2 and cross clusters, illustrated in Fig. 4.3. For the 2 × 2 cluster, out of the nine cells of the 3 × 3 cluster, only the 2 × 2 zone leading to the largest energy is retained. For the cross cluster, out of the nine cells of the 3 × 3 cluster, the four corner cells are removed.

The study is based on three simulation samples of the decay $B_s^0 \to \phi\gamma$. This decay provides a wide spectrum of photon energy. These samples correspond to three instantaneous luminosity conditions, $\mathscr{L} = 10^{33}$, 2×10^{33} and $3 \times 10^{33}\,\mathrm{cm}^{-2}\,\mathrm{s}^{-1}$ and therefore to three pile-up conditions with $\nu = 3.8$, $\nu = 7.6$ and $\nu = 11.4$, respectively. The intermediate sample corresponds to the expected highest instantaneous luminosity for the upgrade period and the third sample provides extreme conditions in order to investigate the limits of the reconstruction. Throughout all this study the three simulated samples are merged to make one global $B_s^0 \to \phi\gamma$ sample.

4.2.1 Energy measurement with alternative cluster shapes

Using a smaller cluster to measure the photon energy reduces automatically any inopportune contribution of another particle inside the photon cluster. Intuitively, the pile-up effect should be reduced by a factor 4/9 and 5/9 for the 2 × 2 and cross shapes respectively, with respect to the standard 3 × 3. However with smaller clusters a larger fraction of the shower is not contained anymore. If the leakage is too significant, the gain with the pile-up effect reduction can be spoiled by a degradation of the overall energy resolution. That is why the energy resolution with standard and alternative clusters is analysed.

The energy resolution is defined as $(E_{\text{true}} - E_{\text{rec}})/E_{\text{true}}$, where E_{true} is the true photon energy, and E_{rec} is the reconstructed photon energy, for a given cluster. The resolution is computed for each cluster shape and for several photon categories. The categories are related to the three areas of the ECAL (inner, middle and outer zones) and the number of primary vertices (PV) in the event. The photons which are studied come from $B_s^0 \to \phi\gamma$ simulated samples, already mentioned. Only photon candidates with transverse momentum $p_{\text{T}} > 250$ MeV/c, originating from the interaction region ($\Delta r < 10$ mm and $\Delta z < 150$ mm) and successfully associated to a true simulated photon are considered in this study. Only non-converted photons are analysed.

As can be seen in Fig. 4.4 the photon energy resolution distributions obtained do not have a Gaussian shape. A tail is present on the left side of the distributions due to the reconstructed

energy being larger than the true energy. This tail is a consequence of pile-up effects and is larger for low energy photons, in the innermost region of the ECAL. The right part of the distribution (reconstructed energy lower than the true photon energy according to the simulation) does however possess a Gaussian profile.

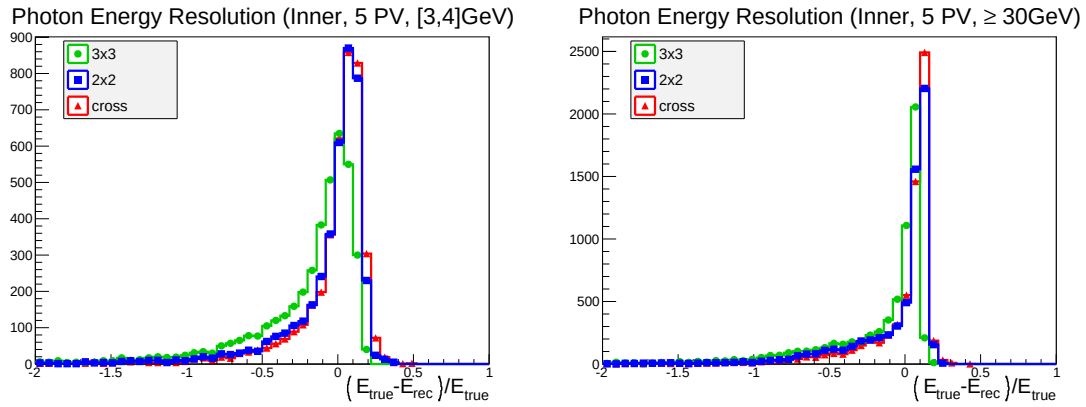

(a)

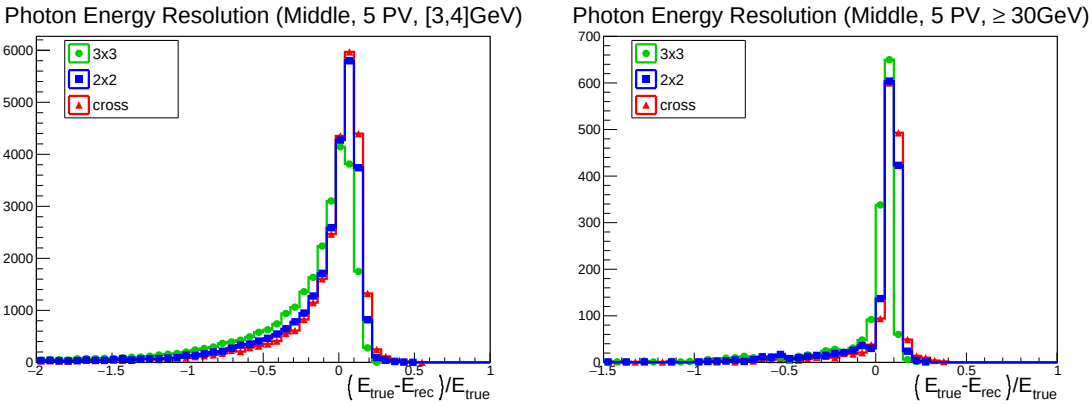

(b)

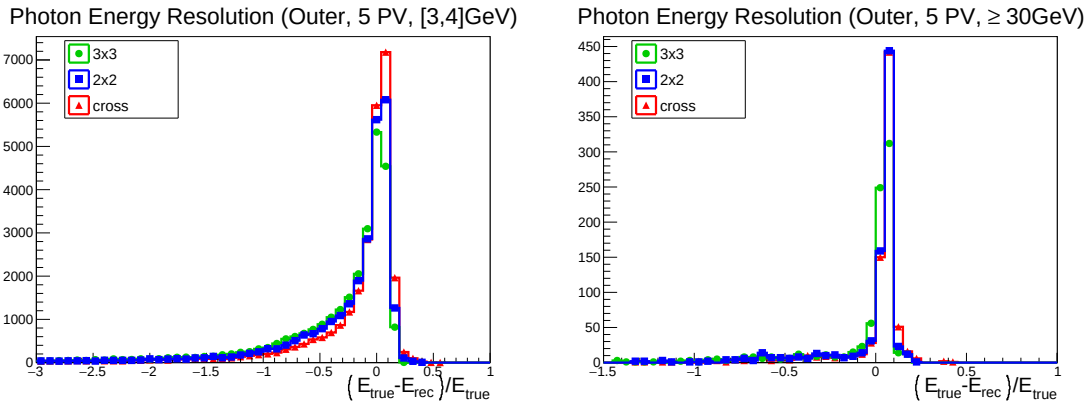

(c)

Figure 4.4 – Energy resolution in the ECAL inner (a), middle (b) and outer (c) regions, for events with 5 primary vertices, in two energy range [3,4] GeV (left) and ≥ 30 GeV (right) and for the 3×3 (green), 2×2 (blue) and cross (red) clusters. The pile-up effect is clearly visible, especially in the inner area at low energy.

To quantify the pile-up effect the energy resolution distributions are fitted with a Crystal Ball function [139],

$$f(x;\alpha,n,\mu,\sigma) \equiv N \cdot \begin{cases} e^{-\frac{(x-\mu)^2}{2\sigma^2}} & \text{for } \frac{x-\mu}{\sigma} > -\alpha, \\ A\left(B - \frac{x-\mu}{\sigma}\right)^{-n} & \text{otherwise.} \end{cases} \tag{4.14}$$

Out of the four parameters of this function, only α and n are related to the left tail and the pile-up effect. The parameters σ and μ are related at first order to the resolution observed on the right tail of the distribution and to the position of the maximum of the resolution distribution, respectively. A positive μ indicates an average energy loss in the reconstruction. The parameter α defines the start and the size of the tail: a smaller α is related to a larger tail. Hence, α is strongly related to the observed pile-up and a reconstruction that maximizes α reduces the pile-up. The parameter n tunes the amplitude of the tail but has less effect than α. Fig. 4.5 illustrates the Crystal Ball function tail behaviour for different values of α and n.

The energy resolution is measured for the three reconstructions and fitted using the model described above. For all the regions of the detector, energy ranges and number of PVs, the 2×2 and cross shape clusters give larger α values than the 3×3 type. Even if sometimes the n

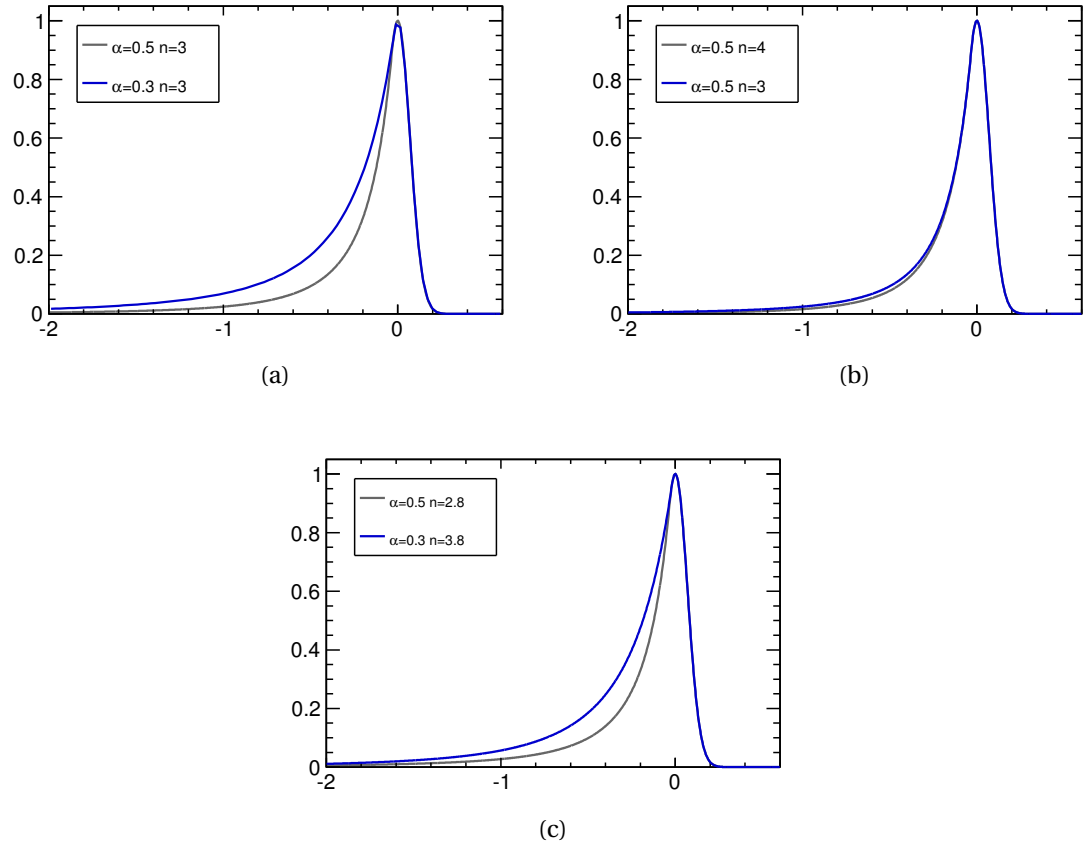

Figure 4.5 – Crystal Ball distribution for $\mu = 0$, $\sigma = 0.07$, and different values of α but same n (a), for same α but different n (b) and different α and n (c). The α parameter tunes the start and the size of the tail and n its amplitude. For different values of n, the tail size is mostly defined by α.

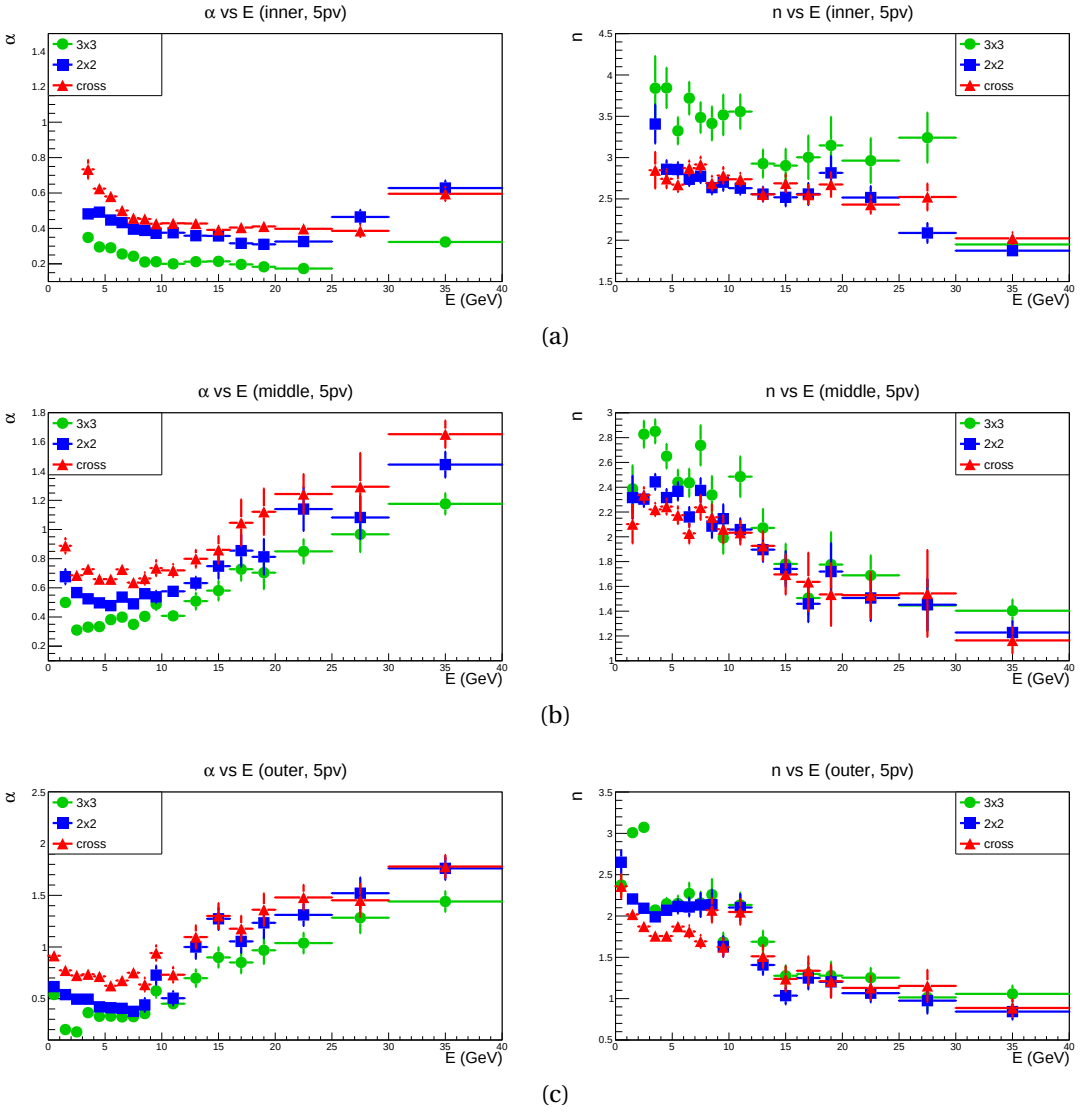

Figure 4.6 – Fitted values of α (left) and n (right) Crystal Ball parameters describing the photon energy resolution, as a function of the photon energy, for five primary vertices, in the ECAL inner (a), middle (b) and outer (c) regions, and for the 3×3 (green), 2×2 (blue) and cross (red) clusters. The α parameter is always significantly higher for reduced clusters than for 3×3 clusters, with n parameters not excessively different, highlighting smaller pile-up tails for 2×2 and cross clusters.

parameter is larger for 3×3 clusters, for instance in the inner region, the tail due to the pile-up effect is smaller with 2×2 and cross clusters. Indeed, the parameter α is always larger for the reduced clusters and n has a limited influence on the tail (see Fig. 4.5c). Moreover, cross clusters seem to give slightly better results than the 2×2 type. The results on α and n for five primary vertices (the average value expected after the upgrade) are shown in Fig. 4.6. The fit results are confirmed qualitatively by comparing the distributions of Fig. 4.4.

Therefore smaller clusters reduce the pile-up effect, but they potentially lead to a higher energy leakage and may degrade the resolution, especially in the inner region whose cells are approximately $4 \times 4\,\mathrm{cm}^2$ in size to be compared to the 3.5 cm Molière radius. The average leakage

can be estimated with the fitted μ parameter. The larger the energy leakage, the larger the μ parameter as can be seen from the uncorrected results drawn in Fig. 4.7. The uncorrected results correspond to the fit performed before the application of an energy leakage correction. Before this correction, the μ values are positive and logically larger for the reduced clusters than for the 3×3 clusters. Moreover the leakage is more important in the inner region than in the outer one (see Fig. 4.7). This energy bias can be corrected. A simple correction factor β is evaluated in order to recover the proper energy scale, such that

$$E_{\text{rec}}^{\text{corr}} = (1+\beta)E_{\text{rec}} \tag{4.15}$$

and

$$\left\langle \frac{E_{\text{true}} - E_{\text{rec}}^{\text{corr}}}{E_{\text{true}}} \right\rangle \sim 0. \tag{4.16}$$

Therefore the correction factor

$$\beta = \frac{\mu}{1-\mu} \tag{4.17}$$

is computed for each energy bin, in each ECAL region, but is averaged over the number of PVs. As can be seen in the left-hand side of Fig. 4.7, the energy bias is essentially eliminated by this correction. And after the correction, the tail parameters α and n are not changed. Therefore the higher energy leakage in the reduced clusters does not impact the conclusions on the performances with respect to the pile-up. The σ parameter fitted after the leakage correction is similar for 2×2 and 3×3 clusters, whereas there is a slight degradation for the cross cluster (right-hand side of Fig. 4.7). This can be easily understood: whenever a photon hits a seed cell not close to its centre, a 2×2 cluster will contain a larger fraction of the energy than a cross cluster.

In conclusion, energy reconstruction with 2×2 and cross clusters mitigates to a large degree the effect of the pile-up with respect to the current reconstruction, without spoiling the energy resolution (especially for the 2×2 type). This study shows that the photon energy measurement after the upgrade will benefit from adopting a reduced size cluster reconstruction. The 2×2 method is chosen in order to maintain the performances in term of resolution. The effect on the position reconstruction must also be analysed and is presented in the next section.

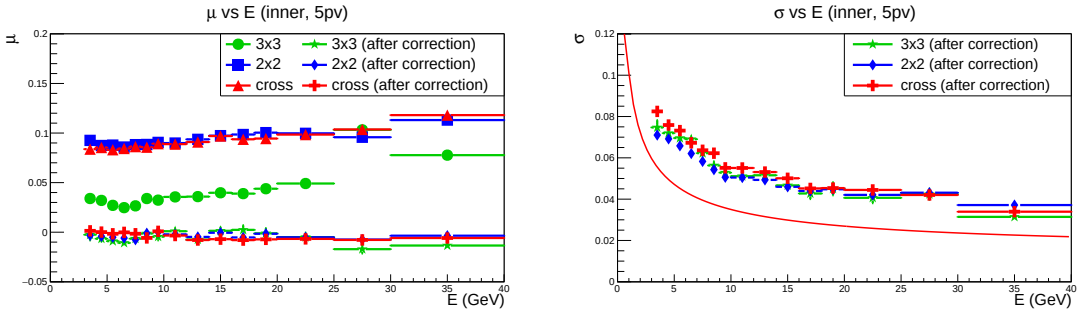

(a)

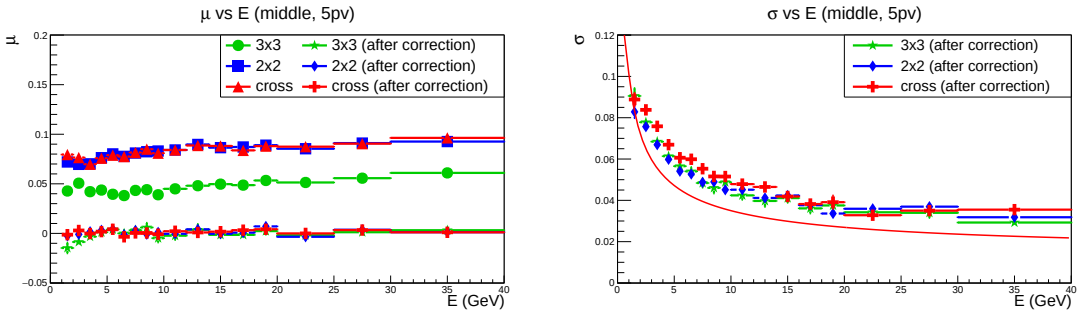

(b)

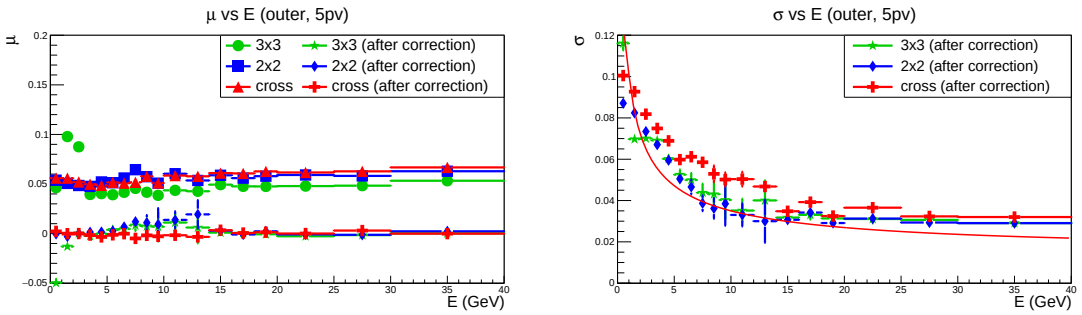

(c)

Figure 4.7 – Fitted values of μ (left) and σ (right) Crystal Ball parameters describing the photon energy resolution, as a function of the photon energy, for five primary vertices, in the ECAL inner (a), middle (b) and outer (c) region, and for the 3×3 (green), 2×2 (blue) and cross (red) clusters. The μ parameter is plotted before and after the energy leakage correction described in the text, whereas σ is shown only after the correction. With the energy leakage corrected ($\mu \sim 0$), the σ parameter of the 3×3 and 2×2 clusters are similar, whereas it is slightly degraded for the cross type. The red curve on the σ plot is an approximation of the calorimeter resolution, $\sigma(E) = \frac{10\%}{\sqrt{E}} \oplus 1.5\%$.

4.2.2 Position measurement with alternative cluster shapes

As explained in Sec. 4.1.4, the photon position is reconstructed from the energy barycentre of the cluster cells. The barycentre needs to be corrected because of the non linear transverse profile of the showers. This section presents the work performed to determine whether position reconstruction is possible with the 2×2 and cross clusters, and improves the performances at high luminosity with respect to the standard 3×3 clusterisation. First, a preliminary toy study has been performed to determine if the S-shape correction is also adapted to the reduced clusters. Then, using again the $B_s^0 \to \phi\gamma$ simulated samples, position corrections are determined and the resolutions obtained with the three cluster types are compared.

Toy simulation of the position reconstruction

In order to see the difference in the barycentre position reconstruction between the considered cluster shapes, a simple toy simulation is performed. The electromagnetic shower is supposed to follow a simple exponential distribution $E(r) = E_0 e^{-\frac{r}{b}}$, with the transverse extension parameter b set to 10%, 13% and 15% to emulate the outer, middle and inner region, respectively. Energy deposits are generated according to this distribution. In each cell the energy deposit is reconstructed, and the barycentre position deduced. For the 3×3 (2×2) cluster the barycentre is calculated with the 9 (4) cells. For the cross cluster the x (y) barycentre is made with the 3 horizontal (vertical) cells constituting the cross shape. Looking at the distributions of the true position as a function of the energy barycentre, illustrated in the left-hand side of Fig. 4.8, the expected S-shape is observed. With an exponential transverse profile, the barycentre is shifted toward the cell centre compared to the true position, especially as the cell size increases. The 3×3 and cross S-shapes are identical (the curves are superimposed). However, the 2×2 S-shape contains a discontinuity when the photon hits the centre of the cell ($X_{\text{true}} = 0$). Since with the 2×2 clusters the cells are not symmetrically located around the seed, the barycentre cannot be at the seed centre. If the photon hits the seed centre and no energy is deposited in the three other cells, the barycentre can point to the seed centre. However, as soon as there is some energy in the three cells surrounding the seed, the barycentre is shifted away from the seed centre, towards the other cells. This discontinuity is larger when the cell size is smaller. The S-shape correction is determined for this toy simulation. The 3×3 and cross corrections correspond to the S-shape expression $S(X_{\text{b}}, b)$ given by Eq. (4.12). The correction parameter b is determined by a fit to the S-shape. For the 2×2 cluster, in addition to $S(X_{\text{b}}, b)$ two terms are added, one logarithmic and one linear, to describe the discontinuity. The result of these corrections is illustrated in the right-hand side of Fig. 4.8. A linear dependence between the reconstructed and the true photon position is recovered. However, the correction for the 2×2 does not suppress completely the discontinuity.

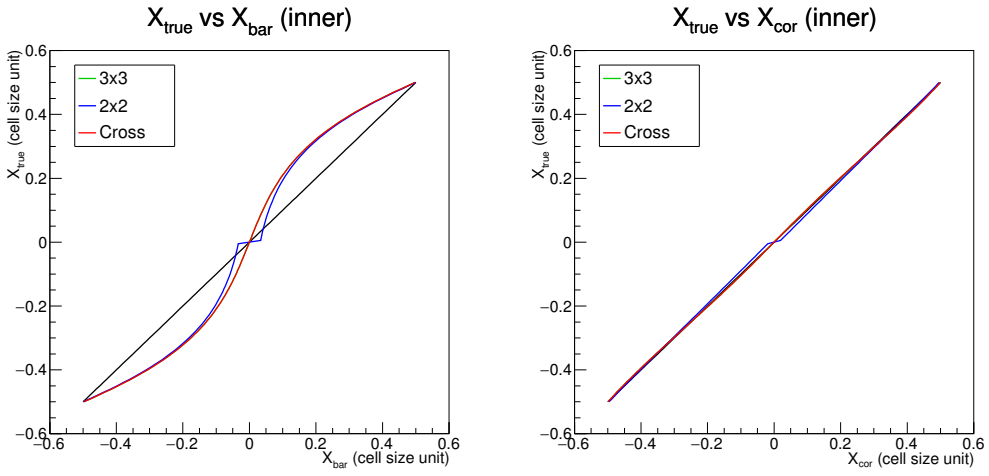

(a)

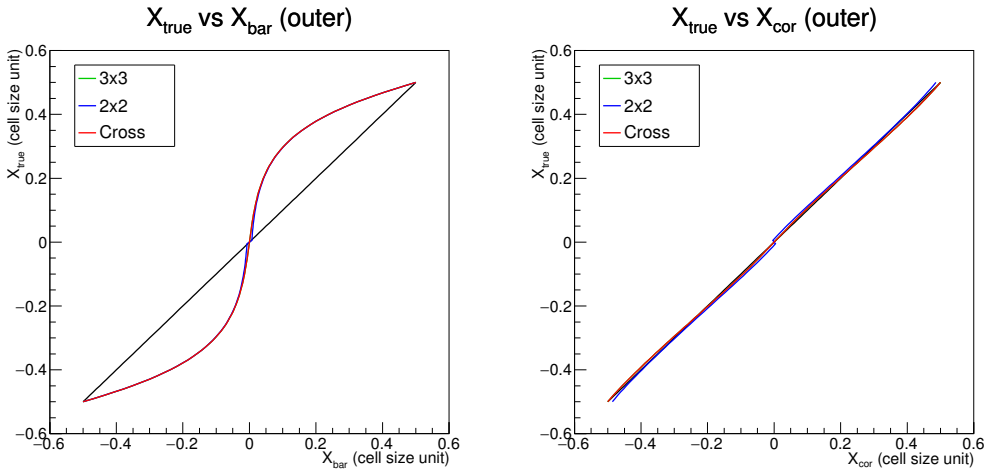

(b)

Figure 4.8 – True position as a function of the barycentre (left) and corrected (right) x-position with 3×3 (green), 2×2 (blue) and cross (red) clusters, according to a toy simulation of the inner (a) and outer (b) regions of the ECAL.

Correction to the position measurement with the reduced cluster size

Similarly to the study made on the energy reconstruction, the $B_s^0 \to \phi\gamma$ simulated samples are used to determine the correction to be applied on the barycentre position for the alternative cluster shapes. Here, only the photons coming from the B_s^0 decay are taken into account.

First, the S-shape is determined for the three cluster types and the three calorimeter areas. The non linear relation between the true position and the reconstructed one is clearly seen in Fig. 4.9. As expected from the toy study, the S-shapes of the 3×3 and cross clusters are similar and those of the 2×2 cluster show a discontinuity when the photon hit the cell close to its centre. The S-shape corrected position for the 3×3 and cross clusters are expressed as

$$X_{\text{cor}} = b \,\text{asinh}\left(2X_{\text{b}} \sinh\frac{1}{2b}\right), \tag{4.18}$$

and for the 2×2 clusters as

$$X_{\text{cor}} = b \,\text{asinh}\left(2X_{\text{b}} \sinh\frac{1}{2b}\right) + c \,\ln X_{\text{b}}, \tag{4.19}$$

with the positions in cell size unit. The classical S-shape $S(X_{\text{b}}, b)$ term can be recognised. The logarithmic term for the 2×2 cluster is used to try to correct the discontinuity at $X_{\text{b}} \sim 0$. The correction parameters b and c have to be determined. Thus, an optimisation is performed to minimise the χ^2 defined as

$$\chi^2_{\text{cor}}(\vec{p}) \equiv \sum_{\gamma \text{ cand.}} \left(X_{\text{true}} - X_{\text{cor}}(\vec{p})\right)^2 + \left(Y_{\text{true}} - Y_{\text{cor}}(\vec{p})\right)^2, \tag{4.20}$$

with $\vec{p}$ the correction parameters. The result of the minimisation are summarised in Table 4.1. Notice that the uncertainty returned by the minimisation should be taken as a rough estimation, since the χ^2 is not properly normalised. The difference between the three calorimeter regions is seen with an increasing value of the b parameter for a smaller cell size. For the 2×2 correction, the minimisation is performed in two steps. First the b is evaluated with the logarithmic term c fixed to zero. Then the c parameter is determined with b fixed to the value found at the first step. This procedure is needed because the minimisation cannot converge properly with b and c varying simultaneously.

The result of the S-shape correction for the cross and 2×2 clusters, in the inner region, is illustrated in Fig. 4.10. The linear relation between the true photon position and the reconstructed position is well recovered for the cross clusters. The result for the 3×3 shapes is similar.

Table 4.1 – Parameters of the S-shape correction determined for the 3×3, cross and 2×2 clusters.

	3×3	cross	2×2
Inner	$b = 0.181 \pm 0.006$	$b = 0.149 \pm 0.004$	$b = 0.20 \pm 0.02$
			$c = 0.009 \pm 0.002$
Middle	$b = 0.159 \pm 0.005$	$b = 0.140 \pm 0.003$	$b = 0.16 \pm 0.02$
			$c = 0.010 \pm 0.002$
Outer	$b = 0.132 \pm 0.003$	$b = 0.111 \pm 0.002$	$b = 0.12 \pm 0.02$
			$c = 0.010 \pm 0.001$

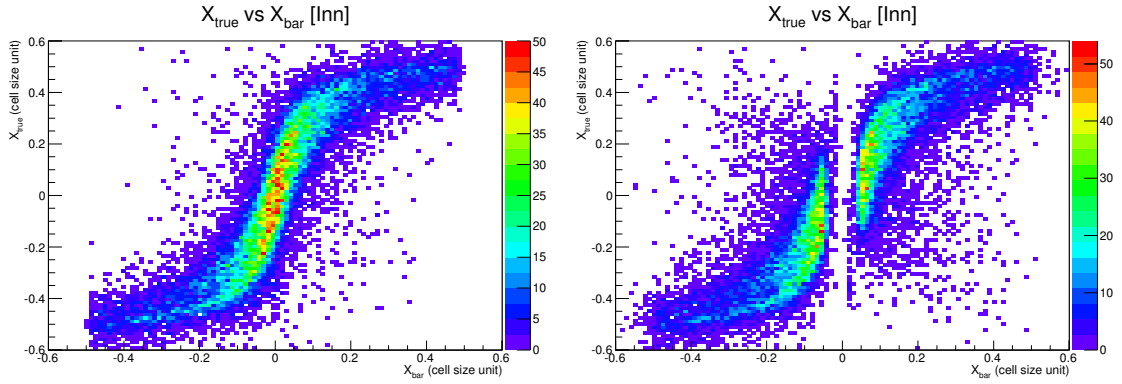

(a)

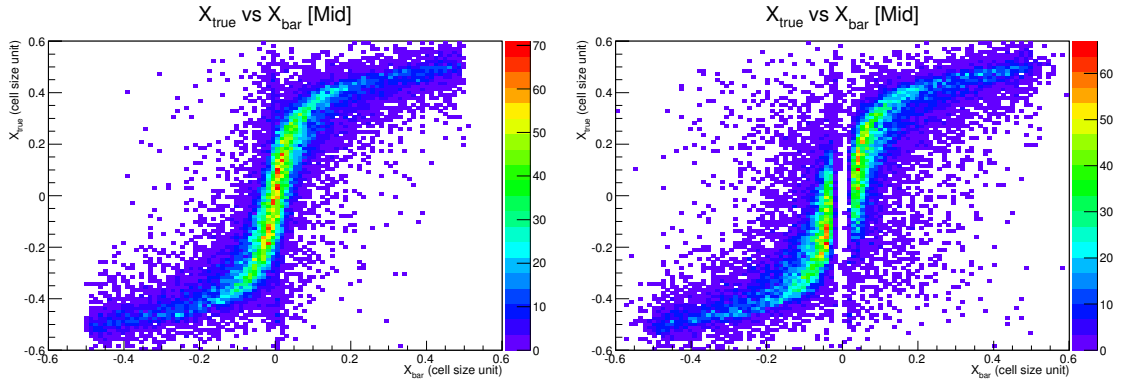

(b)

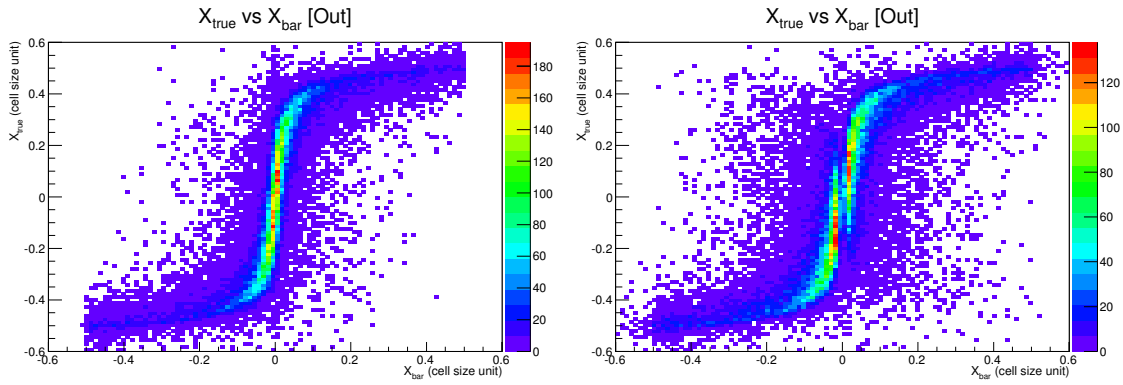

(c)

Figure 4.9 – True photon position as a function of the energy barycentre reconstructed with cross (left) and 2 × 2 (right) clusters, in the inner (a), middle (b) and outer (c) regions of the ECAL.

However the correction for the 2 × 2 is not satisfactory. Even though the relation between true and reconstructed position is more linear after the S-shape correction, the discontinuity around the cell centre is still present. Hence, the 2 × 2 clusters cannot provide good performances on the position reconstruction. They are not considered further in this study.

The S-shape correction is not perfect. As can be seen in Fig. 4.10a, there is some dispersion around the $(X_{\text{cor}}, X_{\text{true}})$ diagonal. Therefore some additional corrections are needed to improve

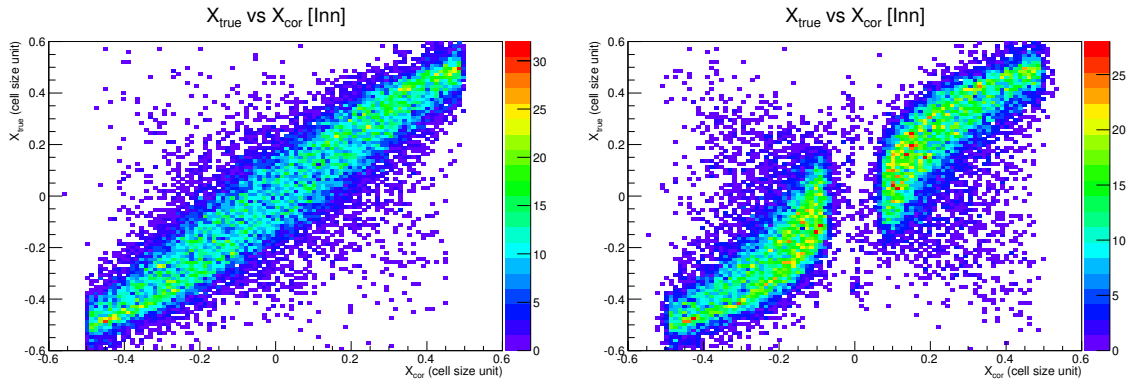

(a) (b)

Figure 4.10 – True photon position as a function of the reconstructed position after the S-shape correction with cross (a) and 2 × 2 (b) clusters, in the inner region of the ECAL.

the position resolution. A correction has to be made depending on the photon incidence angle θ_x (θ_y) on the x (y) direction. There is a linear dependence between the residuals remaining after the S-shape correction $X_{\text{cor}} - X_{\text{true}}$ ($Y_{\text{cor}} - Y_{\text{true}}$) and the incidence angle θ_x (θ_y). This is highlighted in the left-hand side of Fig. 4.11. For instance, at high positive θ_x, *i.e.* in the positive x direction, the photon does not strike the calorimeter surface perpendicularly. It shifts the reconstructed position at higher x, hence at lower X values (see Fig. 4.2). The residuals on Y have a similar dependence on θ_y. It has been also checked that the residuals on X (Y) do not depend on the incidence angle in the other direction θ_y (θ_x). The positions after the S-shape correction ($X_{\text{cor}}, Y_{\text{cor}}$) are therefore corrected with a simple linear relation

$$\begin{aligned} X_{\text{Tcor}} &= X_{\text{cor}} - a_{\text{Tx}}\,\theta_x, \\ Y_{\text{Tcor}} &= Y_{\text{cor}} - a_{\text{Ty}}\,\theta_y, \end{aligned} \tag{4.21}$$

where $a_{\text{T}x}$ and $a_{\text{T}y}$ are correction parameters (the index 'T' stands for 'theta' correction). They are determined with a similar minimisation procedure used for the S-shape correction, and are based on the residuals shown in the left-hand side of Fig. 4.11 (after S-shape correction). The X and Y are analysed separately. The fitted values are summarised in Table 4.2. The result of this correction can be seen in the right-hand side of Fig. 4.11. The residuals $X_{\text{Tcor}} - X_{\text{true}}$ are not anymore dependent on the incidence angle.

After the incidence angle correction, applied to suppress a global calorimeter effect, some non negligible local residuals remain (Fig. 4.12, left). An oscillation pattern can be recognised that was already present in Fig. 4.11 (particularly visible in the outer region). These remaining residuals are corrected with

$$\begin{aligned} X_{\text{Rcor}} &= X_{\text{Tcor}} - A_x\,\sin\left(2\pi X_{\text{Tcor}}\right), \\ Y_{\text{Rcor}} &= Y_{\text{Tcor}} - A_y\,\sin\left(2\pi Y_{\text{Tcor}}\right), \end{aligned} \tag{4.22}$$

where A_x and A_y are correction parameters which are fitted on the residuals distributions. The values obtained by the minimisation are in Table 4.3. The result of this correction is illustrated on the right-hand side of Fig. 4.12.

Table 4.2 – Parameters of the photon incidence angle correction determined for the 3×3 and cross clusters.

	3×3	cross
Inner	$a_{\mathrm{T}x} = -1.22 \pm 0.99$	$a_{\mathrm{T}x} = -1.50 \pm 0.99$
	$a_{\mathrm{T}y} = -1.51 \pm 0.41$	$a_{\mathrm{T}y} = -1.50 \pm 0.41$
Middle	$a_{\mathrm{T}x} = -0.83 \pm 0.45$	$a_{\mathrm{T}x} = -0.93 \pm 0.45$
	$a_{\mathrm{T}y} = -0.80 \pm 0.21$	$a_{\mathrm{T}y} = -0.76 \pm 0.21$
Outer	$a_{\mathrm{T}x} = -0.34 \pm 0.03$	$a_{\mathrm{T}x} = -0.35 \pm 0.03$
	$a_{\mathrm{T}y} = -0.35 \pm 0.04$	$a_{\mathrm{T}y} = -0.37 \pm 0.04$

Table 4.3 – Parameters of the residual correction determined for the 3×3 and cross clusters.

	3×3	cross
Inner	$A_x = -0.046 \pm 0.010$	$A_x = -0.033 \pm 0.009$
	$A_y = -0.050 \pm 0.010$	$A_y = -0.036 \pm 0.009$
Middle	$A_x = -0.054 \pm 0.010$	$A_x = -0.053 \pm 0.009$
	$A_y = -0.056 \pm 0.010$	$A_y = -0.052 \pm 0.009$
Outer	$A_x = -0.073 \pm 0.008$	$A_x = -0.060 \pm 0.008$
	$A_y = -0.069 \pm 0.008$	$A_y = -0.059 \pm 0.008$

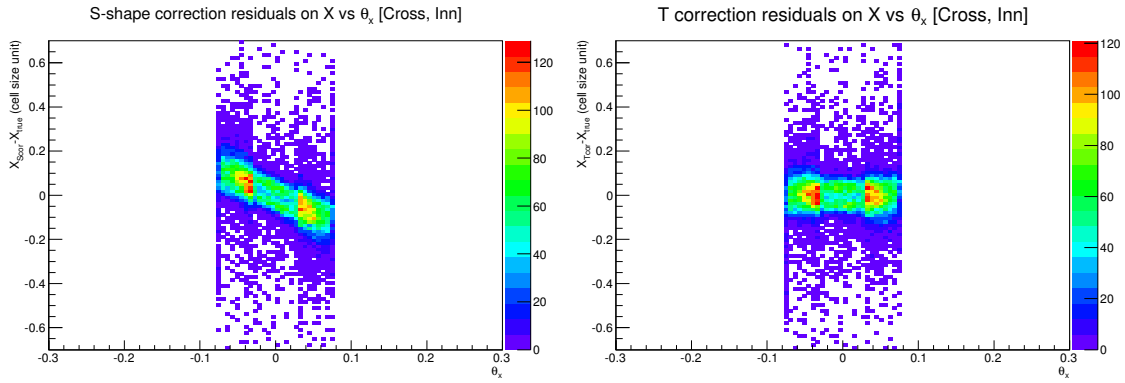

(a)

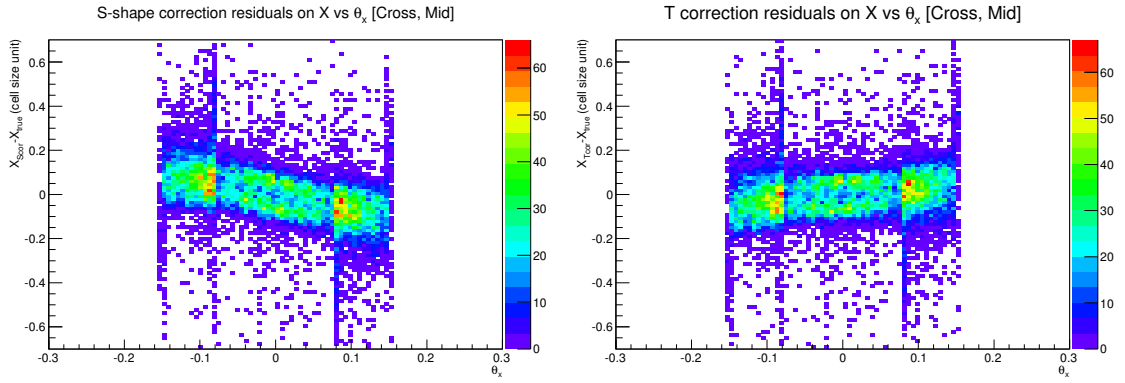

(b)

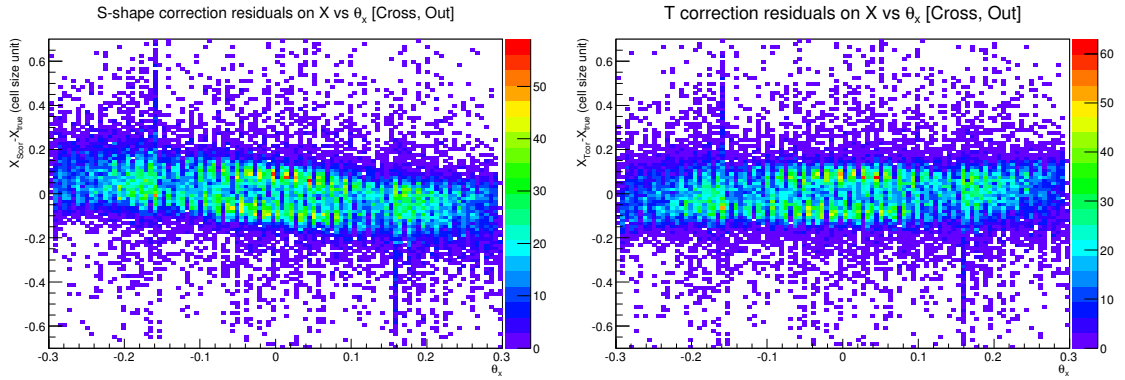

(c)

Figure 4.11 – Residuals on the reconstructed photon position after the S-shape correction (left) and the incidence angle correction (right) as a function of the photon incidence angle θ_x, with cross clusters, in the inner (a), middle (b) and outer (c) regions of the ECAL. This also affects 3×3 clusters

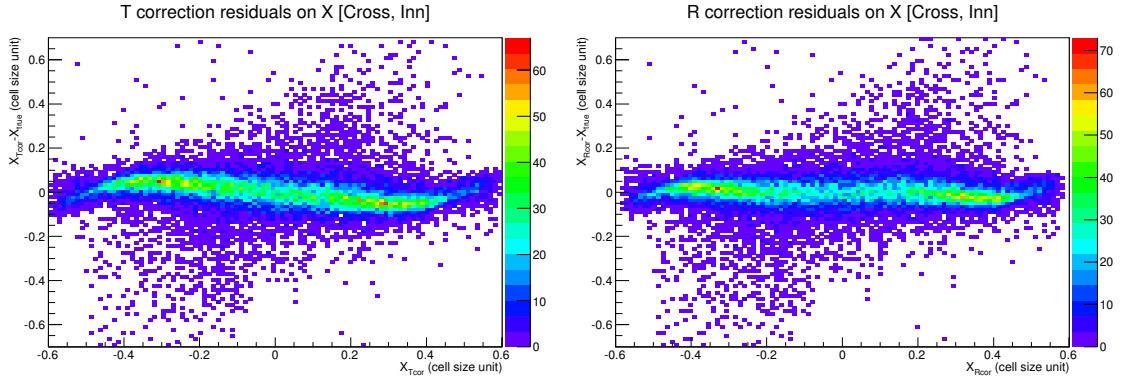

(a)

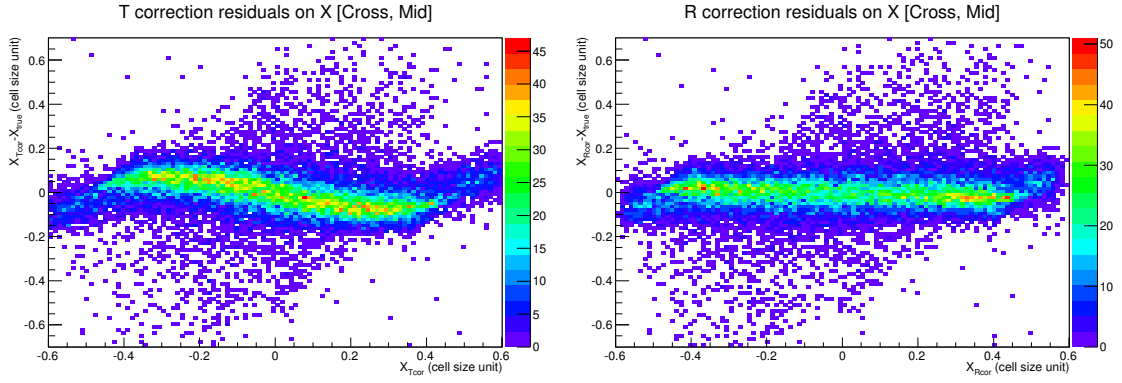

(b)

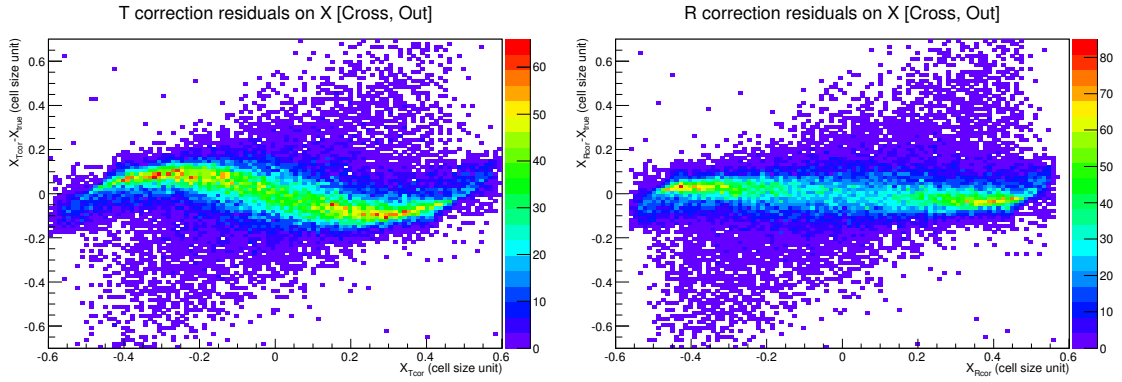

(c)

Figure 4.12 – Residuals on the reconstructed photon position after the incidence angle correction (left) and the residual correction (right) as a function of the photon reconstructed position, with cross clusters, in the inner (a), middle (b) and outer (c) regions of the ECAL.

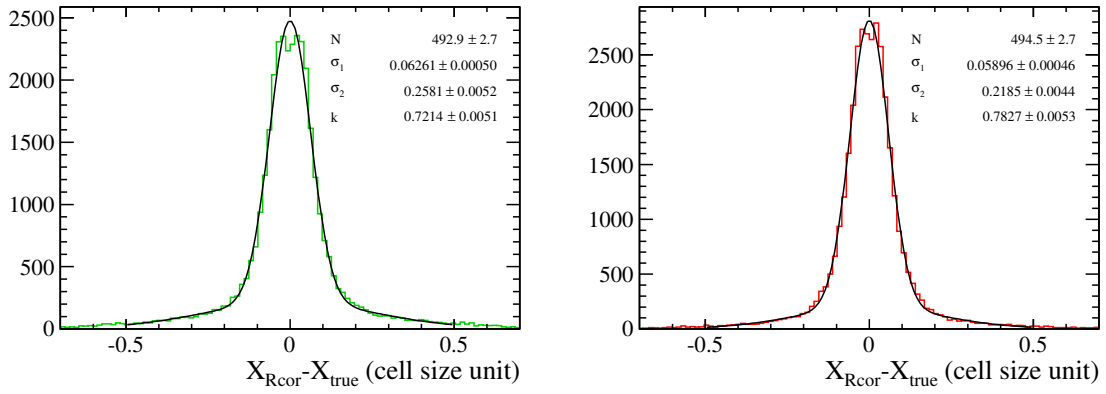

(a) 3 × 3 clusters (b) cross clusters

Figure 4.13 – Resolution on the reconstructed photon position after the three corrections described in the text, for 3 × 3 (a) and cross (b) clusters in the outer ECAL region.

In summary, three corrections are made to the reconstructed position with the energy barycentre: the S-shape correction, the incidence angle correction and the final residuals correction. The 2 × 2 clusters are problematic because of the discontinuity at $X \sim 0$. The comparison of the position resolution with 3 × 3 and cross clusters shows that the cross reconstruction is more accurate. As illustrated in Fig. 4.13 for the outer region, the distributions of the residual between the final measured position X_{Rcor} and the true position is narrower with cross clusters. To quantify this improvement, the residuals are fitted with a double Gaussian distribution. From this fit is deduced the effective resolution

$$\sigma_{\text{eff}} \equiv \sqrt{k\sigma_1^2 + (1-k)\sigma_2^2}, \tag{4.23}$$

where σ_1 and σ_2 are the widths of the two Gaussian distributions and k the proportion between the core and the wider component. The effective resolutions are summarised in Table 4.4. Depending on the ECAL region, the cross clusters show an improvement on the resolution between 15 and 22% compared to the 3 × 3 clusters. The improvement is relatively lower in the middle region since a lower pile-up effect is expected.

The effect of the position resolution on the B_s^0 invariant mass reconstruction can be seen on the simulated $B_s^0 \to \phi\gamma$ candidates. The B_s^0 mass distribution is made with the true four-

Table 4.4 – Effective resolution on the photon position obtained with the 3 × 3 and cross clusters.

ECAL region	σ_{eff}		Improvement
	3 × 3	cross	
inner	0.103	0.084	18%
middle	0.117	0.100	15%
outer	0.146	0.114	22%

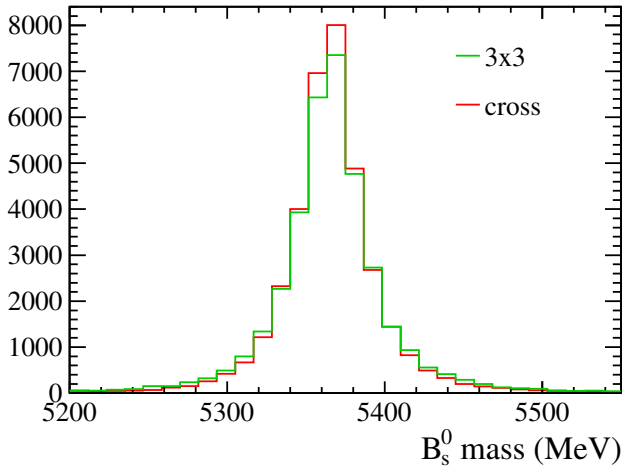

Figure 4.14 – Reconstructed invariant mass from the simulated decay $B_s^0 \to \phi\gamma$, taking the true four-momentum of the ϕ and the true energy of the photon. The position is reconstructed either with 3×3 clusters (green) of cross clusters (red). Only photons from the outer region of the ECAL are considered.

momentum of the ϕ and the true energy of the photon. The photon position is reconstructed either with the 3×3 or the cross clusters. Thus, only the effect of the position resolution appears on the distributions. Fig. 4.14 shows the corresponding distribution for the outer region of the calorimeter. The mass shape is slightly narrower with the cross clusters than the 3×3, in all the three ECAL regions. This improvement in the mass resolution with cross clusters can roughly be evaluated with the standard deviation of the histograms (rms). Table 4.5 compares the standard deviation obtained with the two cluster types. The cross clusters improve the mass resolution of 7 to 12% with regards to 3×3 clusters, following the ECAL region. Again, the improvement is relatively lower in the middle region since a lower pile-up effect is expected. Moreover the energy of the photons in $B_s^0 \to \phi\gamma$ decays is large, therefore the relative effect of pile-up is lower. The improvement of the cross shape clustering varies oppositely to the photon energy with respect to the standard reconstruction. As a consequence, the improvement on the mass resolution observed on the $B_s^0 \to \phi\gamma$ decay is expected to be larger for other decays involving photons with a softer energy spectrum.

Table 4.5 – Standard deviation (rms) of the reconstructed mass of $B_s^0 \to \phi\gamma$ candidates, taking the true four-momentum of the ϕ and the true energy of the photon.

ECAL region	Mass resolution (rms)		Improvement
	3×3	cross	
inner	25.7 MeV	23.3 MeV	9%
middle	29.6 MeV	27.6 MeV	7%
outer	37.4 MeV	33.0 MeV	12%

4.2.3 Conclusion and Prospects

In conclusion, adopting alternative cluster shapes from the standard 3×3 improves the robustness of the photon measurement in high luminosity conditions such as after the LHCb upgrade.

For the energy measurement, 2×2 clusters reduce the pile-up effect while keeping the resolution similar to the 3×3 clusters one. With the dedicated corrections, the cross clusters show better performance than 3×3 clusters in term of position measurement.

To emphasise more the reduction of the pile-up effect, the same study can be performed with decays producing photons at low energy, such as $D^{*0} \to D^0\gamma$. Since the additional energy due to pile-up does not drastically depend on the photon energy, the pile-up effect is relatively more important for low energy photons. The two clusterisations (2×2 and cross-shape) have been implemented in the reconstruction software of the LHCb calorimeter (`Brunel`) altogether with their corrections. The Run II data will be already used to validate this new reconstruction in realistic conditions.

Chapter 5

Measurement of the CKM angle γ with a Dalitz analysis of the $B^0 \to DK^{*0}$ decays

Contents

This chapter reports the main work carried out during this thesis, which is the measurement of the CKM angle γ with a Dalitz analysis of the $B^0 \to DK^{*0}$ decays (charge conjugation is implied throughout this chapter, unless otherwise stated). The sample used in this analysis is the $3\,\text{fb}^{-1}$ of proton-proton collision data provided by the LHC at a centre-of-mass energy of 7 and 8 TeV, and collected by the LHCb experiment during 2011 and 2012.

5.1 Analysis introduction

The CKM angle γ, defined as $\gamma \equiv \arg\left(-\frac{V_{ud}V^*_{ub}}{V_{cd}V^*_{cb}}\right)$, is the least well known CKM parameter. The most precise direct measurement to date comes from the LHCb collaboration, with a precision just below 10° [10]. As explained in Chap. 2, this parameter can be measured without any significant contribution of new physics and is therefore a benchmark for the standard model. A precise measurement of this angle is crucial to check the consistency of the CKM model, and constraint new physics scenarios. To measure it, a process involving interference between $b \to u$ and $b \to c$ transitions is required, such as $B^0 \to DK^{*0}$ decays, where D stands either for a D^0 or a $\overline{D}^0$ (the corresponding diagrams are again illustrated in Fig. 5.1). The $B^0 \to DK^{*0}$ decays are particularly interesting since they have a large interference magnitude $r_{B^0} \sim 0.3$ (see Sec. 2.6). In the similar $B^0_s \to D\overline{K}^{*0}$ decays, the interference is suppressed by a factor λ^2 ($\lambda = \sin\theta_C \sim 0.22$ is the sine of

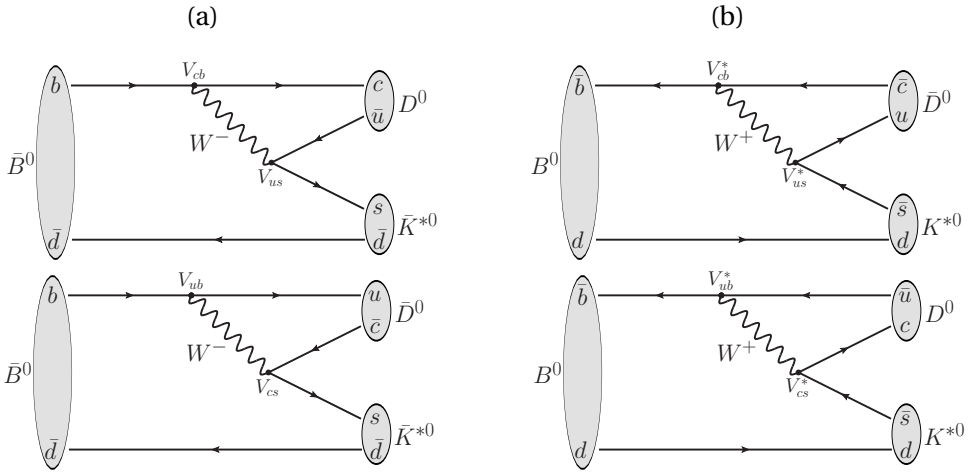

Figure 5.1 – Feynman diagrams involved in the $\overline{B}^0 \to D\overline{K}^{*0}$ (a) and $B^0 \to DK^{*0}$ (b) decays. Transitions proportional to $|V_{cb}|^2$ are at the top and transitions proportional to $|V_{ub}|^2$ are at the bottom. All diagrams are colour-suppressed.

the Cabbibo angle). Therefore, this channel is not used for measuring γ, but can be used as a control mode.

The present analysis selects the D mesons decaying in the $K^0_S\pi^+\pi^-$ state, to perform an amplitude analysis of the Dalitz plot, following the so-called GGSZ model dependent method (see Sec. 2.3.1). The *CP* violation observables

$$z_\pm = r_{B^0} e^{i(\delta_{B^0} \pm \gamma)} \tag{5.1}$$

are present in the expression of the Dalitz plot distributions

$$\mathscr{P}_- \propto |A_D|^2 + |z_-|^2 \left|A_{\overline{D}}\right|^2 + 2\kappa \mathscr{R}e\left[z_- A_D^* A_{\overline{D}}\right], \tag{5.2}$$

$$\mathscr{P}_+ \propto \left|A_{\overline{D}}\right|^2 + |z_+|^2 |A_D|^2 + 2\kappa \mathscr{R}e\left[z_+ A_{\overline{D}}^* A_D\right], \tag{5.3}$$

of the $\overline{B}^0 \to D\overline{K}^{*0}$ and $B^0 \to DK^{*0}$ candidates respectively (for a detailed description of these PDF expressions, see Sec. 2.6.1). Thus, a fit of the Dalitz plot determines the cartesian parameters

$$x_\pm \equiv \mathscr{R}e(z_\pm), \tag{5.4}$$

$$y_\pm \equiv \mathscr{I}m(z_\pm), \tag{5.5}$$

then information on γ can be determined from $(x_\pm, y_\pm)$ through a frequentist interpretation.

5.2 Candidates selection

5.2.1 Datasets and simulation

The analysis is based on the full Run 1 LHCb dataset, corresponding to 1 fb^{-1} of pp collisions at $\sqrt{s} = 7$ TeV (2011 data) and 2 fb^{-1} at $\sqrt{s} = 8$ TeV (2012 data). It exploits the candidates preselected by a dedicated stripping lines (see Sec. 3.2.7), whose cuts are summarised in Table 5.1. They are based on momentum (p), transverse momentum (p_T), quality of track reconstruction (track χ^2/ndf), impact parameter significance (χ^2_{IP}), distance of closest approach (DOCA), quality of

vertex reconstruction (χ^2_{vtx}) and lifetime (τ) requirements. In addition there are also cuts on the angle between the momentum of the reconstructed particle and the flight direction made by the production and decay vertices (θ_{dira}). Finally, a BDT is also used in the stripping. This BDT is trained to select $B \to Dh$ generic decays, using the p_{T} of the B meson, its flight distance significance and the good reconstruction quality of the B and D decay vertices.

The events are required to be triggered at the hardware trigger level L0 by the signal candidates, on the hadronic line (hadron Trigger On Signal, `L0HadronTOS`, see Sec. 3.2.6) or by the part of the event which is not associated to the signal, on any line (global Trigger Independent of Signal, `L0GlobalTIS`, see Sec. 3.2.6). Hence, two categories of signal candidates can be made: TOS and NotTOS.

- Candidates are TOS when at least one of the tracks of the signal B^0 meson fired the L0 trigger,
- candidates are NotTOS when no signal track fired the L0 trigger but at least one of the tracks not associated to the signal fired the trigger (candidates are not `L0HadronTOS` but are `L0GlobalTIS`).

This distinction is particularly relevant for the efficiency computation (see Sec. 5.3.1). At the first level of the software trigger (HLT1) the signal candidates must pass a specific line relying on track information, and at the second level (HLT2) they must pass the topological trigger lines for b-hadron multi-body decays described in Sec. 3.2.6.

In order to estimate the efficiency and to describe the B invariant mass distribution, several simulated samples were generated with the `Gauss` application [106]. These samples correspond to $B^0 \to DK^{*0}$ signal, the $B^0_s \to D\overline{K}^{*0}$ control channel and the specific backgrounds $B^0_s \to D^{*0}(D^0\gamma)\overline{K}^{*0}$, $B^0_s \to D^{*0}(D^0\pi^0)\overline{K}^{*0}$ and $B^0 \to D\rho^0$. The $B^0 \to DK^{*0}$ and $B^0_s \to D\overline{K}^{*0}$ samples are generated with a phase-space model. This means that they are produced uniformly across the D^0 Dalitz plane (especially useful for efficiency computation, see Sec. 5.3). All the samples were simulated with the 2012 data taking conditions and with loose generator level cuts in order to avoid generating too many events that would have been later rejected by the stripping selection. These cuts are listed in appendix A. It has been checked that this loose selection introduce no acceptance biases on the D^0 Dalitz plane (Fig. A.1).

5.2.2 K^0_{S} categories and masses used in the analysis

Before developing the selection, the K^0_{S} categories and the invariant mass variables used in the analysis are presented.

K^0_{S} reconstruction categories

Two categories of K^0_{S} candidates exist, defined according to the reconstruction of their daughter tracks (see Fig. 3.11 of Chap. 3). The K^0_{S} meson made from two *Longstream* tracks – made of hits in the VELO and the trackers – are called *Long-Long* (LL). Those made from two *Downstream* tracks – made with only hits in the trackers – are called *Down-Down* (DD). Compared to the DD, the LL candidates are reconstructed with a better accuracy thanks to the VELO information. They have better mass and flight distance resolutions. Fig. 5.3 shows this difference of mass resolution between the LL and DD candidates. It can be also noticed that the background (data sidebands) is more peaking for the DD candidates. Hence, it contains a higher proportion of true K^0_{S}.

Table 5.1 – Stripping selection for $B^0 \to DK^{*0}$ candidates

Particle	Variable	Cut value
Charged particles	p	$> 1\,\text{GeV}$
	p_T	$> 100\,\text{MeV}$
	Track χ^2/ndf	< 3
	Min χ^2_IP	> 4
K^0_S	p_T	$> 250\,\text{MeV}$
	$m(\pi^+\pi^-)$	$\in [467;527]\,\text{MeV}$
	$p(\pi^\pm)$	$> 2\,\text{GeV}$
	Min χ^2_IP	> 9(LL) or > 4(DD)
	Max DOCA$\chi^2(\pi^\pm,\pi^\mp)$	< 25
	χ^2_vtx	< 25
D^0	$\lvert m(K^0_\text{S}\pi^+\pi^-) - m_{PDG}(D^0)\rvert$	$< 100\,\text{MeV}$
	$\sum_{daughters} p_\text{T}$	$> 1.8\,\text{GeV}$
	Max DOCA$(K^0_\text{S},\pi^+,\pi^-)$	$< 0.5\,\text{mm}$
	χ^2_vtx/ndf	< 10
	Distance to PV significance	> 36
	$\cos\theta_\text{dira}$	> 0
At least one daughter (K^0_S or $\pi^\pm$)	p	$> 5\,\text{GeV}$
	p_T	$> 500\,\text{MeV}$
	Track χ^2/ndf	< 2.5 (if $\pi^\pm$)
	Distance to PV significance	> 1000 (if K^0_S)
K^{*0}	$p(K^\pm,\pi^\mp)$	$> 2\,\text{GeV}$
	$p_\text{T}(K^\pm) + p_\text{T}(\pi^\mp)$	$> 1\,\text{GeV}$
	$m(K^\pm\pi^\mp)$	$< 5.2\,\text{GeV}$
	Max DOCA$(K^\pm,\pi^\mp)$	$< 0.5\,\text{mm}$
	χ^2_vtx/ndf	< 16
	Distance to PV significance	> 16
	$\cos\theta_\text{dira}$	> 0
B^0	$m(DK^{*0})$	$\in [4.45;6]\,\text{GeV}$
	$p_\text{T}(D^0) + p_\text{T}(K^{*0})$	$> 5\,\text{GeV}$
	χ^2_vtx/ndf	< 10
	τ_{B^0}	$> 0.2\,\text{ps}$
	Min χ^2_IP	< 25
	$\cos\theta_\text{dira}$	> 0.999
	Stripping BDT output	> 0.05
At least two daughters	p	$> 5\,\text{GeV}$
	p_T	$> 500\,\text{MeV}$
	Track χ^2/ndf	< 2.5 (if $K^\pm$ or $\pi^\pm$)
	Distance to PV significance	> 1000 (if K^0_S)
One track	p	$> 10\,\text{GeV}$
	p_T	$> 1.7\,\text{GeV}$
	Track χ^2/ndf	< 2.5
	Min χ^2_IP	> 16
	Min IP	$> 0.1\,\text{mm}$
Global event cut	$N_\text{long tracks}$	< 250

Masses of B^0, D^0 and K^0_S with constraints

The `DecayTreeFitter` package [140] enables the whole $B^0 \to DK^{*0}$ decay chain to be refitted with some constraints on the intermediate resonance masses and the B^0 meson flight direction. Three kinds of refit are performed:

KsFit is the refit constraining the K^0_S mass, and requiring the B^0 to point to the primary vertex.

DFit is the refit constraining the D^0 mass, and requiring the B^0 to point to the primary vertex.

PVFit is the refit constraining the K^0_S and D^0 masses, and requiring the B^0 to point to the primary vertex.

The K^0_S constraint improves significantly the D^0 mass resolution, and removes any difference between the LL and DD candidates. Fig. 5.2 compares the mass distribution obtained with and without constraint on the K^0_S mass and the B^0 flight direction. It can be noticed that these constraints do not modify the background distributions and do not produce a peak. The data sidebands distributions are unchanged once the constraints are applied.

The D^0 mass constraint does not improve significantly the K^0_S mass resolution on the signal, however it smears significantly the background distribution, especially for the DD candidates (see Fig. 5.3). Without a D^0 mass constraint, the K^0_S mass for the background is peaking. Therefore the background is composed of real K^0_S. With a D^0 mass constraint, the K^0_S mass for the background peaks much less. If the D^0 mass is required, the K^0_S daughters momentum are modified by the refit such that it do not make a K^0_S mass anymore (whereas it should since they are real K^0_S). Therefore this D^0 mass constraint makes the K^0_S mass window efficient in selecting K^0_S mesons coming from a $D \to K^0_S \pi^+ \pi^-$ decay.

Because of the broad natural width of the K^{*0}, its mass resolution is unchanged if the mass constraints on the K^0_S and D^0, and the PV constraint are applied. Therefore, in all the analysis the K^{*0} mass is taken without any constraint.

In summary, if not explicitly stated otherwise, the mass variables used in the analysis are the following:

B^0 **mass:** mass with the K^0_S and D^0 masses and the PV constraints,

D^0 **mass:** mass with the K^0_S mass and PV constraints,

K^{*0} **mass:** mass without constraint,

K^0_S **mass:** mass with the D^0 mass and PV constraints,

Dalitz coordinates: squared masses with the K^0_S and D^0 masses and the PV constraints (except for $m^2(K\pi) = m^2_{K^{*0}}$, used to described the B^0 Dalitz plot, where no constraint is applied). The D^0 mass constraint especially improves the resolution on the Dalitz coordinates and ensure that the reconstructed events are inside the kinematically allowed region.

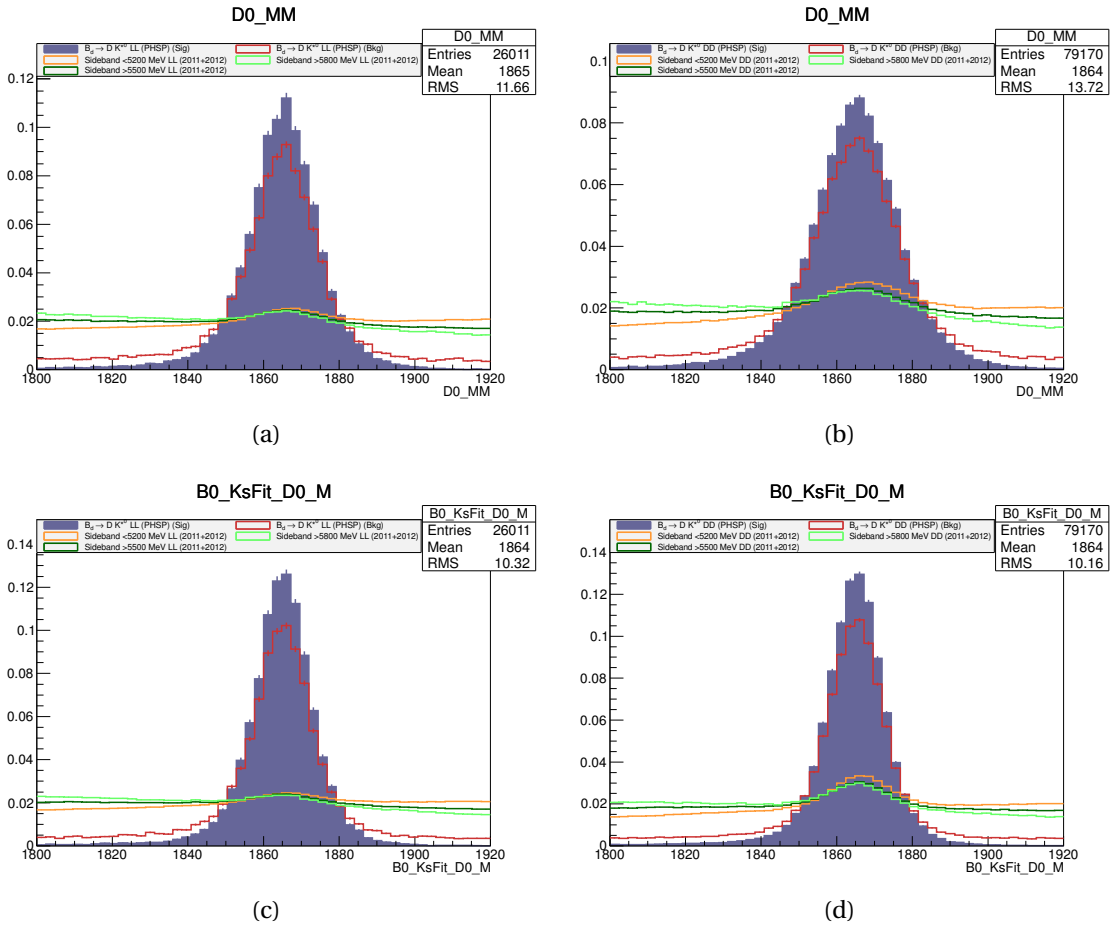

Figure 5.2 – D^0 invariant mass distributions without constraint on LL (a) and DD (b) candidates, and constraining the K^0_S mass and the B^0 flight direction of LL (c) and DD (d) candidates. The blue distributions correspond to the MC $B^0 \to DK^{*0}$ truth matched signal (*i.e.* candidates with correct true ID and correct daughters and mother), the red distributions to the signal failing the truth-matching, the orange distributions to the $m_{B^0} < 5.2\,\text{GeV}$ data sideband and the (dark) green distributions to the $m_{B^0} > 5.8\,\text{GeV}$ ($> 5.5\,\text{GeV}$) data sideband.

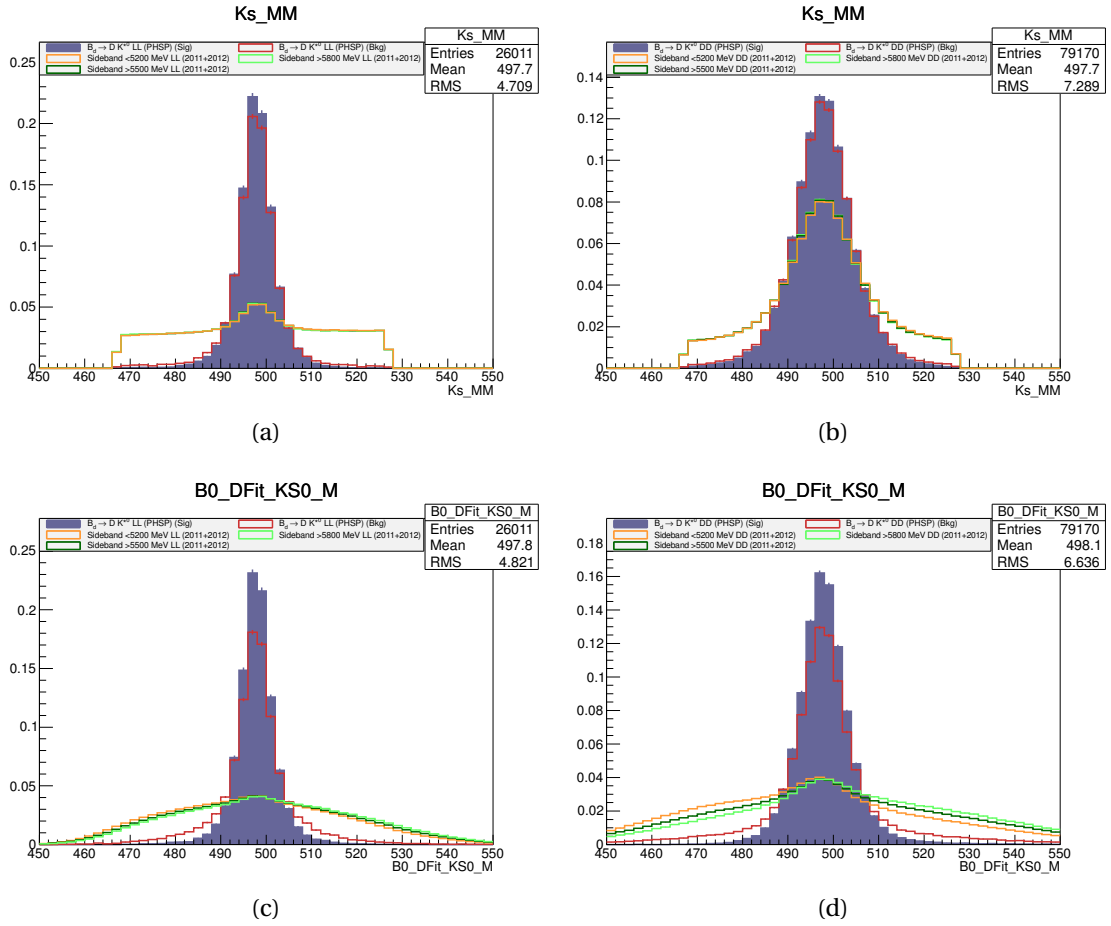

Figure 5.3 – K^0_S invariant mass distributions without constraint on LL (a) and DD (b) candidates, and constraining the D^0 mass and the B^0 flight direction of LL (c) and DD (d) candidates. The blue distributions correspond to the MC $B^0 \to DK^{*0}$ truth matched signal(*i.e.* candidates with correct true ID and correct daughters and mother), the red distributions to the signal failing the truth-matching, the orange distributions to the $m_{B^0} < 5.2\,\text{GeV}$ data sideband and the (dark) green distributions to the $m_{B^0} > 5.8\,\text{GeV}$ ($> 5.5\,\text{GeV}$) data sideband.

5.2.3 BDT selection

In order to efficiently remove the combinatorial background a Boosted Decision Trees (BDT) is trained [141, 142]. A BDT is based on two concepts: *Decision Tree* and *Boosting*.

A Decision Tree is an algorithm which classifies events in two categories, signal and background. It uses a set of discriminating variables to apply a sequence of binary splits. One split corresponds to a simple cut on one variable and produces two branches. The cut value is optimised with a separation criteria such as the *Gini index* $p(1-p)$, where $p \equiv S/(S+B)$ is the purity with S and B the numbers of signal and background events in the new branches, respectively. The splitting sequence is repeated with other variables until a maximal number of branches is reached or until the final branches, called *leaves*, contain pure signal event or pure background event samples. The sample of signal and background events used to determined this classification is called the *training sample*.

A Decision Tree has a simple structure and is trained quite quickly. However it suffers from the statistical fluctuations present in the training sample. A splitting can be chosen because of a peculiar fluctuation, and will not be adapted to another sample which does not have this fluctuation. In such case, the Decision Tree will not show optimal selection performances. The Boosting procedure overcomes this limitation and significantly enhances the selection performance compared to a unique Decision Tree. Boosting consists in training sequentially a Decision Tree with a reweighted version of the initial training data. Each reweighted data version gives one Decision Tree (typically, a BDT contains between few hundreds to one thousand trees). The reweighting is made such that the events which are misclassified (*e.g.* landing on a signal leaf whereas it is a background event) have a weight increased, or boosted. Thus, a tree at a given iteration will have a training more focused on the misclassified events. The final output decision of the BDT $F(\vec{x};\vec{p})$ is the weighted majority vote among all the N trees,

$$F(\vec{x};\vec{p}) = \sum_{i=0}^{N} \beta_i T(\vec{x};\vec{a}_i), \qquad \vec{p} = \left((\beta_0,\vec{a}_0),...,(\beta_N,\vec{a}_N)\right), \tag{5.6}$$

where $\vec{x}$ is the set of discriminating variables, β_i are the boosting weights, $\vec{a}_i$ are the parameters defining each trees and $T(\vec{x},\vec{a}_i)$ the tree decision ($+1$ for an event classified as signal, -1 for one classified as background). The Boosting determines the optimal parameters $\vec{p}$ by minimising the loss function $L(F,y)$ between the model response $F(\vec{x};\vec{p})$ and the true value y. In this analysis, the BDT uses the *Gradient Boost* algorithm, implemented in the TMVA package [143]. It uses a binomial log-likelihood loss function

$$L(F,y) = \ln\left(1+e^{-2Fy}\right). \tag{5.7}$$

Particular care must be taken during the BDT training to avoid its *overtraining*. A classifier is overtrained when its decision is well adapted to the training dataset and less for an independent dataset. This means that the classifier has "learnt" too much from the training sample. For a BDT it can happen when the number of trees or their depth are too large. In this case the performance of the BDT is high on the training sample, but poorer on another sample. That is why the performance of a BDT must be evaluated on a testing sample after the training.

Preselection for the BDT training

In the present analysis, a loose preselection is applied on the training sample. This preselection, detailed in table 5.2, removes the most obvious background candidates and focuses the BDT

Table 5.2 – Preselection applied for the BDT training (PRESEL_BDT).

Particle	Variable	Cut value
K^{*0}	$\mathrm{DLL}_{K\pi}$ (K^+)	> 3
	$\mathrm{DLL}_{K\pi}$ (π^-)	< 3
	$\lvert m(K^+\pi^-) - m_{PDG}(K^{*0})\rvert$	< 100 MeV
D^0	$\lvert m(K^0_S\pi^+\pi^-) - m_{PDG}(D^0)\rvert$ with PV and K^0_S mass constraint	< 51 MeV (5σ)
K^0_S	$\lvert m(\pi^+\pi^-) - m_{PDG}(K^0_S)\rvert$ with PV and D^0 mass constraint [2]	< 24.1 MeV (LL) (5σ)
		< 33.2 MeV (DD) (5σ)

on events more difficult to reject. It consists of a particle identification [1] (PID) selection on the K^{*0} daughters, to remove double candidates (inherent of the PID swap between the two K^{*0} daughters), and wide mass windows on the K^{*0}, D^0 and K^0_S.

Crossed BDT motivation

The BDT is trained on two reference samples for the signal and the background. The signal training sample is the truth matched $B^0 \to DK^{*0}$ simulated sample, after the preselection described above. The candidates are also truth matched, which means that only candidates with correct true ID and correct filiation in the decay tree are retained. The signal sample is composed of 17787 LL candidates and 55992 DD candidates. The background training sample is the data in the B^0 mass upper sideband (from 2011 and 2012 data), also preselected by the selection described above. To have an efficient BDT selection it is important to have high statistics training samples, with properties as close as possible to the signal and the background that we want to disentangle. That is why an upper sideband above 5.5 GeV is chosen as the background training sample. This sideband is made of 10828 LL candidates and 7599 DD candidates. If the sideband above 5.8 GeV would have been chosen instead, only 3741 LL and 2448 DD candidates would have been available. Moreover the 5.5 GeV upper sideband has not the only advantage to have three times the statistics of the 5.8 GeV upper sideband. It includes also a kinematic and topological region closer to the signal one (see appendix B). Despite these two advantages of the 5.5 GeV sideband, a small bias could be introduced in the B^0 mass fit developed further. The fit range is [4.9; 5.8] GeV in order to constrain well the combinatorial background (described by an exponential). Hence there is an overlap between the BDT training range and the fitting range. Some events are used both to train the selection and to estimate the signal and background yields. To get rid of any potential bias a crossed BDT method is developed. This method has been already used in LHCb, for instance in the $B^0_{(s)} \to K^0_S hh'$ analysis [144] or in the $B^0 \to K^{*0}\mu^+\mu^-$ selection [84] (even in a more complex way with a 10-folding). The principle is to split randomly the data in half (by throwing a uniform random number). It makes two samples called A and B. Two independent BDTs, BDTA and BDTB, are trained on the upper sideband of samples A and B.

[1] The particle identification algorithm used in LHCb is presented in Sec. 3.2.5 of Chap. 3

[2] It should be noticed that because of a bug in the code, the preselection cut on the K^0_S mass for the DD events has not the PV and D^0 mass constraint. This bug has a negligible effect since this cut is loose (the stripping cuts on the K^0_S mass is at 30 MeV, without any constraint). On the 7599 candidates in the $m_{B^0} > 5.5$ GeV sidebands, 187 should have been removed from the training. That is why it has been decided to not retrain the BDT after bug correction (but it has been corrected each time the full selection is applied).

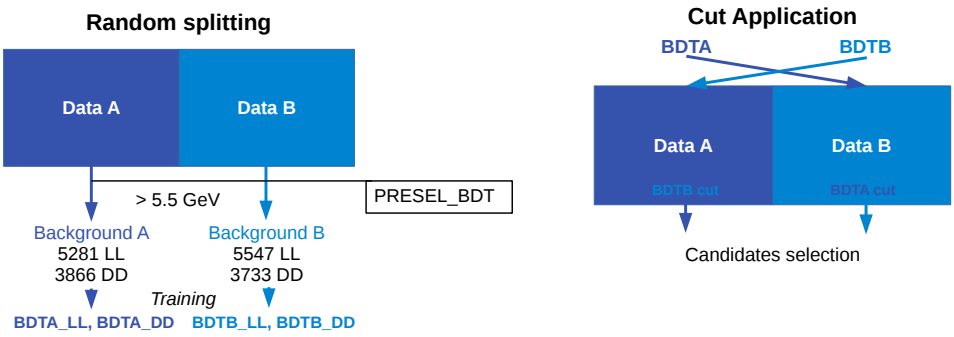

Figure 5.4 – Crossed BDT principle: data splitting and BDT selection application.

Then for the selection, BDTA is applied to sample B and BDTB is applied to sample A (hence the name *crossed* BDT). Thus the candidates are selected in a fully unbiased way.

To take advantage of their different topology, the LL and DD candidates are separately selected with independent crossed BDTs. Since LL K^0_S have hits in the VELO, their tracks are much better measured than the DD K^0_S. For instance the impact parameter and the flight distance of a LL K^0_S are more accurate. A comparison between LL and DD distributions can be found in appendix C.

Eventually four independent BDTs are trained: BDTA_LL, BDTB_LL, BDTA_DD and BDTB_DD. In the following they will all be gathered under the general denomination (crossed) BDT. A summary of the multivariate selection process is illustrated in Fig. 5.4.

Training

After several tests on different training tuning, the version of the BDT with the best performance (good ROC curve and no sign of overtraining) turns out to use a Gradient Boosting algorithm with the following parameters:

- number of trees: 200
- shrinkage: 0.1
- bagging fraction: 0.6
- separation type: Gini index
- number of cuts: 20
- maximal depth of the trees: 5

The shrinkage parameter reduces the learning rate during the training, by controlling the weight of the individual trees. Small shrinkage value of 0.1 enhance the robustness of the BDT. The bagging fraction sets the fraction of the sample used in each iteration of the training procedure. This bagging, which consists in using random subsamples of the training sample, also enables the BDT answer to stabilise.

The signal and background training samples have the following size:

- Signal:
  - LL: 17787
  - DD: 55992
- Background:
  - LL: A 5281 / B 5547
  - DD: A 3866 / B 3733

Table 5.3 – Discriminating variables used by the BDT. The symbol † denotes a variable with different distributions for LL and DD candidates.

Variable name	Description
log(B0_IPCHI2_OWNPV)	B^0 χ^2_{IP} w.r.t PV
log(Sum2_IPS)†	Sum of χ^2_{IP} w.r.t PV over K^0_S daughters
log(Sum4_IPS)	Sum of χ^2_{IP} w.r.t PV over all final particles, except K^0_S daughters
log(B0_ENDVERTEX_CHI2_NDOF)	B^0 χ^2_{vtx}/ndf
log(D0_ENDVERTEX_CHI2_NDOF)	D^0 χ^2_{vtx}/ndf
log(Ks_FDCHI2_OWNPV)†	K^0_S flight distance signif. w.r.t PV
log(D0_FDCHI2_OWNPV)	D^0 flight distance signif. w.r.t PV
log(B0_FDCHI2_OWNPV)	B^0 flight distance signif. w.r.t PV
Ks_DKs_FDSig†	K^0_S flight distance signif. w.r.t the D^0
D0_BD_FDSig	D^0 flight distance signif. w.r.t the B^0
log(D0_PT)†	D^0 p_{T}
log(Kst_PT)†	K^{*0} p_{T}
log(B0_PT)	B^0 p_{T}
log(acos(B0_DIRA_OWNPV))	B^0 pointing angle
Kst_BKstarK_DecayAngle	cosine of the K^{*0} helicity angle ($\cos\theta^*$)
log(B0_PVFit_chi2/B0_PVFit_nDOF)	DecayTreeFitter vertex refit χ^2/ndf

To maximise the selection performances the full statistics is used to train the BDT. This choice does not prevent from having an independent sample for the testing (explained in the following). The variables used to discriminate the signal and the background are summarised in Table 5.3. Their distributions and their ranking can be found in appendix C. The K^0_S daughters impact parameters are added separately from the four other final particles to take into account the K^0_S LL/DD specificity. All variables are symmetric with regards to the D^0 direct daughters pions to avoid any bias on the Dalitz plane. All positive variables are put under natural logarithm transformation. This reduces the spread in the distributions. The inclusion of the cosine of the K^{*0} helicity angle ($\cos\theta^*$) in the BDT does not affect the γ extraction, as explained in sections 5.4.5. The K^0_S and D^0 flight distance significances compared respectively to the D^0 and the B^0 are defined as:

$$\texttt{Ks\_DKs\_FDSig} \equiv \frac{z_{K^0_S} - z_{D^0}}{\sqrt{\sigma^2_{z_{K^0_S}} + \sigma^2_{z_{D^0}}}}, \tag{5.8}$$

$$\texttt{D0\_BD\_FDSig} \equiv \frac{z_{D^0} - z_{B^0}}{\sqrt{\sigma^2_{z_{D^0}} + \sigma^2_{z_{B^0}}}}. \tag{5.9}$$

They are particularly useful to select real D^0 (K^0_S) mesons, well separated from their B^0 (D^0) mother. Even though the BDT was trained with the data upper sideband as a background sample,

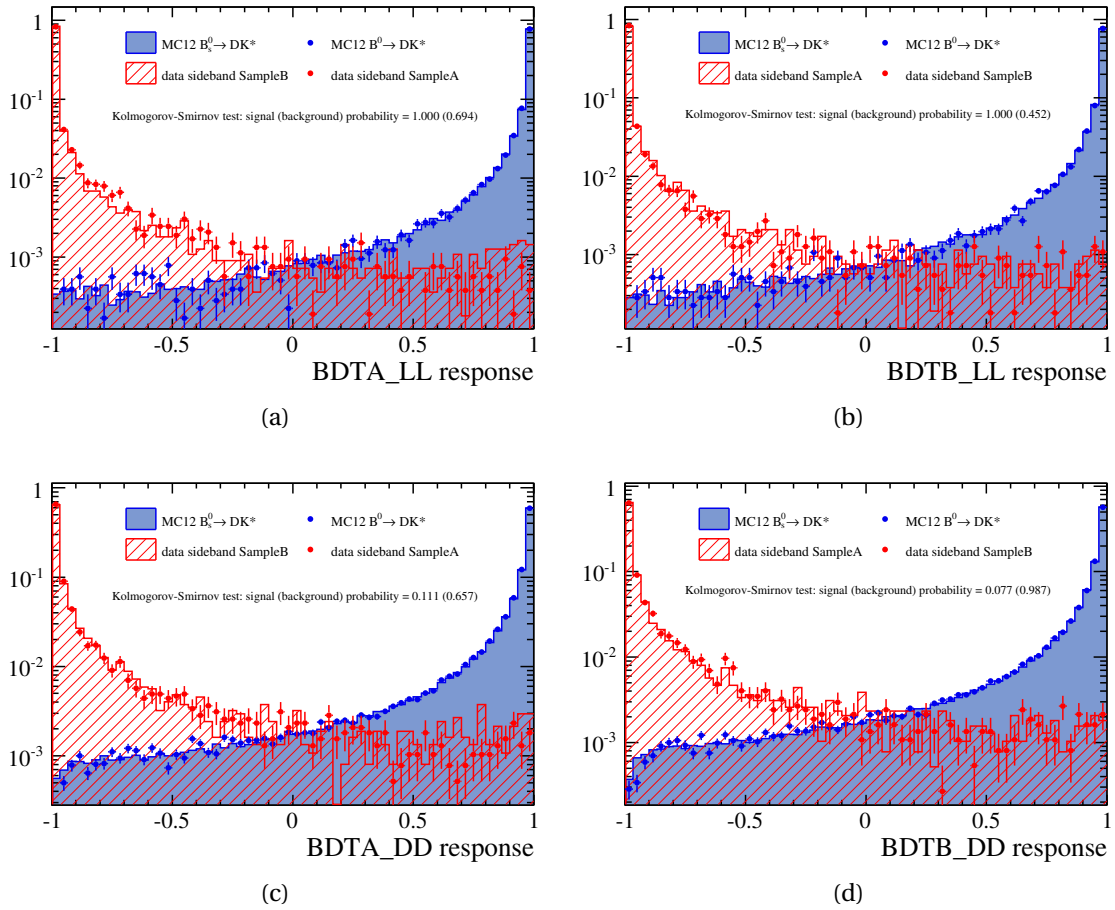

Figure 5.5 – BDT output distribution of training (histograms with markers) and test (filled histograms) samples, for BDTA_LL (a), BDTB_LL (b), BDTA_DD (c) and BDTB_DD (d) (vertical log-scale).

therefore trained against combinatorial-like events, it will significantly reject charmless and $B^0 \to D(\pi\pi\pi\pi)K^{*0}$ backgrounds thanks to the presence of these two variables. Events with D^0 and K^0_S vertices that are significantly detached from the B^0 and D^0 vertices respectively will be favoured by the BDT.

To check with the BDT output that there is no overtraining, we require signal and background samples that are independent of those used during the training process. Hence, the $B^0_s \to D\overline{K}^{*0}$ MC sample is used as a signal test sample. For the background test sample, the sideband orthogonal to the one used during the training is taken. That means that for a BDTA, trained on sideband A, the background test sample is the sideband B (and vice-versa). Fig. 5.5 superimposes the distribution of the BDT output for the training and testing samples relative to the four BDTs. All distributions are in good agreement between the training and the testing samples. Therefore there is no evidence of overtraining and the performance of the BDT is considered to be optimal. Moreover the BDT output value is not correlated to the B^0 mass. Fig. 5.6 shows the reconstructed B^0 mass on "wrong sign" candidates as a function of the BDTA output value, and no correlation appears. Wrong sign candidates are non physical candidates of the sort $D^0 \to K^0_S \pi^\pm \pi^\pm$ reconstructed in the data.

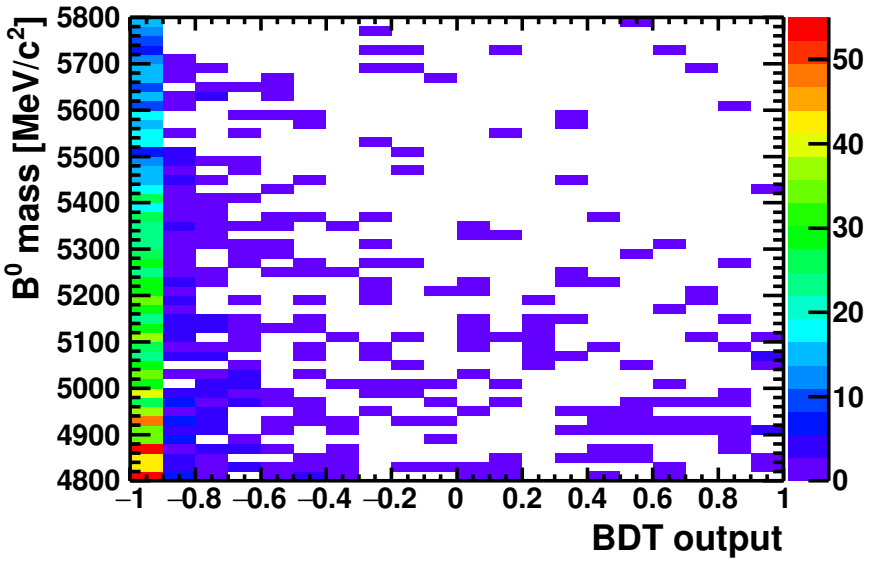

Figure 5.6 – B^0 mass reconstructed with wrong sign candidates as a function of the BDTA output value.

Signal significance and purity estimation

The signal (S) and signal plus background (S+B) yields are estimated to determine the signal sensitivity in the data with this crossed BDT. To estimate S, a rudimentary fit is performed on the full data set after a tight preselection (detailed in Table 5.4) and afterwards a cut is applied on the BDT output. The fit model is composed of a simple gaussian with fixed mean and width for the B_s^0 peak, and an exponential to describe the combinatorial background. Only the range $[4800;4950] \cup [5331;5800]$ MeV is taken into account to be sensitive only to the $B_s^0 \to D\overline{K}^{*0}$ decay and the combinatorial background. Examples of this fit can be seen at Fig. 5.10. This fit determines the B_s^0 yield. The B^0 signal yield S is deduced with a scale factor k, accounting for the relative differences for B^0 and B_s^0 mesons in the branching ratios, the lifetimes and the hadronisation (f_s/f_d):

$$k \equiv \frac{N_{B^0}}{N_{B_s^0}} = \frac{f_d}{f_s} \cdot \frac{\mathscr{B}(B^0 \to \overline{D}^0 K^*)}{\mathscr{B}(B_s^0 \to \overline{D}^0 \overline{K}^*)} \cdot \frac{\tau_{B_s^0}}{\tau_{B^0}} = 0.35 \pm 0.12. \tag{5.10}$$

Note that the $\mathscr{B}$ $(B_s^0 \to \overline{D}^0 \overline{K}^*)$ value used here [145] is not the latest one. With the updated value [20] the scale factor is equal to $k = 0.47 \pm 0.11$ (and is the value to be compared with the ouput of the final mass fit in Sec.5.5). The S+B estimation is simply obtained by counting the numbers of candidates falling in a $\pm 3\sigma$ ($\sigma = 13$ MeV) window around the B^0 mass. With these values three figures of merit (f.o.m.) are computed:

- the significance $S/\sqrt{S+B}$,
- the purity $S/(S+B)$,
- the product of the significance and the purity $S^2/(S+B)^{\frac{3}{2}}$ (called hybrid f.o.m.).

The evolution of the signal significance with an increasing BDT cut is summarised in Fig. 5.7. The similar figures for the purity and the hybrid f.o.m. can be found in Fig. 5.8 and Fig. 5.9

Table 5.4 – Tight preselection applied for signal and background estimation

Particle	Variable	Cut value
K^{*0}	$\mathrm{DLL}_{K\pi}$ (K^+)	> 3
	$\mathrm{DLL}_{K\pi}$ (π^-)	< 3
	$\eta(K^+)$	< 5
	$\eta(\pi^-)$	< 5
	$\lvert m(K^+\pi^-) - m_{PDG}(K^{*0})\rvert$	$< 50\,\mathrm{MeV}$
D^0	$\lvert m(K^0_S\pi^+\pi^-) - m_{PDG}(D^0)\rvert$ with PV and K^0_S mass constraint	$< 30\,\mathrm{MeV}$ (3σ)
K^0_S	$\lvert m(\pi^+\pi^-) - m_{PDG}(K^0_S)\rvert$ with PV and D^0 mass constraint	$< 14.4\,\mathrm{MeV}$ (LL) (3σ)
		$< 19.9\,\mathrm{MeV}$ (DD) (3σ)
$B^\pm \to DK^\pm$ veto	$\lvert m(D^0K^\pm) - m_{PDG}(B^\pm)\rvert$	$> 50\,\mathrm{MeV}$

respectively. These figures each comprise four plots organised as follows: the left and right columns correspond to the application of different BDT to the same data sample A and B respectively. The top and bottom rows correspond to the application of BDT A and B respectively. Two important features can be observed:

1. On the same data sample (plots in the same column) BDTA and BDTB have the same significance. The evolution of the significance *vs.* the BDT cut value applied is identical. With two different BDTs applied on a same sample an identical response is observed. Therefore the crossed BDT is not overtrained. This endorses the conclusion drawn in section 5.2.3.

2. With the same BDT (plots in the same row) applied on the different samples different shapes are observed (especially for the low statistics LL category). However the shapes are fully statistically compatible. For instance if we focus on the worst case of BDTA_LL (dashed line in the top row plots) with a cut at 0.7, we measure for sample A

$$S = 21 \pm 3 \qquad S+B = 48 \pm 7 \qquad S/\sqrt{S+B} = 3.0 \pm 0.4 \qquad S/(S+B) = 0.44 \pm 0.06 \qquad S^2/(S+B)^{\frac{3}{2}} = 1.3 \pm 0.3,$$

and for sample B:

$$S = 14 \pm 3 \qquad S+B = 50 \pm 7 \qquad S/\sqrt{S+B} = 2.0 \pm 0.4 \qquad S/(S+B) = 0.28 \pm 0.05 \qquad S^2/(S+B)^{\frac{3}{2}} = 0.6 \pm 0.2.$$

Hence the statistical fluctuations between samples A and B induce different f.o.m. shapes for a same BDT. But the discrepancy is not significant. Fig. 5.10 shows the fit result with no BDT cut, and with a BDT cut at 0.7, with the same BDTA_LL on samples A and B. The difference in S and B is already visible before cutting on the BDT.

To conclude, BDTA and BDTB are not overtrained and perform alike on the same data sample. Given that a Dalitz plot analysis is not directly sensitive to the signal significance, but more to the background contamination, a preliminary working point at 0.7 was chosen for all the four BDTs. It appeared as a good compromise between a good signal significance and a good purity. Ultimately the selection working point is fixed at 0.75 with the sensitivity study on the cartesian parameters based on pseudo experiments (see Sec. **??**).

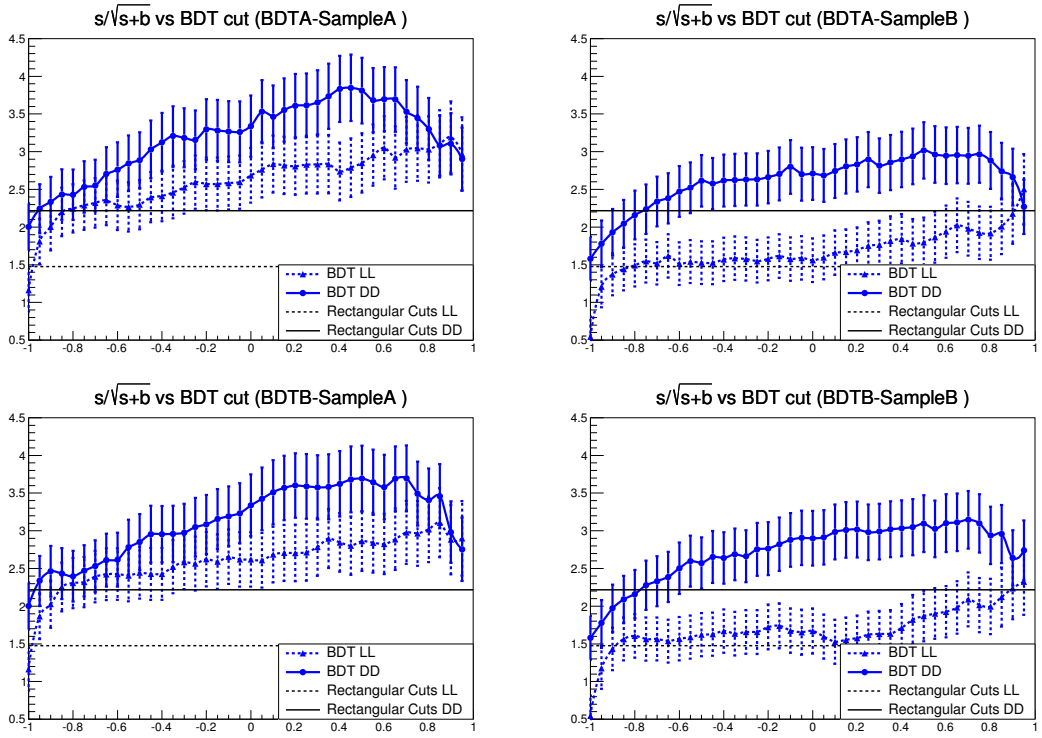

Figure 5.7 – Estimation of the signal significance for several BDT cut values, with BDTA (top plots) and BDTB (bottom plots), data sample A (left column) and data sample B (right column). DD candidates are in solid lines, whereas LL candidates are in dashed lines. The straight black lines represents the significance obtained with a rectangular cuts selection developed at the early stage of the analysis.

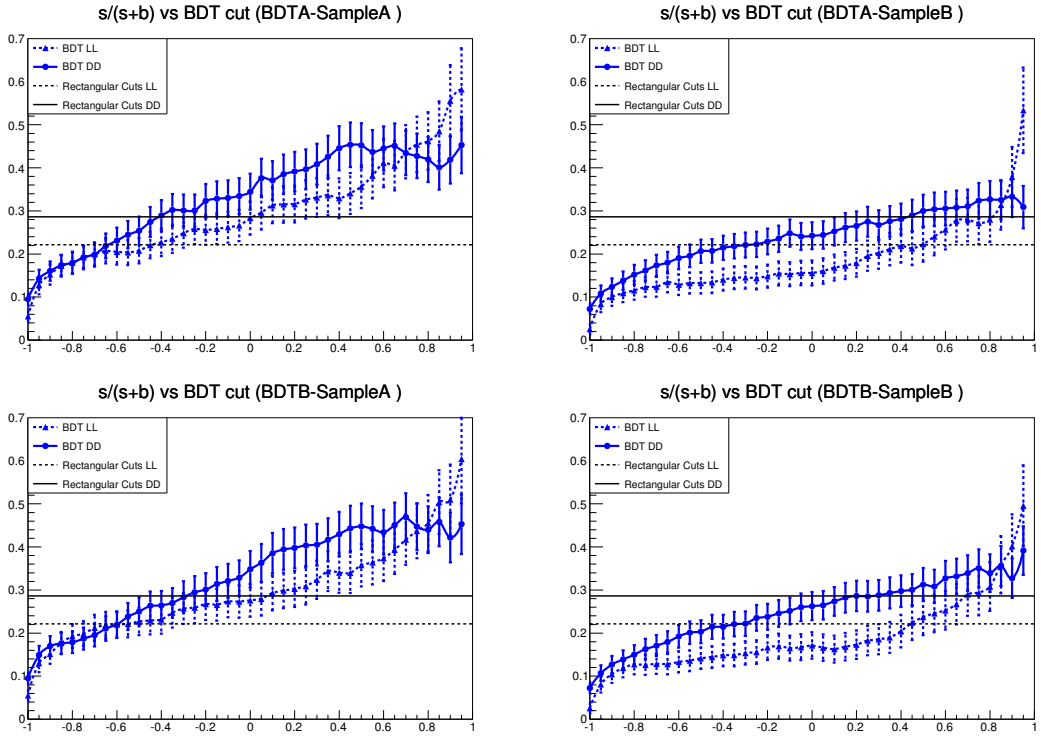

Figure 5.8 – Estimation of the signal purity for several BDT cut values, with BDTA (top plots) and BDTB (bottom plots), data sample A (left column) and data sample B (right column). DD candidates are in solid lines, whereas LL candidates are in dashed lines. The straight black lines represents the purity obtained with a rectangular cuts selection developed at the early stage of the analysis.

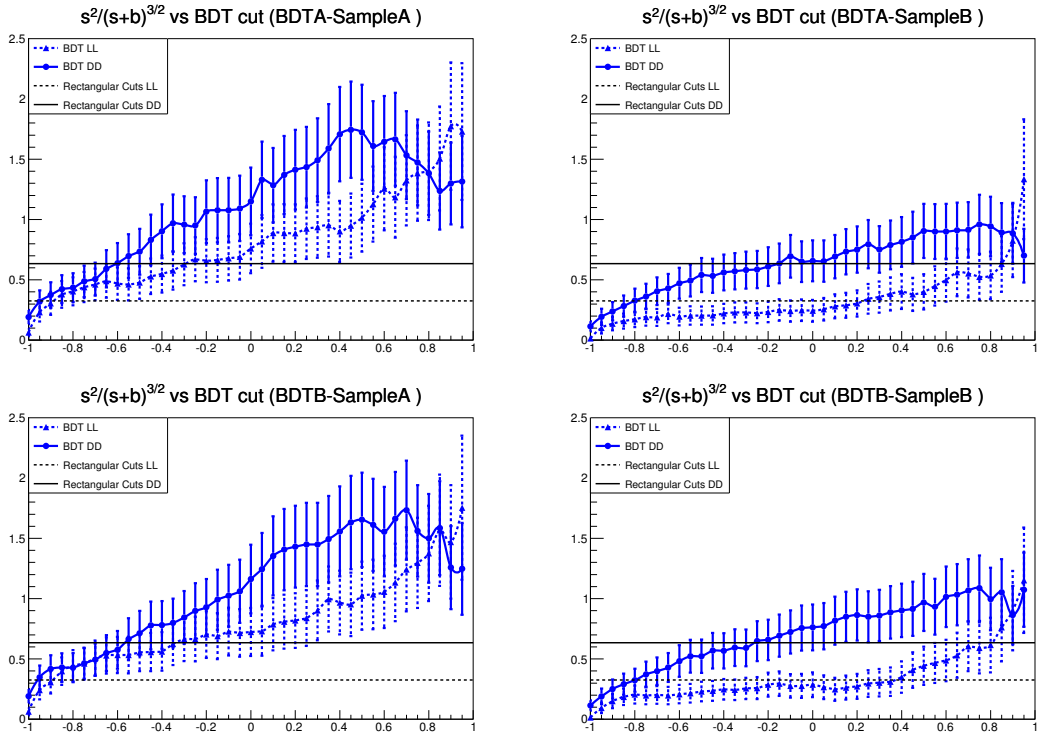

Figure 5.9 – Estimation of the hybrid f.o.m. for several BDT cut values, with BDTA (top plots) and BDTB (bottom plots), data sample A (left column) and data sample B (right column). DD candidates are in solid lines, whereas LL candidates are in dashed lines. The straight black lines represents the hybrid fom obtained with a rectangular cuts selection developed at the early stage of the analysis.

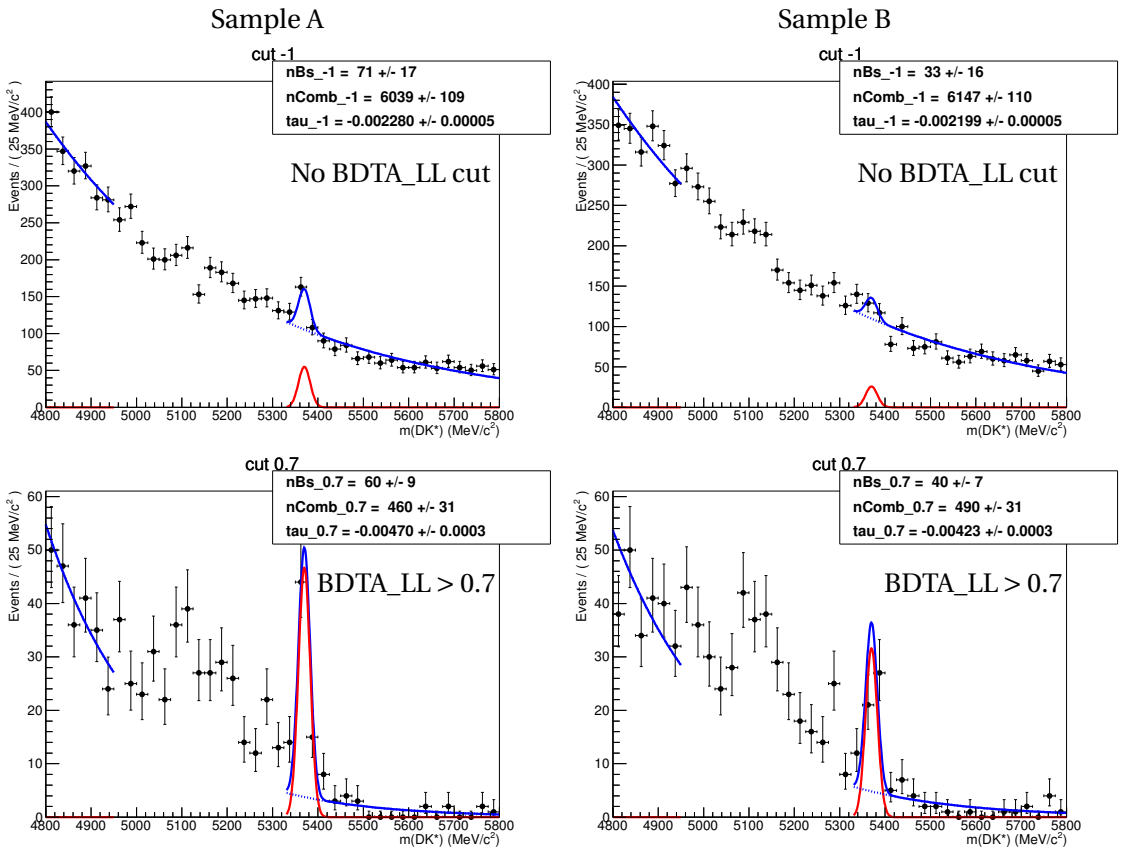

Figure 5.10 – B_s^0 yield estimation with no BDT cut (top plots) and with a BDTA_LL cut at 0.7 (bottom plots). Left (right) column corresponds to the data sample A (B).

Summary of the selection

The full selection consists of:

- the stripping and trigger requirements defined in Sec. 5.2.1,
- the tight preselection detailed on Table 5.4,
- an extra PID cut on the K^+ daughter of the K^{*0} to remove more $B^0 \to D\rho^0$ background: $\mathrm{DLL}_{K\pi}(K^\pm) > 5$ (see Sec. 5.5.6 for the cut value justification),
- a BDT cut at 0.75 (determined by the sensitivity study explained in Sec. 5.7.4),
- a cut on the cosine of the $K^*(892)^0$ helicity angle $|\cos\theta^*| > 0.4$.

Even if the K^{*0} helicity angle is one of the BDT discriminating variables, the extra cut at 0.4 is applied to improve the purity by rejecting specifically the partially reconstructed background $B^0_{(s)} \to D^{*0}K^{*0}$ in helicity states 001 and 100 (see Sec.5.5.2). This is because the 001 and 100 helicity components have a θ^* angular distribution proportional to $\sin^2\theta^*$, whereas the signal follows a $\cos^2\theta^*$ distribution. On top of all the other cuts, the extra $\cos\theta^*$ cut has a signal efficiency of 93% for a background efficiency on $B^0_{(s)} \to D^{*0}K^{*0}$ 001 and 100 of 45%. It is particularly interesting to remove these helicity contributions since they are those which leak the most under the signal peak (see Sec.5.5.2). Furthermore, the BDT is trained on the upper B^0 mass sideband, which has a flat distribution with respect to $\cos\theta^*$. Therefore it cannot efficiently remove this specific background.

5.2.4 Study of the charmless background

To ensure that after the BDT selection there is no contamination from charmless background, that do no have D meson in the final state, the D^0 mass sidebands (Fig. 5.11a) are checked. Such background does not peak in the D^0 mass distribution, but does peak in the B^0 mass distribution. Even if the BDT contains a cut on the χ^2/ndf of the decay chain refit with a D^0 mass constraint, it is safe to look at the D^0 sidebands after a BDT cut. As shown later in Sec. 5.5.7, dedicated to the combinatorial D^0 background study, the D^0 mass distribution of wrong sign D^0 candidates ($D^0 \to K^0_S\pi^\pm\pi^\pm$) is flat even if a BDT cut is applied (Fig. 5.50).

The full selection described in Sec. 5.2.3 is applied, except the D^0 mass window. Fig. 5.11 represents the B^0 invariant mass of these D^0 sidebands candidates, after this selection and with or without an additional cuts on the D^0 flight distance significance (defined by Eq. (5.9)). Although the D^0 sidebands statistics is low, no peaking structure can be observed in the B^0 and B^0_s mass region, even without a cut on the D^0 flight distance. Moreover with a looser BDT cut (at 0.4) no peak appears neither. Hence it can be safely deduced that after the BDT cut, any charmless background contribution is negligible.

Another a posteriori crosscheck confirms this statement with the sWeighted distribution of the D flight distance significance (Fig. 5.85), made for the Data/MC comparison in Sec. 5.8.3. No peak appears at low D flight distance significance in the data, compared to the distribution expected from simulation.

5.2.5 Study of the $D^0 \to \pi\pi\pi\pi$ background

Another possible background source which has been observed in the $B^\pm \to DK^\pm$ analysis is the $D^0 \to \pi\pi\pi\pi$ decay. It can only occur for the LL candidates, where two pions can fake a K^0_S. This

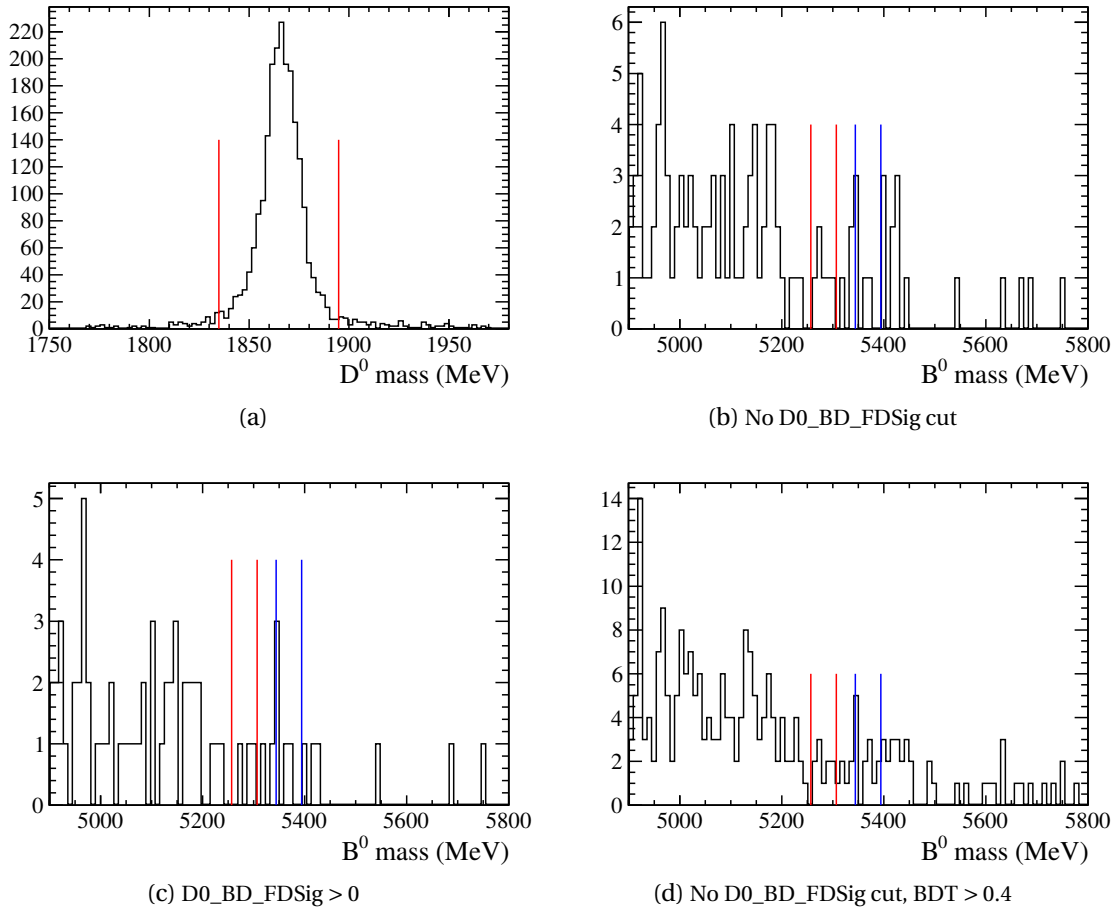

(a)

(b) No D0_BD_FDSig cut

(c) D0_BD_FDSig > 0

(d) No D0_BD_FDSig cut, BDT > 0.4

Figure 5.11 – (a) D^0 invariant mass distribution on data after full selection (except for the D^0 mass window). The red lines represent the cuts applied to obtain the D^0 mass sidebands. (b) B^0 invariant mass in data D^0 sidebands, after full selection except the D^0 mass window, with an additional cut on the D^0 flight distance significance (c), and with a looser BDT cut at 0.4 (d). The red (blue) lines delimit the B^0 (B_s^0) regions.

background peaks in both D^0 and B^0 mass distributions. Here the variable which can suppress this background is the K_S^0 flight distance, defined in Eq. (5.8), which is included in the BDT. To ensure that this contribution is negligible the K_S^0 sidebands are studied for LL candidates (Fig. 5.12a). The full selection is applied, except for the K_S^0 mass window. Fig. 5.12 represents the B^0 mass distributions for candidates lying in the K_S^0 sidebands, after the full selection, with an additional cut on the K_S^0 flight distance significance and with a very looser BDT cut. After the full selection, the K_S^0 sidebands contain few events. If a cut on the flight distance significance of the K_S^0 is applied in addition, there is not a strong depletion. Hence, this does not suggest there is a contamination from $D^0 \to \pi\pi\pi\pi$ events. Moreover, if the BDT cut is set to a very loose value compared to the nominal selection (0 instead of 0.75), no significant peak appears in the B^0 or B_s^0 region. A systematic effect is estimated when an additional cut is applied on the K_S^0 flight distance significance of LL candidates (see Sec. 5.8.1).

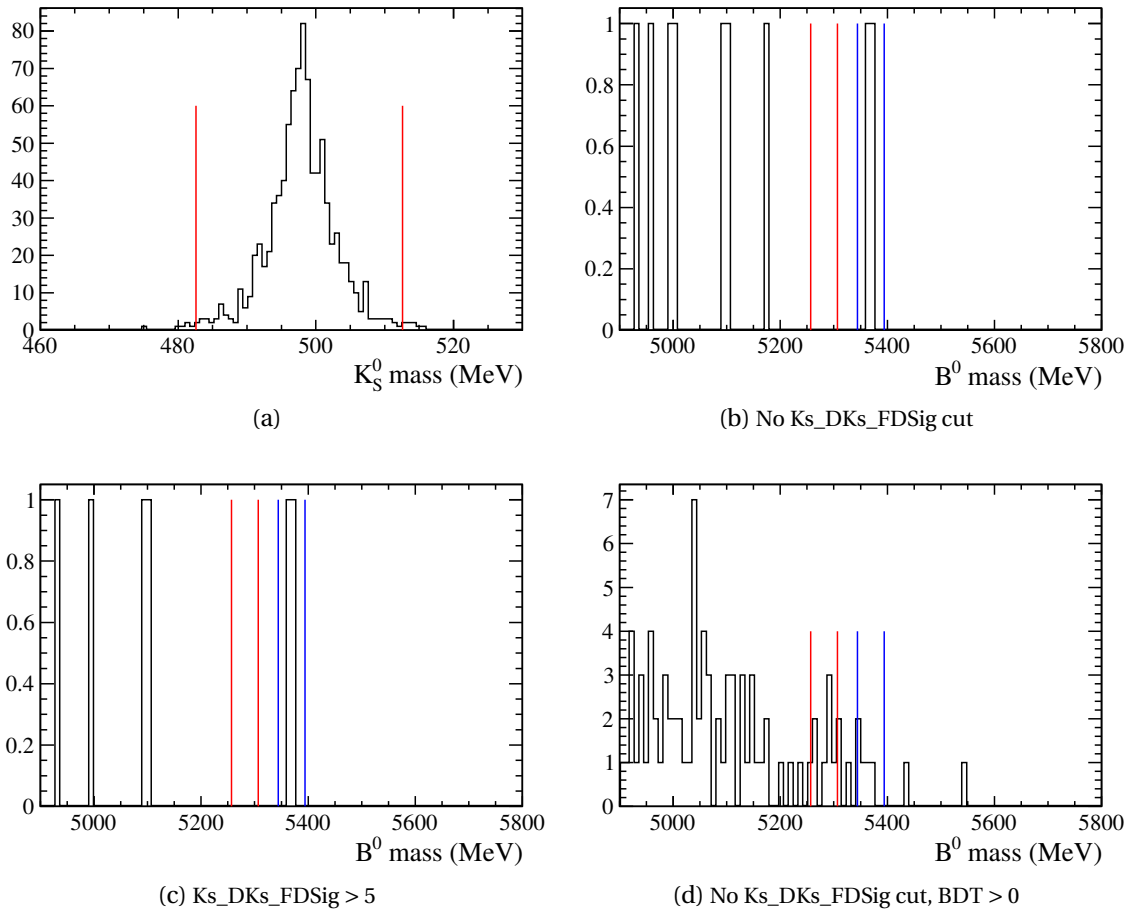

(a)

(b) No Ks_DKs_FDSig cut

(c) Ks_DKs_FDSig > 5

(d) No Ks_DKs_FDSig cut, BDT > 0

Figure 5.12 – (a) K^0_S invariant mass distribution on data after full selection (except for the K^0_S mass window). The red lines represent the cuts applied to obtain the K^0_S mass sidebands. (b) B^0 invariant mass in data K^0_S sidebands, after full selection (except the K^0_S mass window) with an additional cut on the K^0_S flight distance significance (c), and with a looser BDT cut at 0 (d). The red (blue) lines delimit the B^0 (B^0_s) regions.

5.3 Efficiency across the D^0 Dalitz plane

A key point of the analysis is the knowledge the selection efficiency across the Dalitz plane. A variation of the efficiency across the Dalitz plane artificially distorts the distribution. Hence it can produce a bias on the *CP* violation parameters determination. That is why the description of the efficiency must be taken into account in the Dalitz fit. This description can be obtained through two methods.

It can be fitted directly on data, taking the $B_s^0 \to D\overline{K}^{*0}$ decay as a control sample. The drawbacks of this method are the limited statistics available (around 200 $B_s^0 \to D\overline{K}^{*0}$ events) and the assumption of no *CP* violation in this control channel. An alternative control sample could be the $B^\pm \to D\pi^\pm$ decay, analogue of the $B_s^0 \to D\overline{K}^{*0}$ decay for the $B^\pm \to DK^\pm$ transition. In this case the statistics available would be much larger. However, the relation between the $B^\pm \to D\pi^\pm$ and the $B^0 \to DK^{*0}$ efficiencies is not direct and needs some input from simulation.

The description of the efficiency can be also obtained directly from $B^0 \to DK^{*0}$ simulated data. In this case, particular attention must be paid to the data/MC agreement. The efficiency can be expressed as

$$\varepsilon^{TT}(m_-^2, m_+^2) = \varepsilon_{\text{acc}}\, \varepsilon_{\text{gen}}\, \varepsilon_{\text{rec}}^{TT}\, \varepsilon_{\text{strip}}^{TT}\, \varepsilon_{\text{sel}}^{TT}\, \varepsilon_{\text{trig}}^{TT}\, \varepsilon_{\text{PID}}^{TT}, \tag{5.11}$$

where ε_{acc} is the detector geometrical acceptance, ε_{gen} the generator level cuts efficiency (see Appendix A), ε_{rec} the reconstruction efficiency, $\varepsilon_{\text{strip}}$ the stripping efficiency, ε_{sel} the offline selection efficiency (excluding the PID selection and the trigger requirements), $\varepsilon_{\text{trig}}$ the trigger efficiency (after the offline selection) and ε_{PID} the efficiency of the PID selection (on top of all the other selection criteria). It should be noticed that the reconstruction splits the candidates in two non overlapping categories, depending on the Track Type (TT) of the reconstructed K_S^0 (LL or DD). That is why LL and DD efficiencies are computed separately, especially as the offline selection is different for the two categories.

This section presents the efficiency of the selection obtained with the MC-based method. The $B_s^0 \to D\overline{K}^{*0}$ MC sample is particularly useful since it has high statistics (one million events after stripping), whereas the $B^0 \to DK^{*0}$ sample was not generated with a stripping filtering [3]. This means that the statistics available after selection with the $B_s^0 \to D\overline{K}^{*0}$ sample is more than twice the $B^0 \to DK^{*0}$ sample one. It has also been checked that the efficiency profile obtained with the $B^0 \to DK^{*0}$ sample is in good agreement with the profile obtained with the $B_s^0 \to D\overline{K}^{*0}$ sample.

The events were generated with a phase-space (PHSP) model. Therefore the Dalitz plot of the selected candidates gives directly the relative efficiency variation across the Dalitz plane (we do not care about the absolute efficiency value). The PID and trigger selections are not well reproduced in the simulation. That is why the Dalitz plot after full selection except any PID cuts and trigger requirements is made. To include the effect of the PID and trigger selection some data-driven correction weights are applied (see Sec. 5.3.1 and Sec. 5.3.2). The Dalitz plot of LL and DD candidates passing the stripping (Fig. 5.13) illustrates the effect of the geometrical acceptance, the reconstruction and the stripping. This effect is sizeable and is the main source of distortion as it will be seen later. Throughout the study presented in this section the simulated candidates are truth matched.

[3] A simulated sample can be stripping filtered. In this case only the generated events passing the stripping selection are stored. It enables to produce samples with a large statistics, without taking an unreasonable disk space.

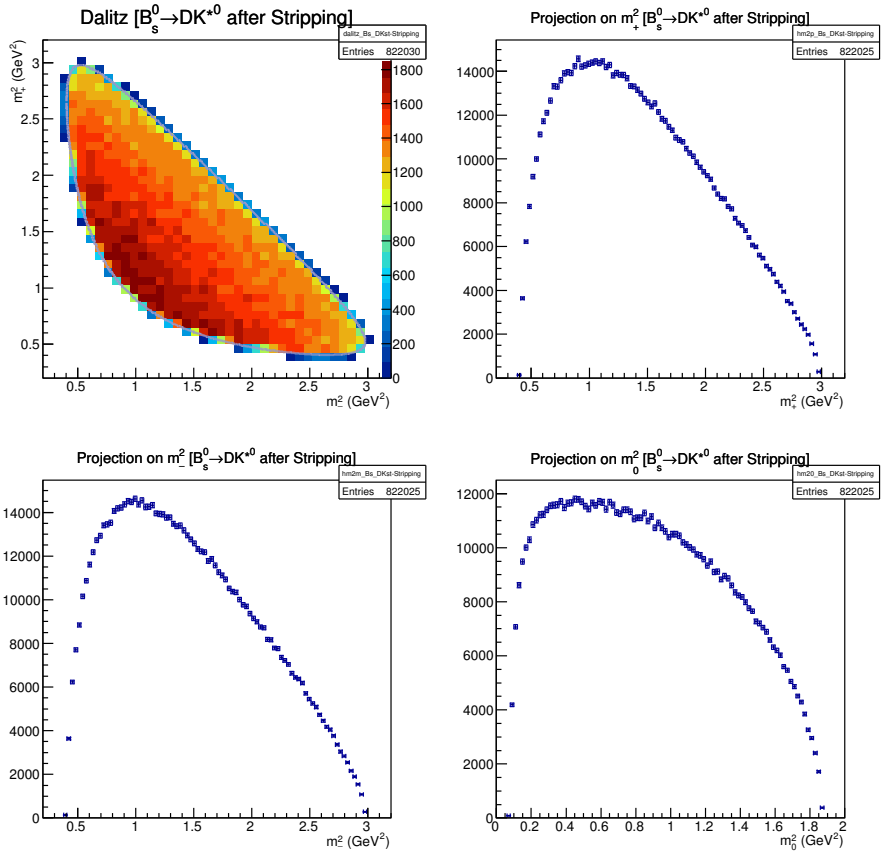

Figure 5.13 – Dalitz plot and its projections of simulated $B^0_s \to D\overline{K}^{*0}$ candidates after stripping selection. The generation model is phase space and LL and DD categories are merged.

5.3.1 Trigger weights

As shown in [146, 147], the simulation does not reproduce well the L0 trigger efficiency. That is why a reweighting is applied on the $B^0_s \to D\overline{K}^{*0}$ candidates in simulation passing the full selection without any PID and trigger requirement. This reweighting is deduced from look-up tables which give for several bins of transverse energy the probability that an individual track (a kaon or a pion in the present case) can be `L0HadronTOS` [4]. These efficiencies are obtained from well identified pions and kaons, daughters of D^0 mesons, coming themselves from D^{*+} decays. From this invidual track weights, an event weight is computed assuming no correlation between the tracks. Then the L0 correction weights for the Dalitz plot are obtained by averaging the event weights in each Dalitz plot bin.

As explained in Sec. 5.2.1 two categories of events must be distinguished: TOS and NotTOS. The L0 look-up tables give directly the TOS efficiency ε_{TOS}. The NotTOS efficiency is determined by taking the `L0GlobalTIS` events (according to the MC) and computing from the tables the probability not to be TOS, $1-\varepsilon_{\text{TOS}}$. Since the `L0Hadron` threshold was different in 2011 and 2012 the efficiency is computed for each year and then combined according to the recorded

[4] See Sec. 3.2.6 of Chap. 3 for a description of the L0Hadron and TOS categories

luminosity fractions:

$$\varepsilon_{\rm TOS} = \frac{\mathscr{L}_{2011}}{\mathscr{L}_{2011}+\mathscr{L}_{2012}}\varepsilon^{2011}_{\rm TOS} + \frac{\mathscr{L}_{2012}}{\mathscr{L}_{2011}+\mathscr{L}_{2012}}\varepsilon^{2012}_{\rm TOS}. \tag{5.12}$$

The TOS efficiency combining the 2011 and 2012 years is shown on Fig. 5.14 and 5.15. Since it is easier to fire the trigger with one $\pi^{\pm}$ track of high $p_{\rm T}$ than with two π^+ and π^- tracks with intermediate $p_{\rm T}$, a better trigger efficiency is observed in the top left and bottom right corner of the Dalitz plot. However the effect is very small. The NotTOS efficiency combining the 2011 and 2012 years is shown on Fig. 5.16 and 5.17. The feature complementary to the TOS efficiency can be observed, also with a small amplitude. A signal candidate fails more easily to fire the trigger (*i.e.* cannot be TOS) if the two pions have intermediate $p_{\rm T}$, rather than if one pion has a high $p_{\rm T}$. Therefore the NotTOS efficiency is larger at the Dalitz plot centre compared to the corners. The TOS and NotTOS efficiency are then combined according to the fractions found in the selected data candidates:

$$\varepsilon_{\rm L0} = f_{\rm TOS}\varepsilon_{\rm TOS} + (1-f_{\rm TOS})\varepsilon_{\rm NotTOS} \tag{5.13}$$

In the B^0 signal region, a total of 95 TOS candidates are selected for 46 NotTOS candidates (including signal and background). This combination is represented on Fig. 5.18 and 5.19. These are the correction weights used to account for the trigger effect on the Dalitz plot.

Two sources of uncertainties must be evaluated for this reweighting procedure: the *calibration* and the *reference* uncertainties. The calibration uncertainty is the uncertainty related to the size of the sample used to calibrate the data. The reference uncertainty is the uncertainty arising from the size of the $B^0_s \to D\overline{K}^{*0}$ reference sample. Hence the total uncertainty is expressed as

$$\sigma_i^{\rm tot} = \sigma_i^{\rm calib} \oplus \sigma_i^{\rm ref}. \tag{5.14}$$

The individual track calibration weights have an uncertainty which depends on the calibration data sample size. To propagate this uncertainty to the correction weights on the Dalitz plane, one thousand alternative efficiency tables are randomly generated (according to the efficiency errors given by the nominal look-up tables). The correction weights on the Dalitz plot are smeared according to the calibration uncertainty and all the tracks falling in the same bin in $p_{\rm T}$ have the same efficiency for a given alternative table. These one thousand alternative tables make one thousand alternative trigger efficiency Dalitz plots.

Then the uncertainty due to the limited statistics of the $B^0_s \to D\overline{K}^{*0}$ reference sample must be propagated. That is why the alternative Dalitz plot are smeared once more according to the weighted Poisson fluctuation, which is equal to the square root of the sum of the squared weights (computed in each bin i of the nominal dalitz plot)

$$\sigma_i^{\rm ref} = \sqrt{\sum_{k=1}^{N_i} \varepsilon_k^2}, \tag{5.15}$$

where N_i is the number of $B^0_s \to D\overline{K}^{*0}$ candidates in the bin i and ε_k the candidate trigger efficiency. After this smearing the one thousand alternative trigger efficiency Dalitz plots include the effect of the calibration uncertainty and the statistical uncertainty of the reference sample. These alternative efficiency Dalitz plots are used to determine the systematic uncertainty arising from the efficiency description (see Sec. 5.8.3).

The High Level Trigger (HLT) efficiency across the Dalitz plane is studied directly from the simulated $B^0_s \to D\overline{K}^{*0}$ sample. It is expected that the HLT has a small impact on the Dalitz

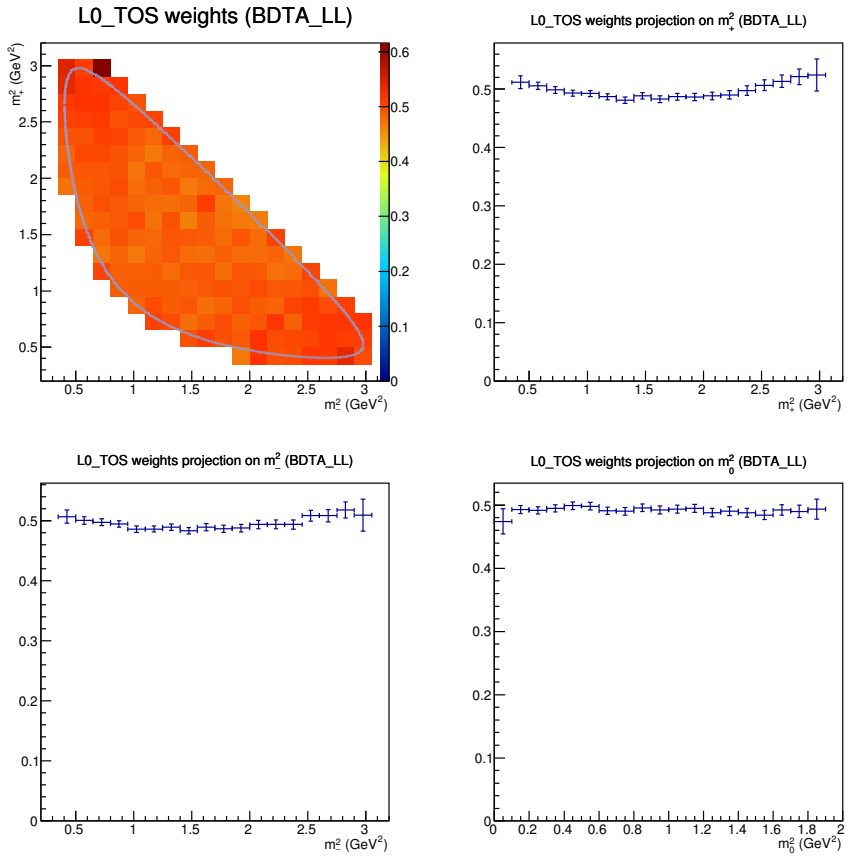

Figure 5.14 – L0 Hadron TOS efficiency weights over the Dalitz plane and their projections for simulated $B_s^0 \to D\overline{K}^{*0}$ LL candidates, selected with BDTA.

distribution, since the overall HLT efficiency on top of the full selection is larger than 97%. The effect of applying the HLT requirements on top of the full selection is shown in Fig. 5.20. It corresponds to the Dalitz plots ratio between events passing the full selection, HLT requirements included, and events passing the selection without applying the HLT requirements. It can be seen that the HLT efficiency is completely uniform across the Dalitz plane. Therefore it is decided to not apply the HLT requirements on the MC sample to estimate the total selection efficiency. A systematic uncertainty derived from this choice is determined (see 5.8.3).

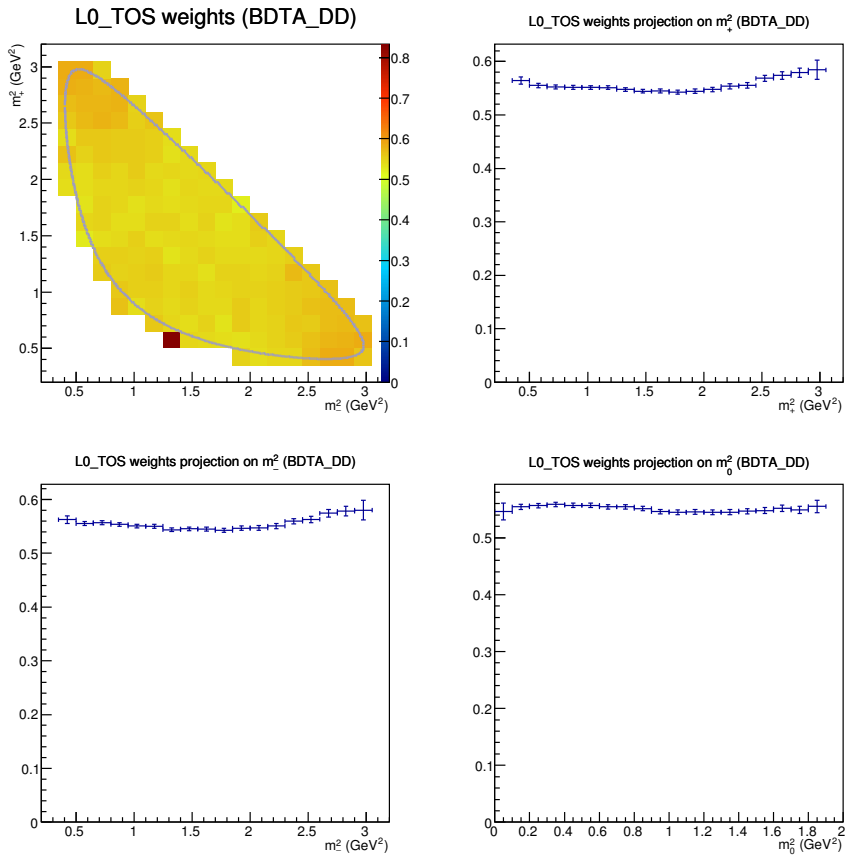

Figure 5.15 – L0 Hadron TOS efficiency weights over the Dalitz plane and their projections for simulated $B^0_s \to D\overline{K}^{*0}$ DD candidates, selected with BDTA.

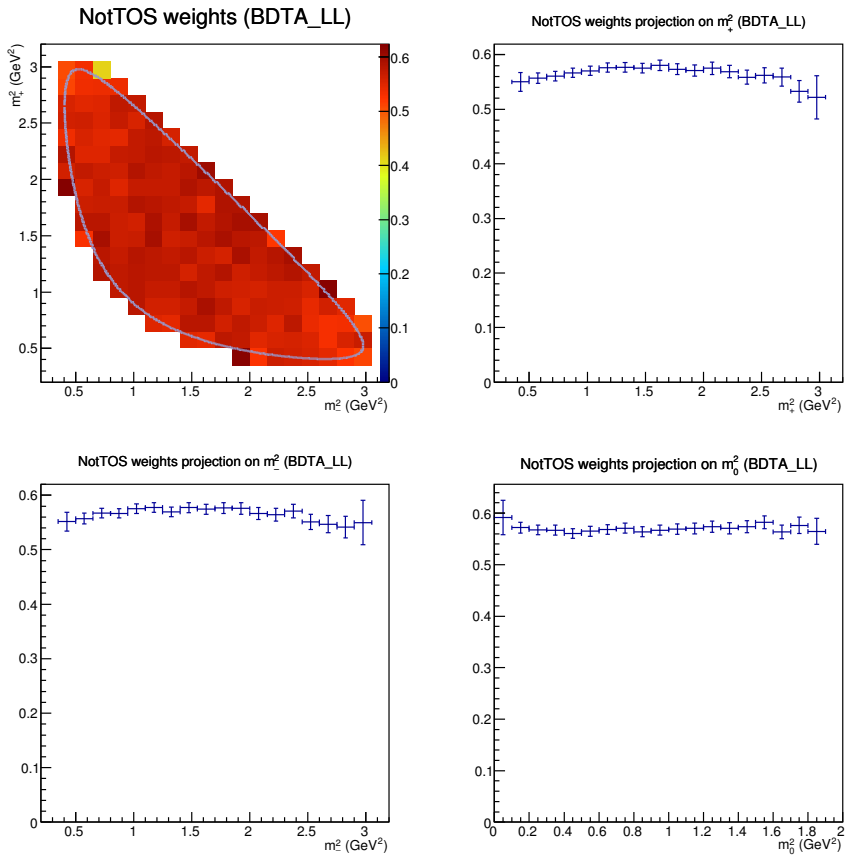

Figure 5.16 – L0 Hadron NotTOS efficiency weights over the Dalitz plane and their projections for simulated $B_s^0 \to D\overline{K}^{*0}$ LL candidates, selected with BDTA.

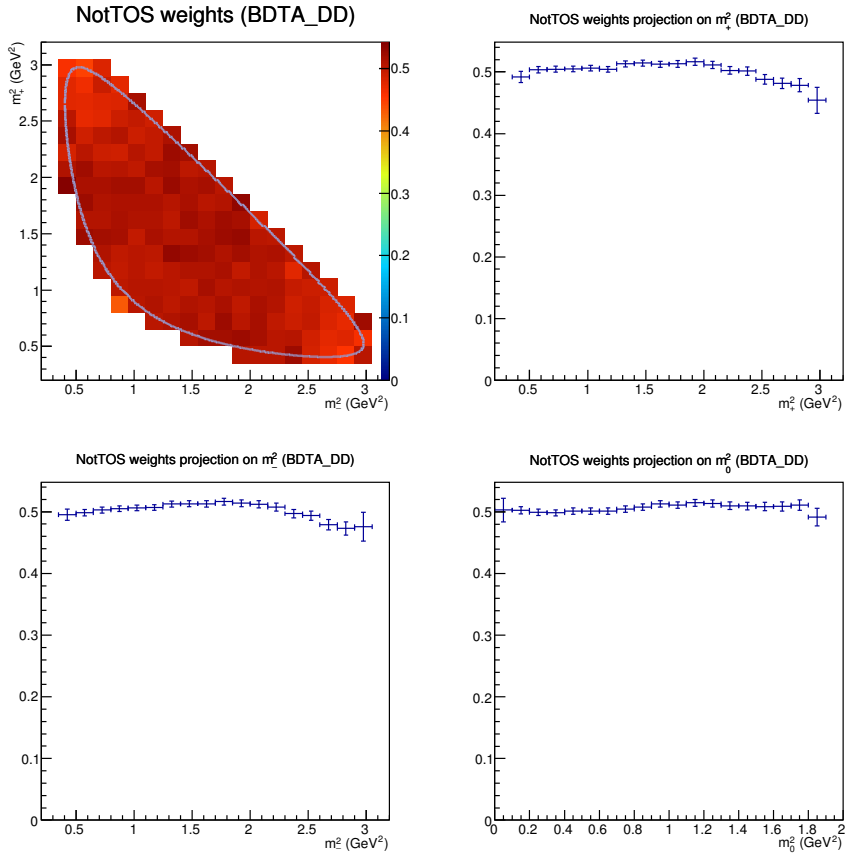

Figure 5.17 – L0 Hadron NotTOS efficiency weights over the Dalitz plane and their projections for simulated $B^0_s \to D\overline{K}^{*0}$ DD candidates, selected with BDTA.

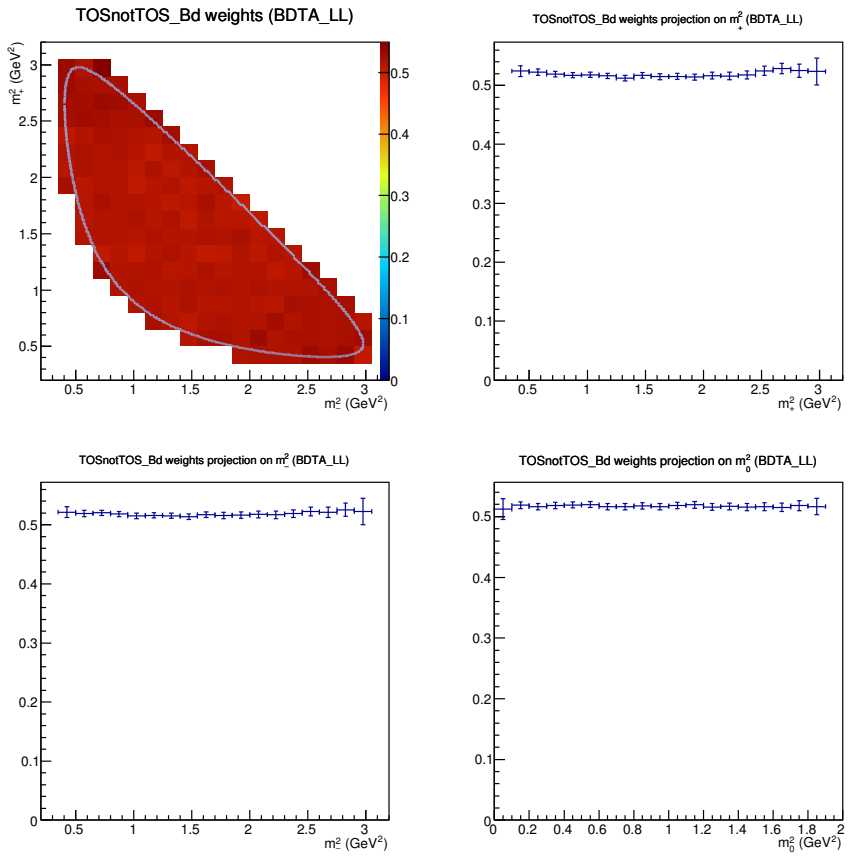

Figure 5.18 – Combined L0 Hadron TOS and NotTOS efficiency weights over the Dalitz plane and their projections for simulated $B_s^0 \to D\overline{K}^{*0}$ LL candidates, selected with BDTA.

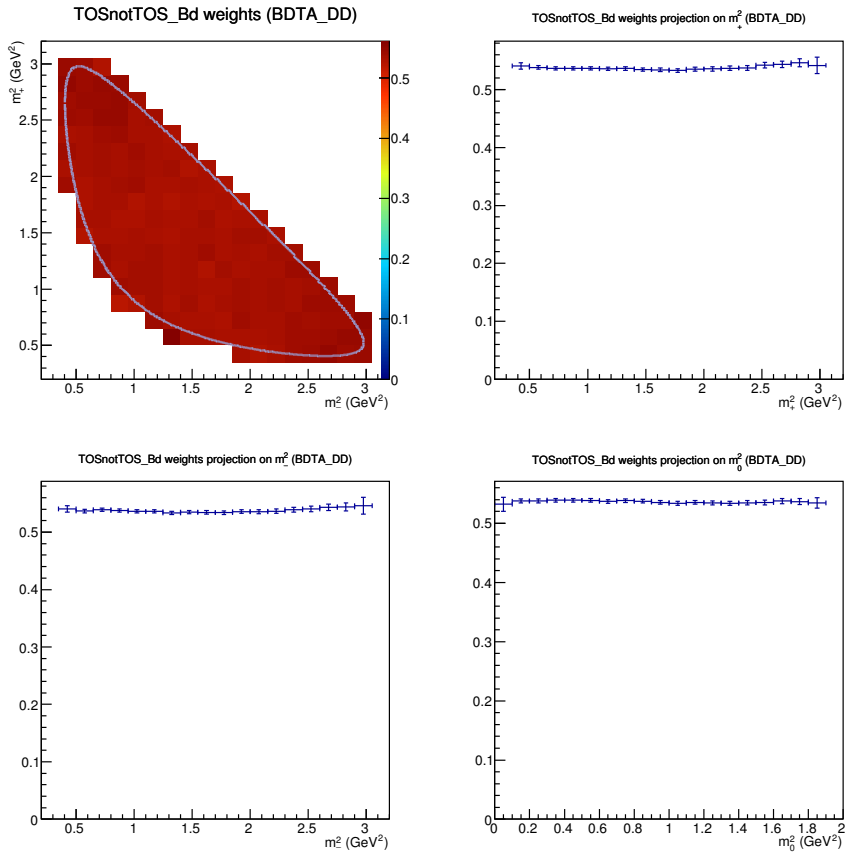

Figure 5.19 – Combined L0 Hadron TOS and NotTOS efficiency weights over the Dalitz plane and their projections for simulated $B_s^0 \to D\overline{K}^{*0}$ DD candidates, selected with BDTA.

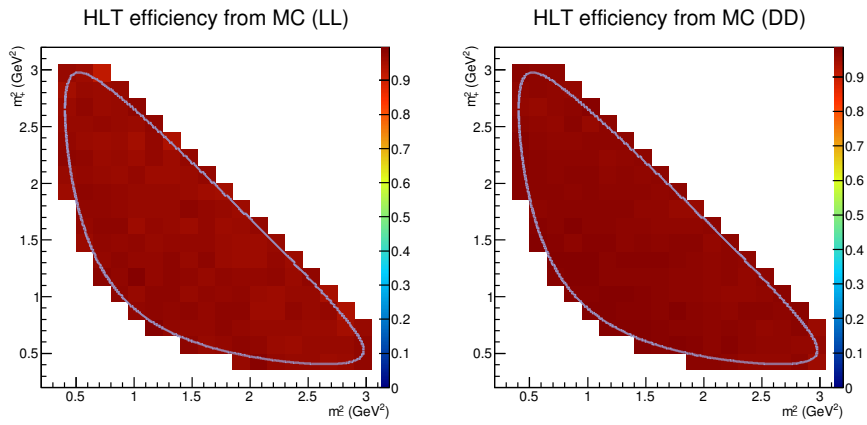

Figure 5.20 – High Level Trigger efficiency over the Dalitz plane for simulated $B_s^0 \to D\overline{K}^{*0}$ LL (left) and DD (right) candidates, selected with BDTA.

5.3.2 PID weights

In the selection there are two PID requirements on the K^{*0} daughters with $\mathrm{DLL}_{K\pi}(K^+) > 5$ and $\mathrm{DLL}_{K\pi}(\pi^-) < 3$. The simulation is known to not reproduce well the DLL distributions. Therefore the PID selection efficiency cannot directly be evaluated on the simulated samples. The LHCb collaboration has developed a common tool providing PID efficiency reference tables for a given set of cuts on the DLL variables. These calibration tables are made from $D^{*+} \to D^0(K^-\pi^+)\pi^+$ decays found in the data with a high statistics and purity. In this decay, the flavour of the D^0 meson is unambiguously determined from the charge of the excited D^{*+} meson. Thus, the kaons and the pions can be distinguished only by their charge, and especially without cutting on PID variables. Therefore, the correct DLL distributions for kaons and pions can be obtained directly on data.

The efficiency of a cut on $\mathrm{DLL}_{K\pi}$ is assumed to depend on a small set of kinematic variables, in the present case, the momentum p and the pseudorapidity η. Indeed, it is found on simulation that the RICH performance has the strongest dependence on these two variables. Hence, the efficiency of the PID cuts applied on the $B^0 \to DK^{*0}$ signal is obtained from the following procedure:

1. two dimensional efficiency histograms corresponding to the $\mathrm{DLL}_{K\pi}(K^+) > 5$ and $\mathrm{DLL}_{K\pi}(\pi^-) < 3$ cuts are computed in a given binning in p and η, making use of the $D^{*+} \to D^0(K^-\pi^+)\pi^+$ calibration sample,

2. this calibration is applied to the $B^0_s \to D\overline{K}^{*0}$ simulated reference sample, with an efficiency weight assigned to each individual $B^0_s \to D\overline{K}^{*0}$ event, depending on its (p,η) bin.

The calibration is applied to the $B^0_s \to D\overline{K}^{*0}$ reference sample after full selection except the PID cuts, but with the trigger requirements imposed. After the calibration every candidates has an individual weight corresponding to its PID efficiency. Consequently, a plot of the PID efficiency over the Dalitz plot can be obtained with the same binning scheme as the trigger efficiency. It should be noticed that only the year 2012 is considered, to agree with the simulation condition used for the $B^0_s \to D\overline{K}^{*0}$ sample. Fig. 5.21 and 5.22 show the PID efficiency computed with the data-driven calibration for LL and DD events. The distribution of this efficiency is flat. This is expected because the PID cuts are on the K^{*0} daughters and have no effect on the D daughters.

The uncertainty on the efficiency is estimated in the same way as the trigger efficiency. From the nominal calibration histograms in bin of (p,η) one thousand alternative histograms are generated. When the PID efficiency is evaluated in a given (p,η) bin from the calibration sample, its uncertainty is also determined. Therefore, the alternative calibration histograms are made by smearing the nominal histogram with the corresponding calibration uncertainty. These alternative histograms make in total one thousand alternative plots of the PID efficiency over the Dalitz plot. They include the efficiency fluctuations due to the uncertainty on the calibration weight. Then the statistical uncertainty coming from the size of the reference sample is also propagated by smearing with the Poisson fluctuation as described in Eq. 5.15.

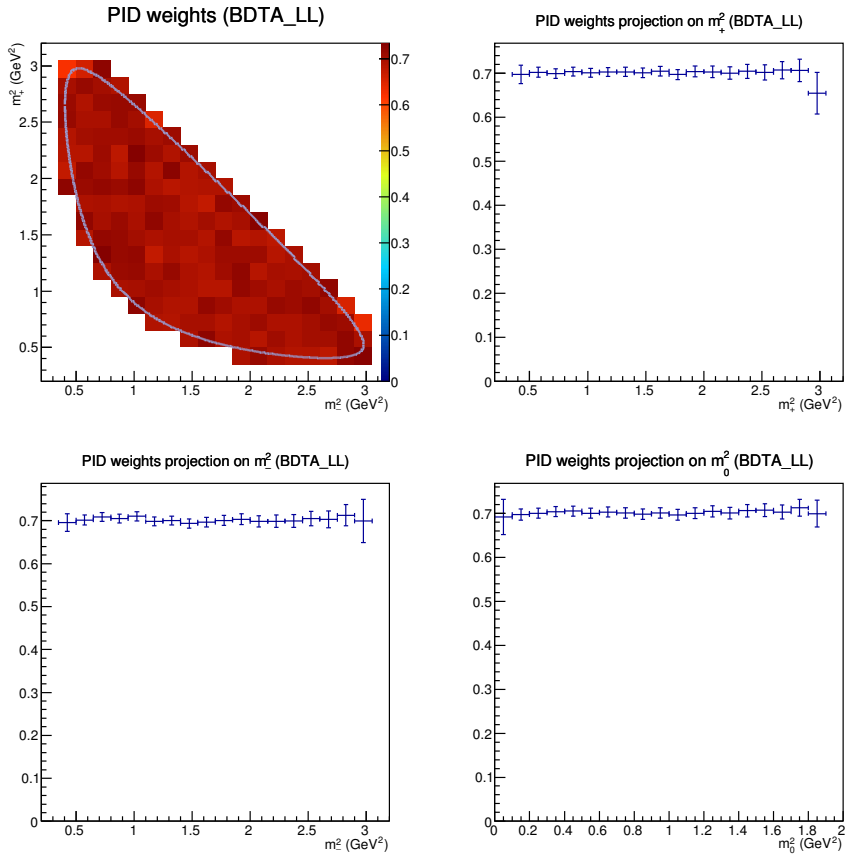

Figure 5.21 – PID efficiency weights over the Dalitz plane and their projections for simulated $B^0_s \to D\overline{K}^{*0}$ LL candidates, selected with BDTA.

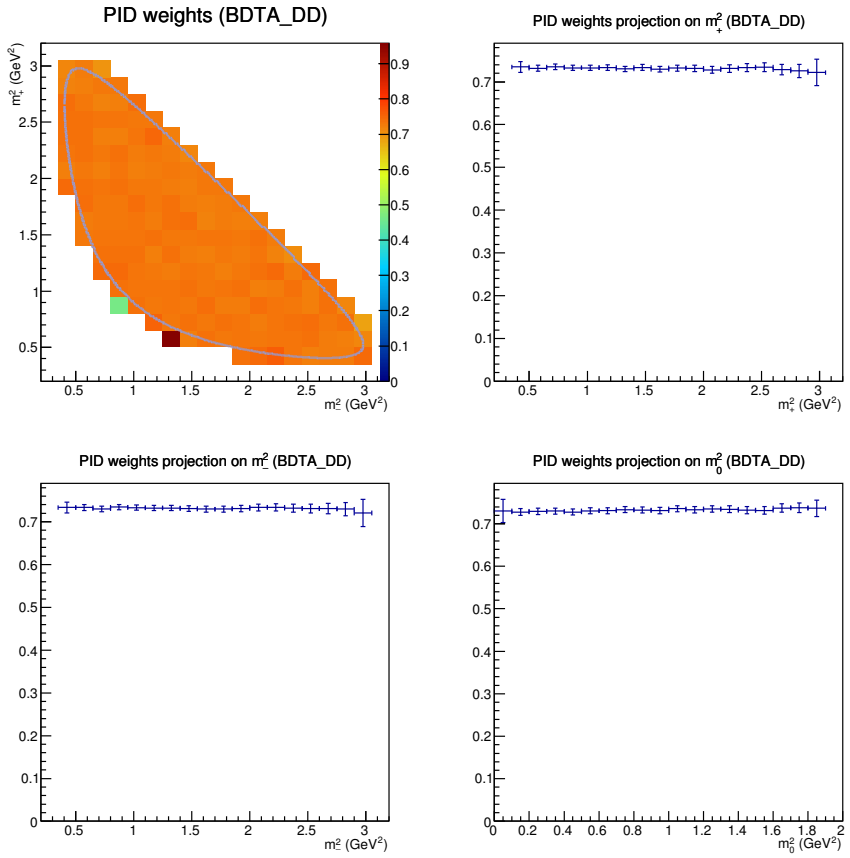

Figure 5.22 – PID efficiency weights over the Dalitz plane and their projections for simulated $B_s^0 \to D\overline{K}^{*0}$ DD candidates, selected with BDTA.

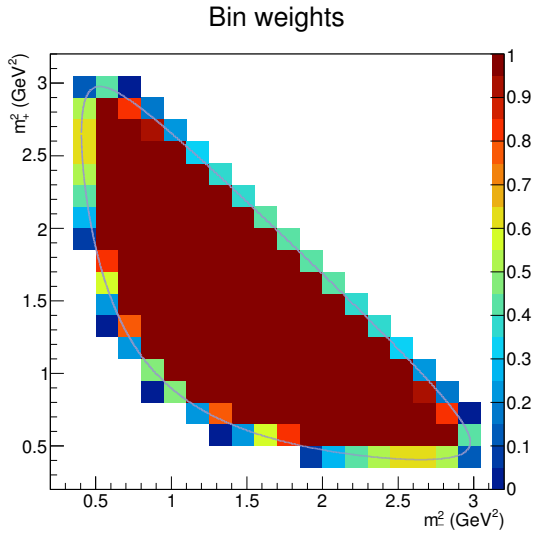

Figure 5.23 – Inverse of the correction weights for the bin edge effect ($1/w_i$).

5.3.3 Bin edge correction

Some special care must be taken to the bins at the edge of the Dalitz plot. The bins which are not fully inside the kinematically allowed region are artificially less populated than the bins totally covered by this region (these are the blueish bins in Fig. 5.13 for instance). Hence a correction of this edge effect must be applied. For a given bin i a weight w_i is applied, which is equal to the ratio between the total bin surface A_i^{tot} and the bin surface inside the kinematic limit A_i^{inside}:

$$w_i = \frac{A_i^{\text{tot}}}{A_i^{\text{inside}}}. \tag{5.16}$$

These correction weights are obtained by generating one billion $D \to K^0_S \pi^+ \pi^-$ phase space events with the `TGenPhaseSpace` ROOT class. Their inverses are shown in Fig. 5.23.

5.3.4 Total efficiency

Finally the trigger and PID efficiency weights are combined (Fig. 5.24 and 5.25) before being applied to the Dalitz plot after selection. The weight distribution is approximately flat. The trigger and PID selection have a tiny effect on the Dalitz plot, especially compared to the stripping effect. The bin edge correction is then applied and the resulting Dalitz plots are symmetrised along their diagonal, since no significant asymmetry between the π^+ and the π^- in the selection process occurs. These final Dalitz plots after selection with the BDTA, taking into account the trigger and PID efficiency, are on Fig. 5.26. To have a continuous two dimensional description of the efficiency an interpolation of the efficiency histograms of Fig. 5.26 is performed with a cubic spline (a type of piecewise polynomial of degree three). The result of this interpolation is shown in Fig. 5.27. These are the splines used as an input to the full fit (see Sec. 5.7). A comparison of the efficiency obtained with BDTA and BDTB can be observed in Fig. 5.28. It shows the efficiency ratio between the BDTA and the BDTB selections. No significant discrepancy can be seen between the two BDTs. Therefore the splines obtained with the BDTA are used in the baseline fit and a systematic uncertainty is estimated using alternatively the BDTB splines.

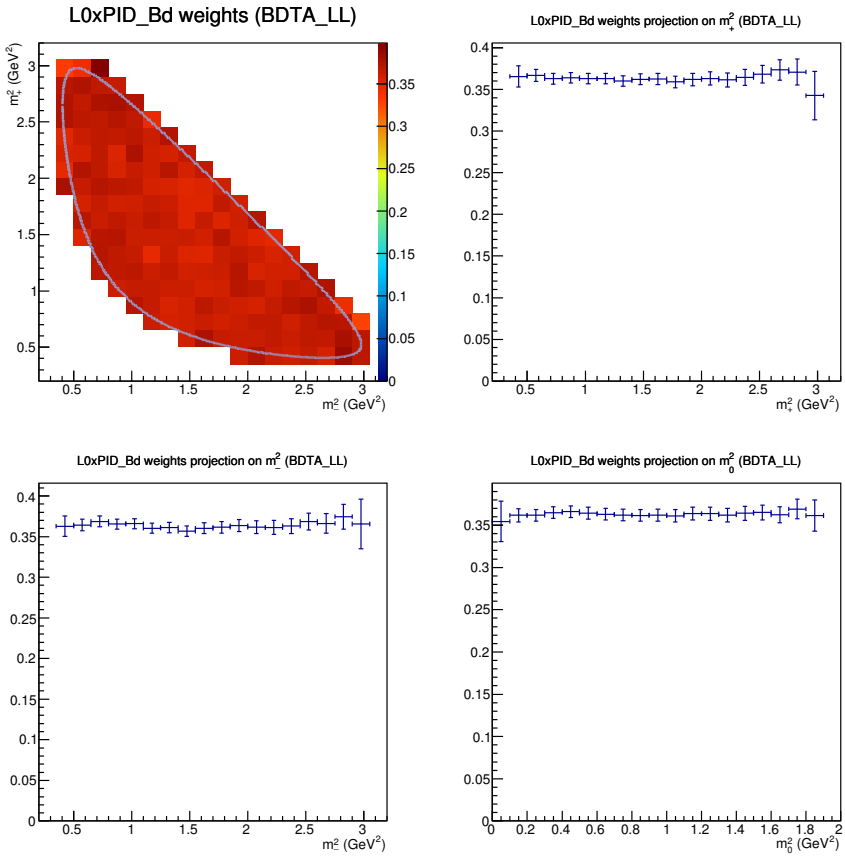

Figure 5.24 – Combined L0 and PID efficiency weights over the Dalitz plane for simulated $B^0_s \to D\overline{K}^{*0}$ LL candidates, selected with BDTA.

The one thousand trigger and PID efficiency weights are also combined to make a total of one thousand alternative Dalitz plots, making one thousand alternative splines. These splines are used to estimate the systematic uncertainty due to the efficiency description (see Sec. 5.8.3).

It has been checked that the efficiency obtained with the $B^0 \to DK^{*0}$ MC sample instead of the $B^0_s \to D\overline{K}^{*0}$ gives the same results (except with a poorer statistical accuracy, since the $B^0 \to DK^{*0}$ sample is not stripping filtered). The TOS and NotTOS proportion found in the data in the B^0 and B^0_s regions are slightly different. For a BDT cut at 0.75, among the 141 B^0 candidates, 95 are TOS (67%) and 46 are NotTOS (33%). Among the 204 B^0_s candidates, 122 are TOS (60%) and 82 are NotTOS (40%). This difference makes the combination of TOS and NotTOS efficiency slightly different. Nevertheless, since the total L0 efficiency is rather flat, there is no visible difference between the total B^0 and B^0_s efficiency. The corresponding systematic uncertainty is evaluated and its value is very small (Sec. 5.8.3).

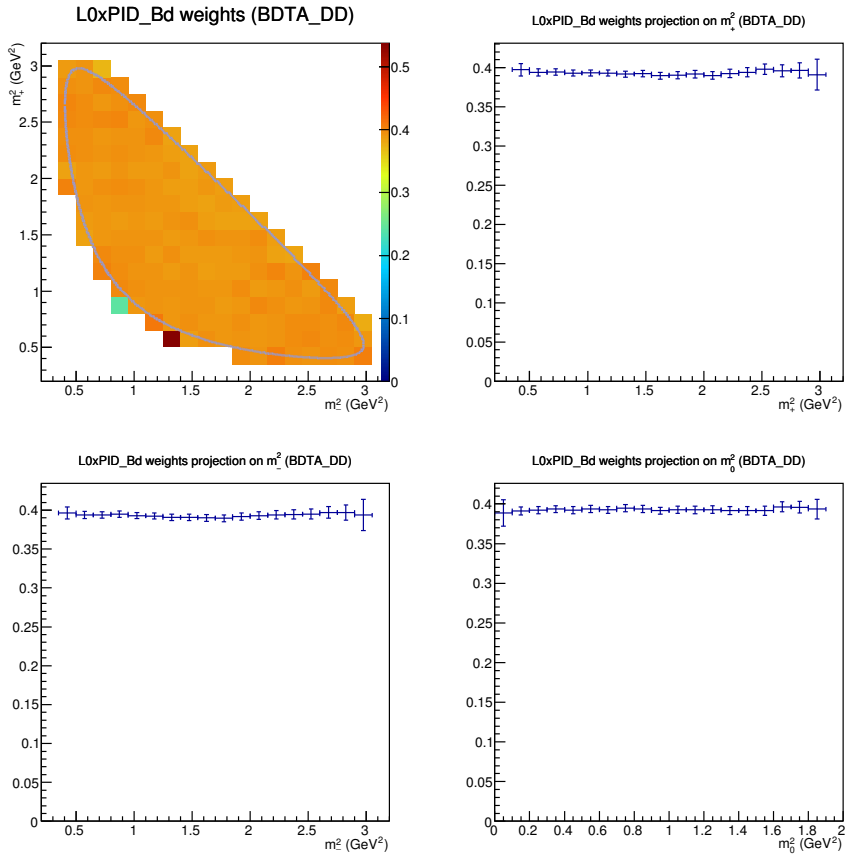

Figure 5.25 – Combined L0 and PID efficiency weights over the Dalitz plane for simulated $B^0_s \to D\overline{K}^{*0}$ DD candidates, selected with BDTA.

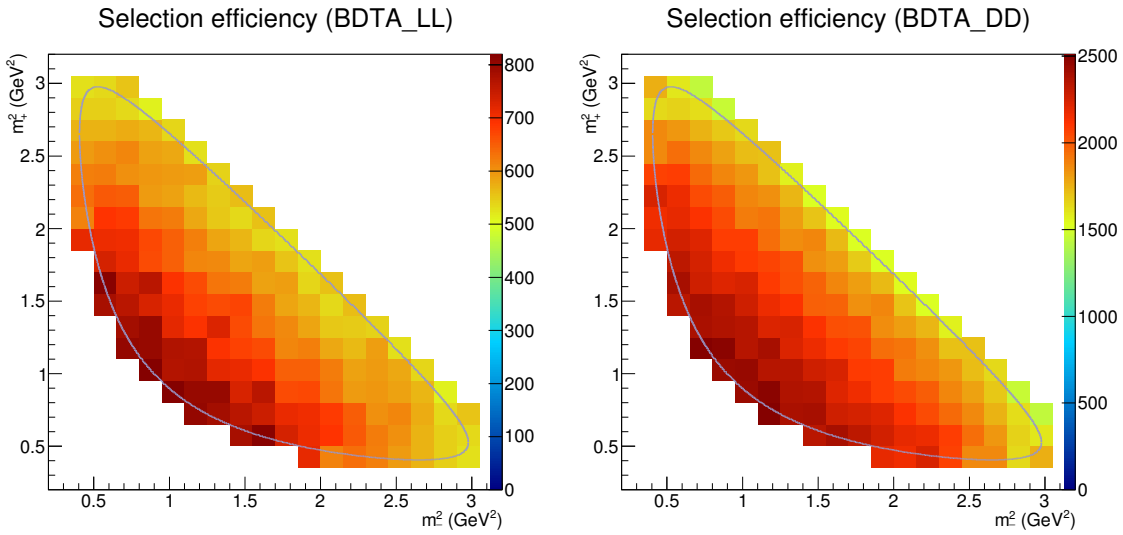

(a) (b)

Figure 5.26 – Total selection efficiency taking into account the trigger and PID selection, for simulated $B_s^0 \to D\overline{K}^{*0}$ LL (a) and DD (b) candidates, selected with BDTA.

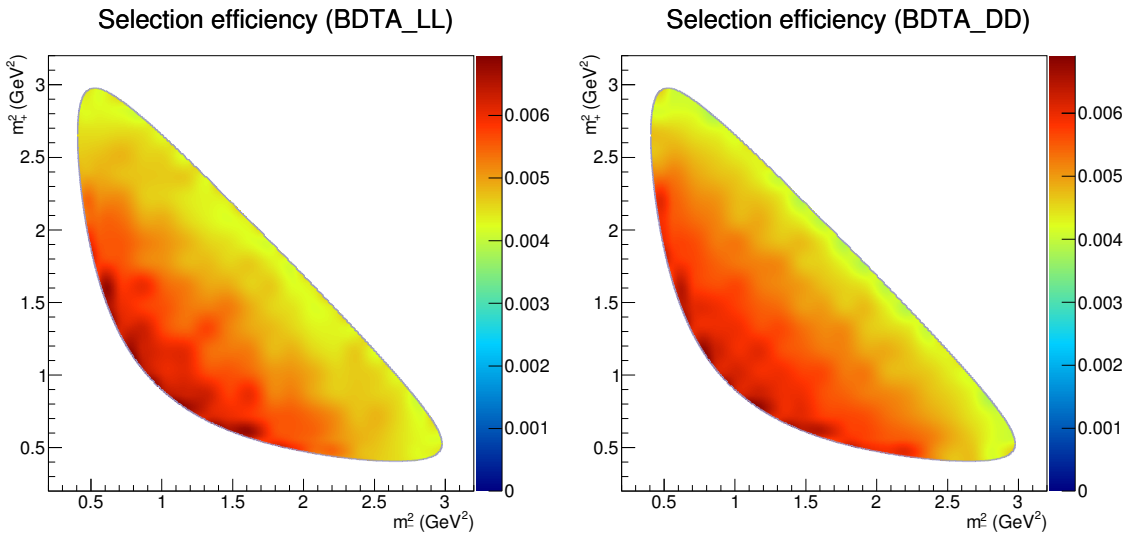

(a) (b)

Figure 5.27 – Cubic spline interpolation of the selection efficiency for simulated $B_s^0 \to D\overline{K}^{*0}$ LL (a) and DD (b) candidates, selected with BDTA.

(a) (b)

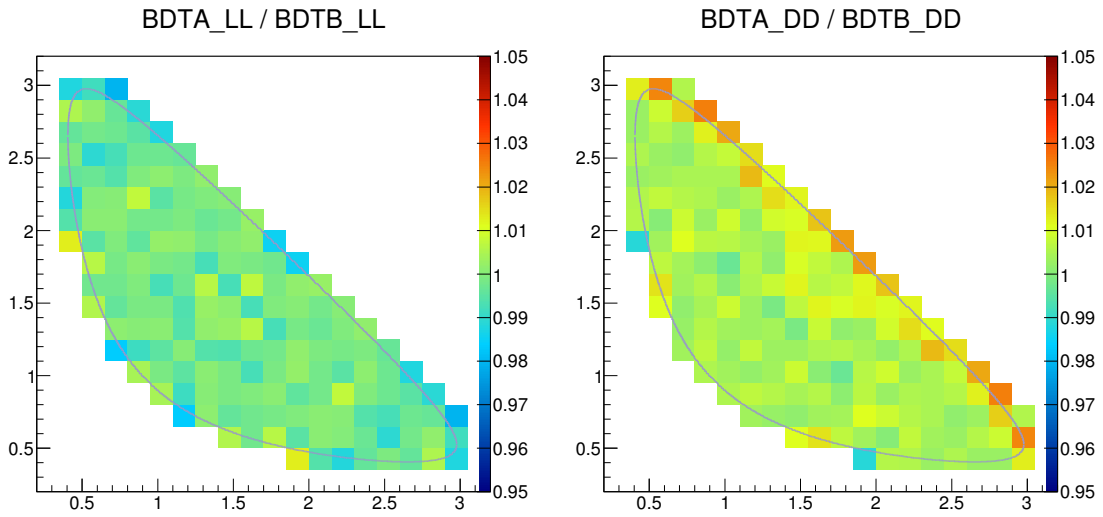

Figure 5.28 – Selection efficiency ratio between BDTA and BDTB for simulated $B^0_s \to D\overline{K}^{*0}$ LL (a) and DD (b) candidates.

5.4 Efficiency across the B^0 Dalitz plane.

Even though the present analysis is focused on the $D \to K^0_S\pi^+\pi^-$ Dalitz plane distribution of events coming from $B^0 \to DK^{*0}$ decay, the efficiency across the $B^0 \to DK\pi$ Dalitz plane has also to be determined. Indeed, the extraction of γ requires a precise determination of κ and r_{B^0}, and the efficiency profile over the K^{*0} region in the $B^0 \to DK\pi$ Dalitz plane may alter the r_{B^0} and κ values, as explained further in Sec. 5.9.1.

The determination of the selection efficiency across the B^0 Dalitz plane is similar to the one across the D Dalitz plane, except for the simulation sample used. The simulated $B^0 \to DK^{*0}$ signal sample coming from the LHCb official production used in this section, and only in this section, is not modelled with a scalar to vector-scalar amplitude for the $B^0 \to DK^{*0}$ transition (unlike the samples used in the previous section). The $m^2(D\pi)$ and $m^2(DK)$ variables are generated with a flat distribution, instead of a parabolic one if the K^{*0} helicity was taken into account (see for instance Fig. 5.29). This flat distribution on $m^2(D\pi)$ and $m^2(DK)$ is useful to correctly assess the selection efficiency over the whole region of the B^0 Dalitz plane which is considered. Since the simulated signal sample does not correspond to a phase space generation over the B^0 Dalitz plane, the candidate distributions after the full selection are not directly proportional to the efficiency. Therefore, the ratio between the Dalitz plots after the full selection and at the generation level has to be made.

Notice that in this section the $|\cos\theta^*| > 0.4$ cut present in the selection is never directly applied. It corresponds to a cut along $m^2(D\pi)$, which is represented on the Dalitz plots by two dashed grey lines (see for instance Fig. 5.29). This approach avoids the edge effect for bins which are only partially inside the $|\cos\theta^*| > 0.4$ region.

5.4.1 Geometrical acceptance

To evaluate the effect of the geometrical acceptance of the detector, 100000 events are privately generated without simulating the detector response. The same model as the sample of the LHCb official production is used (with a flat distribution along $m^2(D\pi)$), except that no generator cut is applied. The Dalitz plot and its projections are shown on Fig. 5.29. The solid black lines represent the ± 50 MeV window around the K^{*0} mass and the dashed grey lines represent the $|\cos\theta^*| > 0.4$ cut. Then, the detector geometrical acceptance is applied by requiring that all the particles in the final state lie in a $10 < \theta < 300$ mrad cone around the beam axis. The Dalitz plot after this geometrical acceptance is shown on Fig. 5.30. The Dalitz profile is almost not distorted by this cut, especially in the $|\cos\theta^*| > 0.4$ region. Therefore the geometrical acceptance has a negligible effect on the region of the B^0 Dalitz plane considered in the analysis.

5.4.2 Generator cuts efficiency

Although the generator cuts have been designed to not alter the D^0 Dalitz plane, this is not the case on the B^0 Dalitz plane. Fig. 5.31 is the Dalitz plot made with the generated events of the official production. A drop can be observed at low $m^2(D\pi)$ values. As explained just before this drop cannot be a detector geometrical acceptance effect, but it is due to the generator cuts described in appendix A. Indeed, when these cuts (which are looser or equal to the stripping cuts) are applied to the private sample used to determine the geometrical acceptance, a similar efficiency drop at low $m^2(D\pi)$ is observed (Fig. 5.32). This efficiency drop originates from the momentum cuts on the K^{*0} daughter pion. When all the generator cuts are applied, except those on the K^{*0} pion, the depletion at low $m^2(D\pi)$ disappears (Fig. 5.33).

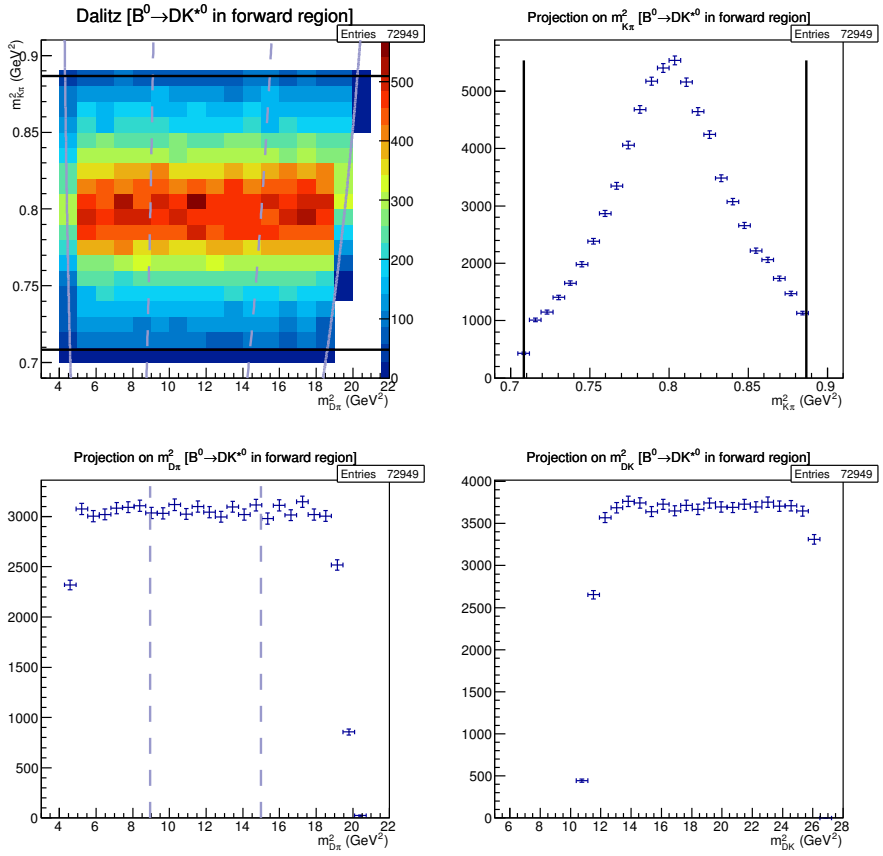

Figure 5.29 – Dalitz plot and its projections of simulated $B^0 \to DK^{*0}$ events in a 2π solid angle toward the LHCb detector (private production, without generator cuts). The solid black lines represent the ± 50 MeV window around the K^{*0} mass and the dashed grey lines represent the $|\cos\theta^*| > 0.4$ cut.

This behaviour means that making the ratio of the Dalitz plot with selected events and generated events from the official production does not correctly give the total efficiency. The generator cuts efficiency must be taken into account.

To determine the profile of the generator cuts efficiency, a ratio is made between the Dalitz plots obtained with the private generation (without generator cuts) and the one obtained with the official generation (with the generator cuts). It is shown in Fig. 5.34. This ratio does not give the absolute efficiency value, only the shape over the Dalitz plane, which is what is needed.

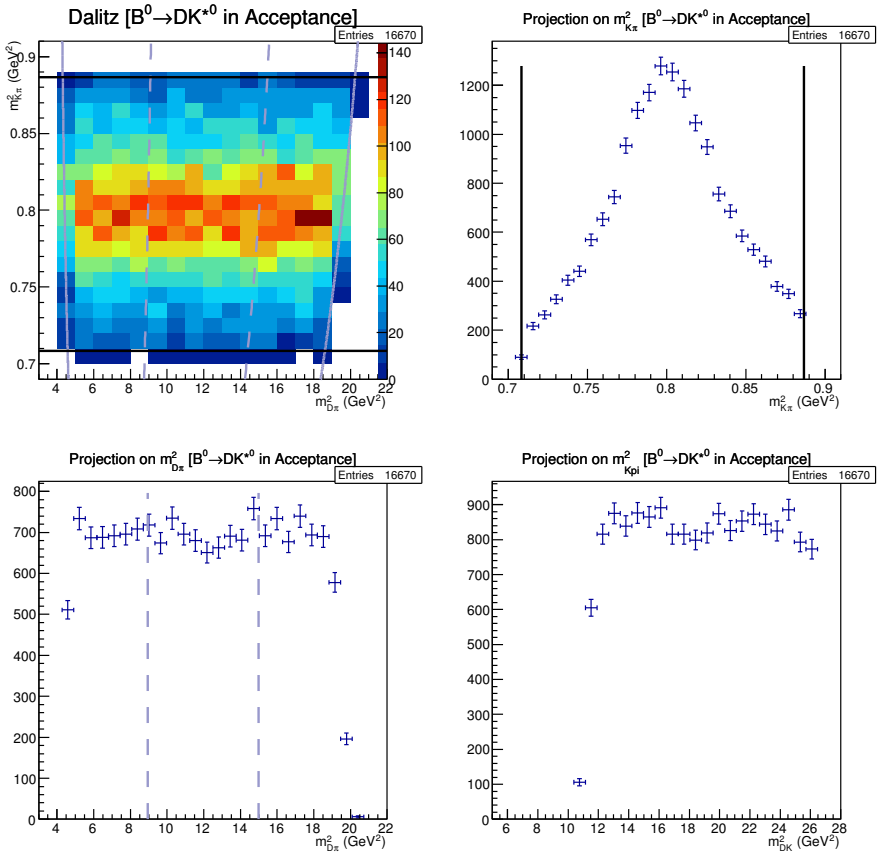

Figure 5.30 – Dalitz plot and its projections of simulated $B^0 \to DK^{*0}$ events in the LHCb detector geometrical acceptance, without applying the generator cuts (private production). The solid black lines represent the $\pm 50\,\text{MeV}$ window around the K^{*0} mass and the dashed grey lines represent the $|\cos\theta^*| > 0.4$ cut.

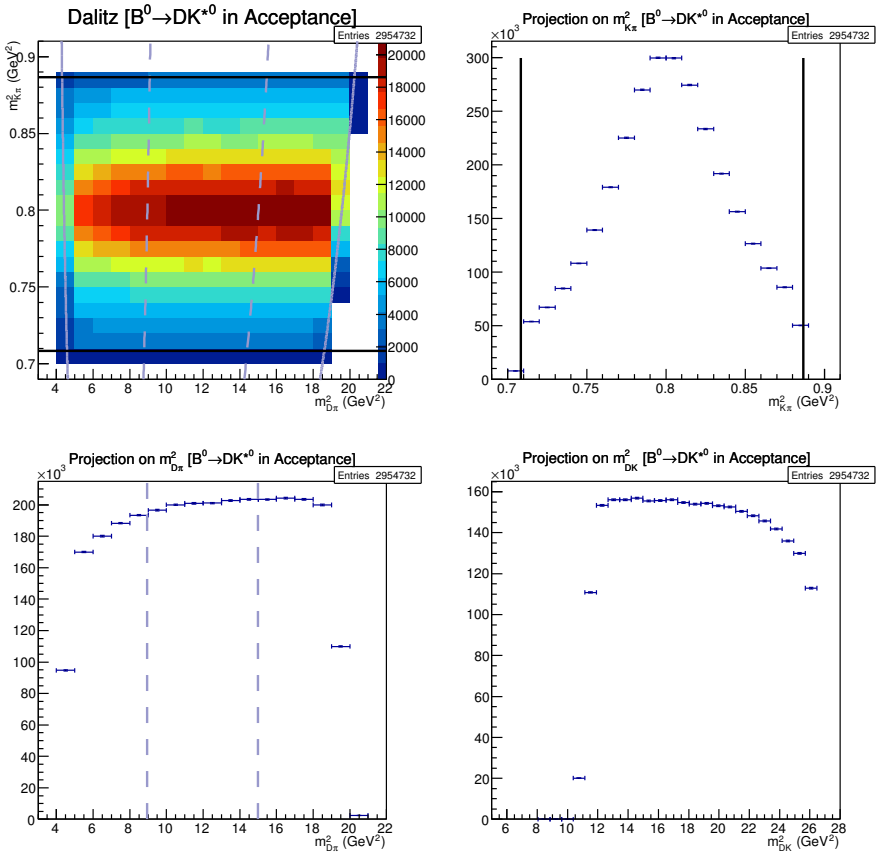

Figure 5.31 – Dalitz plot and its projections of simulated $B^0 \to DK^{*0}$ events in the LHCb detector geometrical acceptance, with the generator cuts applied (official production). The solid black lines represent the $\pm 50\,\text{MeV}$ window around the K^{*0} mass and the dashed grey lines represent the $|\cos\theta^*| > 0.4$ cut.

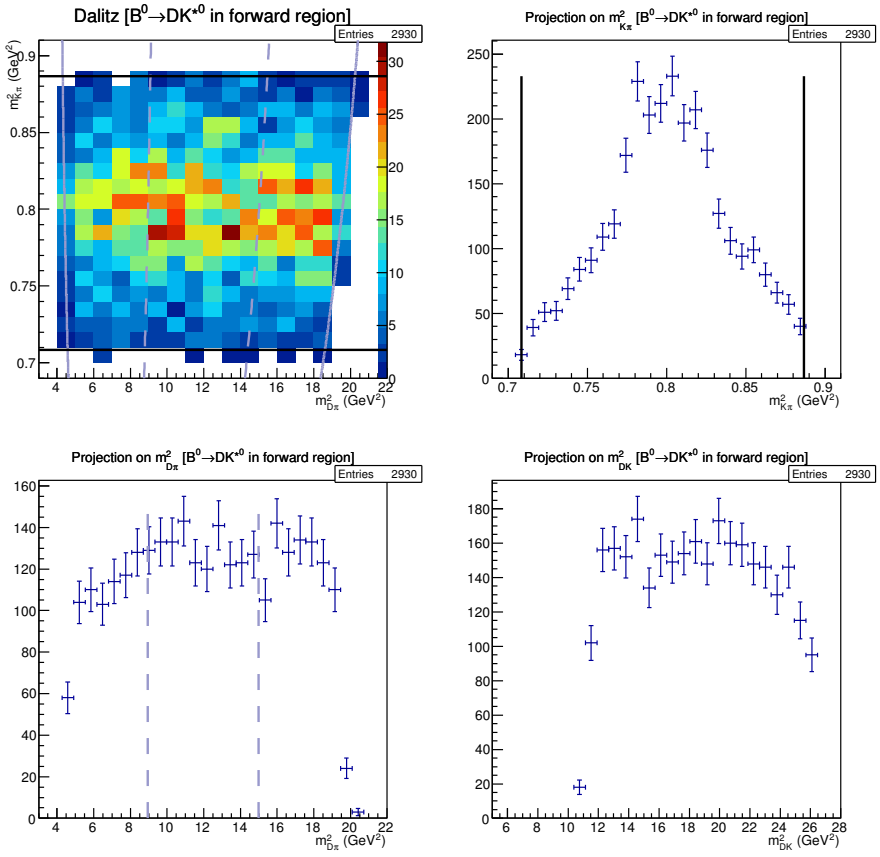

Figure 5.32 – Dalitz plot and its projections of simulated $B^0 \to DK^{*0}$ events in a 2π solid angle toward the LHCb detector, with the generator cuts applied (private production). The solid black lines represent the $\pm 50\,\text{MeV}$ window around the K^{*0} mass and the dashed grey lines represent the $|\cos\theta^*| > 0.4$ cut.

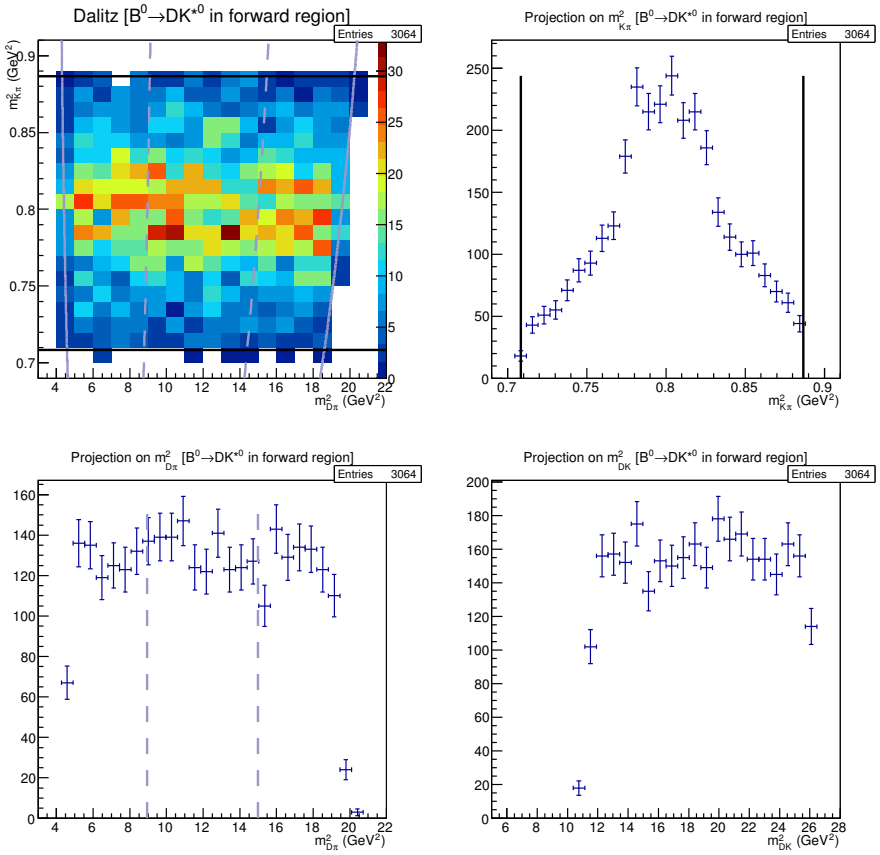

Figure 5.33 – Dalitz plot and its projections of simulated $B^0 \to DK^{*0}$ events in a 2π solid angle toward the LHCb detector, with the generator cuts applied except those on the K^{*0} daughter pion (private production). The solid black lines represent the ± 50 MeV window around the K^{*0} mass and the dashed grey lines represent the $|\cos\theta^*| > 0.4$ cut.

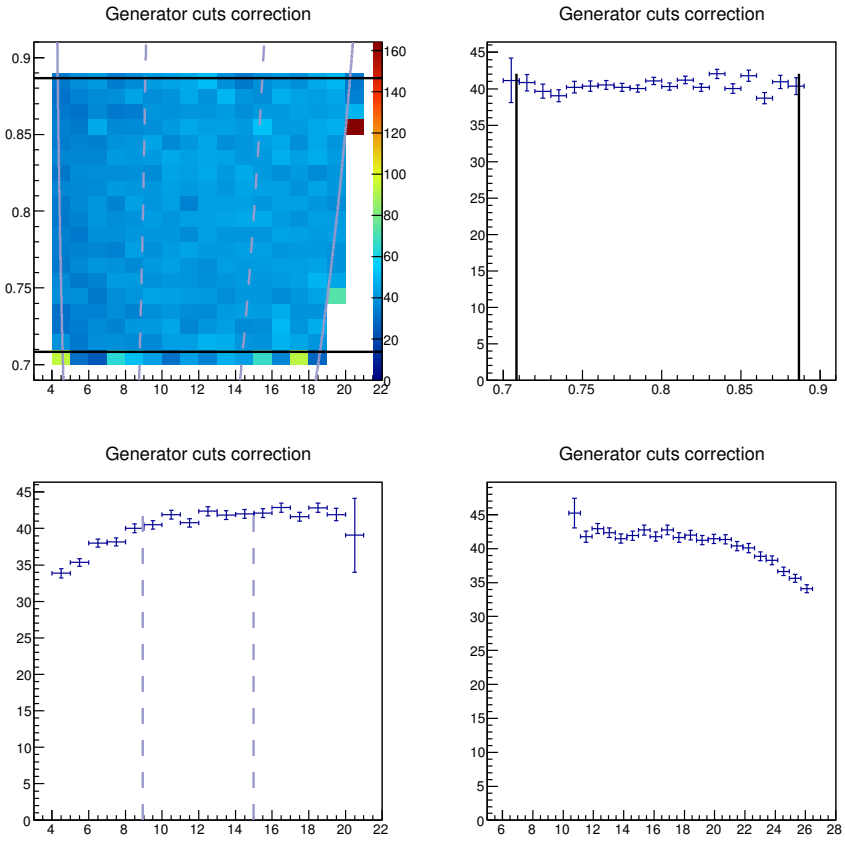

Figure 5.34 – Generator cuts efficiency over the B^0 Dalitz plane. The solid black lines represent the $\pm 50\,\text{MeV}$ window around the K^{*0} mass and the dashed grey lines represent the $|\cos\theta^*| > 0.4$ cut.

5.4.3 Trigger efficiency

The trigger efficiency is obtained with the method explained in Sec. 5.3.1, but with the $B^0 \to DK^{*0}$ sample whose distribution is flat along $m^2(D\pi)$. The TOS and NotTOS efficiency for DD candidates after BDTA are on Fig. 5.35. The distributions obtained on LL candidates are similar. The TOS efficiency is larger if the kaon has a high momentum, which corresponds to a low $m^2(D\pi)$.

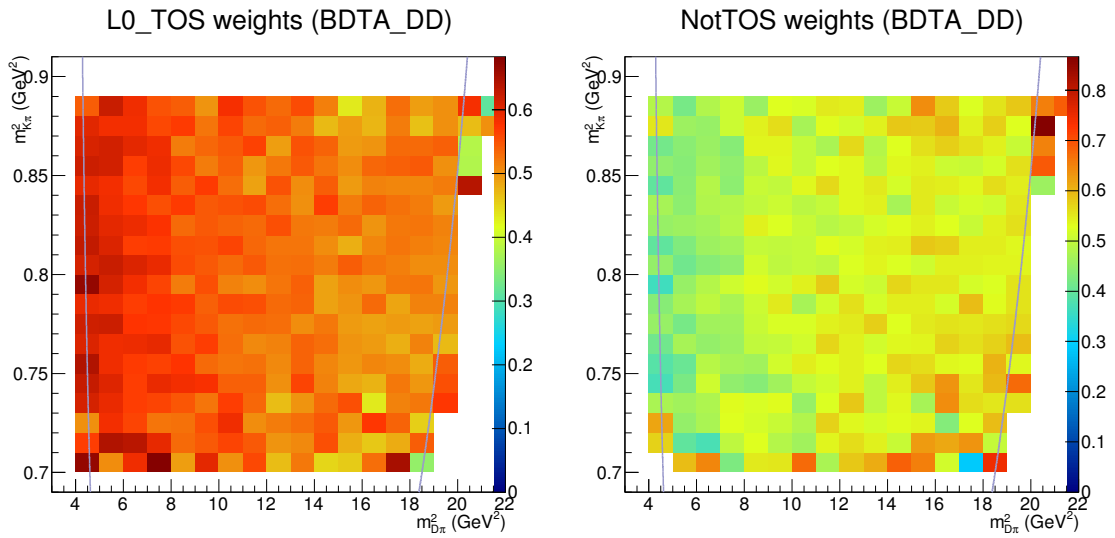

(a) (b)

Figure 5.35 – Trigger efficiency over the B^0 Dalitz plane, for TOS (a) and NotTOS (b) DD candidates after BDTA.

5.4.4 PID efficiency

The PID efficiency is obtained with the method explained in Sec. 5.3.2, but with the $B^0 \to DK^{*0}$ sample whose distribution is flat along $m^2(D\pi)$. The PID cut is tighter on the kaon ($\mathrm{DLL}_{K\pi} > 5$) than on the pion ($\mathrm{DLL}_{K\pi} < 3$). That is why the PID efficiency is essentially sensitive to the kaon momentum. It is larger if the kaon has a low momentum, which corresponds to a low $m^2(D\pi)$ (Fig. 5.36).

5.4.5 Total efficiency

After taking into account the generator cuts, the selection, the trigger and the PID efficiency, the total efficiency is obtained (Fig. 5.37). It is important to compare this efficiency to the one obtained in the ADS/GLW analysis [59]. Indeed, the combination of the measurements performed in the $B^0 \to DK^{*0}$ ADS/GLW and the present GGSZ analyses depends on their efficiency compatibility (see Sec. 5.9.1). To make the comparison the ratio between the ADS/GLW and the GGSZ efficiency is made (Fig. 5.38). It can be observed that this ratio is constant on the $|\cos\theta^*| > 0.4$ region (the considered region in both analyses). Therefore the r_{B^0} and κ values are expected to be the same in both analyses.

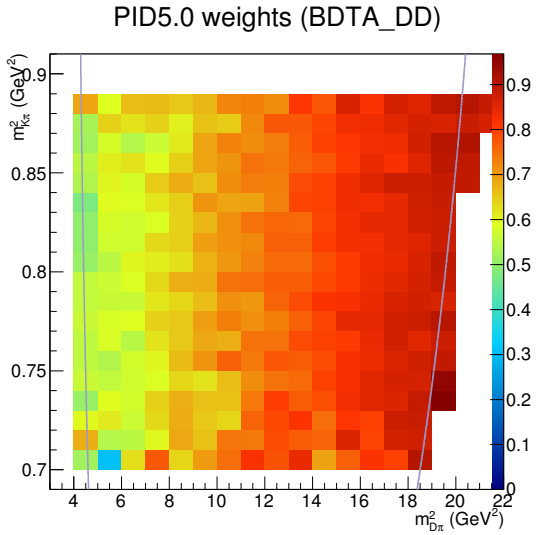

Figure 5.36 – PID efficiency over the B^0 Dalitz plane for DD candidates after BDTA.

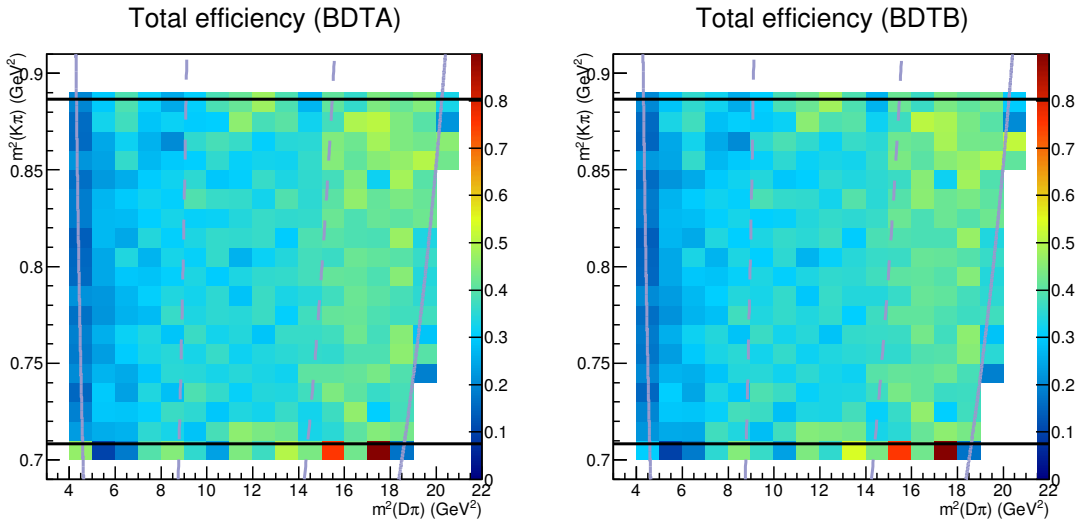

Figure 5.37 – Total efficiency across the B^0 Dalitz plane for BDTA (left) and BDTB (right). The solid black lines represent the ±50 MeV window around the K^{*0} mass and the dashed grey lines represent the $|\cos\theta^*| > 0.4$ cut.

The BDT includes $\cos\theta^*$ among its discriminating variables. Hence this could potentially produce an efficiency distortion on the $m^2(D\pi)$ coordinate, with respect to the ADS/GLW method. However this is not the case, and it is safe to include $\cos\theta^*$ inside the BDT. As it can be observed on Fig. 5.39, the BDT efficiency compared to the stripping is flat in the $|\cos\theta^*| > 0.4$ region.

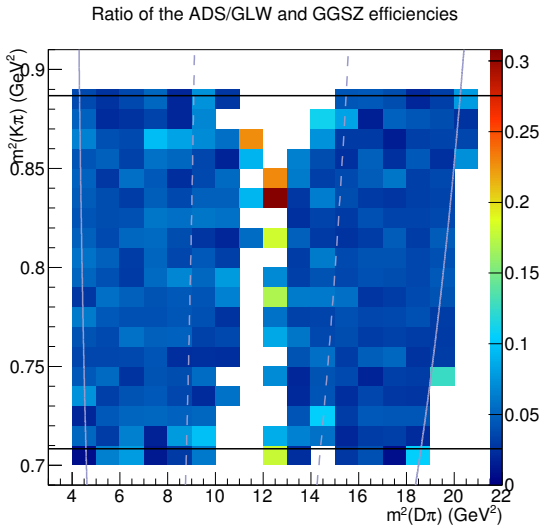

Figure 5.38 – Efficiency ratio between the ADS/GLW and GGSZ analyses across the B^0 Dalitz plane (BDTA). The solid black lines represent the ±50 MeV window around the K^{*0} mass and the dashed grey lines represent the $|\cos\theta^*| > 0.4$ cut.

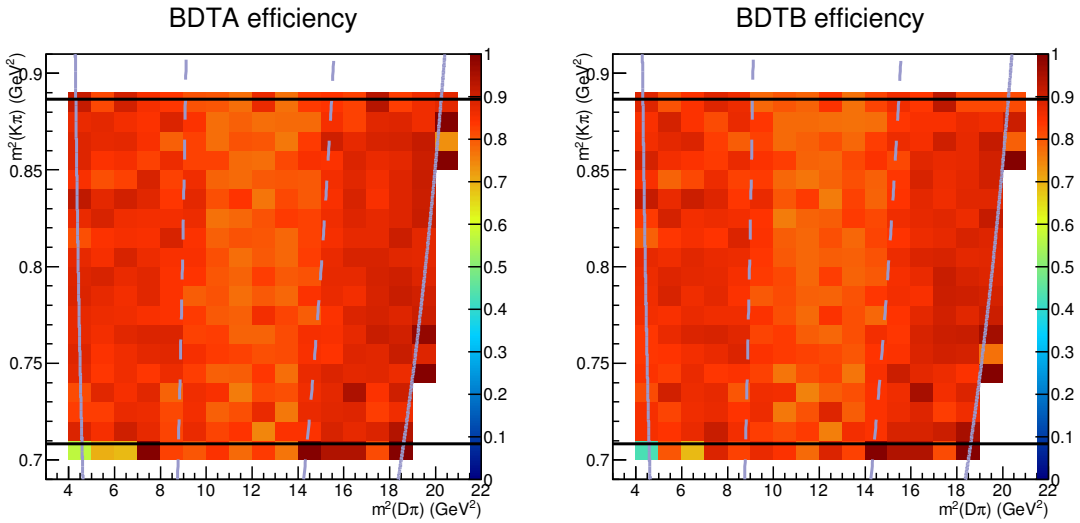

Figure 5.39 – BDT efficiency compared to the stripping across the B^0 Dalitz plane, for BDTA (left) and BDTB (right). The solid black lines represent the ±50 MeV window around the K^{*0} mass and the dashed grey lines represent the $|\cos\theta^*| > 0.4$ cut.

5.5 Mass fit and background identification

Before analysing the Dalitz plot, the signal and the different background contributions must be determined. This is achieved by performing an unbinned extended maximum likelihood fit on the B^0 reconstructed invariant mass. The two categories LL and DD are fitted simultaneously. This mass fit fixes the signal and background yields and the PDF mass shapes used in the fit of the Dalitz plot (see Sec. 5.7). In the following the full selection is applied on all the samples.

5.5.1 Signal PDF

To determine the best model for the B invariant mass distributions of the $B^0_{(s)} \to DK^{*0}$ decays, the truth matched MC samples are fitted. The truth matching consists in checking the true ID of the decay chain and the relations among the particles. Among all the models tested, the double Crystal Ball function (CB) [139] describes the signal peak with the best accuracy. In order to avoid a too complex model some simplifications are adopted. For a given peak, the two Crystal Ball functions have a common mean and a common width. The same shape is used to describe either the B^0 or the B^0_s peak, and LL or DD candidates. The model retained is shown on Fig. 5.40.

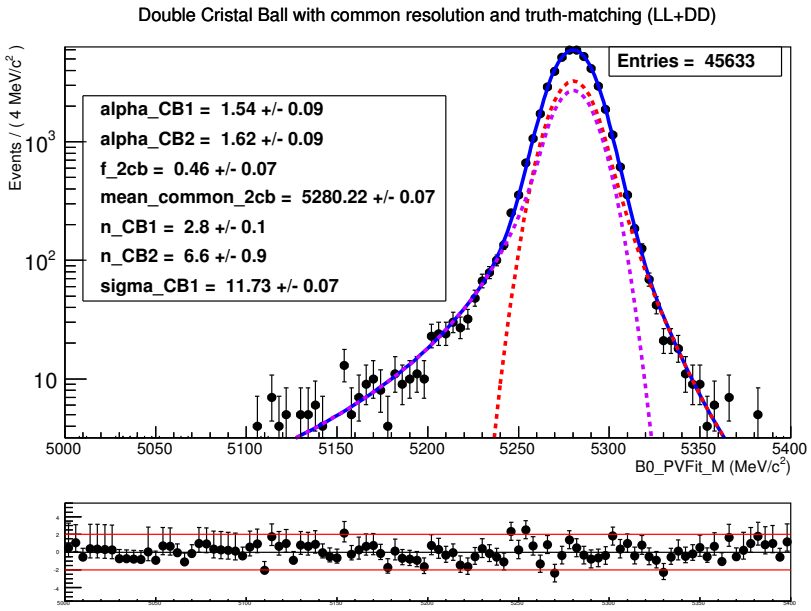

Figure 5.40 – Fit of the B^0 reconstructed invariant mass of simulated $B^0 \to DK^{*0}$ LL and DD candidates. The model used is a double Crystal Ball with common mean and width, and is the one retained to fit the data. The two Crystal Ball components are represented separately by the dashed red and purple lines.

Hence the model describing the $B^0_{(s)} \to DK^{*0}$ signal is expressed as

$$\begin{aligned} f_{\rm sig}(m; N_{B^0}, N_{B^0_s}, \mu, \sigma) &\equiv N_{B^0}\left[f \cdot g(m; \mu - \delta m, \sigma, \alpha_1, n_1) + (1-f)\cdot g(m; \mu - \delta m, -\sigma, \alpha_2, n_2)\right] \\ &+ N_{B^0_s}\left[f \cdot g(m; \mu, \sigma, \alpha_1, n_1) + (1-f)\cdot g(m; \mu, -\sigma, \alpha_2, n_2)\right], \end{aligned} \tag{5.17}$$

where

- N_{B^0} is the number of signal B^0 events.
- $N_{B^0_s}$ is the number of B^0_s events.
- g is a simple Crystal Ball function.
- μ is the mean of the B^0_s peak.
- δm is the mass difference between the B^0 and the B^0_s mesons. It is fixed to the PDG value $\delta m = 87.19\,\text{MeV}$ [20].
- σ is the width of the B^0 and B^0_s peaks.
- $\alpha_{\{1,2\}}$ are the double Crystal Ball functions tail parameters. They are fixed from the values obtained in the simulation, $\alpha_1 = 1.54$ and $\alpha_2 = 1.62$, and the same values are used for B^0 and B^0_s.
- $n_{\{1,2\}}$ are the tail amplitudes of the double Crystal Ball. They are fixed from the values obtained in the simulation, $n_1 = 2.8$ and $n_2 = 6.6$, and the same values are used for B^0 and B^0_s.
- f is the fraction of the lower mass tail Crystal Ball. It is fixed from the value obtained in the simulation, $f = 0.46$, and the same value is used for B^0 and B^0_s.

Only the yields N_{B^0} and $N_{B^0_s}$ are different between LL and DD categories. All the other signal parameters are shared among these categories.

5.5.2 Background PDFs

Combinatorial background

The combinatorial background is modelled with a decreasing exponential distribution with a slope λ,

$$f_{\rm comb}(m; N_{\rm comb}, \lambda) = N_{\rm comb} \cdot \mathrm{e}^{\lambda m}|\lambda|. \tag{5.18}$$

The yield $N_{\rm comb}$ and the slope λ are different between LL and DD categories.

Partially reconstructed $B^0_{(s)} \to D^{*0}(D^0\gamma/\pi^0)K^{*0}$ background

An important source of background comes from the partially reconstructed $B^0_{(s)} \to D^{*0}(D^0\gamma/\pi^0)K^{*0}$ decays. Soft photons or neutral pions coming from the D^{*0} decay are difficult to reconstruct and easily missed in the $B^0_{(s)}$ candidate reconstruction. Hence the reconstructed invariant mass of this background has a rather broad distribution at a lower mass than the B^0 or B^0_s meson. $B^0_s \to D^{*0}\overline{K}^{*0}$ background is particularly annoying since it overlaps with the $B^0 \to DK^{*0}$ signal range. The shape of this background is described with a non analytic representation. From the simulated distributions a kernel density estimation [148] is performed exploiting the `RooKeysPdf` method provided by the `RooFit` package.

Since $B^0_{(s)} \to D^{*0}K^{*0}$ is a decay of pseudo scalar to vector-vector mesons, the angular momentum conservation implies that the $B^0_{(s)}$ daughters can be in one of three helicity configurations, corresponding to three unknown decay amplitudes:

- $\mathscr{A}_{100}$, the decay amplitude when the D^{*0} and K^{*0} are produced in helicity state +1.
- $\mathscr{A}_{010}$, the decay amplitude when the D^{*0} and K^{*0} are produced in helicity state 0.
- $\mathscr{A}_{001}$, the decay amplitude when the D^{*0} and K^{*0} are produced in helicity state −1.

The reconstructed DK^{*0} invariant mass depends only on θ', the angle between the D^0 momentum in the D^{*0} rest frame and the D^{*0} momentum in the $B^0_{(s)}$ rest frame. The θ' distribution can be expressed for $D^{*0} \to D^0\pi^0$ decay as [149, 150]

$$I(\theta') \propto \frac{1}{2}\left(|\mathscr{A}_{001}|^2 + |\mathscr{A}_{100}|^2\right)\sin^2\theta' + |\mathscr{A}_{010}|^2\cos^2\theta', \tag{5.19}$$

and for $D^{*0} \to D^0\gamma$ decay as

$$I(\theta') \propto \frac{1}{2}\left(|\mathscr{A}_{001}|^2 + |\mathscr{A}_{100}|^2\right)(1+\cos^2\theta') + |\mathscr{A}_{010}|^2\sin^2\theta'. \tag{5.20}$$

Since the 001 and 100 configurations follow the same angular dependence expressed in Eq. 5.19 and Eq. 5.20, no distinction can be made between these two contributions in the DK^{*0} mass spectrum. Therefore only the 010 and 001 states have been simulated to obtain the shape describing the three helicity configurations. Fig. 5.41 shows the invariant mass distributions, and their kernel estimation superimposed, of the $B^0_s \to D^{*0}\overline{K}^{*0}$ background for the the 010 and 001 helicity configurations and for $D^{*0} \to D^0\pi^0$ and $D^{*0} \to D^0\gamma$ decays. The distributions obtained for LL and DD candidates and with a cut on BDTA or BDTB are similar. In the nominal mass fit the RooKeys used are those obtained with LL and DD candidates (taken separately), with a cut on BDTA. To take into account the data/MC agreement, a smearing and a mass shift is applied before making the final RooKeys. The B^0_s peak has a position $\mu_{\rm MC} = 5367.5\,$MeV in the MC and $\mu_{\rm data} = 5370.6\,$MeV in the data. Therefore a mass shift of 3.1 MeV is applied. The B^0 peak has a width of $\sigma_{\rm MC} = 11.73\,$MeV in the MC sample and a width of $\sigma_{\rm data} = 13\,$MeV in the data. Therefore a smearing of $\sqrt{13^2 - 12^2} = 5\,$MeV is applied [5].

The function describing this partially reconstructed background is expressed as

$$\begin{aligned} f^{TT}_{\rm part}(m) &= N^{s\,TT}_{\rm part}\left\{\alpha_{010}\mathscr{F}^{TT}_{010}(m) + (1-\alpha_{010})\mathscr{F}^{TT}_{101}(m)\right\} \\ &+ N^{d\,TT}_{\rm part}\left\{\alpha_{010}\mathscr{F}^{TT}_{010}(m-\delta m) + (1-\alpha_{010})\mathscr{F}^{TT}_{101}(m-\delta m)\right\}, \end{aligned} \tag{5.21}$$

with,

$$\mathscr{F}^{TT}_{010}(m) = G^{TT}_{010}f^{TT}_{\gamma 010}(m) + (1-G^{TT}_{010})f^{TT}_{\pi^0 010}(m), \tag{5.22}$$

$$\mathscr{F}^{TT}_{101}(m) = G^{TT}_{101}f^{TT}_{\gamma 001}(m) + (1-G^{TT}_{101})f^{TT}_{\pi^0 001}(m). \tag{5.23}$$

The index TT stands for the Track Type, either LL or DD. $N^{s\,TT}_{\rm part}$ ($N^{d\,TT}_{\rm part}$) is the yield of the partially reconstructed $B^0_s \to D^{*0}\overline{K}^{*0}$ ($B^0 \to DK^{*0}$) decays. The relative proportion between the helicity contributions 001 and (100 + 001) (written as 101) is described with the α_{010} parameter.

[5] The mean and resolution values here correspond to a previous iteration of the mass fit, slightly different from the final version.

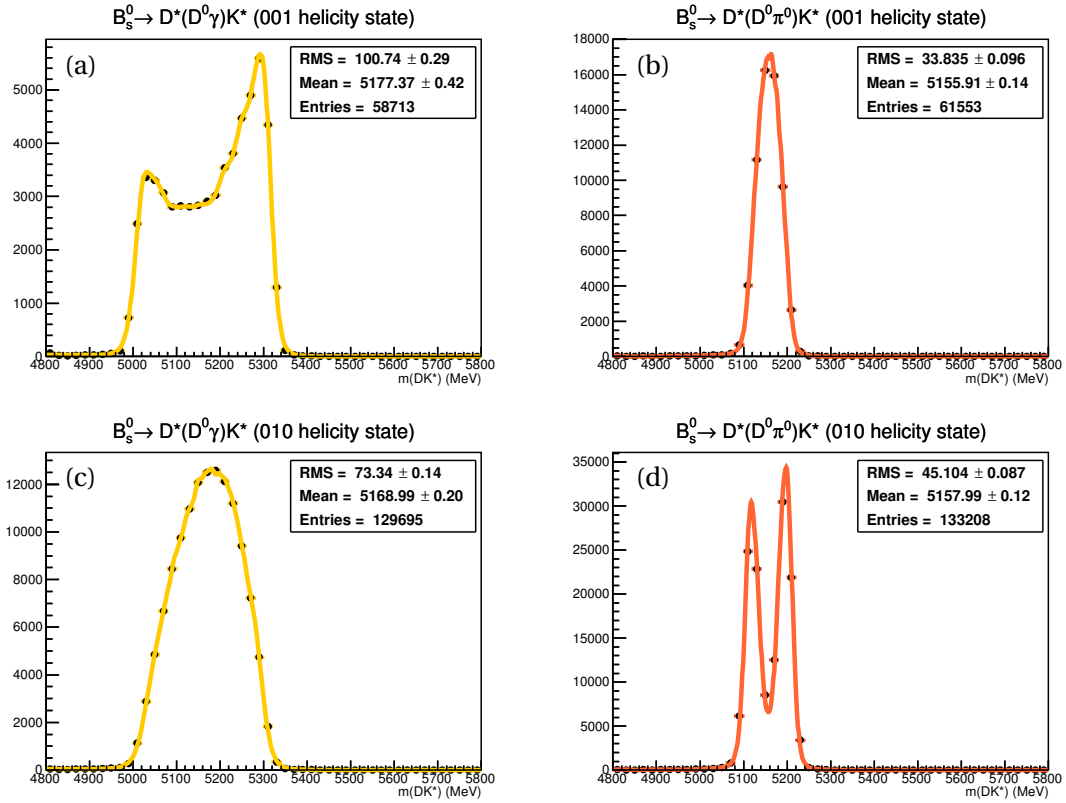

Figure 5.41 – Reconstructed DK^{*0} invariant mass distributions and their kernel estimation superimposed, from simulated $B_s^0 \to D^{*0}(D^0\gamma)\overline{K}^{*0}$ (a) and $B_s^0 \to D^{*0}(D^0\pi^0)\overline{K}^{*0}$ (b) decays in helicity state 001 and $B_s^0 \to D^{*0}(D^0\gamma)\overline{K}^{*0}$ (c) and $B_s^0 \to D^{*0}(D^0\pi^0)\overline{K}^{*0}$ (d) decays in helicity state 010. Only DD candidates after a cut on BDTA are plotted.

As a baseline, α_{010} is the same for the $B^0 \to DK^{*0}$ and $B_s^0 \to D\overline{K}^{*0}$ components. $f_{\gamma X}^{TT}$ and $f_{\pi^0 X}^{TT}$ are the RooKeys PDF for a given helicity state X, determined with the $B_s^0 \to D^{*0}\overline{K}^{*0}$ simulated samples as explained above. G_X^{TT} is the proportion between the $D^{*0} \to D^0\gamma$ and $D^{*0} \to D^0\pi^0$ contributions. It is a fixed parameter of the mass fit and is defined as

$$G_X^{TT} \equiv \frac{g_X^{TT}}{g_X^{TT} + p_X^{TT}}, \tag{5.24}$$

where the g_X^{TT} and p_X^{TT} factors are the products of the branching ratio and the selection efficiency

$$g_X^{TT} = \mathcal{B}(D^{*0} \to D^0\gamma)\varepsilon_{\text{gen}}^X(D^{*0} \to D^0\gamma)\varepsilon_{\text{strip}}^X(D^{*0} \to D^0\gamma)\varepsilon_{\text{sel}}^{X\,TT}(D^{*0} \to D^0\gamma), \tag{5.25}$$

$$p_X^{TT} = \mathcal{B}(D^{*0} \to D^0\pi^0)\varepsilon_{\text{gen}}^X(D^{*0} \to D^0\pi^0)\varepsilon_{\text{strip}}^X(D^{*0} \to D^0\pi^0)\varepsilon_{\text{sel}}^{X\,TT}(D^{*0} \to D^0\pi^0). \tag{5.26}$$

The generator efficiency ε_{gen} includes the detector acceptance and the generator level cuts. $\varepsilon_{\text{stripping}}$ is the stripping efficiency, and ε_{sel} the selection efficiency. They are summarised in Table 5.5. The nominal mass fit uses the selection efficiency obtained with BDTA.

Table 5.5 – Branching ratio and efficiency for $B_s^0 \to D^{*0}\overline{K}^{*0}$ partially reconstructed background.

Quantity	$D^{*0} \to D^0\pi^0$		$D^{*0} \to D^0\gamma$	
	LL	DD	LL	DD
Branching ratio	$(61.9 \pm 2.9)\%$		$(38.1 \pm 2.9)\%$	
$\varepsilon_{\text{gen}}^{010}$	$(6.32 \pm 0.06)\%$		$(6.36 \pm 0.02)\%$	
$\varepsilon_{\text{gen}}^{001}$	$(6.72 \pm 0.08)\%$		$(6.76 \pm 0.02)\%$	
$\varepsilon_{\text{strip}}^{010}$	$(1.177 \pm 0.002)\%$		$(1.177 \pm 0.002)\%$	
$\varepsilon_{\text{strip}}^{001}$	$(1.158 \pm 0.002)\%$		$(1.144 \pm 0.002)\%$	
$\varepsilon_{\text{sel}}^{010\text{ BDTA}}$	$(9.73 \pm 0.04)\%$	$(26.06 \pm 0.06)\%$	$(9.54 \pm 0.04)\%$	$(25.66 \pm 0.06)\%$
$\varepsilon_{\text{sel}}^{010\text{ BDTB}}$	$(9.73 \pm 0.04)\%$	$(27.77 \pm 0.06)\%$	$(9.53 \pm 0.04)\%$	$(25.26 \pm 0.06)\%$
$\varepsilon_{\text{sel}}^{001\text{ BDTA}}$	$(4.59 \pm 0.03)\%$	$(12.13 \pm 0.04)\%$	$(4.45 \pm 0.03)\%$	$(11.86 \pm 0.04)\%$
$\varepsilon_{\text{sel}}^{001\text{ BDTB}}$	$(4.59 \pm 0.03)\%$	$(12.03 \pm 0.04)\%$	$(4.44 \pm 0.03)\%$	$(11.73 \pm 0.04)\%$

Misidentified $B^0 \to D\rho^0$ background

Another source of background comes from the misidentified $B^0 \to D\rho^0$ mode. One of the ρ^0 daughter pions in the $\rho^0 \to \pi^+\pi^-$ decay can be taken as a kaon. It makes up a K^{*0} candidate and results in a B^0 candidate with a larger mass compared to the nominal one. To have a model of the invariant mass distribution of this misidentified background the same technique as the $B_{(s)}^0 \to D^{*0}K^{*0}$ background is used. The distribution is built from a kernel estimation performed on the $B^0 \to D\rho^0$ simulated sample, reconstructed as $B^0 \to DK^{*0}$, after full selection except for the PID cuts. The PID cuts effect is obtained through the reweighting provided by the PID calibration samples (see Sec. 5.3.2). In this way the K-π misidentification efficiency is correctly modelled, avoiding a data-MC disagreement. Fig. 5.42 shows the mass distribution and the kernel estimation superimposed for DD candidates after BDTA selection. As the yield of this background is rather low and estimated with a large statistical uncertainty, a gaussian constraint is applied to the yield ratio, denoted ρ, between the $B^0 \to D\rho^0$ and $B_s^0 \to D\overline{K}^{*0}$ components. Hence the $B^0 \to D\rho^0$ PDF is expressed as

$$f_{D\rho^0}^{tt} = \rho^{tt}\, N_{B_s^0}^{tt}\, g_{D\rho^0}^{tt}, \tag{5.27}$$

where $g_{D\rho^0}$ is the corresponding `RooKeys`. The ratio ρ is computed as

$$\rho \equiv \frac{n(B^0 \to D\rho^0)}{n(B_s^0 \to D\overline{K}^{*0})} = \frac{f_d}{f_s}\frac{\mathscr{B}(B^0 \to D\rho^0)}{\mathscr{B}(B_s^0 \to D\overline{K}^{*0})}\frac{\varepsilon(B^0 \to D\rho^0)}{\varepsilon(B_s^0 \to D\overline{K}^{*0})}. \tag{5.28}$$

Taking into account the efficiency given by the Monte-Carlo simulation, with the PID efficiency given by the PID calibration package, the following values are obtained:

$$\rho^{LL} = (3.92 \pm 0.96)\%, \tag{5.29}$$

$$\rho^{DD} = (3.81 \pm 0.93)\%. \tag{5.30}$$

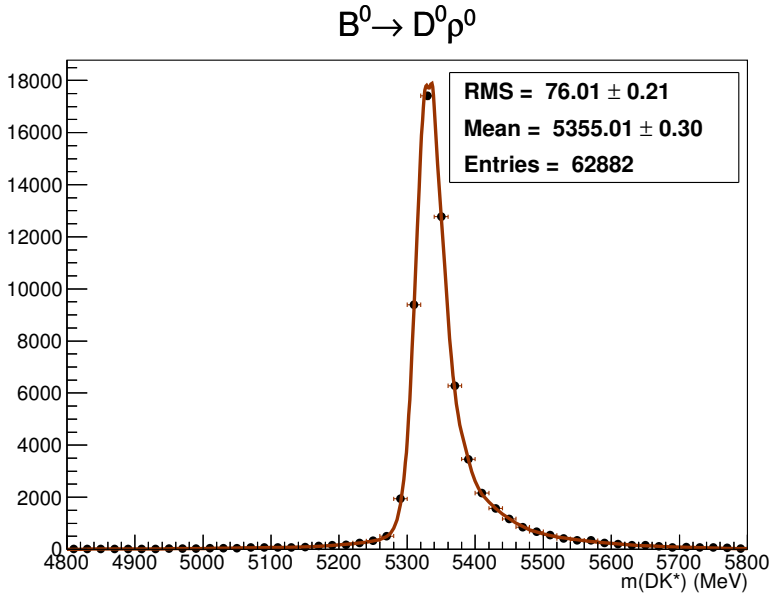

Figure 5.42 – Reconstructed DK^{*0} invariant mass distribution and its kernel estimation superimposed, obtained from simulated misidentified $B^0 \to D\rho^0$ DD candidates (BDTA cut).

Table 5.6 – Constant parameters used in the B^0 invariant mass fit.

Constant Parameter	Value	Description
δm	87.19 MeV	Mass shift between B^0 and B_s^0
f	0.46214	Fraction of the Crystal Ball with the lower mass tail
α_1	1.5422	α parameter of the CB with the lower mass tail
α_2	1.6196	α parameter of the CB with the upper mass tail
n_1	2.7836	n parameter of the CB with the lower mass tail
n_2	6.6324	n parameter of the CB with the upper mass tail
G_{010}^{LL}	0.38006	$D^{*0} \to D^0\gamma / D^{*0} \to D^0\pi^0$ proportion in helicity state 010 (LL)
G_{010}^{DD}	0.38107	$D^{*0} \to D^0\gamma / D^{*0} \to D^0\pi^0$ proportion in helicity state 010 (DD)
G_{101}^{LL}	0.37434	$D^{*0} \to D^0\gamma / D^{*0} \to D^0\pi^0$ proportion in helicity state 100 + 001 (LL)
G_{101}^{DD}	0.37633	$D^{*0} \to D^0\gamma / D^{*0} \to D^0\pi^0$ proportion in helicity state 100 + 001 (DD)

5.5.3 Mass fit parameters

To summarise, the B^0 and B_s^0 peaks are described with two double Crystal Ball functions which share the same width. The mass difference between the two peaks is fixed to its PDG value [20]. The combinatorial background is described with an exponential, with separate slopes for LL and DD candidates. The misidentified $B^0 \to D\rho^0$ background and the partially reconstructed $B_{(s)}^0 \to D^{*0}K^{*0}$ background are described with non analytical function obtained from the simulation. The different helicity contributions, 010 and 100 + 001, of the $B_{(s)}^0 \to D^{*0}K^{*0}$ background are described separately. The relative proportion between $D^{*0} \to D^0\pi^0$ and $D^{*0} \to D^0\gamma$ is fixed, taking into account the relative difference in branching fraction and efficiency. Table 5.6 gathers all the constant parameters of the mass fit, and Table 5.7 all the floating parameters.

Table 5.7 – Free parameters used in the B^0 invariant mass fit.

Free Parameter	Designation	Description
μ	`Bs_mean`	Central value of B_s^0 peak
σ	`sigma_CB1`	Width of B^0 and B_s^0 peaks
$N_{B^0}^{LL}$	`nBd_LL`	Signal yield (LL)
$N_{B^0}^{DD}$	`nBd_DD`	Signal yield (DD)
$N_{B_s^0}^{LL}$	`nBs_LL`	$B_s^0 \to D\overline{K}^{*0}$ yield (LL)
$N_{B_s^0}^{DD}$	`nBs_DD`	$B_s^0 \to D\overline{K}^{*0}$ yield (DD)
λ^{LL}	`combi_tau_LL`	Combinatorial slope (LL)
λ^{DD}	`combi_tau_DD`	Combinatorial slope (DD)
N_{comb}^{LL}	`ncombi_LL`	Combinatorial yield (LL)
N_{comb}^{DD}	`ncombi_DD`	Combinatorial yield (DD)
$N_{\text{part}}^{d\ LL}$	`Npart_d_LL`	$B^0 \to D^{*0}K^{*0}$ yield (LL)
$N_{\text{part}}^{d\ DD}$	`Npart_d_DD`	$B^0 \to D^{*0}K^{*0}$ yield (DD)
$N_{\text{part}}^{s\ LL}$	`Npart_s_LL`	$B_s^0 \to D^{*0}\overline{K}^{*0}$ yield (LL)
$N_{\text{part}}^{s\ DD}$	`Npart_s_DD`	$B_s^0 \to D^{*0}\overline{K}^{*0}$ yield (DD)
α_{010}	`alpha010`	$010/(100+001)$ helicity components proportion
ρ^{LL}	`fracDrho_LL`	$B^0 \to D\rho^0/B_s^0 \to D^{*0}\overline{K}^{*0}$ yield ratio (LL)
ρ^{DD}	`fracDrho_DD`	$B^0 \to D\rho^0/B_s^0 \to D^{*0}\overline{K}^{*0}$ yield ratio (DD)

5.5.4 Mass fit result

The invariant mass fit is performed on the full Run 1 dataset. Fig 5.43 shows the data distribution and the fit result superimposed for the LL and DD categories separated. Fig. 5.44 shows the data distribution and the fit result superimposed with LL and DD categories merged. The B^0 and B_s^0 peaks are clearly seen, and the background description of partially reconstructed $B_{(s)}^0 \to D^{*0}K^{*0}$ and misidentified $B^0 \to D\rho^0$ is satisfactory. The results on all the free parameters are summarised in Table 5.8. They correspond to an estimation over the full fit range. The parameter correlations appear in the matrix of Fig. 5.45. However the signal region, which is used to make the Dalitz plot, is a ± 25 MeV window around the fitted B^0 peak central value. Therefore, the signal and background yields used for the final Dalitz fit (see Sec. 5.7) are computed for this signal region. They are summarised in Table 5.9. In total 99 signal candidates are present for 42.9 background candidates. It results in a signal significance of 8.3 and a purity of 70%. The yields obtained in the B_s^0 region (± 25 MeV window around the fitted B_s^0 peak) are in Table 5.10 and lead to a B^0/B_s^0 yield ratio of $N_d/N_s = 0.54 \pm 0.08$, in good agreement with the scale factor of $k = 0.47 \pm 0.11$ mentioned in Sec. 5.2.3.

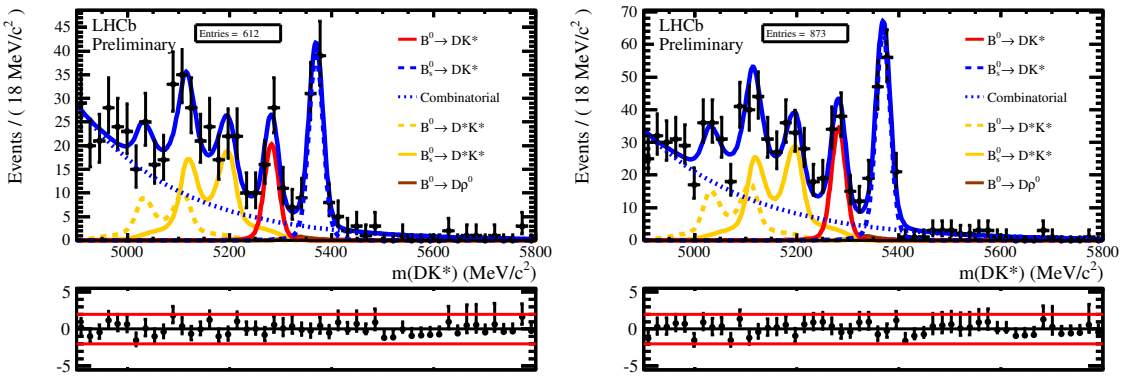

Figure 5.43 – Invariant mass fit of $B^0 \to DK^{*0}$ candidates for LL (left) and DD (right) categories. B^0 peak is in red, B_s^0 peak is in dashed blue, $B_s^0 \to D^{*0}\overline{K}^{*0}$ is in solid orange, $B^0 \to D^{*0}K^{*0}$ is in dashed orange, $B^0 \to D\rho^0$ is in brown and combinatorial background is in dotted blue.

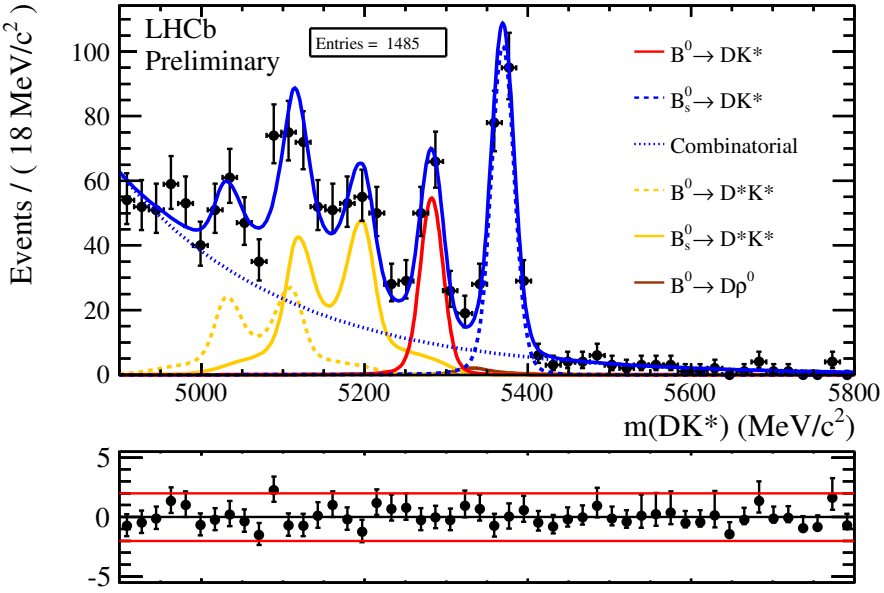

Figure 5.44 – Invariant mass fit of $B^0 \to DK^{*0}$ candidates for LL and DD categories merged.

Table 5.8 – Result of the mass fit (on the full fit window).

Free Parameter	Designation	Fitted Value
μ	`Bs_mean`	5369^{+1}_{-1} MeV
$N^{d\ DD}_{\text{part}}$	`Npart_d_DD`	103^{+25}_{-24}
$N^{d\ LL}_{\text{part}}$	`Npart_d_LL`	61^{+22}_{-21}
$N^{s\ DD}_{\text{part}}$	`Npart_s_DD`	174^{+23}_{-22}
$N^{s\ LL}_{\text{part}}$	`Npart_s_LL`	117^{+20}_{-19}
α_{010}	`alpha010`	$0.9^{+0.1}_{-0.1}$
λ^{DD}	`combi_tau_DD`	$-0.00473^{+0.0003}_{-0.0003}$
λ^{LL}	`combi_tau_LL`	$-0.00508^{+0.0004}_{-0.0004}$
ρ^{DD}	`fracDrho_DD`	$0.039^{+0.009}_{-0.009}$
ρ^{LL}	`fracDrho_LL`	$0.039^{+0.010}_{-0.010}$
$N^{DD}_{B^0}$	`nBd_DD`	70^{+11}_{-10}
$N^{LL}_{B^0}$	`nBd_LL`	41^{+9}_{-8}
$N^{DD}_{B^0_s}$	`nBs_DD`	129^{+13}_{-12}
$N^{LL}_{B^0_s}$	`nBs_LL`	79^{+10}_{-9}
N^{DD}_{comb}	`ncombi_DD`	391^{+32}_{-30}
N^{LL}_{comb}	`ncombi_LL`	310^{+28}_{-26}
σ	`sigma_CB1`	$14.1^{+1.0}_{-0.9}$ MeV

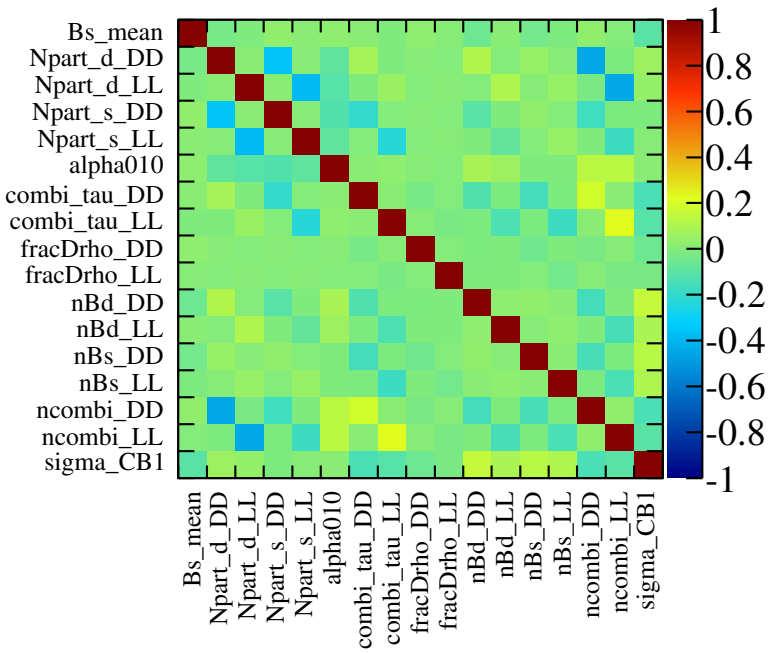

Figure 5.45 – Correlation matrix of the fitted parameters.

Table 5.9 – Total yields in the B^0 signal region.

Component	Yield		
	Total	LL	DD
$N(B^0 \to DK^{*0})$	99 ± 12	37 ± 7	62 ± 9
N(Comb)	26.9 ± 1.8	11.5 ± 1.1	15.5 ± 1.3
$N(B_s^0 \to D^{*0}\overline{K}^{*0})$	13.6 ± 2.0	5.3 ± 1.0	8.2 ± 1.4
$N(B^0 \to D^{*0}K^{*0})$	0.12 ± 0.03	0.054 ± 0.021	0.065 ± 0.019
$N(B^0 \to D\rho^0)$	0.61 ± 0.11	0.23 ± 0.07	0.36 ± 0.09
$N(B_s^0 \to D\overline{K}^{*0})$	1.7 ± 0.3	0.65 ± 0.13	1.06 ± 0.20
Total background	42.9 ± 2.6	17.8 ± 1.5	25.2 ± 1.9

Table 5.10 – Total yields in the B_s^0 region.

Component	Yield		
	Total	LL	DD
$N(B_s^0 \to D\overline{K}^{*0})$	184 ± 14	70 ± 9	114 ± 11
N(Comb)	17.6 ± 1.7	7.4 ± 1.1	10.2 ± 1.3
$N(B_s^0 \to D^{*0}\overline{K}^{*0})$	0.21 ± 0.04	0.104 ± 0.022	0.109 ± 0.023
$N(B^0 \to D\rho^0)$	2.3 ± 0.4	0.90 ± 0.24	1.4 ± 0.4
$N(B^0 \to DK^{*0})$	negligible	negligible	negligible
Total background	20.1 ± 1.8	8.4 ± 1.1	11.8 ± 1.3

5.5.5 Mass fit with a reduced range

The [4.9, 5.0] GeV region in the reconstructed B^0 mass spectrum can be polluted by sources of background other than the combinatorial component. The contribution of the $B^0 \to D^{*0}K^{*0}$ partially reconstructed background is very low in this region. Any contribution of other partially reconstructed background can artificially increase the exponential combinatorial background fraction. To check the mass fit result stability, a fit is performed with a range reduced to [5, 5.8] GeV. The results are shown on Fig. 5.46 with LL and DD categories separated, and on Fig. 5.47 with LL and DD categories merged. The signal and background yields obtained with the reduced range are in Table 5.11. The results are in rather good agreement with those obtained with the nominal range. Some hint of discrepancy could be seen for instance in the combinatorial yield (26.9 ± 1.8 with the nominal range and 24.6 ± 2.2 with the reduced range). A systematic uncertainty accounting for the contribution of $B^+ \to \overline{D}^0 K^+\pi^+\pi^-$ and $B^+ \to \overline{D}^0\pi^+\pi^+\pi^-$ background is determined in Sec. 5.8.2.

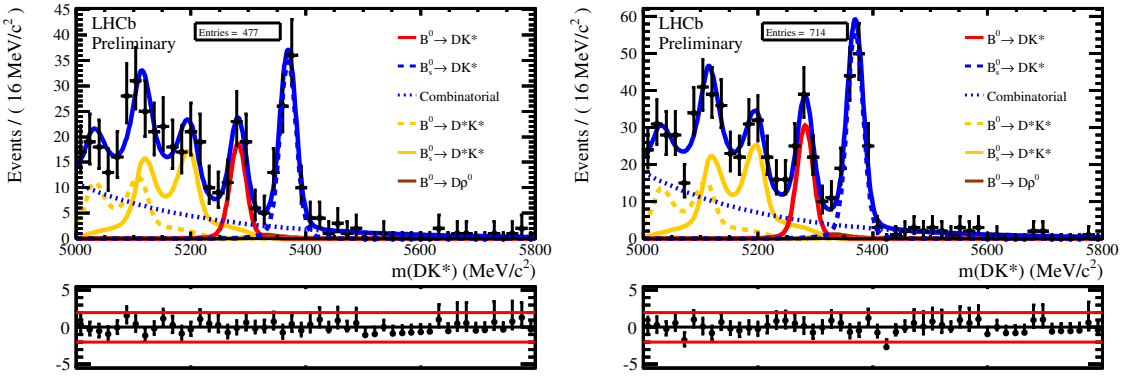

Figure 5.46 – Invariant mass fit of $B^0 \to DK^{*0}$ candidates with the reduced range [5.0, 5.8] GeV for LL (left) and DD (right) categories. B^0 peak is in red, B_s^0 peak is in dashed blue, $B_s^0 \to D^{*0}\overline{K}^{*0}$ is in solid orange, $B^0 \to D^{*0}K^{*0}$ is in dashed orange, $B^0 \to D\rho^0$ is in brown and combinatorial background is in dotted blue.

Table 5.11 – Total yields in the B^0 signal region, with the reduced range.

Component	Yield		
	Total	LL	DD
$N(B^0 \to DK^{*0})$	101 ± 12	38 ± 7	63 ± 10
N(Comb)	24.6 ± 2.2	9.6 ± 1.3	14.9 ± 1.6
$N(B_s^0 \to D^{*0}\overline{K}^{*0})$	14.3 ± 2.2	5.7 ± 1.1	8.5 ± 1.5
$N(B^0 \to D^{*0}K^{*0})$	0.16 ± 0.06	0.09 ± 0.04	0.08 ± 0.04
$N(B^0 \to D\rho^0)$	0.62 ± 0.12	0.25 ± 0.07	0.37 ± 0.09
$N(B_s^0 \to D\overline{K}^{*0})$	1.76 ± 0.32	0.68 ± 0.14	1.08 ± 0.21
Total background	41.4 ± 3.2	16.4 ± 1.9	25.0 ± 2.5

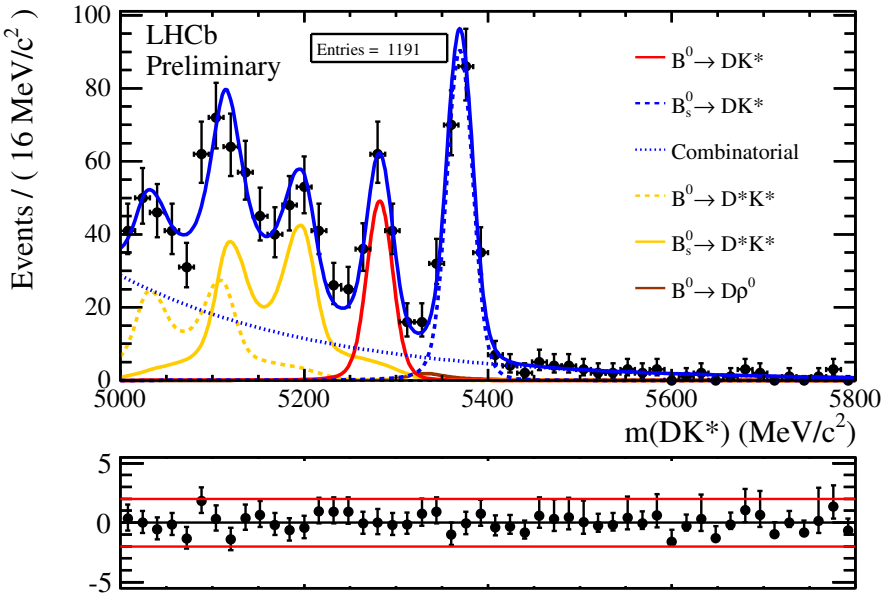

Figure 5.47 – Invariant mass fit of $B^0 \to DK^{*0}$ candidates with the reduced range [5.0, 5.8] GeV for LL and DD categories merged.

5.5.6 Kaon PID cut justification

Initially it was chosen to apply the same PID cut on the kaon candidate as for the ADS/GLW analysis, which means cutting at 3 on $\mathrm{DLL}_{K\pi}$ on both K^{*0} daughters. Indeed it is important to align the K^{*0} candidates selection between ADS/GLW and GGSZ analysis to not jeopardise the γ combination (see Sec. 5.9.1). Nevertheless the opportunity to tighten the PID selection has been investigated. A signal and background yield comparison for several $\mathrm{DLL}_{K\pi}$ cuts on the kaon is summarised in Table 5.12. This study was performed with a former mass fit version, without constraint on the $B^0 \to D\rho^0$ yield and without the $\cos\theta^*$ cut. Cutting at $\mathrm{DLL}_{K\pi} > 5$ for the kaon, compared to 3, keeps $(98 \pm 17)\%$ of the signal while cutting $(59 \pm 30)\%$ of the $B^0 \to D\rho^0$ background. This background is dangerous, since it partially peaks in the $B^0 \to DK^{*0}$ signal region. The $\mathrm{DLL}_{K\pi}$ cut at 5 improves a lot the purity of the signal with a moderate signal efficiency reduction. This estimation is consistent with the one performed with the simulated samples, using the PID calibration tool. The PID efficiency ratio are found to be (for the DD candidates)

$$\frac{\varepsilon_{B_s^0 \to D\bar{K}^{*0}}(\mathrm{DLL}_{K\pi}(K) > 5)}{\varepsilon_{B_s^0 \to D\bar{K}^{*0}}(\mathrm{DLL}_{K\pi}(K) > 3)} = (94.09 \pm 0.08)\%, \tag{5.31}$$

$$\frac{\varepsilon_{B^0 \to D\rho^0}(\mathrm{DLL}_{K\pi}(K) > 5)}{\varepsilon_{B^0 \to D\rho^0}(\mathrm{DLL}_{K\pi}(K) > 3)} = (46.17 \pm 0.14)\%. \tag{5.32}$$

5.5.7 Fake D^0 background estimation

Two categories can be distinguished among the combinatorial backgrounds: the combinatorial D^0 or the combinatorial K^{*0} candidates. In the first case the D^0 candidate is not a real particle, whereas in the second case the D^0 candidate is real. Hence these two different backgrounds

Table 5.12 – Signal and background yields comparison for several PIDK cuts on the kaon.

Component	Yield				
	Nominal: $BDT > 0.75$ $\mathrm{DLL}_{K\pi}(K) > 5$	$BDT > 0.75$ $\mathrm{DLL}_{K\pi}(K) > 3$	$BDT > 0.8$ $\mathrm{DLL}_{K\pi}(K) > 3$	$BDT > 0.75$ $\mathrm{DLL}_{K\pi}(K) > 6$	$BDT > 0.7$ $\mathrm{DLL}_{K\pi}(K) > 6$
$N(B^0 \to DK^{*0})$	106 ± 12	108 ± 14	106 ± 13	98 ± 12	102 ± 13
$N(\mathrm{Comb})$	33.7 ± 2.1	44.0 ± 2.4	37.3 ± 2.3	29.8 ± 2.0	33.0 ± 2.1
$N(B_s^0 \to D^{*0}\overline{K}^{*0})$	19.7 ± 2.6	22.8 ± 2.8	23.1 ± 2.8	19.2 ± 2.5	20.1 ± 2.6
$N(B^0 \to D^{*0}K^{*0})$	0.17 ± 0.04	0.19 ± 0.04	0.19 ± 0.04	0.16 ± 0.04	0.16 ± 0.04
$N(B^0 \to D\rho^0)$	2.2 ± 1.5	5.4 ± 1.7	6.3 ± 1.8	1.8 ± 1.3	2.4 ± 1.5
$N(B_s^0 \to D\overline{K}^{*0})$	1.6 ± 0.3	1.4 ± 0.3	1.4 ± 0.3	1.4 ± 0.3	1.4 ± 0.3
Total background	57.3 ± 3.2	74 ± 4	68.2 ± 3.5	52.5 ± 3.0	57.2 ± 3.2

are called "fake D^0" and "real D^0". It is important to disentangle these two backgrounds since their distribution on the Dalitz plane is different. The fake D^0 distribution is flat, whereas the real D^0 candidates are described through the $D \to K^0_S\pi^+\pi^-$ model (see Sec. 5.6). In order to estimate the fake D^0–real D^0 proportion in the combinatoric background, two methods have been investigated: fitting the $m(K^0_S\pi^+\pi^-)$ invariant mass and counting the number of wrong sign (WS) $D^0 \to K^0_S\pi^\pm\pi^\pm$ candidates. The WS candidates are a good proxy to mimic non physical background due to random combination of tracks.

Mass fit of the D candidates

To distinguish the fake and real D^0 a fit to the $m(K^0_S\pi^+\pi^-)$ invariant mass is performed on the D^0 candidates passing the full selection. Real D^0 are described with a gaussian. Fake D^0 are described with a constant polynomial.

A first fit is performed on the D^0 candidates in the B^0_s region (± 25 MeV around the fitted B^0_s mass). The mean and the width of the gaussian are let free. The fit is performed simultaneously on LL and DD candidates, with a common mean for these two categories. The result of this fit is represented on Fig. 5.48. Since in the B^0_s region the statistics is higher, this fit enables to fix the width of the gaussian for the second fit performed on the D^0 candidates of the B^0 signal mass region. The result of the second fit is represented on Fig. 5.49. As it is an extended fit, it estimates directly the respective yields of the fake and real D^0 candidates, given in Table 5.13.

The statistical sensitivity is poor. Nevertheless it shows that the proportion of fake D^0 candidates is low. For comparison, the estimated total combinatorial yields, including the fake

Table 5.13 – Yields of fake and real D^0 candidates lying in the $B^0 \to DK^{*0}$ signal region.

Yield	LL	DD
n_{fakeD}	2^{+6}_{-4}	2^{+5}_{-3}
n_{realD}	53^{+9}_{-8}	84^{+10}_{-10}

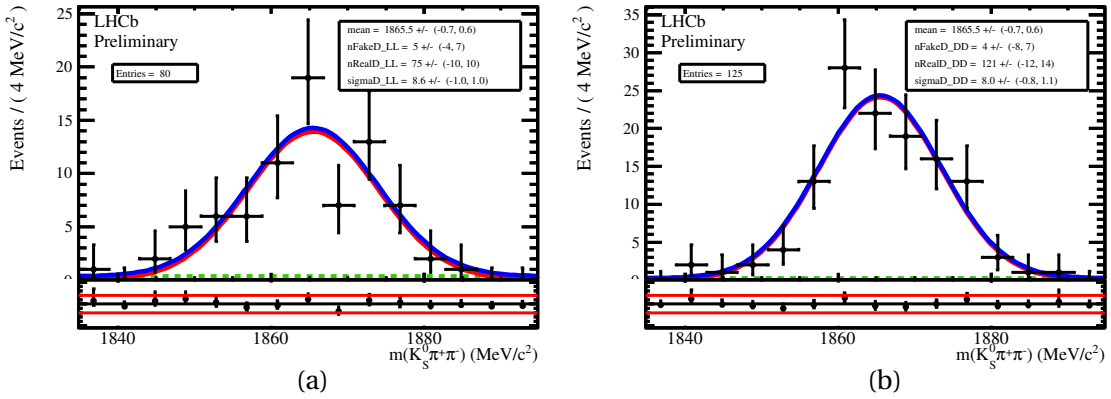

Figure 5.48 – Fit to $m(K^0_S\pi^+\pi^-)$ invariant mass of LL (a) and DD (b) candidates from the B^0_s region. The gaussian is in red and the polynomial function in dashed green.

D^0 and some real D^0 candidates, are respectively of 11.5 and 15.5 for LL and DD categories.

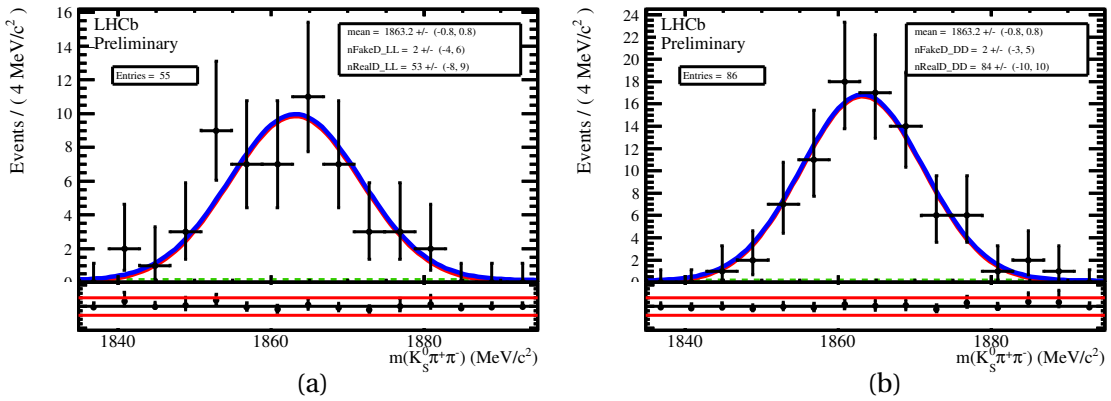

Figure 5.49 – Fit of $m(K^0_S\pi^+\pi^-)$ invariant mass of LL (a) and DD (b) candidates from the B^0 region. The gaussian is in red and the polynomial function in dashed green.

To check that the constant polynomial is a reasonable model for the fake D^0 candidates, the D^0 mass distribution of WS candidates is studied. Fig. 5.50 shows this distribution after preselection and with several BDT cuts. The distributions are flat, even after BDT selections keeping more signal-like candidates. Moreover no correlation between the BDT output value and the D^0 mass distribution appears (Fig. 5.51).

Wrong sign candidates estimation

Another possible method is to estimate the number of WS candidates left after full selection. The selection is therefore applied on WS candidates. The B^0 invariant mass distribution of this WS candidates can be seen on Fig. 5.52. After full selection, no event remains in the B^0 signal region. If a 95% confidence level is assumed for a Poisson variable, no event corresponds to an interval of [0.;3.09] at the 95% confidence level. Taking into account the 0.1 prescale applied to

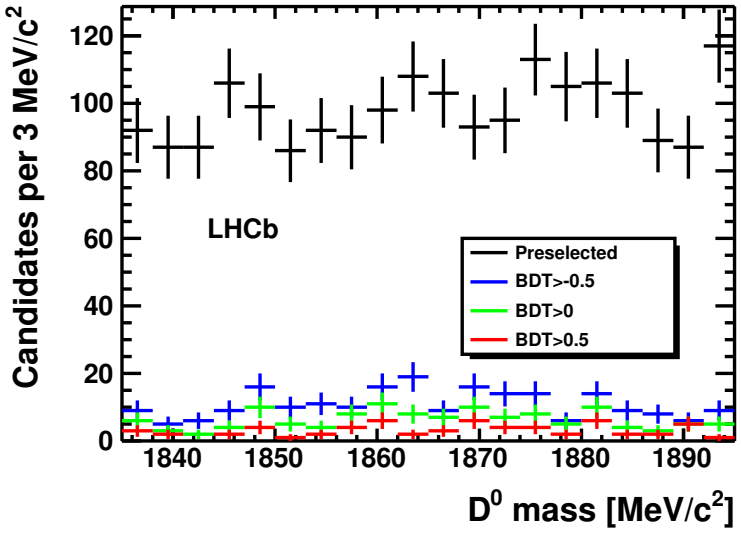

Figure 5.50 – D^0 mass distribution for WS candidates after preselection and several BDT cut.

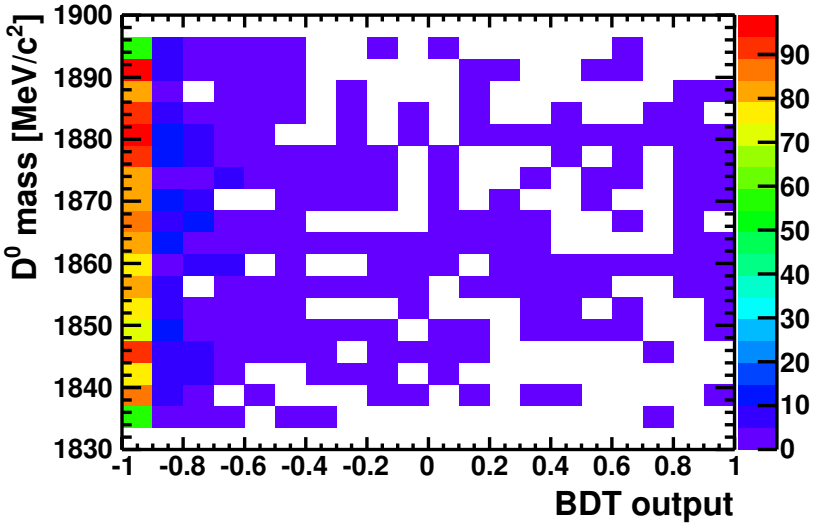

Figure 5.51 – D^0 mass distribution for WS candidates after preselection as a function of the BDT ouput value.

the WS lines [6], between 0 and 31 fake D^0 events are expected, among the total 142 combinatorial candidates. Therefore both estimations, with the D^0 mass fit and with the WS candidates, are in agreement. However, due to the low statistics, the WS estimation is less precise.

It is clear that the combinatorial background is mainly composed of real D^0 candidates. As a baseline the numbers of fake D^0 candidates n_{fakeD} estimated with the mass fit are assumed, with

[6] To prevent the WS events, which are pure background, from taking an unreasonable amount of the trigger bandwidth, they are prescaled. Only 10% of the events which in principle fire the trigger are kept.

$n^{LL}_{\text{fakeD}} = 2$ and $n^{DD}_{\text{fakeD}} = 2$. A systematic uncertainty is deduced from this hypothesis, by varying these estimations within their statistical uncertainty. Which means assuming $n^{LL}_{\text{fakeD}} = 0$ or 8 and $n^{DD}_{\text{fakeD}} = 0$ or 7.

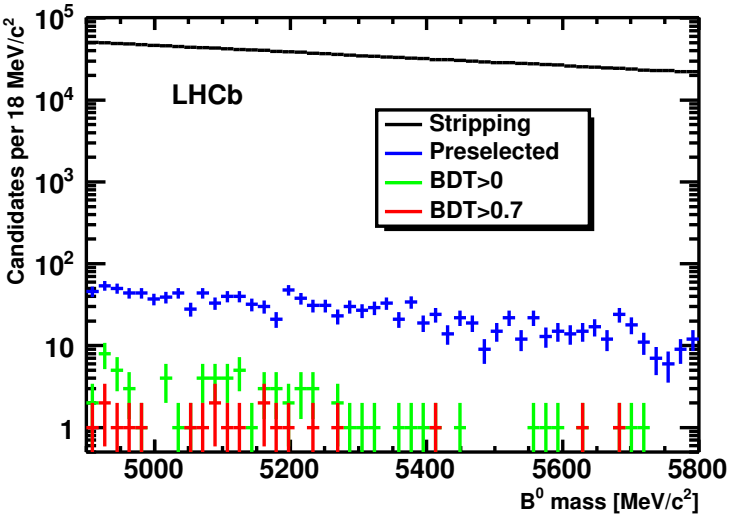

Figure 5.52 – B^0 invariant mass of WS candidates after stripping (black), preselection (blue), BDT cut at 0 (green) and at 0.7 (red). The extra $|\cos\theta^*| > 0.4$ cut is not applied

5.5.8 Mass fit stability study

Because of the low statistics available, it is important to check that the mass fit result is stable and has no strong bias. Therefore a toy study is performed by generating ten thousand pseudo datasets from the nominal fit result. These pseudo datasets are then fitted with the nominal fit model. From these ten thousand fits the pull distributions of the floating parameters are made. Some parameters have non gaussian errors, therefore the pulls are made with the asymmetric errors given by the MINOS algorithm [151]. Hence the pull for a given parameter x is defined as

$$\mathscr{P}_x \equiv \begin{cases} \frac{x_{\text{fit}} - x_{\text{gen}}}{\sigma^+} & \text{if } x_{\text{fit}} - x_{\text{gen}} < 0, \\ \frac{x_{\text{fit}} - x_{\text{gen}}}{\sigma^-} & \text{otherwise,} \end{cases} \tag{5.33}$$

where x_{fit} is the fitted parameter value on a given pseudo dataset, x_{gen} is the generated value (coming from the nominal fit result) and $\sigma^{\pm}$ the asymmetric statistical uncertainties.

Only the combinatorial yields (Fig. 5.55) and the Crystal Ball PDF width (Fig. 5.56) show evidence of bias. Nevertheless these biases are small and can be neglected in the analysis. They could be corrected with the following formula

$$x_{\text{cor}} = x_{\text{meas}} - \mu_{\text{pull}}\sigma_{\text{meas}}, \tag{5.34}$$

where x_{cor} is the bias-corrected parameter value, x_{meas} is the measured parameter value with an uncertainty of σ_{meas} and μ_{pull} the identified bias. It would give on the combinatorial LL yields $N^{LL}_{\text{comb}} = 391^{+32}_{-30}$ a correction equal to $\mu_{\text{pull}}\sigma_{\text{meas}} = -0.053 \times 32 \approx -1.7$. Similarly, on the Crystal

Ball width $\sigma = 14.1^{+1.0}_{-0.9}$, it would give a correction of -0.035 MeV. These corrections being very small compared to the statistical uncertainty of the parameters, the effect of these biases are neglected in the rest of the analysis.

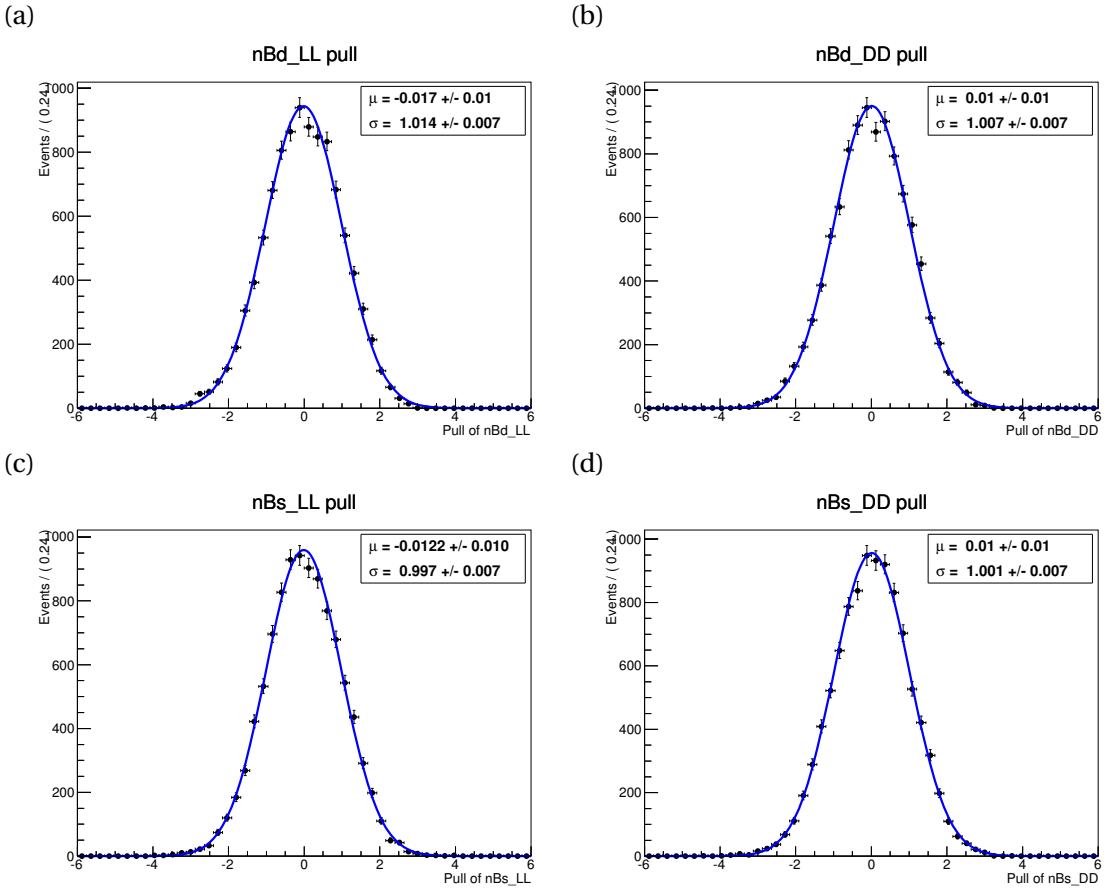

Figure 5.53 – Pull distributions of the $B^0 \to DK^{*0}$ yields of LL (a) and DD (b) categories and of the $B^0_s \to D\overline{K}^{*0}$ yields of LL (c) and DD (d) categories.

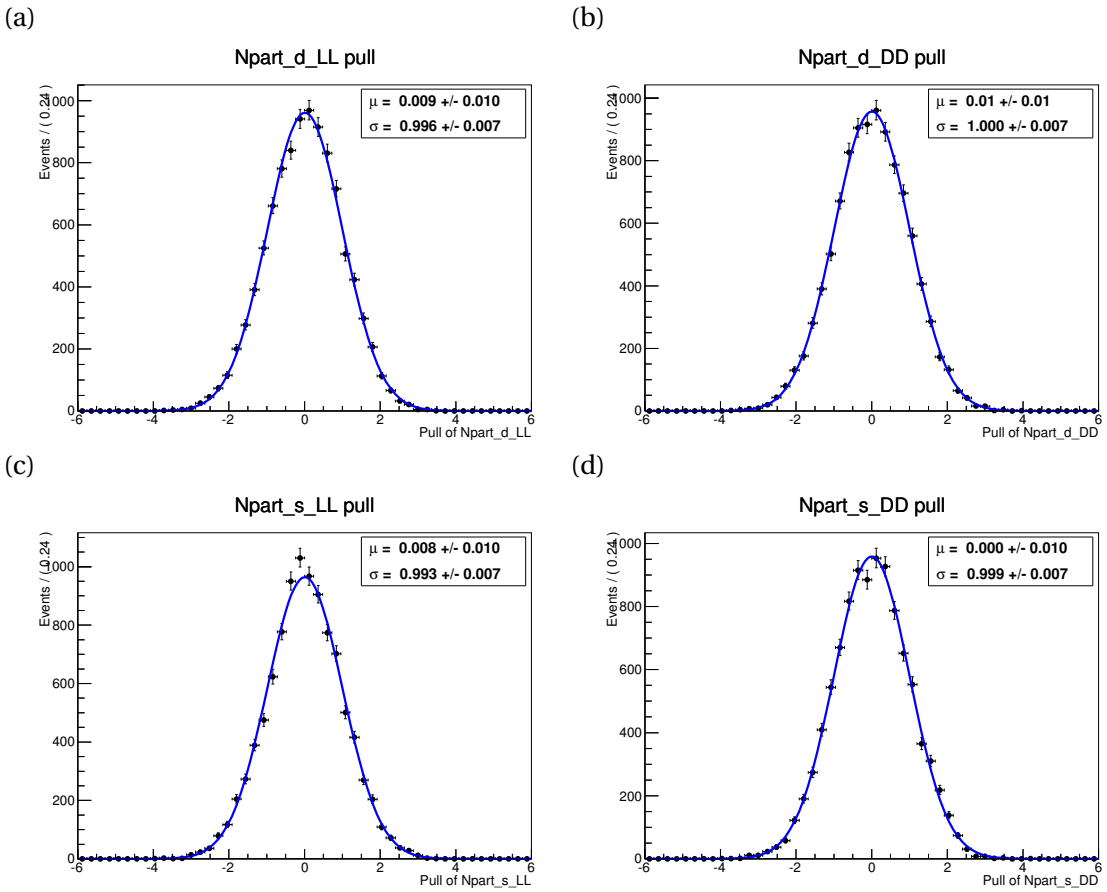

Figure 5.54 – Pull distributions of the $B^0 \to D^{*0}K^{*0}$ yields of LL (a) and DD (b) categories and of the $B_s^0 \to D^{*0}\overline{K}^{*0}$ yields of LL (c) and DD (d) categories.

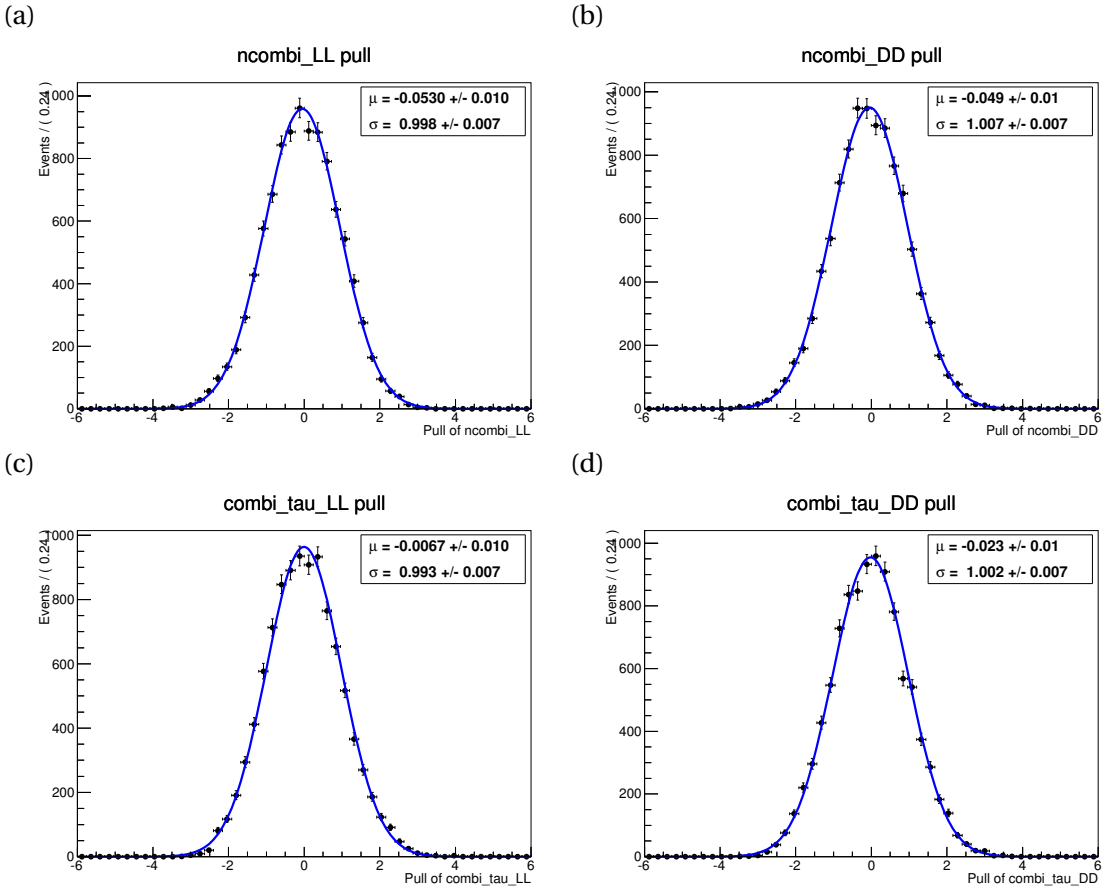

Figure 5.55 – Pull distributions of the combinatorial background yields of LL (a) and DD (b) categories, and of the combinatorial exponential slope of LL (c) and DD (d) categories.

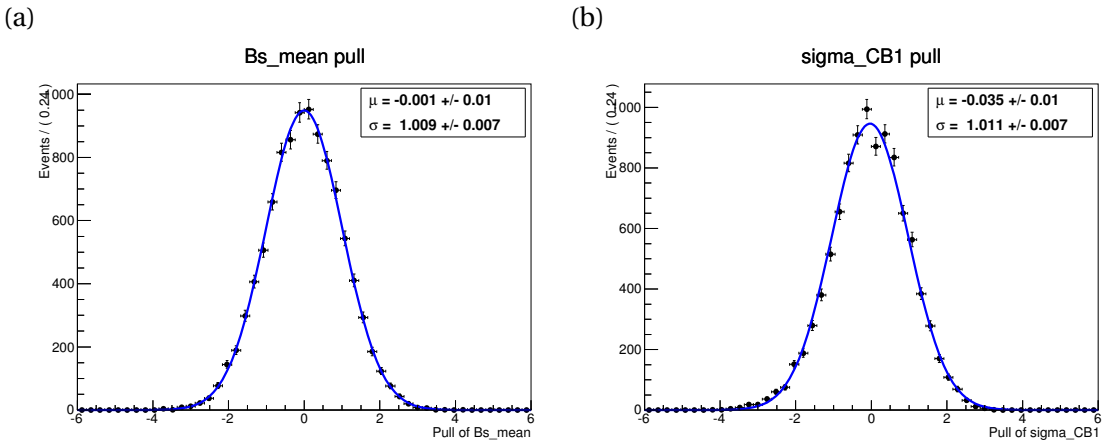

Figure 5.56 – Pull distributions of the mean (a) and the width (b) of the double Crystal Ball PDF modelling the B^0 and B_s^0 peaks.

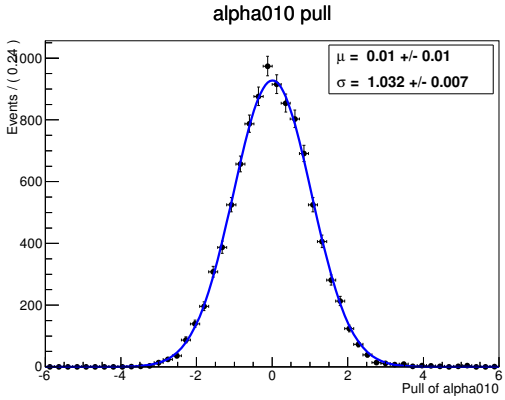

Figure 5.57 – Pull distribution of the helicity component proportion in the $B^0_{(s)} \to D^{*0}K^{*0}$ partially reconstructed background (α_{010} parameter).

5.6 Model of the $D \to K^0_S \pi^+ \pi^-$ decay

As mentioned in Sec. 5.1, the decay amplitude of the $D \to K^0_S \pi^+ \pi^-$ transition (defined in Eq. 2.18 and 2.19) is described with the BaBar model. This empirical model, described in Ref. [51], is used by this collaboration for the γ analysis of the $B^\pm \to D^{(*)} K^{(*)\pm}$ decays [8] and is a mixture of an isobar model for the P- and D-waves contributions, a generalised LASS amplitude for the K-π S-wave contribution and a K-matrix with P-vector approach for the π-π S-wave contribution. The model has been already used by the LHCb $B^\pm \to DK^\pm$ model dependent GGSZ analysis [52]. The present section summarises the main points of this model. A more detailed presentation of the Dalitz plot formalism can be found for instance in Ref. [152].

The partial decay rate of a scalar particle into three daughters, like $D \to abc$, can be expressed as

$$\mathrm{d}\Gamma = \frac{1}{(2\pi)^3} \frac{1}{32 m_D^3} |\mathscr{M}|^2 \mathrm{d}m^2_{ab} \mathrm{d}m^2_{bc}, \tag{5.35}$$

where m_D is the mass of the D meson, m^2_{ab} and m^2_{bc} are the squared invariant masses of the (ab) and (bc) daughter pairs, and $\mathscr{M}$ is the matrix element describing the dynamic of the $D \to abc$ decay. The scatter plot in m^2_{ab} and m^2_{bc} is called a Dalitz plot and is directly linked to the underlying physics in the $D \to abc$ process. The event distribution across the (m^2_{ab}, m^2_{bc}) arises from the variation of $|\mathscr{M}|^2$. If it is constant, the kinematically allowed region of the plot is uniformly populated. In the case of the $D \to K^0_S \pi^+ \pi^-$ decay a total of eleven partial waves is used to describe the dynamics. The Lorentz invariant amplitude is obtained as a coherent sum of quasi-2-body amplitudes

$$\mathscr{M} = \mathscr{M}_{\pi\pi} + a_{K\pi} e^{i\phi_{K\pi}} \mathscr{M}_{K\pi} + \sum_{P,D-waves} a_r e^{i\phi_r} \mathscr{M}_r, \tag{5.36}$$

where:

- $\mathscr{M}_{\pi\pi}$ is the amplitude of the $\pi\pi$ S-wave, described by a K-matrix with P-vector approach.
- $\mathscr{M}_{K\pi}$ is the amplitude of the $K\pi$ S-wave, namely the $K^{*\pm}_0(1430)$ resonance, described by a generalised LASS amplitude.
- $\mathscr{M}_r$ are the amplitudes of the narrow resonances, which are P-waves ($\rho(770)^0$, $\omega(782)$, $K^*(782)^\pm$ and $K^*(1680)^-$) and D-waves ($K^*{}_2(1430)^\pm$ and $f_2(1270)$).

The $a_{K\pi} e^{i\phi_{K\pi}}$ and $a_r e^{i\phi_r}$ are the complex coefficients of the linear combination of the resonances. They are determined by the BaBar collaboration [51] and are parameters of the final Dalitz fit of this analysis.

5.6.1 P and D waves

Since the P and D waves are narrow and isolated resonances, they are modelled by relativistic Breit-Wigner propagators, except for the $\rho(770)^0$ which is modelled with a Gounaris-Sakurai propagator [153] (Δ_r). The angular distribution of the decay products is described through the Zemach formalism ($Z_l(m^2_{ab}, m^2_{ac})$ factors). The spin effect of the resonance is accounted with some effective centrifugal Barrier factors, namely the Blatt-Weisskopf factors ($B_l(q, q_r)$). Hence the Lorentz invariant amplitude of the decay $D \to r(ab)c$ is expressed as

$$\mathscr{M}_r = Z_l(m^2_{ab}, m^2_{ac}) B_l(p, p_r) B_l(q, q_r) \Delta_r(m_{ab}), \tag{5.37}$$

where l is the orbital angular momentum between r and c (which is the spin of r since D, a, b and c are scalars), p is the momentum of c in the (ab) resonance rest-frame, q is the momentum of a (or b) in the (ab) resonance rest-frame, p_r and q_r are p and q values in the case of $m_{ab} = m_r$.

The Zemach factors values are equal to

$$Z_0 = 1, \tag{5.38}$$

$$Z_1 = m_{ac}^2 - m_{bc}^2 - \frac{(m_D^2 - m_c^2)(m_a^2 - m_b^2)}{m_{ab}^2}, \tag{5.39}$$

$$Z_2 = \left[m_{ac}^2 - m_{bc}^2 - \frac{(m_D^2 - m_c^2)(m_a^2 - m_b^2)}{m_{ab}^2} \right]^2 - \tag{5.40}$$

$$- \frac{1}{3} \left[m_{ab}^2 - 2(m_D^2 + m_c^2) + \frac{(m_D^2 - m_c^2)^2}{m_{ab}^2} \right] \left[m_{ab}^2 - 2(m_a^2 + m_b^2) + \frac{(m_a^2 - m_b^2)^2}{m_{ab}^2} \right]. \tag{5.41}$$

Instead of the Zemach factors, the helicity formalism can also be applied. Then, the mass term m_{ab} is replaced by the mass of the resonance m_r. In the nominal model the Zemach factors are used, and a systematic uncertainty is assigned, to take into account the difference with the helicity formalism (Sec. 5.8.5).

The Blatt-Weisskopf factors are equal to

$$B_0^2(q, q_r) = 1, \tag{5.42}$$

$$B_1^2(q, q_r) = \left(\frac{q}{q_r} \right)^2 \frac{(Rq_r)^2 + 1}{(Rq)^2 + 1}, \tag{5.43}$$

$$B_2^2(q, q_r) = \left(\frac{q}{q_r} \right)^4 \frac{(Rq_r)^4 + 3(Rq_r)^2 + 9}{(Rq)^4 + 3(Rq)^2 + 9}, \tag{5.44}$$

where R is an effective radius fixed to $1.5\,\text{GeV}^{-1}$.

5.6.2 K matrix for $\pi\pi$ S-wave

The $\pi\pi$ S-wave is described with a K matrix formalism. Five channels, noted α, are considered: $\pi^+\pi^-$,$K\overline{K}$,4π,$\eta\,\eta$ and $\eta\,\eta'$. With the P vector approach, the decay amplitude is

$$\mathcal{M}_{\pi\pi}(m_{\pi\pi}) = \sum_\alpha \left[I - i\hat{K}(m_{\pi\pi})\rho(m_{\pi\pi}) \right]^{-1}_{\pi\pi,\alpha} \hat{P}_\alpha(m_{\pi\pi}). \tag{5.45}$$

$\hat{K}$ is the matrix describing the S-wave scattering process, ρ is the phase-space matrix and $\hat{P}$ is the initial production vector. This formalism can be viewed as a production of five different states all propagated into the final $\pi\pi$ state through the $\left[I - i\hat{K}(m_{\pi\pi})\rho(m_{\pi\pi}) \right]^{-1}$ scattering term. It supposes that the two-body $\pi\pi$ system does not interact with the rest of the final state in the production process.

The K matrix is expressed as

$$\hat{K}_{ij}(m_{\pi\pi}) = \left(\sum_\alpha \frac{g_{\alpha i}^0 g_{\alpha j}^0}{m_\alpha^2 - m_{\pi\pi}^2} + f_{ij}^{sc} \frac{1\,\text{GeV}^2 - s_0^{sc}}{m_{\pi\pi}^2 - s_0^A} \right) \frac{1\,\text{GeV}^2 - s_0^A}{m_{\pi\pi}^2 - s_0^A} \left(m_{\pi\pi}^2 - \frac{s_A m_\pi^2}{2} \right), \tag{5.46}$$

where all the parameters $g_{\alpha i}^0$, m_α, f_{ij}^{sc}, s_0^{sc}, s_0^A and s_A are fixed by scattering data [154]. All their values are summarised in Tab. 5.14.

Similarly, the P vector is parametrised as

$$\hat{P}_j(m_{\pi\pi}) = \sum_\alpha \frac{\beta_\alpha^0 g_{\alpha j}^0}{m_\alpha^2 - m_{\pi\pi}^2} + f_{\pi\pi,j}^{pr} \frac{1\,\text{GeV}^2 - s_0^{pr}}{m_{\pi\pi}^2 - s_0^{pr}}, \tag{5.47}$$

Table 5.14 – K-matrix parameters from a global analysis of $\pi\pi$ scattering data taken from [154] (unit is in GeV).

m_α	$g^\alpha_{\pi\pi}$	$g^\alpha_{K\bar{K}}$	$g^\alpha_{4\pi}$	$g^\alpha_{\eta\eta}$	$g^\alpha_{\eta\eta'}$
0.65100	0.22889	-0.55377	0.	-0.39899	-0.34639
1.20360	0.94128	0.55095	0.	0.39065	0.31503
1.55817	0.36856	0.23888	0.55639	0.18340	0.18681
1.21000	0.33650	0.40907	0.85679	0.19906	-0.00984
1.82206	0.18171	-0.17558	-0.79658	-0.00355	0.22358
s^{sc}_0	$f^{sc}_{\pi\pi,\pi\pi}$	$f^{sc}_{\pi\pi,K\bar{K}}$	$f^{sc}_{\pi\pi,4\pi}$	$f^{sc}_{\pi\pi,\eta\eta}$	$f^{sc}_{\pi\pi,\eta\eta'}$
-3.92637	0.23399	0.15044	-0.20545	0.32825	0.35412
s^0_A	s_A				
-0.15	1				

where the β^0_α complex production parameters and the production background parameters $f^{pr}_{\pi\pi,j}$ and s^{pr}_0 are determined by the BaBar collaboration, from a tagged $D \to K^0_S \pi^+ \pi^-$ data sample [51]. They are summarised in Tab. 5.15. The parameters $\beta_{\eta\eta'}$, $f^{pr}_{\pi\pi,\eta\eta}$ and $f^{pr}_{\pi\pi,\eta\eta'}$ are fixed to zero due to a lack of sensitivity.

Table 5.15 – P vector parameters determined by the BaBar collaboration [51].

	Amplitude	Phase
$\beta_{\pi\pi}$	5.54 ± 0.06	-0.054 ± 0.007
$\beta_{K\bar{K}}$	15.64 ± 0.06	-3.125 ± 0.005
$\beta_{4\pi}$	44.6 ± 1.2	2.731 ± 0.015
$\beta_{\eta\eta}$	9.3 ± 0.2	2.30 ± 0.02
$f^{pr}_{\pi\pi,\pi\pi}$	11.43 ± 0.11	-0.005 ± 0.009
$f^{pr}_{\pi\pi,K\bar{K}}$	15.5 ± 0.4	-1.13 ± 0.02
$f^{pr}_{\pi\pi,4\pi}$	7.0 ± 0.7	0.99 ± 0.11

5.6.3 Generalised LASS-like parametrisation

The LASS experiment found a broad spinless resonance in the $K^-\pi^+$ spectrum from $K^- p \to K^-\pi^+ n$ scattering [155]. This ${K^*}_0(1430)^\pm$ resonance cannot be described with an usual Breit-Wigner function. Instead a sum of a Breit-Wigner and a non resonant component parametrised with an effective range is used. This LASS parametrisation is generalised to production experi-

ments as

$$\mathcal{M}_{K\pi} = R\sin\delta_R e^{i(\delta_R+\phi_R)} e^{2i(\delta_B+\phi_B)} + B\sin(\delta_B+\phi_B) e^{i(\delta_B+\phi_B)}, \tag{5.48}$$

where

$$\tan\delta_R = \frac{m_r\Gamma(m_{ab})}{m_r^2 - m_{ab}^2}, \tag{5.49}$$

$$\cot\delta_B = \frac{1}{aq} + \frac{rq}{2}, \tag{5.50}$$

with a the scattering length, r the effective interaction range and q the momentum of the resonant particles in the $(K\pi)$ resonance rest frame. All the parameters of this line shape are fixed to those determined by BaBar [51]. Their are summarised in Tab. 5.16.

Table 5.16 – Generalised LASS line shape parameters for the $K\pi$ S-wave component, taken from [51].

Parameter	Value
$M_{K^*_0(1430)}$	$1421.5 \pm 1.6\,\text{MeV}$
$\Gamma_{K^*_0(1430)}$	$247 \pm 3\,\text{MeV}$
B	0.62 ± 0.04
ϕ_B	$-0.100 \pm 0.010\,\text{rad}$
R	1
ϕ_R	$1.10 \pm 0.02\,\text{rad}$
a	$0.224 \pm 0.003\,\text{GeV}$
r	$-15.01 \pm 0.13\,\text{GeV}$

5.7 Full fit

To estimate the *CP* observables $(x_\pm, y_\pm)$ defined in Sec.5.1, an unbinned extended maximum likelihood fit is performed along three variables: the B^0 reconstructed invariant mass (m_{B^0}) and the Dalitz plot coordinates (m^2_+ and m^2_-). Only the candidates falling in a ± 25 MeV window around the fitted B^0 mass are analysed. The full negative log-likelihood of the fit can be expressed as

$$\begin{aligned}\mathscr{L} = &-2\sum_{B^0 cand.} \ln\left(\sum_{c\in\{all\ categ.\}} N_c f_c^{mass}(m_{B^0};\vec{p}_c^{\,mass}) f_c^{B^0\ model}(m^2_+, m^2_-; x_+, y_+, \kappa, \vec{p}_c^{\,model})\right)\\ &-2\sum_{\bar{B}^0 cand.} \ln\left(\sum_{c\in\{all\ categ.\}} N_c f_c^{mass}(m_{B^0};\vec{p}_c^{\,mass}) f_c^{\bar{B}^0\ model}(m^2_+, m^2_-; x_-, y_-, \kappa, \vec{p}_c^{\,model})\right)\\ &+2N\end{aligned} \tag{5.51}$$

where the sum is performed on all the candidates in the signal region. c is the event categories (signal/backgrounds), N_c is the yield of a category c, f_c^{mass} is the mass PDF of category c, $\vec{p}_c^{\,mass}$ are the mass PDF parameters for category c, $f_c^{B\ model}$ is the decay model over the Dalitz plane of category c and $\vec{p}_c^{\,model}$ are the parameters of the decay model for category c. The $(x_\pm, y_\pm)$ cartesian parameters and the κ coherence factor are explicitly written out from $\vec{p}_c^{\,model}$, and enter only in the $B^0 \to DK^{*0}$ signal decay model.

The distortion caused by the selection efficiency is taken into account in the $f_c^{B\ model}$ PDF. This term is the multiplication of the physics decay model ($\mathscr{P}_c^B$) by the efficiency description function (ε, obtained from the spline interpolation described in Sec. 5.3),

$$f_c^{B\ model}(m^2_+, m^2_-) = \mathscr{P}_c^B(m^2_+, m^2_-)\cdot\varepsilon(m^2_+, m^2_-) \tag{5.52}$$

The fit is preformed in two steps:

1. 1D fit of the B mass distribution (called "mass fit"), as explained in Sec. 5.5. It determines the signal and background yields as wells as their mass shape parameters ($\vec{p}_c^{\,mass}$).
2. 3D fit along (m_{B^0}, m^2_+, m^2_-) (called "Dalitz fit"), corresponding to the full likelihood of Eq. 5.51. All the mass shapes and the yields are fixed from the mass fit alone.

5.7.1 Signal description

The signal PDF on the Dalitz plane, as explained in Sec. 2.6.1, is expressed with the functional

$$\mathscr{P}(A, z, \kappa) = \left|A\right|^2 + |z|^2\left|\bar{A}\right|^2 + 2\kappa\mathscr{R}e\left[zA^*\bar{A}\right]. \tag{5.53}$$

With A_D ($A_{\bar{D}}$) corresponding to the decay amplitude of $D^0 \to K^0_S\pi^+\pi^-$ ($\bar{D}^0 \to K^0_S\pi^-\pi^+$) described in Sec. 5.6, the signal PDF is

$$\mathscr{P}_- \propto \mathscr{P}(A_D, z_-, \kappa), \tag{5.54}$$

$$\mathscr{P}_+ \propto \mathscr{P}(A_{\bar{D}}, z_+, \kappa), \tag{5.55}$$

for the $\bar{B}^0$ and B^0 candidates respectively. The κ coherence factor is fixed to 0.93, thanks to the method explained in Sec. 5.9.1.

5.7.2 Background description

The different background components do not follow the same distribution as the signal. The following section presents the models used to describe the considered background component over the Dalitz plane. All the background contributions are taken into account except the $B^0 \to D^{*0}K^{*0}$ component which has a negligible yield of 0.12 (see Tab. 5.9).

$B_s^0 \to D\overline{K}^{*0}$ and $B_s^0 \to D^{*0}\overline{K}^{*0}$ contributions

In the $B_s^0 \to D\overline{K}^{*0}$ and $B_s^0 \to D^{*0}\overline{K}^{*0}$ channels, the Cabbibo-suppressed diagram is negligible (order $\mathcal{O}(\lambda^4)$, where λ is the Wolfenstein parameter) compared to the Cabbibo-favoured one ($\mathcal{O}(\lambda^2)$). Hence, the *CP* violation effect is neglected for $B_s^0 \to D\overline{K}^{*0}$ and $B_s^0 \to D^{*0}\overline{K}^{*0}$, which implies for this channels $r_{B_s^0} = 0$. Hence the Dalitz PDF for this contributions are

$$\mathscr{P}_{B_s^0} = \mathscr{P}(A_{\overline{D}}, 0, 0), \tag{5.56}$$

$$\mathscr{P}_{\overline{B}_s^0} = \mathscr{P}(A_D, 0, 0), \tag{5.57}$$

where $\mathscr{P}(A, z, \kappa)$ is the functional form defined in Eq. 2.37, and A_D ($A_{\overline{D}}$) is the decay amplitude of $D^0 \to K_S^0\pi^+\pi^-$ ($\overline{D}^0 \to K_S^0\pi^-\pi^+$) given by the model explained in Sec.5.6. One important thing to notice, is that a B_s^0 ($\overline{B}_s^0$) candidate corresponds to a $\overline{K}^{*0}$ (K^{*0}) daughter. It is the opposite for the $B^0 \to DK^{*0}$ signal, since a K^{*0} ($\overline{K}^{*0}$) tags a B^0 ($\overline{B}^0$). Hence, on the Dalitz plot of B^0 candidates the contributions of $\overline{B}_s^0 \to DK^{*0}$ and $\overline{B}_s^0 \to D^{*0}K^{*0}$ are taken. On the contrary, for the Dalitz plot of $\overline{B}^0$ candidates the contributions of $B_s^0 \to D\overline{K}^{*0}$ and $B_s^0 \to D^{*0}\overline{K}^{*0}$ are used.

$B^0 \to D\rho^0$ contribution

For the misidentified $B^0 \to D\rho^0$ component, the B flavor state cannot be determined. It results in an incoherent superposition of D flavor states. Hence the Dalitz PDF for this contribution assumes equal probability for the D^0 and $\overline{D}^0$ states:

$$\mathscr{P}_{D\rho^0} = \frac{|A_D|^2 + |A_{\overline{D}}|^2}{2}. \tag{5.58}$$

Combinatorial background

As explained in Sec. 5.5.7, the combinatorial background is composed of fake and real D mesons. The fake D are candidates made by random combination of four tracks faking the $D \to K_S^0\pi^+\pi^-$ decay. Hence this contribution follows a phase space distribution

$$\mathscr{P}_{\text{Comb}}^{\text{fake } D} = 1. \tag{5.59}$$

The real D candidates arise from two random tracks faking the K^{*0} candidates, attached to real D mesons to make some B^0 candidates. Assuming equal probability for the D^0 and $\overline{D}^0$ states, the decay model of this background is an incoherent superposition of D^0 and $\overline{D}^0$ amplitudes

$$\mathscr{P}_{\text{Comb}}^{\text{real } D} = \frac{|A_D|^2 + |A_{\overline{D}}|^2}{2}. \tag{5.60}$$

5.7.3 Fitter validation

In order to check the fitter implementation two kinds of toy studies are performed. First, signal only pseudo-data samples are considered, then pseudo-data samples including all the considered background. The physics input values chosen are $r_{B^0} = 0.24$ [59], $\delta_{B^0} = 336^\circ$ [59], $\gamma = 73.2^\circ$ [11] and a coherence factor of $\kappa = 0.93$. These values are translated in terms of cartesian parameters, see Tab. 5.17.

The generated pseudo-data samples are fitted to make the cartesian parameters pull distributions. The asymmetric errors given by MINOS are used to compute the pulls (as defined in Eq. 5.33).

Table 5.17 – Input values of the cartesian parameters used in the toys generation.

x_-	-0.03	x_+	0.16
y_-	-0.24	y_+	0.18

Signal only toy experiments

A total of one thousand signal only toy experiments are generated, first with one hundred times the signal yield found in the data (around 10000 signal events, Fig. 5.58), then with the same signal level as found in the data (around 100 signal events, Fig. 5.59).

The Dalitz fit is performed on these pseudo-data samples. With one hundred times the signal yield of the data, the resulting pull distributions are in good agreement with a standard normal distribution. However, for sample sizes similar to the yield in the data non gaussian behaviour appears, and some non-negligible biases are seen to occur.

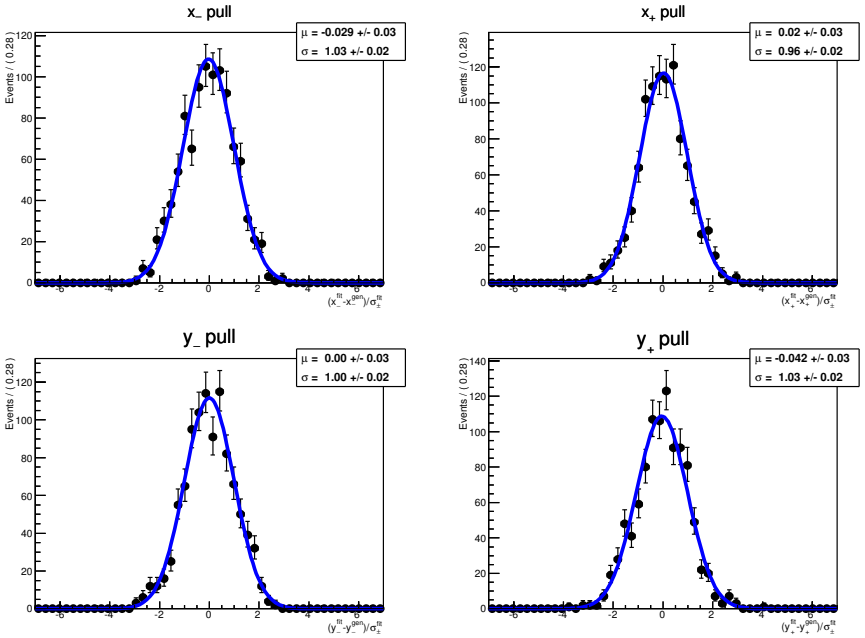

Figure 5.58 – Pull distribution of the fitted cartesian parameters for signal only toy-generation with one hundred times the signal level found in the data.

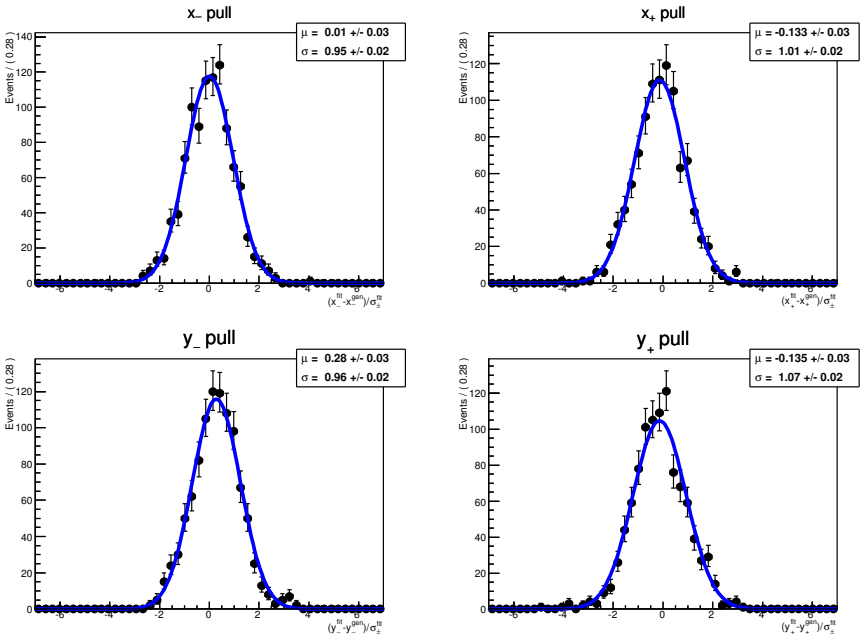

Figure 5.59 – Pull distribution of the fitted cartesian parameters for signal only toy-generation with the signal level found in the data.

Signal and background toy experiments

A total of one thousand pseudo-data experiments are generated, with the same signal and background yields as found in the real data (around 140 events). The Dalitz fit is then performed on these samples. The resulting fitted values, errors, residuals and pull distributions of the cartesian parameters are shown in Fig. 5.60–5.62. As expected from the signal only toy study, some non negligible bias are present and have to be taken into account in the final result. They are directly estimated from the fit result on the data (see Sec. 5.7.6).

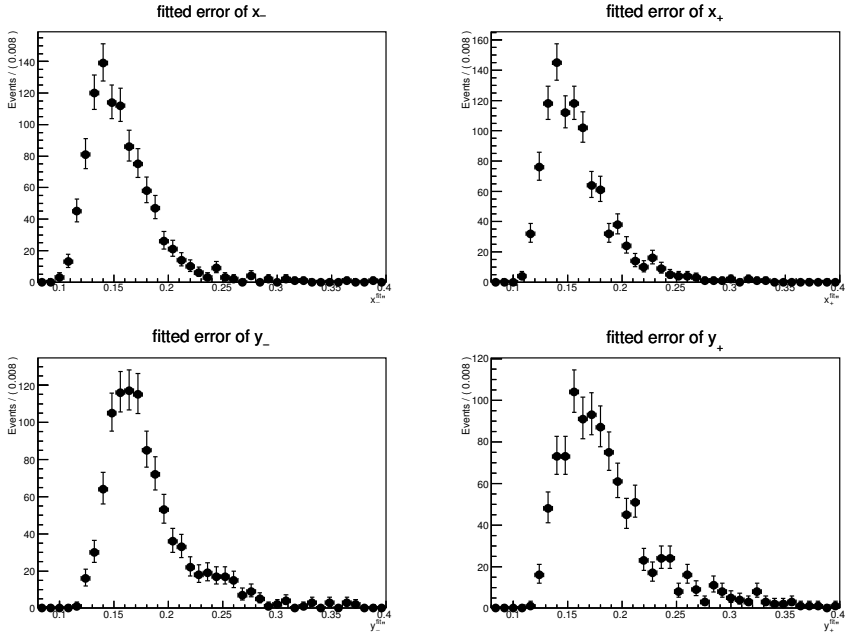

Figure 5.60 – Distributions of the error on the fitted cartesian parameters for pseudo-generation with the signal and background levels found in the data.

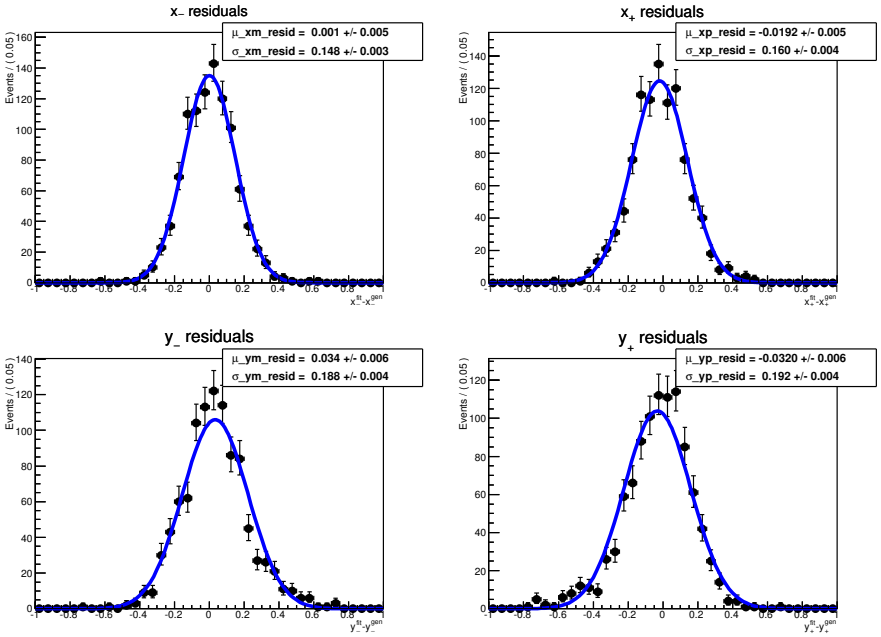

Figure 5.61 – Residual distributions of the fitted cartesian parameters for pseudo-generation with the signal and background levels found in the data.

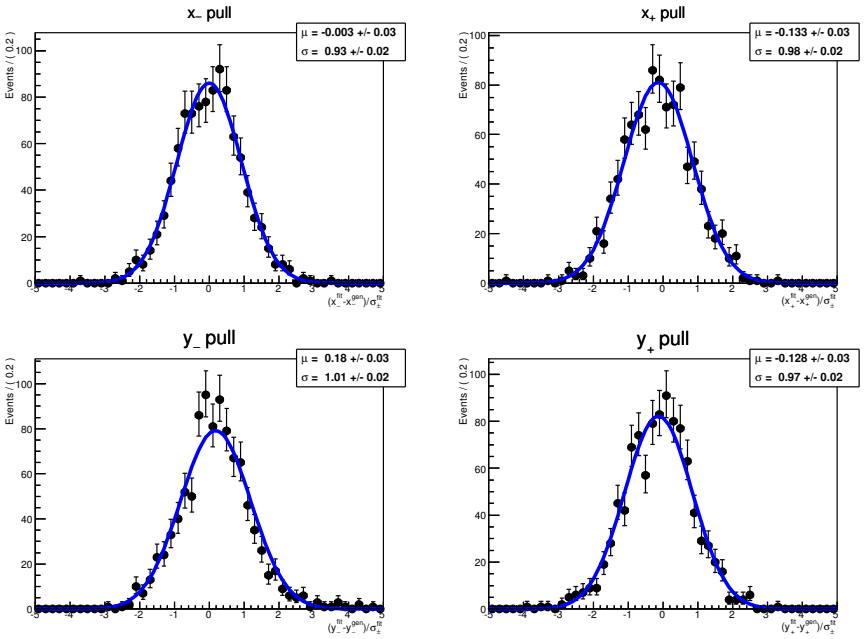

Figure 5.62 – Pull distributions of the fitted cartesian parameters for pseudo-generation with the signal and background levels found in the data.

5.7.4 BDT working point optimisation

With the preliminary sensitivity study of Sec. 5.2.3 a first BDT cut at 0.7 was chosen. However the extensive sensitivity study detailed in this section fixes the best working point at 0.75. The method consists in generating 5×5000 pseudo-experiments corresponding each to five BDT cut values 0.7, 0.75, 0.8, 0.85, 0.9. The Dalitz fit is then performed on these pseudo-experiments. The resulting distributions of the $(x_\pm, y_\pm)$ residuals are then fitted with a gaussian, since the widths of these residuals are the expected sensitivity to these cartesian parameters.

Table 5.18 summarises the background and signal yields obtained in the data for different BDT cuts. The cut at 0.65 is not considered further in the sensitivity study since it gives the same signal level with a worsened purity.

Table 5.18 – Signal and background yields obtained in the data for different BDT cut values.

BDT cut	Signal	Background	Signal ratio	Background ratio
0.65	99 ± 12	51.4 ± 2.8	0.99	1.1
0.7	100 ± 12	46.7 ± 2.7	1	1
0.75	99 ± 12	42.9 ± 2.6	0.99	0.92
0.8	98 ± 12	39.1 ± 2.5	0.98	0.84
0.85	91 ± 11	34.7 ± 2.3	0.91	0.74
0.9	77 ± 10	29.3 ± 2.1	0.77	0.63

The result of this sensitivity study is shown in Fig. 5.63. The statistical uncertainty of the cartesian parameters, estimated as the width of the residuals, is plotted as a function of the BDT cut value. It appears that the cut at 0.75 gives an good sensitivity on $(x_\pm, y_\pm)$, without being close to the increase of the statistical uncertainty after 0.8. Hence this is the final working point which is chosen.

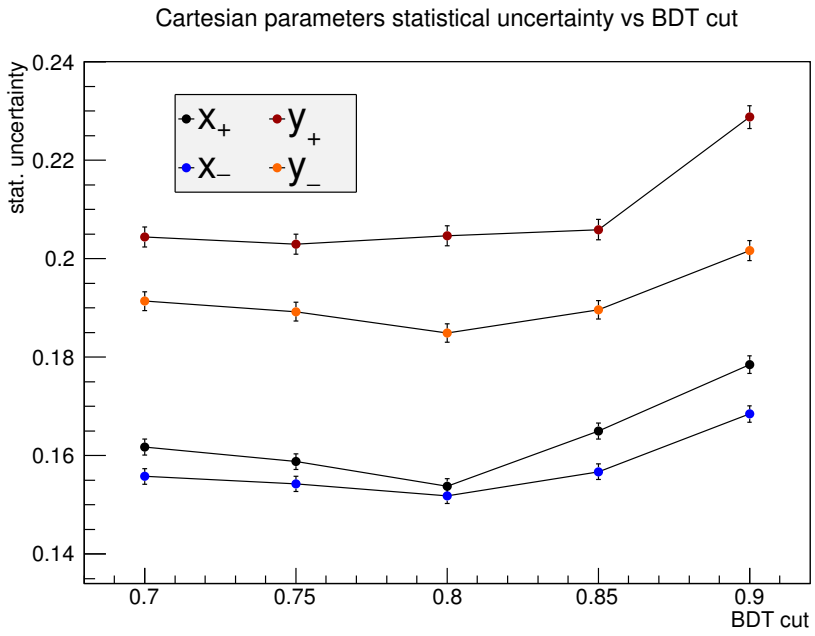

Figure 5.63 – Statistical sensitivity to the cartesian parameters as a function of the BDT cut.

5.7.5 Fit result

In order to avoid introducing some bias during the development of the analysis, the Dalitz fit was blind. The fitted values of the cartesian parameters were unknown. Only their errors were available. The Dalitz plot and its projections with the line shape corresponding to the fit result are shown in Fig. 5.64.

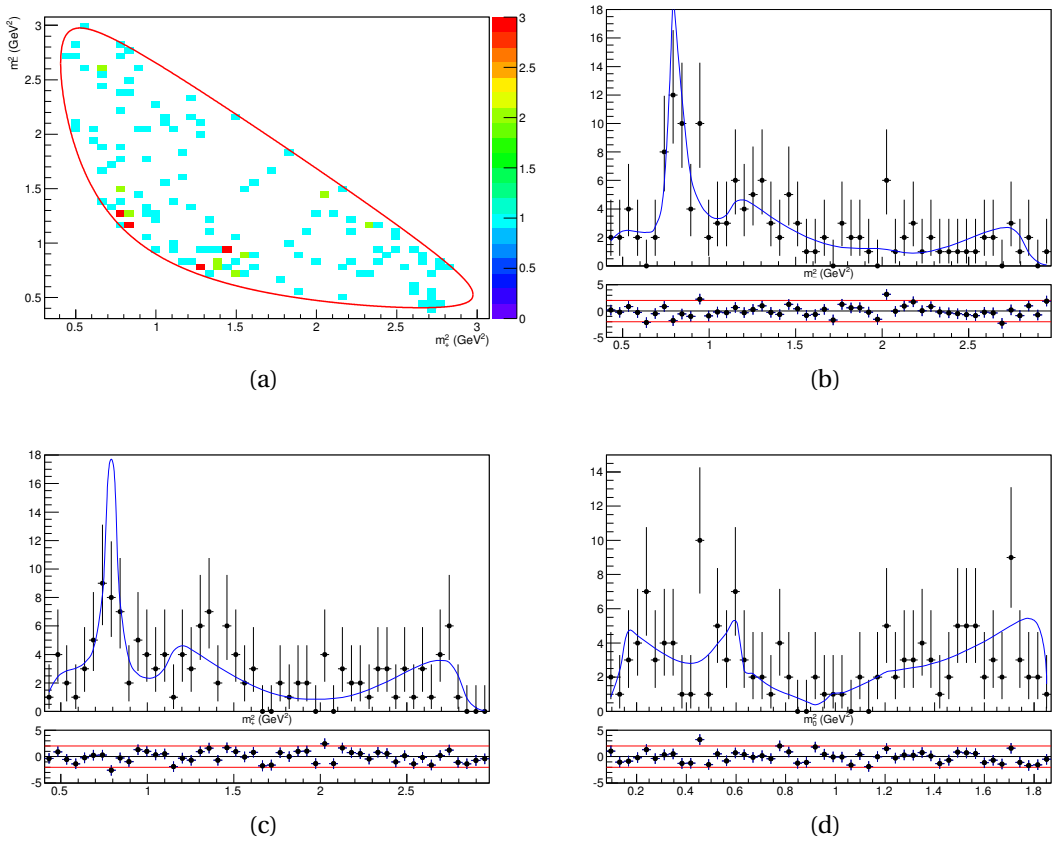

Figure 5.64 – Dalitz plot (a) and its projections on m_-^2 (b), m_+^2 (c) and m_0^2 (d) made with the selected $B^0 \to DK^{*0}$ data candidates. The blue line superimposed on the Dalitz projections corresponds to the fit result.

After unblinding, the fit result on the cartesian parameters is

$$\begin{aligned} x_- &= -0.09^{+0.13}_{-0.13}\,, \\ x_+ &= -0.10^{+0.27}_{-0.26}\,, \\ y_- &= 0.23^{+0.15}_{-0.16}\,, \\ y_+ &= -0.74^{+0.23}_{-0.26}\,. \end{aligned} \tag{5.61}$$

The errors returned by the `HESSE` module are in good agreement with the evaluation performed by the `MINOS` module [151]. They are 0.13, 0.26, 0.15 and 0.23 for x_-, x_+, y_- and y_+ respectively.

The covariance matrix is

$$V = \begin{array}{c} \\ x_- \\ y_- \\ x_+ \\ y_+ \end{array} \begin{array}{c} \begin{array}{cccc} x_- & y_- & x_+ & y_+ \end{array} \\ \begin{pmatrix} 0.017 & 0.0025 & 0. & 0. \\ 0.0025 & 0.024 & 0. & 0. \\ 0. & 0. & 0.068 & -0.0005 \\ 0. & 0. & -0.0005 & 0.056 \end{pmatrix} \end{array}, \tag{5.62}$$

leading to the correlation matrix

$$\tilde{V} = \begin{array}{c} \\ x_- \\ y_- \\ x_+ \\ y_+ \end{array} \begin{array}{c} \begin{array}{cccc} x_- & y_- & x_+ & y_+ \end{array} \\ \begin{pmatrix} 1. & 0.124 & 0. & 0. \\ 0.124 & 1. & 0. & 0. \\ 0. & 0. & 1. & -0.008 \\ 0. & 0. & -0.008 & 1. \end{pmatrix} \end{array}. \tag{5.63}$$

5.7.6 Fit bias

The stability of the Dalitz fit has been first checked with the pseudo-experiments described in Sec. 5.7.3. However, to correctly evaluate the biases on the cartesian parameters, some pseudo-experiments are generated with the values of the cartesian parameters found with the fit to the real data set. These pseudo-experiments are then fitted with the Dalitz fitter. The resulting error, residual and pull distributions are illustrated in Fig. 5.65, 5.66 and 5.67, respectively. The uncertainties returned by the nominal fit, quoted in the previous section, are in good agreement with the uncertainty distributions obtained with the pseudo-experiments (Fig. 5.65). In the residual distributions (Fig. 5.66), a small fraction of the fitted values deviates significantly from the generated ones for the y_- and y_+ parameters, making some satellite residuals (around -0.8 for y_- and 1.3 for y_+). These satellites are significantly away from the generated values, since they can be seen in the tails of the pull distributions (Fig. 5.67). It could highlight some secondary minimum present in the negative log-likelihood. That is why a full likelihood scan is performed in the (x_-, y_-) and (x_+, y_+) spaces to ensure that the nominal fit does not suffer from a secondary minimum (see Fig. 5.96 of Sec. 5.9.2).

The evaluation of the fitter biases is made thanks to a Gaussian fit of the residuals. For the $y_\pm$ distributions, only the pseudo-experiments with residuals smaller than 0.5 are taken into account. The result of this fit is illustrated in Fig. 5.68. The fitted mean of the Gaussians are

$$\begin{aligned} \mu_{x_-} &= -0.001 \pm 0.006, \\ \mu_{x_+} &= 0.008 \pm 0.008, \\ \mu_{y_-} &= -0.034 \pm 0.005, \\ \mu_{y_+} &= 0.038 \pm 0.006. \end{aligned} \tag{5.64}$$

For completeness, the corresponding pulls and their Gaussian fits superimposed are shown in Fig. 5.69. Since the biases are small compared to the statistical uncertainty, their absolute values are taken as systematic uncertainties.

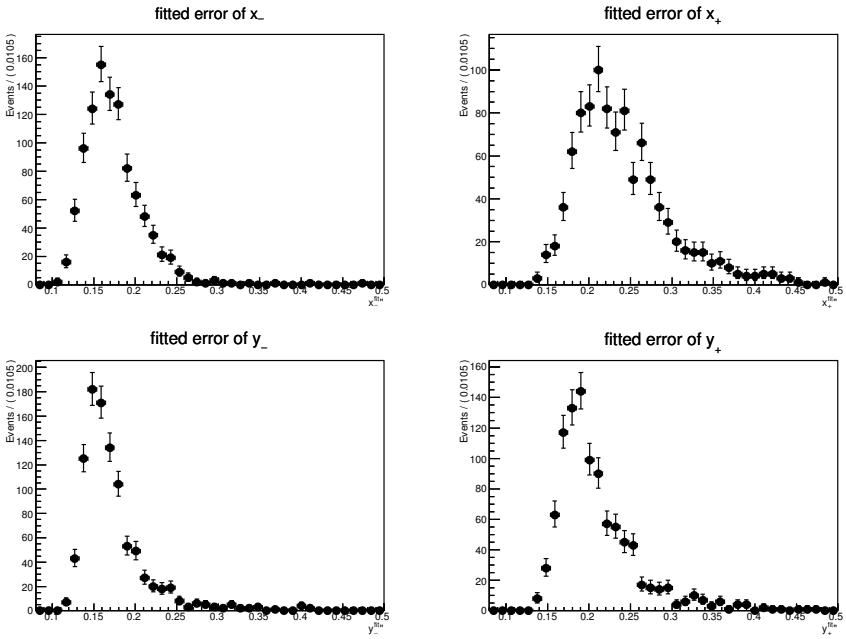

Figure 5.65 – Distributions of the error on the fitted cartesian parameters for pseudo-generation with the cartesian parameters found in data.

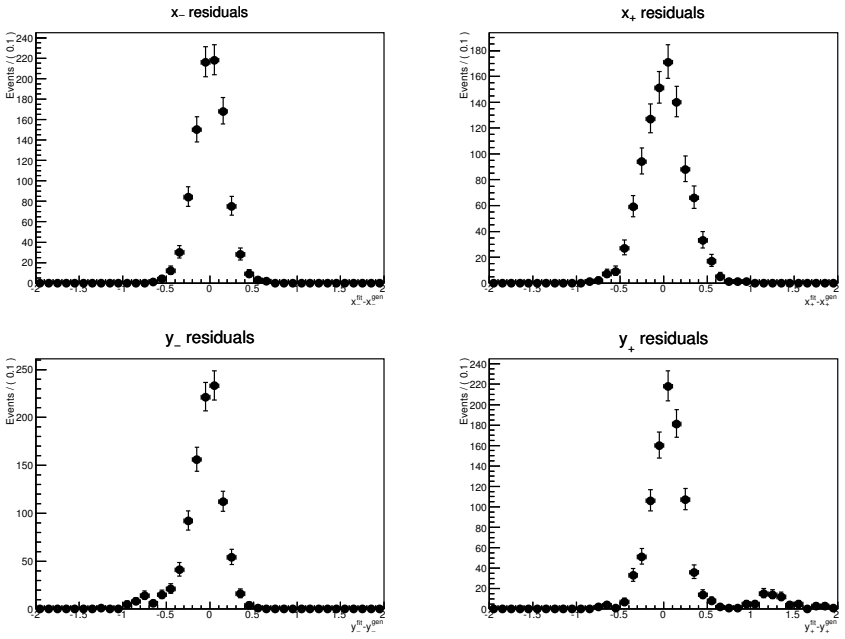

Figure 5.66 – Residual distributions of the fitted cartesian parameters for pseudo-generation with the cartesian parameters found in data.

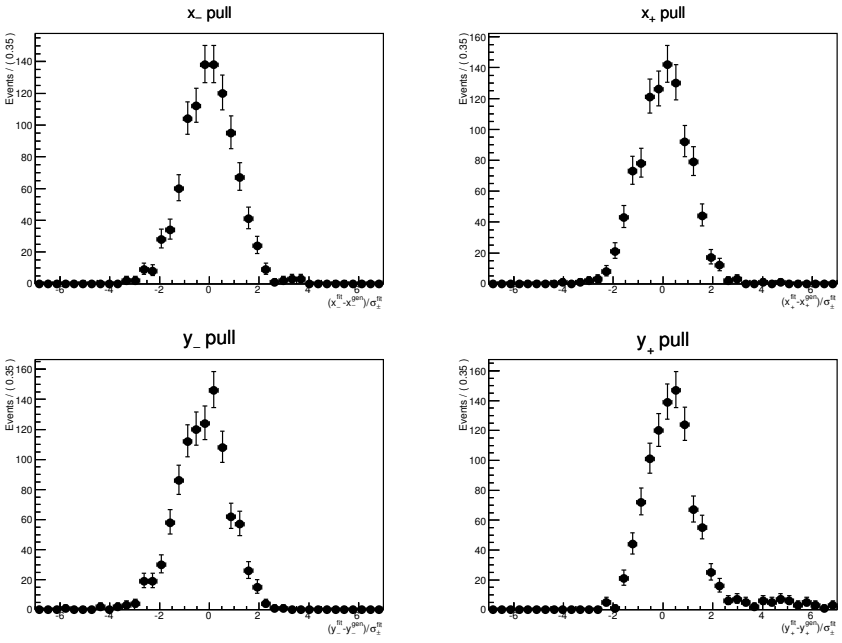

Figure 5.67 – Pull distributions of the fitted cartesian parameters for pseudo-generation with the cartesian parameters found in data.

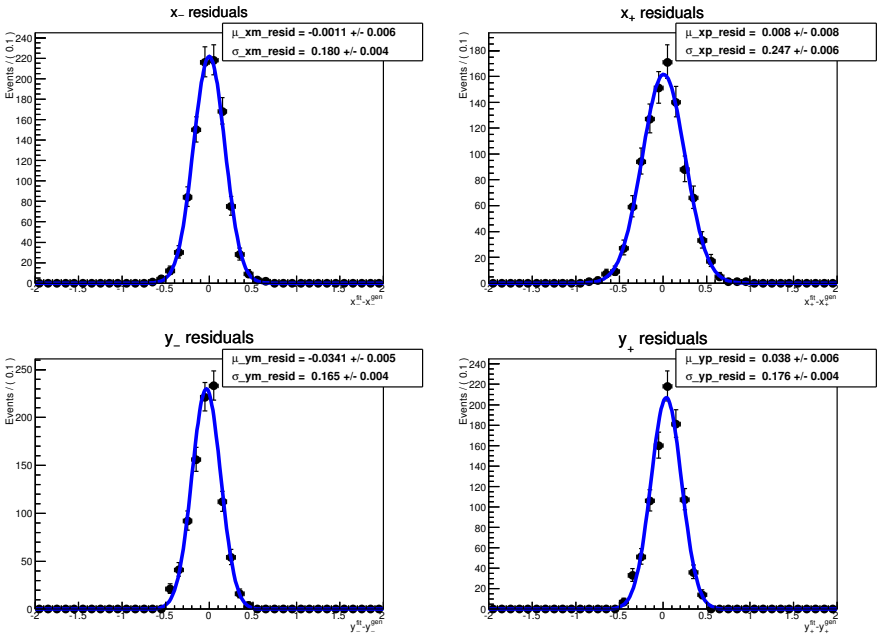

Figure 5.68 – Residual distributions of the fitted cartesian parameters for pseudo-generation with the signal and background levels found in data. Pseudo-experiments with $y_\pm$ residuals larger than 0.5 are not taken into account.

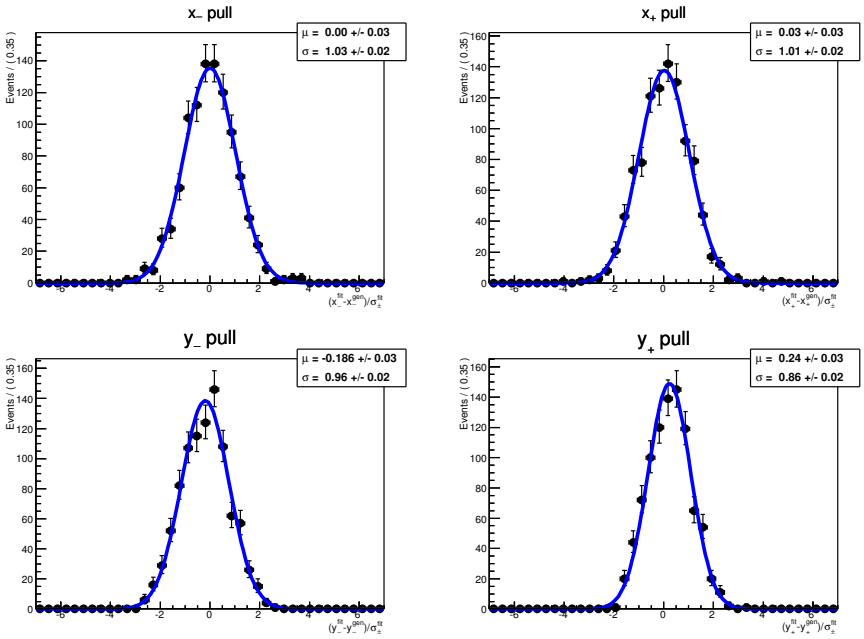

Figure 5.69 – Pull distributions of the fitted cartesian parameters for pseudo-generation with the signal and background levels found in data. Pseudo-experiments with $y_{\pm}$ residuals larger than 0.5 are not taken into account.

5.8 Systematic uncertainties

In addition to the statistical uncertainty on the fitted cartesian parameters, several sources of systematic uncertainty must be taken into account. First the uncertainty on the mass fit result, used as an input to the Dalitz fit, has to be propagated. Then any potential mis-modelling effect of the different background components needs to be evaluated. The non perfect knowledge of the efficiency description over the Dalitz plane produces also an additional uncertainty. Finally the model used for the $D \to K^0_S \pi^+ \pi^-$ decay amplitude has its own limitations to be accounted for. Each time a systematic uncertainty is quoted in percentage of the statistical uncertainty, the latter corresponds to the uncertainty of the nominal fit returned by the `HESSE` module (see Sec. 5.7.5). All the systematic uncertainties have been determined before unblinding the result, by measuring exclusively the deviations to the nominal result (see Eq. 5.65).

5.8.1 Mass fit induced systematic uncertainty.

As explained in Sec. 5.7, the minimisation evaluating the *CP* observables $(x_\pm, y_\pm)$ is performed in two steps. First the mass fit is run. Its results, detailed in Sec. 5.5.4, are used as an input to the 3D minimisation over the (m_{B^0}, m^2_+, m^2_-) space. All parameters related to the mass fit are fixed to their convergence value. To assess the effect of the uncertainty on these parameters, the Dalitz fit is performed several times, with different alternative mass fit result configurations.

Mass fit floating parameters

The floating parameters listed in Table 5.8 are determined by the mass fit with a certain accuracy. In order to evaluate the effect of their uncertainty on the cartesian parameter evaluation, they are all varied within their uncertainties and taking into account their correlations. Only the constraint on the $B^0 \to D\rho^0$ yield is fixed to its nominal value. As it is a special parameter, with a gaussian constraint in the nominal fit, its systematic effect is evaluated separately from the other floating parameters. From this parameter fluctuations, one thousand alternative mass fit results are generated. For each alternative mass fit result one corresponding Dalitz fit is performed. The values of the cartesian parameters obtained from the alternative mass fit results are then compared to the nominal values, by computing the residuals defined as

$$\begin{aligned} \delta x_\pm = &\quad x^{\text{alt}}_\pm - x^{\text{nom}}_\pm, \\ \delta y_\pm = &\quad y^{\text{alt}}_\pm - y^{\text{nom}}_\pm, \end{aligned} \tag{5.65}$$

where $(x^{\text{alt}}_\pm, y^{\text{alt}}_\pm)$ is the alternative cartesian parameter result and $(x^{\text{nom}}_\pm, y^{\text{nom}}_\pm)$ the nominal result.

The distributions of these residuals obtained with this one thousand alternative mass fit results are illustrated in Fig. 5.70. A Gaussian fit on the distributions determine the standard deviation on $(x_\pm, y_\pm)$. The widths of the Gaussians give

$$\begin{aligned} |\delta x_-| = &\quad (17.0 \pm 0.4) \cdot 10^{-3}, \\ |\delta x_+| = &\quad (6.6 \pm 0.1) \cdot 10^{-3}, \\ |\delta y_-| = &\quad (12.1 \pm 0.3) \cdot 10^{-3}, \\ |\delta y_-| = &\quad (39.2 \pm 0.9) \cdot 10^{-3}. \end{aligned} \tag{5.66}$$

Even though some distributions do not behave well like Gaussian, taking the root mean square instead of the fitted width leads to essentially the same values.

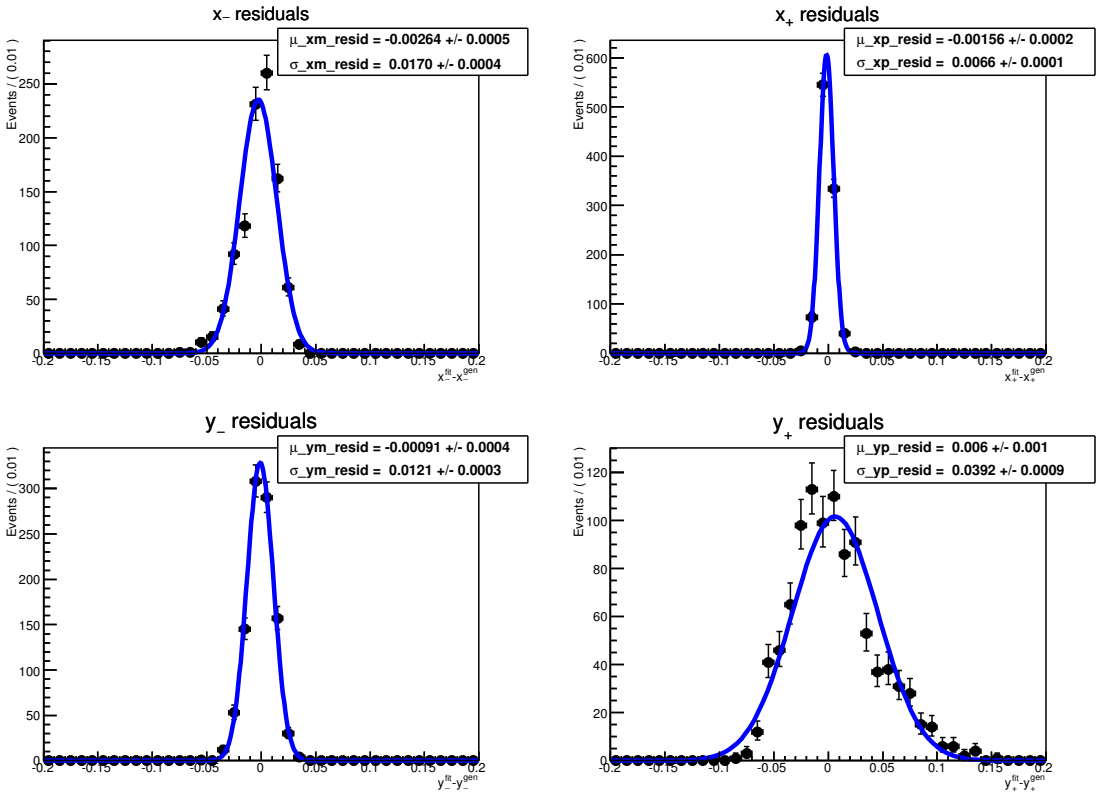

Figure 5.70 – Deviation to the nominal fit values of the cartesian parameters fitted with the alternative mass fit parameters.

$B^0 \to \overline{D}^0\pi^+\pi^-$ background contribution

The yield of the mis-identified $B^0 \to D\rho^0$ background is gaussian-constrained to the values figuring in Eq. 5.30. To take into account the systematic effect arising from the uncertainty on the $B^0 \to D\rho^0$ fraction, the Dalitz fit is repeated with the fraction varied within its $\pm 1\sigma$ uncertainty. The resulting residuals are summarised in Table 5.19.

However $B^0 \to D\rho^0$ is not the only contribution in the general $B^0 \to \overline{D}^0\pi^+\pi^-$ decay. As shown in the $B^0 \to \overline{D}^0\pi^+\pi^-$ Dalitz plot analysis performed by LHCb [156], the other contributions correspond up to half the $B^0 \to D\rho^0$ one. Hence, to determine the effect of a more general $B^0 \to \overline{D}^0\pi^+\pi^-$ contribution in addition to the $B^0 \to D\rho^0$ decay, the $B^0 \to D\rho^0$ fraction is fixed to its upper value ($+1\sigma$) and multiplied by 1.5. The other $B^0 \to \overline{D}^0\pi^+\pi^-$ contributions are assumed to follow the same mass distribution as the $B^0 \to D\rho^0$ mode. The Dalitz fit is then repeated and the resulting deviation on the cartesian parameters are in Table 5.19.

The systematic uncertainty associated to the $B^0 \to \overline{D}^0\pi^+\pi^-$ background contribution is deduced from the largest absolute value of the residuals for each cartesian parameter. This gives

$$\begin{aligned} |\delta x_-| &= (0.98 \pm 0.01) \cdot 10^{-3}, \\ |\delta x_+| &= (0.60 \pm 0.35) \cdot 10^{-3}, \\ |\delta y_-| &= (0.43 \pm 0.02) \cdot 10^{-3}, \\ |\delta y_+| &= (2.02 \pm 0.34) \cdot 10^{-3}. \end{aligned} \tag{5.67}$$

Table 5.19 – Deviation on the cartesian parameters arising from the $B^0 \to \overline{D}^0\pi^+\pi^-$ contribution uncertainty.

$B^0 \to D\rho^0$ fraction variation		δx_- ($\cdot 10^{-3}$)	δx_+ ($\cdot 10^{-3}$)	δy_- ($\cdot 10^{-3}$)	δy_+ ($\cdot 10^{-3}$)
$\rho^{LL}+1\sigma$	$\rho^{DD}+1\sigma$	-0.13 ± 0.01	0.06 ± 0.09	-0.23 ± 0.03	0.45 ± 0.13
$\rho^{LL}-1\sigma$	$\rho^{DD}-1\sigma$	0.45 ± 0.01	-0.35 ± 0.11	0.07 ± 0.02	-0.65 ± 0.02
$\rho^{LL}+1\sigma$	$\rho^{DD}-1\sigma$	-0.02 ± 0.06	-0.15 ± 0.03	0.13 ± 0.01	-0.20 ± 0.07
$\rho^{LL}-1\sigma$	$\rho^{DD}+1\sigma$	0.04 ± 0.05	0.12 ± 0.03	-0.11 ± 0.01	0.17 ± 0.06
$1.5(\rho^{LL}+1\sigma)$	$1.5(\rho^{DD}+1\sigma)$	-0.98 ± 0.01	0.60 ± 0.35	-0.43 ± 0.02	2.02 ± 0.34

These uncertainties represent less than 1% of the statistical uncertainties.

Mass difference between B^0 and B_s^0 peaks

In the nominal mass fit, the mass difference between the B^0 and B_s^0 peaks is fixed to the PDG [20] value $\delta m = (87.19 \pm 0.29)$ MeV. The mass fit is repeated twice with the mass shift varied within its uncertainty. The resulting deviations on the fitted cartesian parameters is summarised in Table 5.20.

Table 5.20 – Deviation on the cartesian parameters arising from the B^0–B_s^0 mass difference uncertainty.

B^0-B_s^0 mass difference variation	δx_- ($\cdot 10^{-3}$)	δx_+ ($\cdot 10^{-3}$)	δy_- ($\cdot 10^{-3}$)	δy_+ ($\cdot 10^{-3}$)
$\delta m + 1\sigma$	-0.53 ± 0.08	-0.50 ± 0.35	-0.64 ± 0.14	-2.33 ± 0.33
$\delta m - 1\sigma$	0.82 ± 0.04	0.21 ± 0.35	0.43 ± 0.18	2.23 ± 0.40

The systematic uncertainty associated to the B^0-B_s^0 mass difference is deduced from the largest absolute value of the residuals for each cartesian parameter. This gives

$$\begin{aligned} |\delta x_-| &= (0.82 \pm 0.04) \cdot 10^{-3}, \\ |\delta x_+| &= (0.50 \pm 0.35) \cdot 10^{-3}, \\ |\delta y_-| &= (0.64 \pm 0.14) \cdot 10^{-3}, \\ |\delta y_+| &= (2.33 \pm 0.33) \cdot 10^{-3}. \end{aligned} \tag{5.68}$$

Mass PDF made with BDTB

In the nominal mass fit the Crystall Ball function for the signal or the different RooKeys PDF, are determined with simulated samples on which the BDTA is applied. To check that this arbitrary choice is not annoying, an alternative mass fit is performed with the mass PDF determined from BDTB instead. Then the Dalitz fit is repeated on data with this alternative mass fit result. The

resulting deviations on the cartesian parameters compared to the nominal result is

$$\begin{aligned} \delta x_- &= (-0.11 \pm 0.04) \cdot 10^{-3}, \\ \delta x_+ &= (0.17 \pm 0.04) \cdot 10^{-3}, \\ \delta y_- &= (-0.42 \pm 0.02) \cdot 10^{-3}, \\ \delta y_+ &= (1.22 \pm 0.11) \cdot 10^{-3}. \end{aligned} \tag{5.69}$$

The systematic uncertainty assigned to this very small effect is the absolute value of these deviations.

Signal PDF

In the nominal mass fit the $B^0 \to DK^{*0}$ and $B_s^0 \to D\overline{K}^{*0}$ peaks are described with a double Crystal Ball function (see Sec.5.5.1). Two types of systematic uncertainties arising from this modelling are investigated:

- the uncertainty on the Crystal Ball parameters which are fixed according to the fit result on the simulated sample,
- the uncertainty due to the use of the Crystal Ball model itself.

To evaluate the effect of the uncertainty on the Crystal Ball parameters, one thousand alternative parameters sets are generated randomly within their uncertainties and taking into account their correlations. The mass fit and the Dalitz fit are repeated accordingly on the data. The distribution of the deviation on the fitted cartesian parameters compared to the nominal result is shown in Fig. 5.71. These distributions are fitted with a Gaussian. It highlights some small but non negligible biases. That is why the quadratic sum of the width and the mean of the fitted Gaussian is taken as a systematic uncertainty:

$$\begin{aligned} |\delta x_-| &= 0.39 \cdot 10^{-3}, \\ |\delta x_+| &= 0.35 \cdot 10^{-3}, \\ |\delta y_-| &= 0.35 \cdot 10^{-3}, \\ |\delta y_+| &= 0.74 \cdot 10^{-3}. \end{aligned} \tag{5.70}$$

To check that these residuals distributions are expected, the same procedure is applied to a pseudo data sample. Around 16k events are generated with the same signal and background level found in the real data. Then the nominal and alternative mass and Dalitz fits are performed again on this sample. The resulting distributions of the deviations on the cartesian parameters compared to the nominal result are shown in Fig. 5.72. The shape of the distributions is close to what is found with the real data, with smaller width thanks to the higher statistic available in the pseudo-data sample.

To evaluate the effect of using a Crytal Ball model (Fig. 5.40), a triple Gaussian function is used instead. The width ratio and the mass shift between the three Gaussians are fixed to the values obtained in the simulation (Fig. 5.73). An alternative mass fit is performed with this triple Gaussian, and the output result is used to perform an alternative Dalitz fit. The resulting

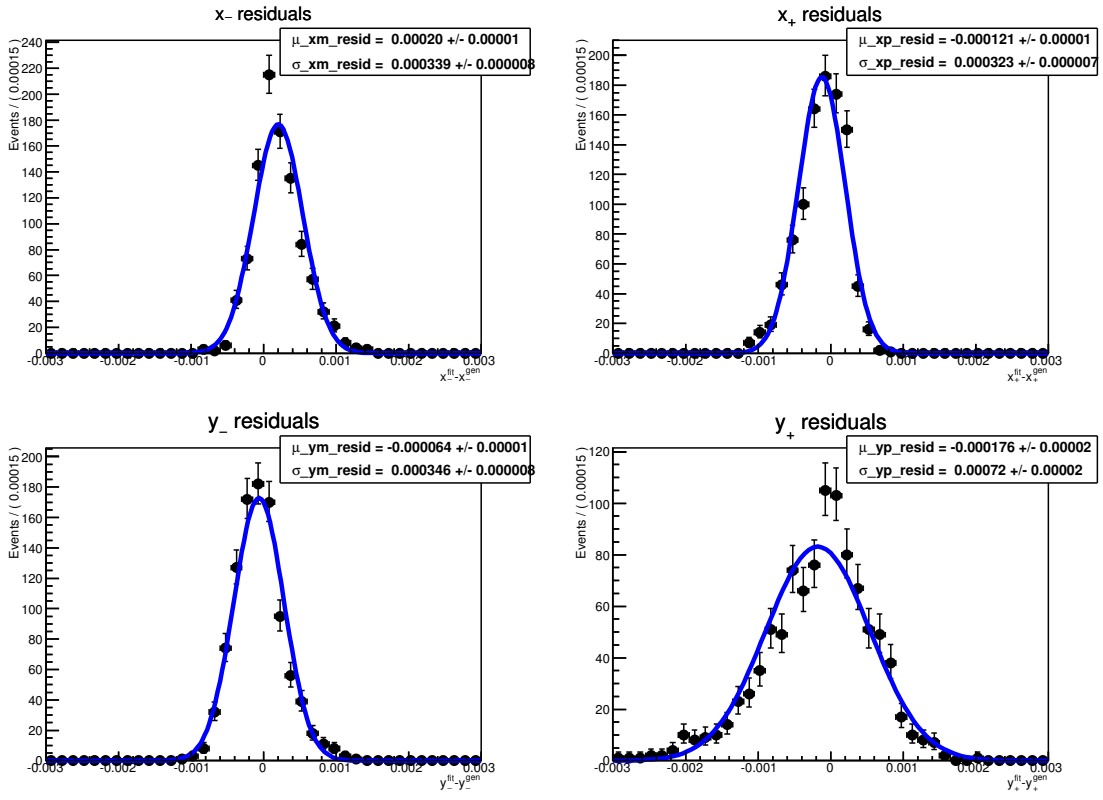

Figure 5.71 – Deviation to the nominal values of the cartesian parameters fitted on data, when the Crystal Ball parameters are varied.

deviations on the cartesian parameters compared to the nominal result are equal to

$$\begin{aligned} \delta x_- &= (4.08 \pm 0.04) \cdot 10^{-3}, \\ \delta x_+ &= (-1.87 \pm 0.99) \cdot 10^{-3}, \\ \delta y_- &= (3.93 \pm 0.21) \cdot 10^{-3}, \\ \delta y_- &= (-9.92 \pm 0.06) \cdot 10^{-3}. \end{aligned} \tag{5.71}$$

The systematic uncertainty assigned to this effect is the absolute value of these deviations.

Proportion of $D^{*0} \to D^0\pi^0/D^{*0} \to D^0\gamma$ in $B^0_{(s)} \to D^{*0}K^{*0}$

In the nominal mass fit the $D^{*0} \to D^0\pi^0/D^{*0} \to D^0\gamma$ decay proportion from the $B^0_{(s)} \to D^{*0}K^{*0}$ background is fixed according to the relative branching fractions and efficiencies (see Sec. 5.5.2). The parameters fixing this proportion, defined in Eq. 5.24, are equal to

$$\begin{aligned} G^{LL}_{010} &= 0.378 \pm 0.033 \\ G^{LL}_{101} &= 0.373 \pm 0.033 \\ G^{DD}_{010} &= 0.379 \pm 0.033 \\ G^{DD}_{101} &= 0.374 \pm 0.033 \end{aligned} \tag{5.72}$$

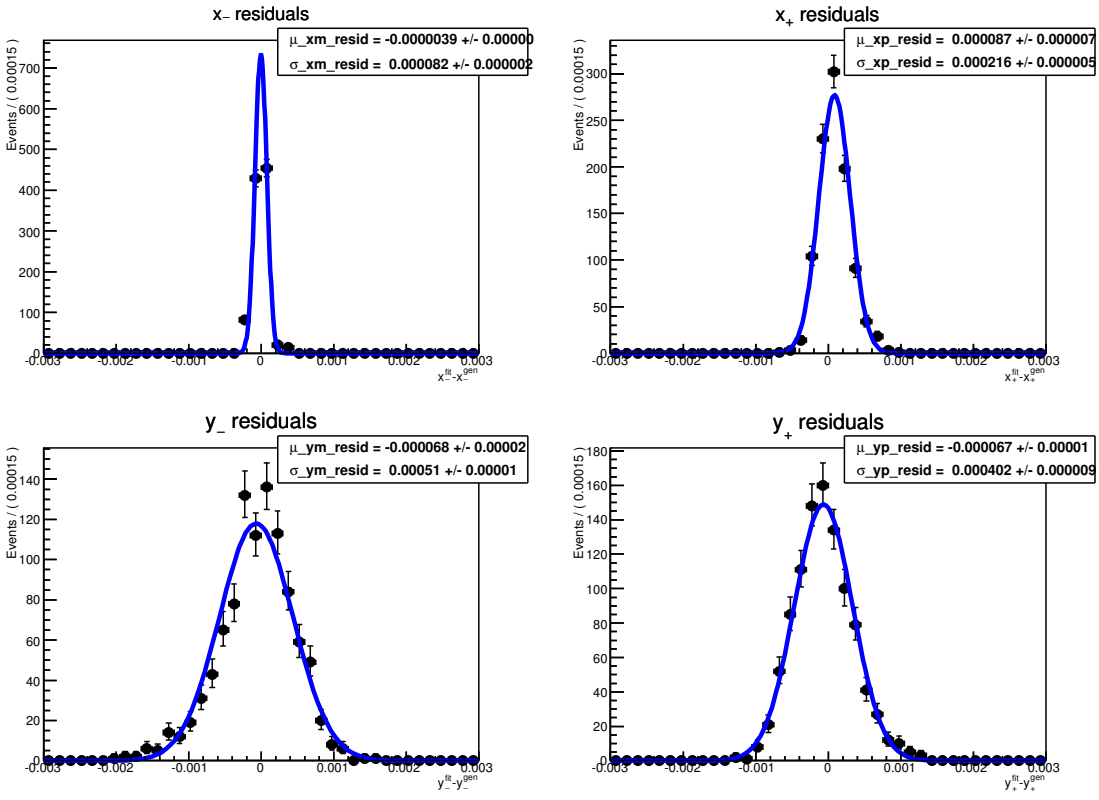

Figure 5.72 – Deviation to the nominal values of the cartesian parameters fitted on pseudo-data, when the Crystal Ball parameters are varied.

To determine the systematic uncertainty arising from fixing these parameters, the mass fit is repeated after varying the G_X^{TT} parameters within their uncertainties. The Dalitz fit is repeated accordingly to determine the resulting deviations on the cartesian parameters, compared to the nominal result. These deviations are summarised in Table 5.21.

Table 5.21 – Deviation on the cartesian parameters arising from fixing the $D^{*0} \to D^0\pi^0/D^{*0} \to D^0\gamma$ proportion in the $B^0_{(s)} \to D^{*0}K^{*0}$ background.

$D^{*0} \to D^0\pi^0/D^{*0} \to D^0\gamma$ proportion				δx_- $(\cdot 10^{-3})$	δx_+ $(\cdot 10^{-3})$	δy_- $(\cdot 10^{-3})$	δy_+ $(\cdot 10^{-3})$
$G^{LL}_{010}+1\sigma$	$G^{DD}_{010}+1\sigma$	$G^{LL}_{101}+1\sigma$	$G^{DD}_{101}+1\sigma$	-1.71 ± 0.48	1.40 ± 0.44	-3.12 ± 0.08	11.97 ± 0.69
$G^{LL}_{010}-1\sigma$	$G^{DD}_{010}-1\sigma$	$G^{LL}_{101}-1\sigma$	$G^{DD}_{101}-1\sigma$	2.66 ± 0.55	-2.07 ± 0.53	3.78 ± 0.16	-14.49 ± 0.68
$G^{LL}_{010}+1\sigma$	$G^{DD}_{010}+1\sigma$	$G^{LL}_{101}-1\sigma$	$G^{DD}_{101}-1\sigma$	-0.42 ± 0.14	0.36 ± 0.12	-0.91 ± 0.02	4.66 ± 0.29
$G^{LL}_{010}-1\sigma$	$G^{DD}_{010}-1\sigma$	$G^{LL}_{101}+1\sigma$	$G^{DD}_{101}+1\sigma$	0.06 ± 0.04	-0.12 ± 0.02	0.30 ± 0.05	-2.88 ± 0.20

The systematic uncertainty associated to the $D^{*0} \to D^0\pi^0/D^{*0} \to D^0\gamma$ proportion is deduced

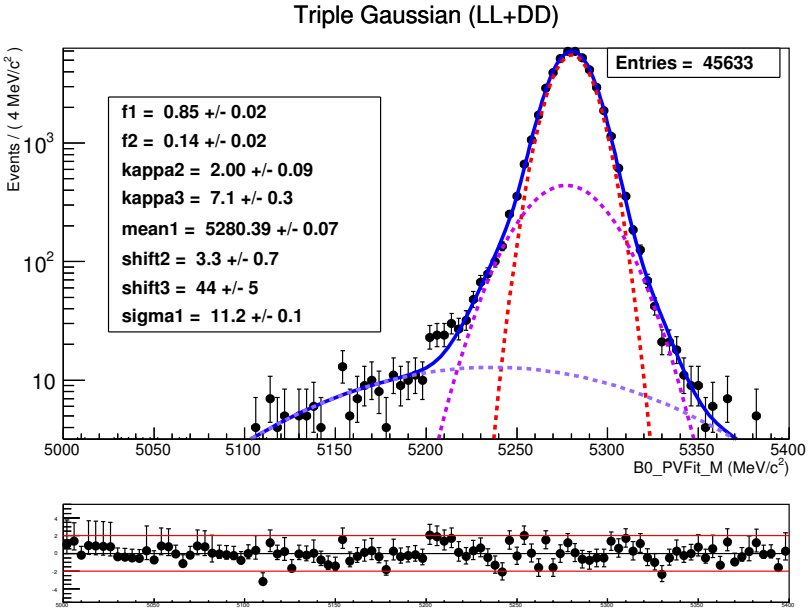

Figure 5.73 – Fit of the B^0 reconstructed invariant mass of simulated $B^0 \to DK^{*0}$ LL and DD candidates, with a triple Gaussian PDF. It is the alternative model to be compared with the double Crystall Ball function used in the nominal mass fit.

from the largest absolute value of the deviations for each cartesian parameter. This gives

$$\begin{aligned} |\delta x_-| = &\quad (2.66 \pm 0.55) \cdot 10^{-3}, \\ |\delta x_+| = &\quad (2.07 \pm 0.53) \cdot 10^{-3}, \\ |\delta y_-| = &\quad (3.78 \pm 0.16) \cdot 10^{-3}, \\ |\delta y_-| = &\quad (14.49 \pm 0.68) \cdot 10^{-3}. \end{aligned} \tag{5.73}$$

$B^0 \to D^{*0}K^{*0}$ effects

Two effects in the treatment of the $B^0 \to D^{*0}K^{*0}$ background are studied.

- In the nominal mass fit, it is assumed that the $B^0 \to D^{*0}K^{*0}$ and $B_s^0 \to D^{*0}\overline{K}^{*0}$ backgrounds have the same helicity components proportion, described with the common parameter α_{010} (see Sec. 5.5.2). To check the effect of this assumption, an alternative mass fit is performed using different parameters α_{010} for $B_s^0 \to D^{*0}\overline{K}^{*0}$ and β_{010} for $B^0 \to D^{*0}K^{*0}$.
- In the nominal Dalitz fit, the $B^0 \to D^{*0}K^{*0}$ contribution is neglected. Two alternative Dalitz fits are performed on data, both without neglecting this contribution (using a model without *CP* violation), and one using the β_{010} parameter and the other not.

The deviations on the cartesian parameters compared to the nominal result, resulting from these two effects, are summarised in Table 5.22.

Table 5.22 – Deviation on the cartesian parameters arising from neglecting the $B^0 \to D^{*0}K^{*0}$ background and using a different helicity proportion parameter for $B^0 \to D^{*0}K^{*0}$ and $B^0_s \to D^{*0}\overline{K}^{*0}$ decays.

$B^0 \to D^{*0}K^{*0}$ neglected	Use β_{010}	δx_- $(\cdot 10^{-3})$	δx_+ $(\cdot 10^{-3})$	δy_- $(\cdot 10^{-3})$	δy_+ $(\cdot 10^{-3})$
yes	yes	-0.25 ± 0.09	0.16 ± 0.02	-0.38 ± 0.04	1.13 ± 0.10
no	yes	-0.42 ± 0.13	0.32 ± 0.10	-0.72 ± 0.04	2.34 ± 0.14
no	no	-0.19 ± 0.05	0.17 ± 0.09	-0.36 ± 0.04	1.26 ± 0.04

The systematic uncertainty associated to the $B^0 \to D^{*0}K^{*0}$ handling is deduced from the largest absolute value of the deviations for each cartesian parameter. This gives

$$\begin{aligned} |\delta x_-| = &\quad (0.42 \pm 0.13) \cdot 10^{-3}, \\ |\delta x_+| = &\quad (0.32 \pm 0.10) \cdot 10^{-3}, \\ |\delta y_-| = &\quad (0.72 \pm 0.04) \cdot 10^{-3}, \\ |\delta y_+| = &\quad (2.34 \pm 0.14) \cdot 10^{-3}. \end{aligned} \tag{5.74}$$

Fake D^0 candidate yield uncertainty

The determination of the amount of fake D^0 among the combinatorial candidates has a large uncertainty. As explained in Sec. 5.5.7, the nominal fit uses $n^{LL}_{\text{fakeD}} = 2$ and $n^{DD}_{\text{fakeD}} = 2$. Alternative Dalitz fits are performed on the data, using $n^{LL}_{\text{fakeD}} = 0$ or 8 and $n^{DD}_{\text{fakeD}} = 0$ or 7. The resulting deviation on the cartesian parameters are summarised in Table 5.23.

Table 5.23 – Deviation on the cartesian parameters arising from the fake D^0 background yield uncertainty.

n^{LL}_{fakeD}	n^{DD}_{fakeD}	δx_- $(\cdot 10^{-3})$	δx_+ $(\cdot 10^{-3})$	δy_- $(\cdot 10^{-3})$	δy_+ $(\cdot 10^{-3})$
8	7	-47 ± 12	-18.1 ± 4.8	16.6 ± 0.9	-16 ± 9
0	0	29 ± 8	8 ± 4	-13.4 ± 0.8	5 ± 3
8	0	-35 ± 12	3 ± 10	4 ± 4	-34 ± 5
0	7	20 ± 8	-11 ± 8	1 ± 3	24 ± 1

The systematic uncertainty associated to the fake D^0 yield uncertainty is deduced from the largest absolute value of the deviations for each cartesian parameter. This gives

$$\begin{aligned} |\delta x_-| = &\quad (47 \pm 12) \cdot 10^{-3}, \\ |\delta x_+| = &\quad (18.1 \pm 4.8) \cdot 10^{-3}, \\ |\delta y_-| = &\quad (16.6 \pm 0.9) \cdot 10^{-3}, \\ |\delta y_+| = &\quad (34 \pm 5) \cdot 10^{-3}. \end{aligned} \tag{5.75}$$

This systematic uncertainty evaluation assumes that the fake D^0 candidates are well described by an uniform distribution across the Dalitz plane (see Sec. 5.7.2). The potential mis-modelling of the fake D^0 background is assessed in Sec. 5.8.2.

Additional cut on the K^0_S flight distance significance

As seen in Sec. 5.2.5, looking at the K^0_S mass sidebands there is no evidence of contamination from the $D^0 \to \pi\pi\pi\pi$ background. Since the statistics is low, this estimation might suffer from fluctuations. As a conservative approach, the effect of applying a strong cut on the K^0_S flight distance significance, Ks_DKs_FDSig > 3 on the LL candidates is evaluated. The mass fit with this additional cut is illustrated in Fig 5.74. This mass fit adopts a strategy slightly different to the nominal version. Here the $B^0 \to DK^{*0}$ yields are formulated in terms of fraction of $B^0_s \to D\overline{K}^{*0}$ yields, with the B^0/B^0_s proportion identical in LL and DD categories. Even if there is an additional cut on the LL sample, the effect should be the same on $B^0 \to DK^{*0}$ and $B^0_s \to D\overline{K}^{*0}$ candidates. Hence, the B^0/B^0_s ratio has to be the same for LL and DD candidates. The resulting yields are summarised in Table 5.24. The LL signal yield decreases from 37 ± 7 in the nominal fit, to 27 ± 4, with a decrease of the LL sample size in the $[4.9, 5.8]$ GeV region from 612 to 493 candidates. Therefore, assuming a correlation of 493/612, this 10 signal event difference has a significance around 2.2σ. This loss cannot only be explained by a reduction of the signal due to the K^0_S flight distance significance cut. Indeed, according to the simulation, this cut has an efficiency around 98.7% on the signal. However, with the given statistics it is difficult to evaluate correctly the source of this loss. Consequently, it is decided to evaluate the systematic effect coming from adding this extra cut on the K^0_S flight distance significance on LL candidates. The Dalitz fit is repeated with this additional cut applied, and the resulting deviations on the cartesian parameters compared to the nominal result are

$$\begin{aligned} \delta x_- &= -0.070 \pm 0.085, \\ \delta x_+ &= 0.054 \pm 0.135, \\ \delta y_- &= 0.005 \pm 0.072, \\ \delta y_+ &= 0.021 \pm 0.121. \end{aligned} \tag{5.76}$$

The uncertainties on these deviations take into account the correlation between the nominal dataset (141 candidates) and the dataset reduced by the additional K^0_S flight distance cut (122 candidates). The systematic uncertainties associated to this effect are taken as the absolute values of these deviations.

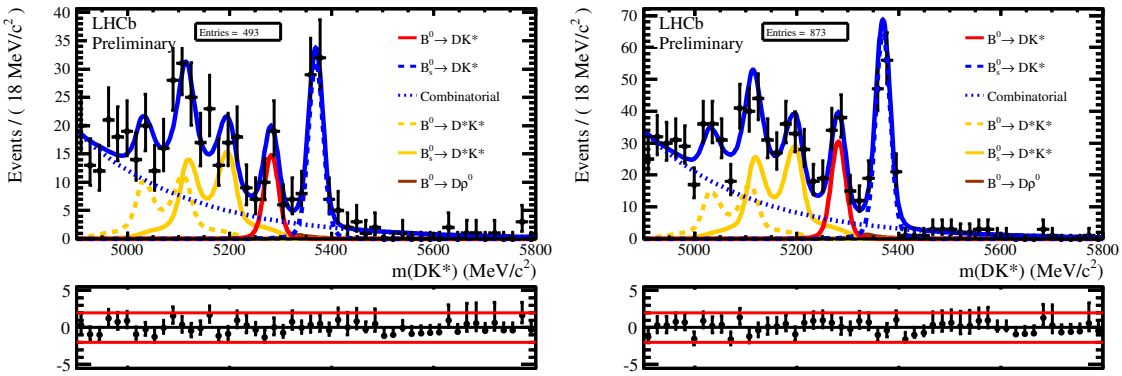

Figure 5.74 – Invariant mass fit of $B^0 \to DK^{*0}$ candidates with an additional cut on the K^0_S flight distance significance for LL candidates. LL (DD) candidates are plotted in left (right).

Table 5.24 – Total yields in the B^0 signal region, with the additional cut on the K^0_S flight distance.

Component	Yield		
	Total	LL	DD
$N(B^0 \to DK^{*0})$	83 ± 11	27 ± 4	56 ± 8
N(Comb)	24.8 ± 1.7	9.4 ± 1.0	15.5 ± 1.3
$N(B^0_s \to D^{*0}\overline{K}^{*0})$	12.9 ± 2.0	4.4 ± 0.9	8.5 ± 1.4
$N(B^0 \to D^{*0}K^{*0})$	0.13 ± 0.03	0.06 ± 0.02	0.07 ± 0.02
$N(B^0 \to D\rho^0)$	0.57 ± 0.11	0.20 ± 0.05	0.37 ± 0.09
$N(B^0_s \to D\overline{K}^{*0})$	1.70 ± 0.31	0.55 ± 0.12	1.15 ± 0.22
Total background	40.1 ± 2.5	14.6 ± 1.3	25.5 ± 1.9

5.8.2 Background description on the Dalitz plane

The $B^0 \to DK^{*0}$ data sample is mainly polluted by two background sources, the combinatorial candidates (with fake or real D^0) and the partially reconstructed $B^0_s \to D^{*0}\overline{K}^{*0}$ decay. To describe them on the Dalitz plane some assumptions are made. In this section, the potential systematic uncertainties arising from these assumptions are evaluated. The effect of the $B^+ \to \overline{D}^0\pi^+\pi^+\pi^-$ and $\Lambda^0_b \to D^0 p\pi^-$ backgrounds is also determined.

Fake D^0 background model

In Sec. 5.8.1, the systematic uncertainty coming from the level of fake D^0 background was determined. Here, the systematic uncertainty arising from a potential mis-modelling on the Dalitz plane is studied. Indeed, in the nominal fit, the fake D^0 background is supposed to be uniformly distributed across the Dalitz plane. This assumption can be partially wrong if an amount of fake D^0 candidates are coming from resonances such as $K^{*\pm}$. This resonance decays as $K^{*\pm} \to K^0_S\pi^\pm$ and can be associated to a random $\pi^\mp$ track to form a fake D^0.

In order to check if any resonance is present among the fake D^0 background, the Dalitz plot projections on m^2_+, m^2_- and m^2_0 are made with the *sPlot* technique [157]. The *sWeights* are taken from the D^0 mass fit made to estimate the amount of fake D^0 background (see Sec. 5.5.7). In this way the real D^0 contribution is subtracted and only the fake D^0 distribution remains. The result of this "fake D^0" weighting is shown in Fig. 5.75 and 5.76. No clear structure is visible. For instance a $K^{*\pm}$ resonance would make a peak around $0.8 - 0.9\,\text{GeV}^2$. However the statistical sensitivity is too poor to draw any conclusion from these distributions. Two other methods are carried out, based on the candidates lying in the D^0 mass sidebands.

First, to have a rough estimation of the maximal fraction of $K^{*\pm}$ resonance present in the fake D^0 background, the D^0 mass sidebands are studied. Indeed candidates with a reconstructed D^0 mass far from the real mass are fake D^0 candidates. The Dalitz plot of the candidates lying outside the $\pm 30\,\text{MeV}$ mass window around the D^0 mass, but passing the preselection requirements, is made (Fig. 5.77). Only the preselection is applied since the statistics is too low after the BDT cut. Here again no visible structure can easily be identified. In a conservative approach, the maximal fraction of $K^{*\pm}$ resonance among the fake D^0 candidates is estimated as the number of events inside the $0.742 < m^2_\pm < 1.042\,\text{GeV}^2$ region compared to the total number of events. The estimate

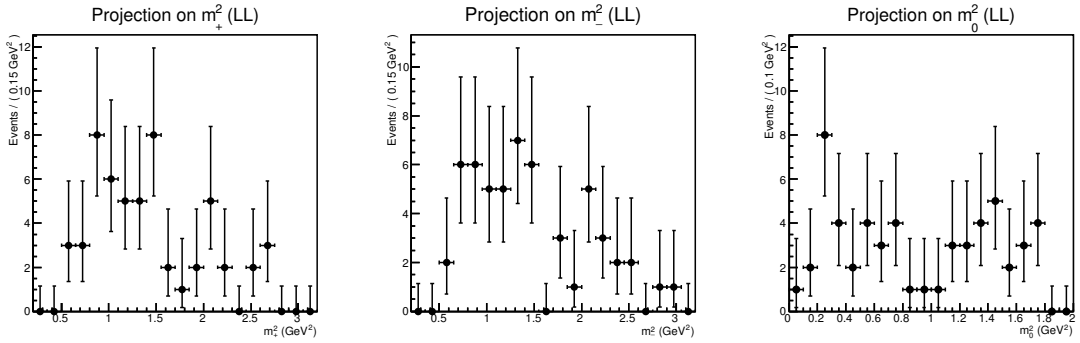

(a)

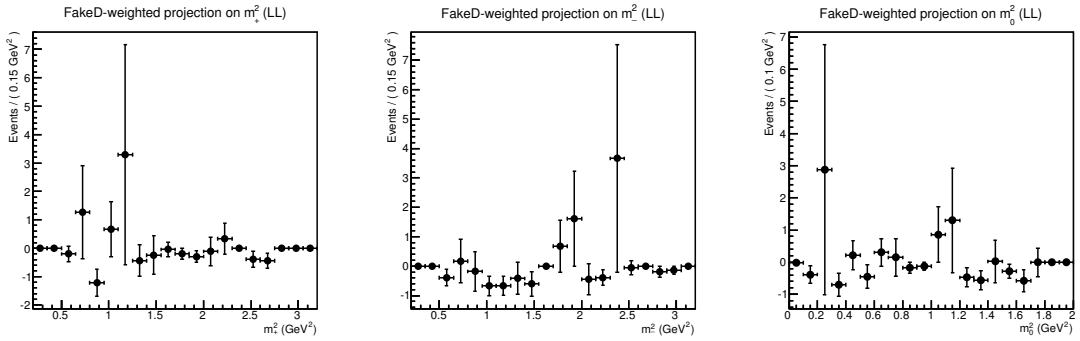

(b)

Figure 5.75 – Dalitz plot projections of $B^0 \to DK^{*0}$ LL candidates found in the data, unweighted (a) and sWeighted to keep only the fake D^0 contribution (b).

yields a maximum of 17%. The Dalitz fit is then performed assuming the fake D^0 background model as 83% of a flat distribution and 17% of a $K^{*\pm}$ resonance. The fake D^0 yields are also set to their maximal upper fluctuation $n^{LL}_{\text{fakeD}} = 8$ and $n^{DD}_{\text{fakeD}} = 7$. The deviations on the fitted cartesian parameters compared to the nominal result are found to be

$$\begin{aligned} \delta x_- &= \quad (-39 \pm 7) \cdot 10^{-3}, \\ \delta x_+ &= \quad (-3 \pm 7) \cdot 10^{-3}, \\ \delta y_- &= \quad (4.6 \pm 0.8) \cdot 10^{-3}, \\ \delta y_+ &= \quad (23 \pm 11) \cdot 10^{-3}. \end{aligned} \tag{5.77}$$

These deviations are smaller in absolute values than those found in Sec.5.8.1, when only the fake D^0 yields vary (and the Dalitz model used is 100% uniform). They are therefore not taken into account.

Another approach to evaluate the uncertainty on the fake D^0 background model consists in taking the Dalitz distribution found in the D^0 mass sidebands (Fig. 5.77). As the BDT efficiency is flat across the Dalitz plane (Fig. 5.78), the Dalitz plot of candidates after preselection in the D^0 sidebands corresponds to the fake D^0 distribution. Thus an alternative Dalitz fit is performed with a spline interpolation on the Dalitz plot from the D^0 sidebands, instead of using a flat model for the fake D^0 model. The fake D^0 yields are set to their maximal upper fluctuation $n^{LL}_{\text{fakeD}} = 8$ and $n^{DD}_{\text{fakeD}} = 7$. The deviations on the fitted cartesian parameters compared to the nominal

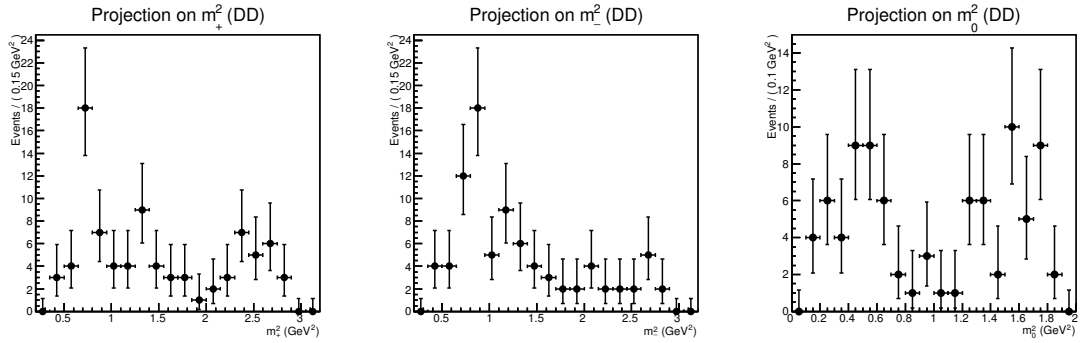

(a)

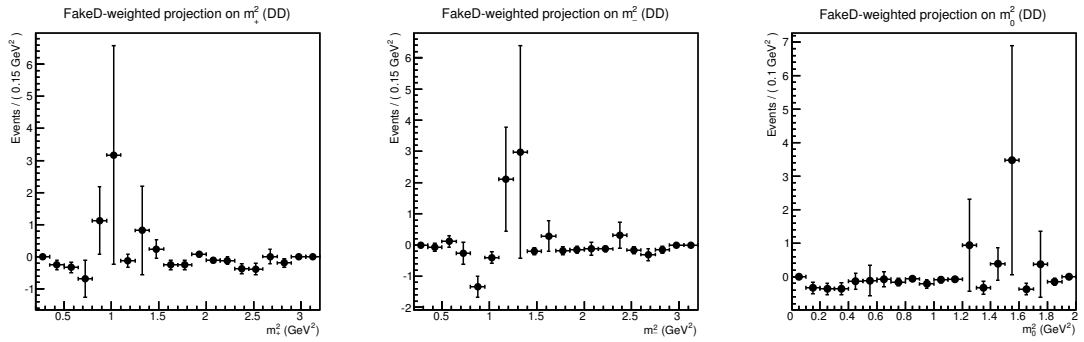

(b)

Figure 5.76 – Dalitz plot projections of $B^0 \to DK^{*0}$ DD candidates found in the data, unweighted (a) and sWeighted to keep only the fake D^0 contribution (b).

result are found to be

$$\begin{aligned} \delta x_- &= (-35 \pm 9) \cdot 10^{-3}, \\ \delta x_+ &= (19 \pm 5) \cdot 10^{-3}, \\ \delta y_- &= (21.7 \pm 0.3) \cdot 10^{-3}, \\ \delta y_+ &= (-24 \pm 11) \cdot 10^{-3}. \end{aligned} \tag{5.78}$$

These deviations are of the same order of magnitude as the deviations obtained with only a variation of the fake D^0 yields (Sec. 5.8.1). The effects of the fake D^0 yield variation and of the mis-modelling of this background are related. As a consequence, there are not added in a quadratic sum. The total systematic uncertainty arising from the fake D^0 background (combining yields and model effect) is taken as the largest absolute values between the deviations obtained when the yields are varied (Eq. 5.75) and when the D^0 sidebands distribution is used instead of an uniform model (Eq. 5.78).

Real D^0 background model

As explained in Sec. 5.7.2, the real D^0 background description on the Dalitz plane assumes equal probability for the D^0 and $\overline{D}^0$ states. These real D candidates are combined with two random tracks corresponding to a fake K^{*0} candidate. This assumption rely on the fact that the D^0 and $\overline{D}^0$ states are produced in equal proportion, in the LHCb acceptance. However LHCb

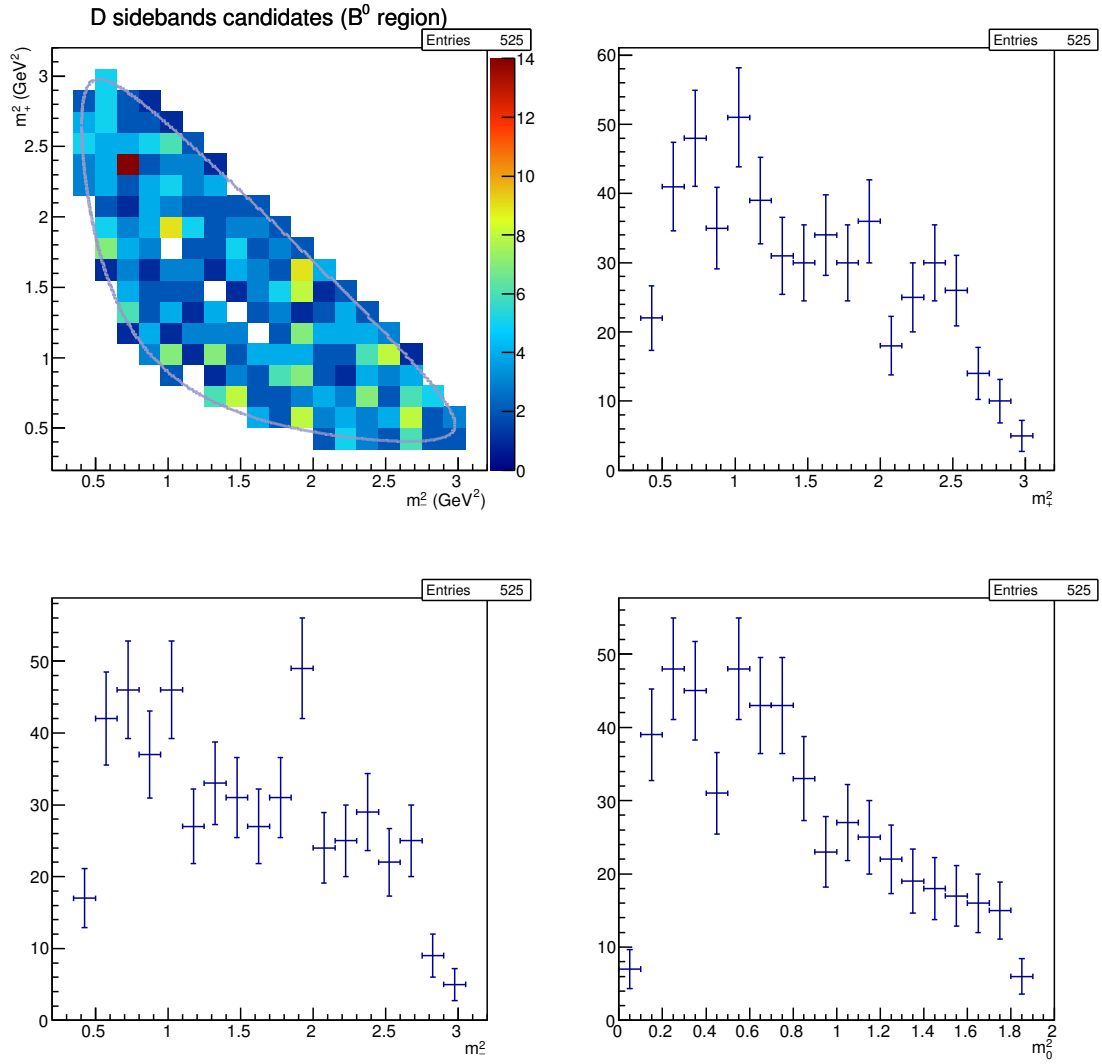

Figure 5.77 – Dalitz plot and its projections of $B^0 \to DK^{*0}$ candidates in the D^0 mass sidebands found in the data (LL and DD candidates are merged).

measured a small $D^{\pm}$ production asymmetry in 7 TeV pp collisions [158]. To determine the potential systematic effect of supposing the D^0 and $\overline{D}^0$ states in equal proportion, the Dalitz fit is repeated including a D^0-$\overline{D}^0$ production asymmetry of -1%. The deviations on the fitted cartesian parameters compared to the nominal result are

$$\begin{aligned} \delta x_- &= (-0.07 \pm 0.04) \cdot 10^{-3}, \\ \delta x_+ &= (-0.16 \pm 0.23) \cdot 10^{-3}, \\ \delta y_- &= (-0.36 \pm 0.05) \cdot 10^{-3}, \\ \delta y_+ &= (-1.05 \pm 0.12) \cdot 10^{-3}. \end{aligned} \tag{5.79}$$

The absolute values of these deviations are taken as the systematic uncertainties arising from the D^0-$\overline{D}^0$ production asymmetry. They correspond to less then 0.5% of the statistical uncertainty.

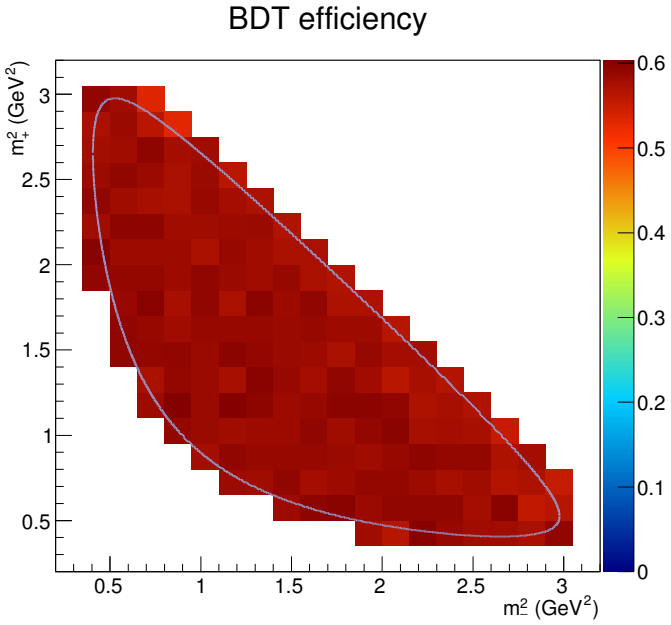

Figure 5.78 – BDT efficiency across the Dalitz plane (LL and DD candidates are merged).

$B_s^0 \to D^{*0}\overline{K}^{*0}$ background model

As explained in Sec. 5.7.2, the decay model for the partially reconstructed background $B_s^0 \to D^{*0}\overline{K}^{*0}$ neglects *CP* violation. This assumption is safe since there is a difference of two order of magnitude – $\mathcal{O}(\lambda^2)$ – between the V_{cb} and V_{ub} diagrams. Therefore the interference is very suppressed, and the *CP* violation effect very small. However the $B_s^0 \to D^{*0}\overline{K}^{*0}$ decay is the second most prominent background. Hence neglecting *CP* violation effect in this background could slightly bias the *CP* violation observables evaluated with the $B^0 \to DK^{*0}$ signal.

In order to determine the systematic effect arising from neglecting *CP* violation in $B_s^0 \to D^{*0}\overline{K}^{*0}$ several alternative Dalitz fits are performed. In each of these fits the *CP* violation parameters relative to $B_s^0 \to D^{*0}\overline{K}^{*0}$ are fixed to $\gamma = 73.2°$ [11], $r_{B_s^0} = 0.02$ (CKM elements magnitude ratio) and $\delta_{B_s^0} = \{0°, 45°, 90°, 135°, 180°, 225°, 270°, 315°\}$. The resulting deviations on the cartesian parameters compared to the nominal fit result are summarised in Table 5.25. The model used to describe the $B_s^0 \to D^{*0}\overline{K}^{*0}$ decays consists in an incoherent sum of $D^{*0} \to D^0\pi^0$ and $D^{*0} \to D^0\gamma$ contributions (the final state being different, they do not interfere). Following the approach explained in Sec. 5.5.2, the relative proportion of $D^{*0} \to D^0\pi^0$ and $D^{*0} \to D^0\gamma$ is set to 62% and 38% respectively. Between the $D^{*0} \to D^0\pi^0$ and $D^{*0} \to D^0\gamma$ decays, there is an effective strong phase shift of π which is taken into account [159].

The systematic uncertainty associated to the *CP* violation effect in $B_s^0 \to D^{*0}\overline{K}^{*0}$ background is deduced from the largest absolute value of the deviations for each cartesian parameter:

$$\begin{aligned} |\delta x_-| &= (2.46 \pm 0.03) \cdot 10^{-3}, \\ |\delta x_+| &= (5.03 \pm 0.24) \cdot 10^{-3}, \\ |\delta y_-| &= (0.75 \pm 0.09) \cdot 10^{-3}, \\ |\delta y_+| &= (0.45 \pm 0.07) \cdot 10^{-3}. \end{aligned} \tag{5.80}$$

This systematic uncertainty corresponds to less than 2% of the statistical uncertainty.

Table 5.25 – Deviation on the cartesian parameters when *CP* violation in the $B_s^0 \to D^{*0}\overline{K}^{*0}$ background is allowed.

$r_{B_s^0}$	γ (°)	$\delta_{B_s^0}$ (°)	δx_- ($\cdot 10^{-3}$)	δx_+ ($\cdot 10^{-3}$)	δy_- ($\cdot 10^{-3}$)	δy_+ ($\cdot 10^{-3}$)
0.02	73.2	0	-0.92 ± 0.04	-0.91 ± 0.36	0.39 ± 0.07	-0.07 ± 0.18
0.02	73.2	45	1.09 ± 0.05	-4.21 ± 0.44	0.54 ± 0.10	0.39 ± 0.10
0.02	73.2	90	2.46 ± 0.03	-5.03 ± 0.24	0.36 ± 0.19	0.07 ± 0.05
0.02	73.2	135	2.41 ± 0.01	-2.93 ± 0.11	-0.03 ± 0.17	-0.02 ± 0.17
0.02	73.2	180	1.17 ± 0.06	0.75 ± 0.40	-0.62 ± 0.08	-0.36 ± 0.26
0.02	73.2	225	-0.83 ± 0.06	4.06 ± 0.47	-0.75 ± 0.09	-0.43 ± 0.18
0.02	73.2	270	-2.28 ± 0.04	4.86 ± 0.27	-0.56 ± 0.19	-0.42 ± 0.03
0.02	73.2	315	-2.150 ± 0.003	2.76 ± 0.08	-0.17 ± 0.16	-0.45 ± 0.07

$B^+ \to \overline{D}^0\pi^+\pi^+\pi^-$ background contribution

In the nominal fit, the potential contribution at low B mass of partially reconstructed $B^+ \to \overline{D}^0 K^+\pi^+\pi^-$ and $B^+ \to \overline{D}^0\pi^+\pi^+\pi^-$ decays is neglected. They can potentially alter the slope of the exponential describing the combinatorial background. To determine the effect of such backgrounds, their description is included in an alternative version of the mass and Dalitz fit. In the mass fit, the $B^+ \to \overline{D}^0 K^+\pi^+\pi^-$ and $B^+ \to \overline{D}^0\pi^+\pi^+\pi^-$ background are described each with `RooKeys` PDF built from simulated samples. As the fit cannot converge when these contributions are simply added, their relative proportion to the $B_s^0 \to D\overline{K}^{*0}$ mode is fixed according to the branching fraction and efficiency:

$$\begin{aligned} \rho^{K\pi\pi} &\equiv \frac{N(B^+ \to \overline{D}^0 K^+\pi^+\pi^-)}{N(B_s^0 \to D\overline{K}^{*0})} = 0.237 \pm 0.110, \\ \rho^{\pi\pi\pi} &\equiv \frac{N(B^+ \to \overline{D}^0\pi^+\pi^+\pi^-)}{N(B_s^0 \to D\overline{K}^{*0})} = 0.134 \pm 0.059. \end{aligned} \tag{5.81}$$

As a conservative approach, the upper fluctuation of these fractions is assumed. The result of this alternative mass fit is illustrated in Fig. 5.79. The resulting yields in the $B^0 \to DK^{*0}$ signal range are summarised in Table 5.26. The $B^+ \to \overline{D}^0 K^+\pi^+\pi^-$ contribution is negligible, whereas a small contribution of $B^+ \to \overline{D}^0\pi^+\pi^+\pi^-$ arises (2 candidates in total). Consequently, the Dalitz fit is performed taking into account this additional $B^+ \to \overline{D}^0\pi^+\pi^+\pi^-$ contribution. Assuming equal mis-ID probability either for π^+ or for π^-, the $B^+ \to \overline{D}^0\pi^+\pi^+\pi^-$ decay cannot be distinguished from the $B^- \to D^0\pi^-\pi^-\pi^+$ one. To make a K^{*0} candidate from mis-identification, in every case a $(\pi^+\pi^-)$ pair is reconstructed, and in the B^+ (B^-) case a π^+ (π^-) is missed by the reconstruction. Therefore, the same model as for the $B^0 \to D\rho^0$, an incoherent sum of D^0 and $\overline{D}^0$ amplitudes, is used on the Dalitz plane. The resulting deviations on the fitted cartesian parameters, compared to the nominal result are

$$\begin{aligned} \delta x_- &= (1.22 \pm 0.40) \cdot 10^{-3}, \\ \delta x_+ &= (-0.73 \pm 0.50) \cdot 10^{-3}, \\ \delta y_- &= (0.97 \pm 0.38) \cdot 10^{-3}, \\ \delta y_+ &= (-2.24 \pm 0.56) \cdot 10^{-3}. \end{aligned} \tag{5.82}$$

The absolute values of these deviations are taken as the systematic uncertainties arising from the $B^+ \to \overline{D}^0\pi^+\pi^+\pi^-$ background contribution. They represent less than 1% of the statistical uncertainties.

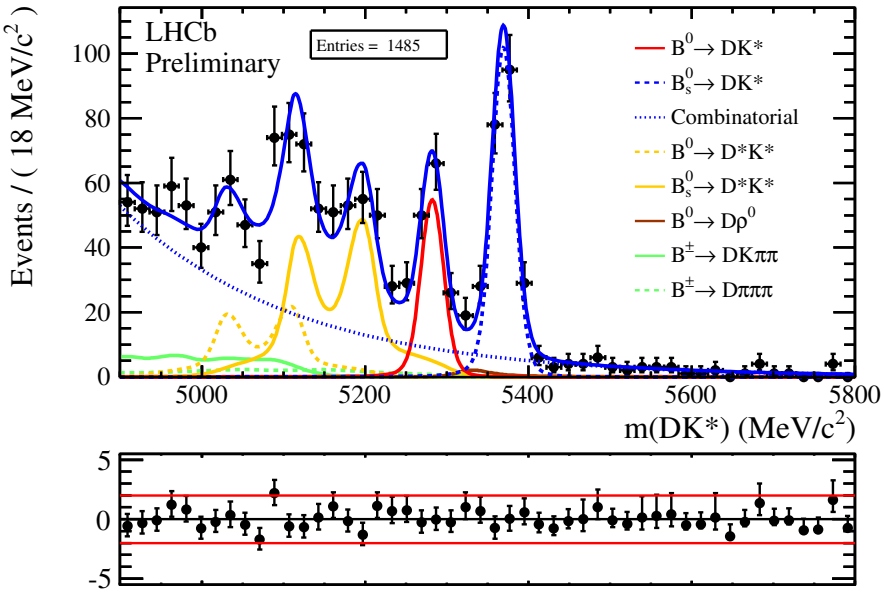

Figure 5.79 – Invariant mass fit of $B^0 \to DK^{*0}$ candidates with the additional contribution of $B^+ \to \overline{D}^0 K^+\pi^+\pi^-$ and $B^+ \to \overline{D}^0\pi^+\pi^+\pi^-$ backgrounds, for LL and DD categories merged.

Table 5.26 – Total yields in the B^0 signal region, with the $B^+ \to \overline{D}^0 K^+\pi^+\pi^-$ and $B^+ \to \overline{D}^0\pi^+\pi^+\pi^-$ contributions included.

Component	Yield		
	Total	LL	DD
$N(B^0 \to DK^{*0})$	99 ± 12	37 ± 7	63 ± 9
$N(\text{Comb})$	24.5 ± 1.7	10.6 ± 1.1	13.9 ± 1.3
$N(B_s^0 \to D^{*0}\overline{K}^{*0})$	13.5 ± 2.2	5.3 ± 1.0	8.2 ± 1.4
$N(B^0 \to D^{*0}K^{*0})$	0.09 ± 0.03	0.04 ± 0.02	0.05 ± 0.02
$N(B^0 \to D\rho^0)$	0.62 ± 0.11	0.25 ± 0.07	0.37 ± 0.09
$N(B_s^0 \to D\overline{K}^{*0})$	1.73 ± 0.31	0.66 ± 0.13	1.07 ± 0.20
$N(B^+ \to \overline{D}^0 K^+\pi^+\pi^-)$	0.111 ± 0.008	0.042 ± 0.005	0.069 ± 0.006
$N(B^+ \to \overline{D}^0\pi^+\pi^+\pi^-)$	2.02 ± 0.15	0.77 ± 0.09	1.25 ± 0.12
Total background	42.6 ± 2.5	17.6 ± 1.5	25.0 ± 2.5

$\Lambda_b^0 \to D^0 p\pi^-$ background contribution

Despite the PID cut on the charged kaon daughter of the K^{*0}, this kaon could in some cases be a mis-identified proton coming from a $\Lambda_b^0 \to D^0 p\pi^-$ decay. In this way, an invariant mass lower than the Λ_b^0 is reconstructed, and could lie into the B^0 mass range. To determine the potential systematic effect arising from this background, alternative versions of the mass and Dalitz fits are performed including the $\Lambda_b^0 \to D^0 p\pi^-$ contribution. The mass distribution is described with a `RooKeys` PDF determined from a simulated sample. The proportion of $\Lambda_b^0 \to D^0 p\pi^-$ relative to the $B_s^0 \to D\overline{K}^{*0}$ mode is fixed according to the branching fraction and efficiency ratios:

$$\rho^{\Lambda_b^0} = 0.00612 \pm 0.00456. \tag{5.83}$$

A conservative approach is adopted by assuming the "1σ" upper fluctuation of this ratio. The result of the corresponding alternative mass fit is illustrated in Fig. 5.80. The yields computed in the $B^0 \to DK^{*0}$ signal range are summarised in Table 5.27. The Dalitz fit is repeated with the same model for $\Lambda_b^0 \to D^0 p\pi^-$ ($\overline{\Lambda}_b^0 \to \overline{D}^0 \overline{p}\pi^+$) as for $\overline{B}_s^0 \to DK^{*0}$ ($B_s^0 \to D\overline{K}^{*0}$) in the $B^0 \to DK^{*0}$ ($\overline{B}^0 \to D\overline{K}^{*0}$) Dalitz plot. The corresponding deviations on the fitted cartesian parameters compared to the nominal result are

$$\begin{aligned} \delta x_- &= (-0.16 \pm 0.06) \cdot 10^{-3}, \\ \delta x_+ &= (0.28 \pm 0.39) \cdot 10^{-3}, \\ \delta y_- &= (-0.66 \pm 0.07) \cdot 10^{-3}, \\ \delta y_+ &= (1.77 \pm 0.19) \cdot 10^{-3}. \end{aligned} \tag{5.84}$$

The absolute values of these deviations are taken as the systematic uncertainties arising from the $\Lambda_b^0 \to D^0 p\pi^-$ background contribution. They represent less than 0.8% of the statistical uncertainties.

Table 5.27 – Total yields in the B^0 signal region, with the $\Lambda_b^0 \to D^0 p\pi^-$ contribution included.

Component	Yield		
	Total	LL	DD
$N(B^0 \to DK^{*0})$	99 ± 12	37 ± 7	62 ± 9
N(Comb)	26.7 ± 1.8	11.4 ± 1.1	15.3 ± 1.3
$N(B_s^0 \to D^{*0}\overline{K}^{*0})$	13.6 ± 2.0	5.3 ± 1.0	8.3 ± 1.4
$N(B^0 \to D^{*0}K^{*0})$	0.12 ± 0.03	0.05 ± 0.02	0.06 ± 0.02
$N(B^0 \to D\rho^0)$	0.61 ± 0.11	0.25 ± 0.07	0.36 ± 0.09
$N(B_s^0 \to D\overline{K}^{*0})$	1.70 ± 0.30	0.65 ± 0.13	1.05 ± 0.20
$N(\Lambda_b^0 \to D^0 p\pi^-)$	0.18 ± 0.01	0.069 ± 0.008	0.11 ± 0.01
Total background	42.8 ± 2.6	17.7 ± 1.5	25.1 ± 1.9

K^{*0} coherence factor

The K^{*0} coherence factor is evaluated with the phenomenological model described in Sec. 5.9.1. Its value is $\kappa = 0.93 \pm 0.04$. In the nominal fit, κ is fixed. Therefore a systematic uncertainty is

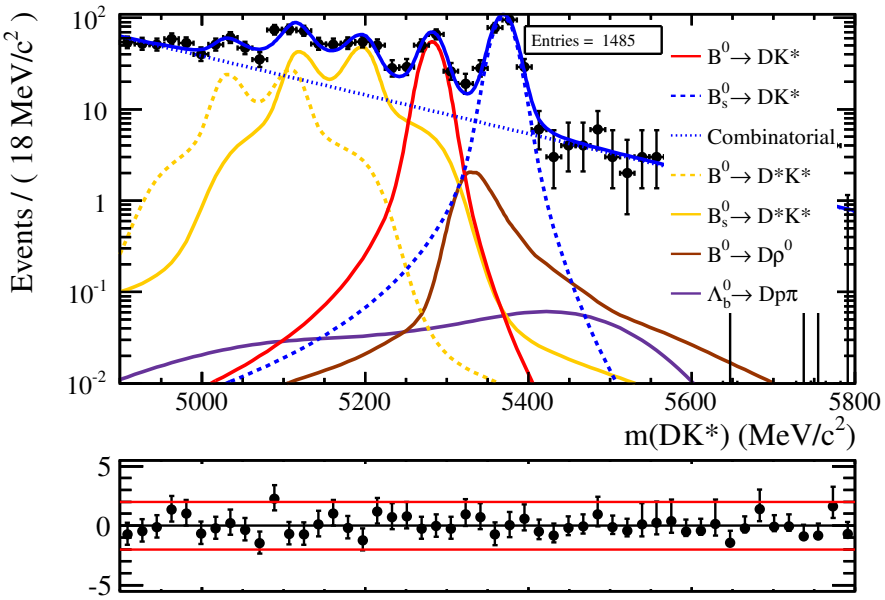

Figure 5.80 – Invariant mass fit of $B^0 \to DK^{*0}$ candidates with the additional contribution of $\Lambda_b^0 \to D^0 p\pi^-$ backgrounds, for LL and DD categories merged. The y-axis is in log-scale.

determined by repeating the fit with κ varied within its uncertainty. Table 5.28 summarises the deviations of the cartesian parameters compared to the nominal result. The largest absolute values of these deviations are taken as the systematic uncertainties arising from the coherence factor:

$$\begin{aligned} |\delta x_-| = &\quad (3.87 \pm 5.07) \cdot 10^{-3}, \\ |\delta x_+| = &\quad (2.66 \pm 10.1) \cdot 10^{-3}, \\ |\delta y_-| = &\quad (2.07 \pm 2.23) \cdot 10^{-3}, \\ |\delta y_+| = &\quad (0.96 \pm 2.54) \cdot 10^{-3}. \end{aligned} \tag{5.85}$$

Table 5.28 – Deviation on the cartesian parameters arising from the κ coherence factor uncertainty.

κ	δx_- $(\cdot 10^{-3})$	δx_+ $(\cdot 10^{-3})$	δy_- $(\cdot 10^{-3})$	δy_+ $(\cdot 10^{-3})$
0.89	3.74 ± 4.78	2.66 ± 10.1	-2.07 ± 2.23	0.96 ± 2.54
0.97	-3.87 ± 5.07	-2.34 ± 10.6	1.64 ± 2.28	-0.65 ± 2.12

5.8.3 Efficiency description on the Dalitz plane

Efficiency variation

As explained in Sec. 5.3, one thousand alternative efficiency Dalitz plots are made to take into account the uncertainty on the efficiency. From these alternative efficiency descriptions one thousand Dalitz fits are performed on the real data. The deviation to the fit result obtained with the nominal efficiency is computed for each alternative fit. The resulting distributions of these deviations are plotted on Fig. 5.81. A Gaussian fit determines the width of these residuals. The biggest one is of the order of $5 \cdot 10^{-3}$, almost two orders of magnitude below the statistical uncertainty.

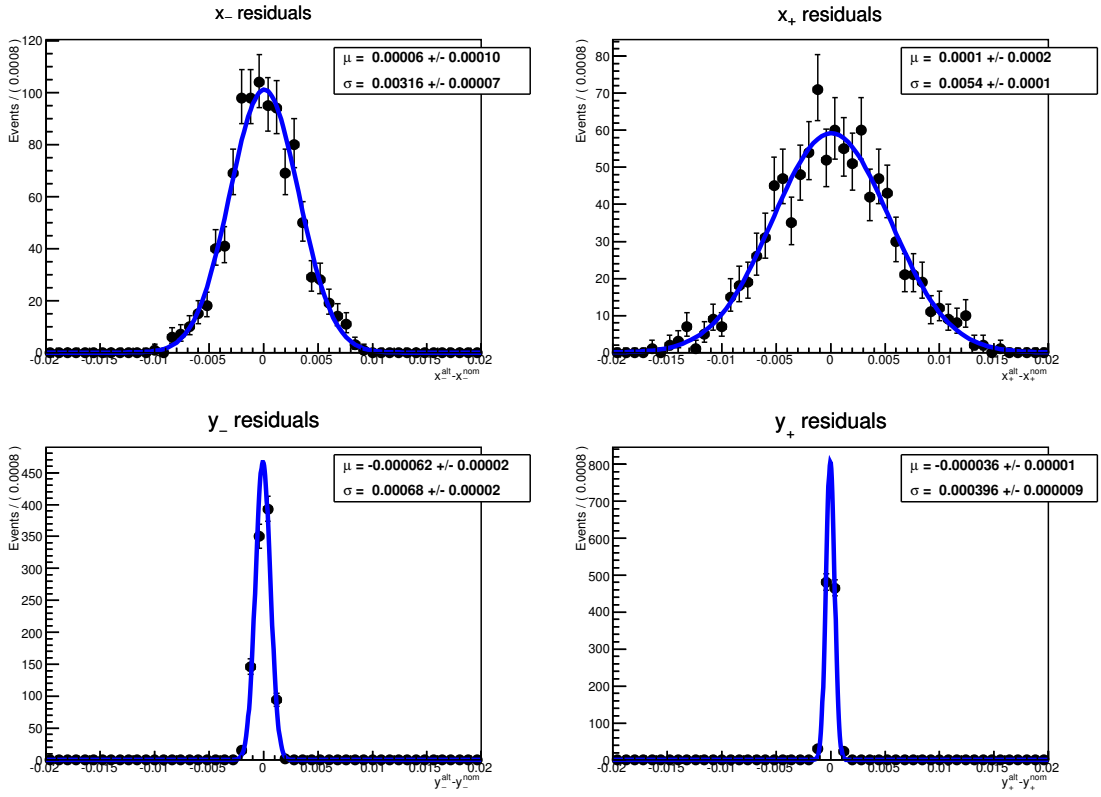

Figure 5.81 – Deviation to the nominal fit values of the cartesian parameters fitted on data with one thousand alternative efficiency description.

The width of the residuals given by the fits on data are different between the cartesian parameters. To check that it is an expected feature, five pseudo datasets of around 16000 signal and background events are generated. Each pseudo datasets are fitted then with the nominal efficiency and with one hundred alternative efficiency. The resulting deviation from the nominal results is in Fig. 5.82. Compared to the results on real data, similar distributions are obtained.

Hence the efficiency systematic is assumed to be the width of the residuals obtained with

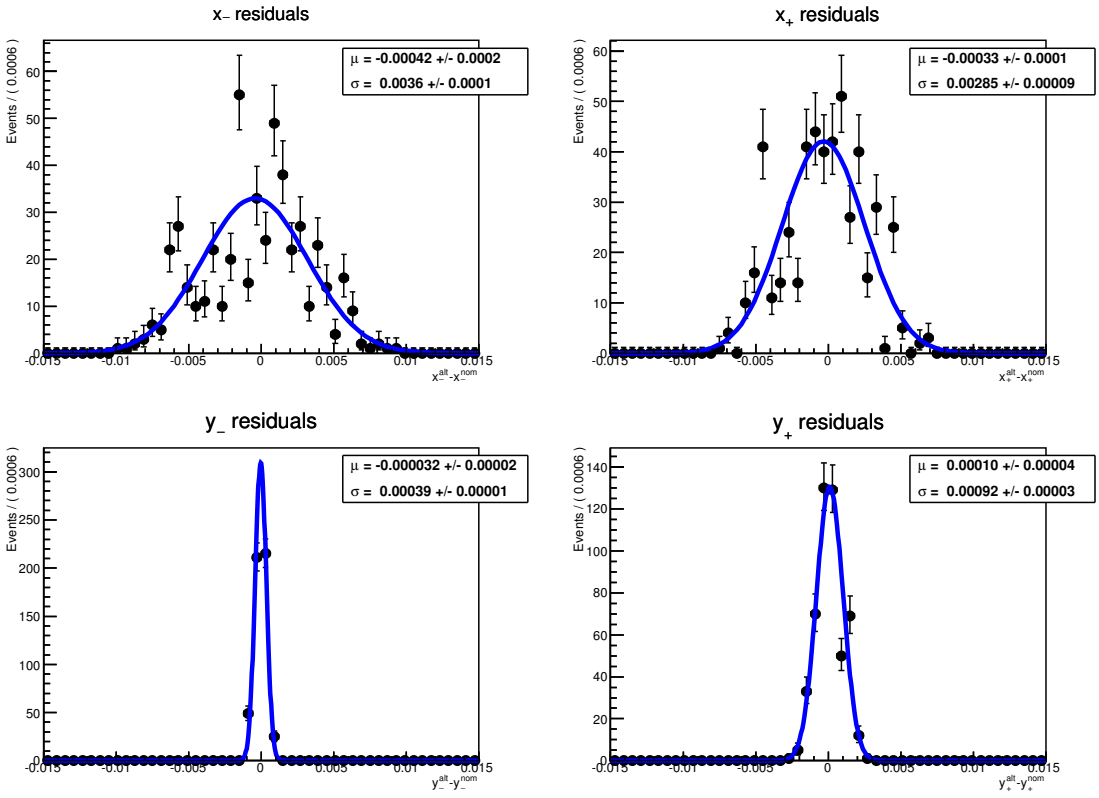

Figure 5.82 – Deviation to the nominal fit values of the cartesian parameters fitted on five different pseudo datasets with one hundred alternative efficiency description.

the alternative fits performed on data:

$$\begin{aligned} |\delta x_-| = &\quad (3.16 \pm 0.07) \cdot 10^{-3}, \\ |\delta x_+| = &\quad (5.4 \pm 0.1) \cdot 10^{-3}, \\ |\delta y_-| = &\quad (0.68 \pm 0.02) \cdot 10^{-3}, \\ |\delta y_+| = &\quad (0.40 \pm 0.01) \cdot 10^{-3}. \end{aligned} \tag{5.86}$$

Efficiency with BDTB

In the nominal efficiency description, the selection applied to the simulated sample implies a cut on BDTA. Since on the data both BDTA and BDTB are applied, in a crossed way, the systematic effect inherent to this arbitrary choice has to be evaluated. This effect is expected to be very small since the efficiency of the BDTA and BDTB are very similar (see Fig. 5.28). An alternative Dalitz fit is performed on the data with the efficiency determined on the simulated sample selected by the BDTB. It gives the following deviations to the nominal results:

$$\begin{aligned} \delta x_- = &\quad (0.24 \pm 0.01) \cdot 10^{-3}, \\ \delta x_+ = &\quad (0.39 \pm 0.03) \cdot 10^{-3}, \\ \delta y_- = &\quad (0.06 \pm 0.02) \cdot 10^{-3}, \\ \delta y_+ = &\quad (-0.04 \pm 0.02) \cdot 10^{-3}. \end{aligned} \tag{5.87}$$

The absolute value of this deviations are taken as the systematic uncertainty due to the use of BDTB instead of BDTA in the efficiency evaluation.

HLT efficiency

As explained in Sec. 5.3.1, the HLT efficiency is uniform across the Dalitz plane. And the selection efficiency is determined without applying the HLT requirements on the simulated sample. To determine the effect of this choice the Dalitz fit is repeated with the efficiency computed with the HLT requirements. The resulting deviations on the cartesian parameters compared to the nominal fit result are

$$\begin{aligned} \delta x_- &= (-3.62 \pm 0.07) \cdot 10^{-3}, \\ \delta x_+ &= (-6.62 \pm 0.39) \cdot 10^{-3}, \\ \delta y_- &= (-0.88 \pm 0.28) \cdot 10^{-3}, \\ \delta y_+ &= (0.39 \pm 0.23) \cdot 10^{-3}. \end{aligned} \tag{5.88}$$

The absolute values of these deviations are taken as the systematic uncertainties due to the HLT efficiency. These uncertainties correspond at most to 2.8% of the statistical ones.

Data/MC agreement

In the determination of the selection efficiency, the simulation is assumed to be reliable, apart from the L0 and PID efficiencies. To ensure that the BDT efficiency is correctly determined, a Data/MC comparison is performed. The distributions of the discriminating variables used in the BDT obtained with the $B_s^0 \to D\overline{K}^{*0}$ simulated sample and with the data are compared. The simulated sample corresponds to $B_s^0 \to D\overline{K}^{*0}$ truth matched candidates after the full selection (using the PID efficiency from the calibration samples). The distributions from data are made with the *sPlot* method [157]. A simplified mass fit is performed only on the mass region between 5325 MeV and 5800 MeV. In this way, the study is focused on $B_s^0 \to D\overline{K}^{*0}$ data candidates with a better signal significance and purity. In the simplified fit model only the contributions of the $B_s^0 \to D\overline{K}^{*0}$ signal and the combinatorial background are taken into account, with a double Crystal Ball function and an exponential respectively. The result of this mass fit is illustrated in Fig. 5.83a and the resulting *sWeights* as a function of the B mass in Fig. 5.83b.

These *sWeights* are then used to make the distributions of the BDT discriminating variables. These distributions are compared to those obtained from the simulated sample. The resulting distributions are drawn in Fig. 5.84–5.88. They are all in good agreement, except for the `DecayTreeFitter` refit χ^2/ndf (Fig. 5.87) and the K^{*0} helicity angle (Fig. 5.88). For these two distributions, some slight discrepancies can be seen. To see if these discrepancies have a significant impact on the efficiency determination, the simulated sample is reweighted to follow the `DecayTreeFitter` χ^2/ndf and $\cos\theta^*$ data distributions. From this reweighted sample, the efficiency across the Dalitz plane is recomputed and the subsequent Dalitz fit performed. The resulting deviations of the cartesian parameters compared to the nominal result are

$$\begin{aligned} \delta x_- &= (-0.68 \pm 0.09) \cdot 10^{-3}, \\ \delta x_+ &= (-2.00 \pm 0.11) \cdot 10^{-3}, \\ \delta y_- &= (-0.29 \pm 0.02) \cdot 10^{-3}, \\ \delta y_+ &= (-0.09 \pm 0.04) \cdot 10^{-3}. \end{aligned} \tag{5.89}$$

The absolute value of these deviations is taken as the systematic uncertainties arising from the Data-MC disagreement on the BDT efficiency. They correspond to less than 0.8% of the statistical uncertainties.

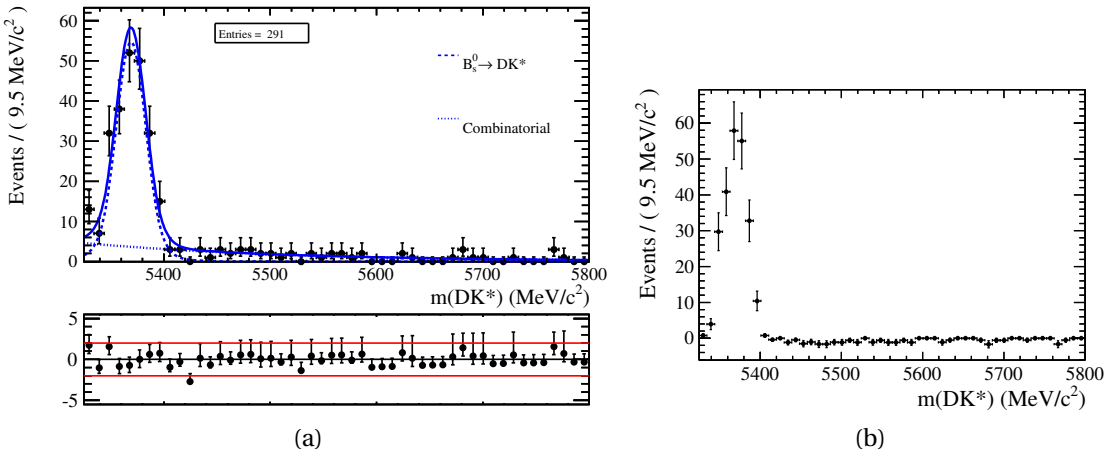

Figure 5.83 – Simplified mass fit of data candidates in the $B_s^0 \to D\overline{K}^{*0}$ region (a) and distribution of the resulting *sWeights* as a function of the B mass (b).

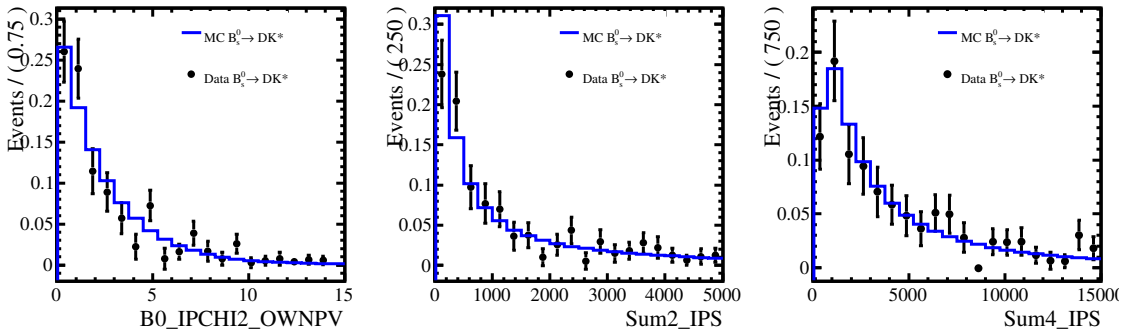

Figure 5.84 – Data-MC comparison for the impact parameters . The $B_s^0 \to D\overline{K}^{*0}$ simulated candidates are in solid blue, while the sWeighted $B_s^0 \to D\overline{K}^{*0}$ data candidates are in black.

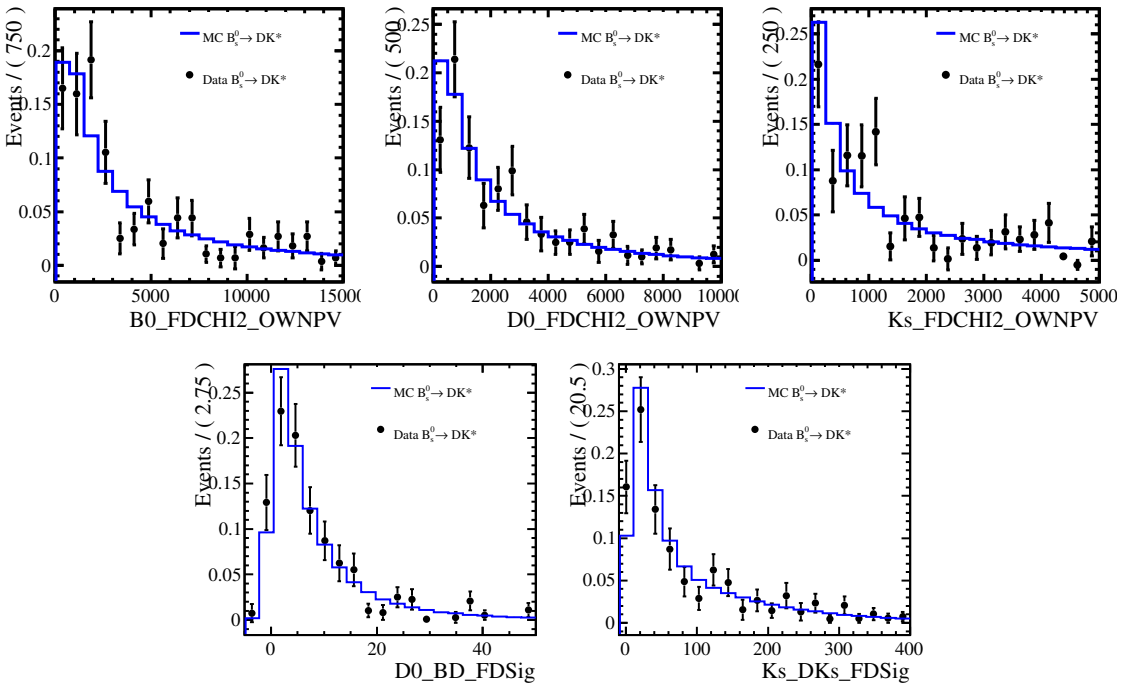

Figure 5.85 – Data-MC comparison for the flight distance significance. The $B_s^0 \to D\overline{K}^{*0}$ simulated candidates are in solid blue, while the sWeighted $B_s^0 \to D\overline{K}^{*0}$ data candidates are in black.

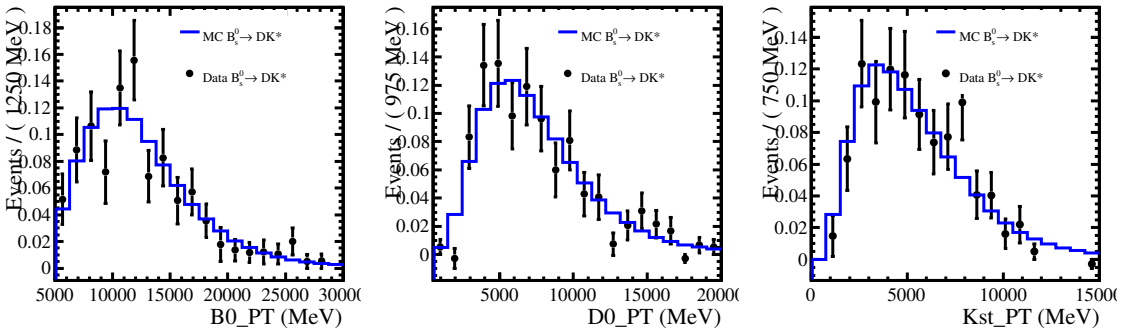

Figure 5.86 – Data-MC comparison for the transverse momemtum. The $B_s^0 \to D\overline{K}^{*0}$ simulated candidates are in solid blue, while the sWeighted $B_s^0 \to D\overline{K}^{*0}$ data candidates are in black.

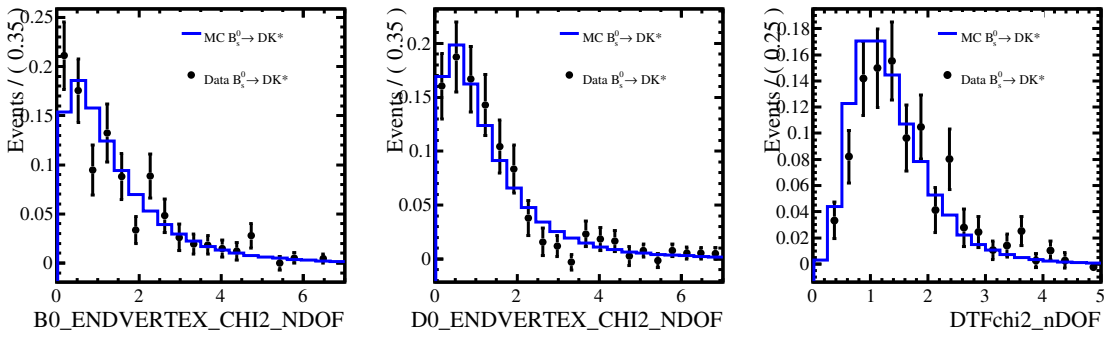

Figure 5.87 – Data-MC comparison for the vertex-related variables. The $B_s^0 \to D\overline{K}^{*0}$ simulated candidates are in solid blue, while the sWeighted $B_s^0 \to D\overline{K}^{*0}$ data candidates are in black.

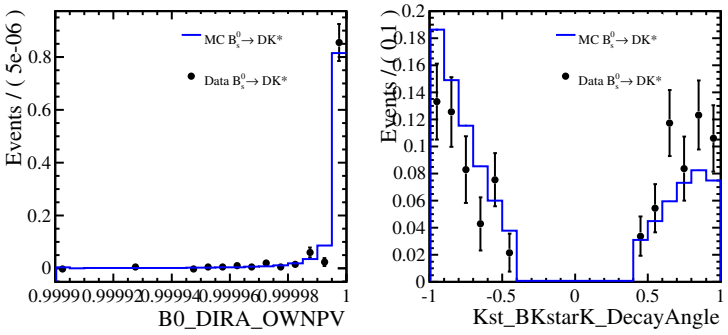

Figure 5.88 – Data-MC comparison for the B^0 pointing angle(left) and K^{*0} helicity angle (right). The $B_s^0 \to D\overline{K}^{*0}$ simulated candidates are in solid blue, while the sWeighted $B_s^0 \to D\overline{K}^{*0}$ data candidates are in black.

Generator level cuts

The $B_s^0 \to D\overline{K}^{*0}$ simulated sample used to determine the efficiency has been produced with some cuts at the `Pythia` level (generators cuts). These cuts are detailed in Appendix A. They were designed to be less tight than the stripping selection. However, there might be some effect of the generator level cuts along the m_0^2 Dalitz coordinates. Looking at Fig. A.1, the efficiency of the cuts on top of the stripping selection might not be completely flat (here a specific MC sample is used without generator cut). To see if this potential non-flatness causes some bias, the generator cuts efficiency distribution along m_0^2 is fitted with a first order polynomial. The result of this fit is illustrated in Fig. 5.89. The fit results in a slight negative slope. In order to measure the effect of this small bias, the $B_s^0 \to D\overline{K}^{*0}$ simulated sample is reweighted according to this slope. The efficiency is then recomputed after this reweighting.The ratio of the efficiency determined with and without the reweighting is illustrated in Fig. 5.90. No noticeable effect can be seen. The Dalitz fit is repeated with the efficiency including the reweighting. The following deviations on the cartesian parameters compared to the nominal fit result are observed:

$$\begin{aligned} \delta x_- &= (3.68 \pm 0.05) \cdot 10^{-3}, \\ \delta x_+ &= (5.82 \pm 0.31) \cdot 10^{-3}, \\ \delta y_- &= (0.62 \pm 0.30) \cdot 10^{-3}, \\ \delta y_+ &= (-0.50 \pm 0.25) \cdot 10^{-3}. \end{aligned} \tag{5.90}$$

The absolute value of these deviations is taken as the systematic uncertainties arising from the generator level cuts efficiency. They correspond to less than 2.8% of the statistical uncertainties.

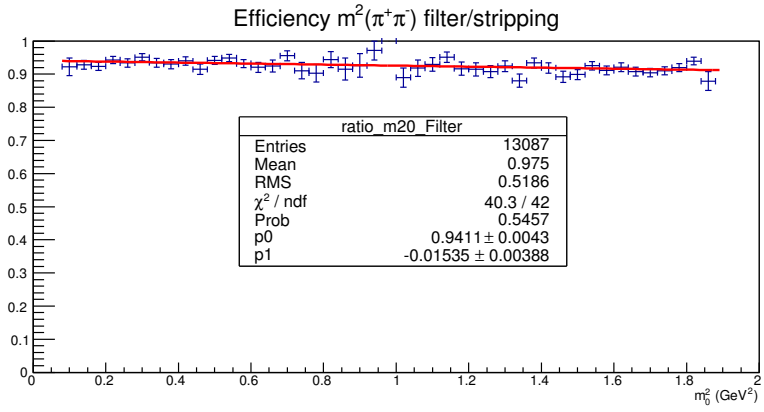

Figure 5.89 – Efficiency distribution along m_0^2 of the generator level cuts after the stripping selection. The fit result with a first order polynomial is superimposed. This determination uses the MC11a $B^0 \to DK^{*0}$ simulated sample.

Fraction of TOS events

As explained in Sec. 5.3.1 and at the end of Sec. 5.3.4, the trigger efficiency description uses the TOS and NotTOS proportion found with the $B^0 \to DK^{*0}$ candidates selected in the data, $f_{\text{TOS}} = (67.4 \pm 3.9)\%$ (95 TOS, 46 NotTOS). This value has a limited statistical accuracy. To evaluate the corresponding systematic uncertainty the Dalitz fit is repeated assuming the fraction of TOS events found with the $B_s^0 \to D\overline{K}^{*0}$ candidates selected in the data, $f_{\text{TOS}} = (59.8 \pm 3.4)\%$ (122 TOS,

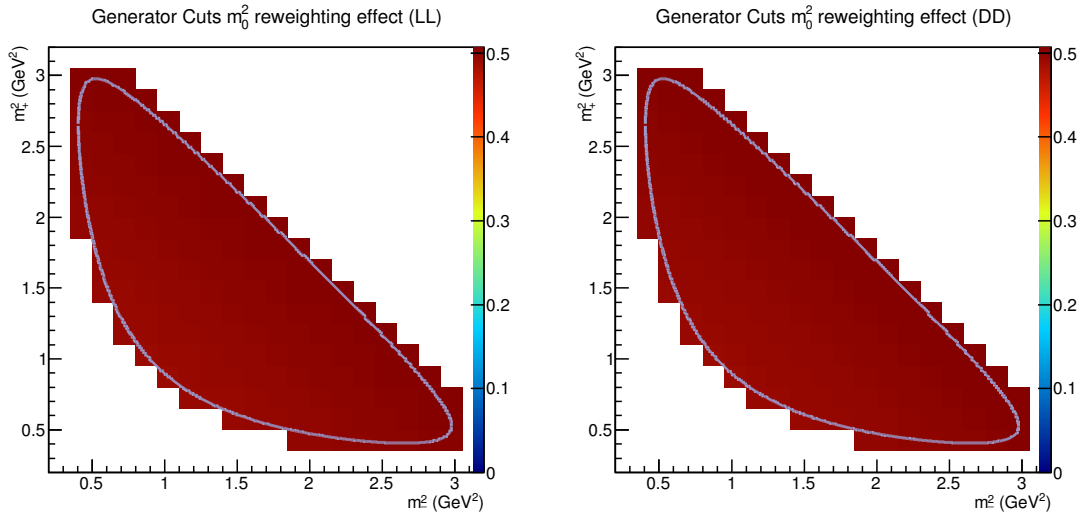

Figure 5.90 – Efficiency ratio across the Dalitz plane when determined with and without the generator level cuts reweighting.

82 NotTOS). This value differs from the nominal one by 1.4σ (assuming binomial errors). The resulting deviations on the fitted cartesian parameters, compared to the nominal result are

$$\begin{aligned} \delta x_- &= (-1.91 \pm 0.02) \cdot 10^{-3}, \\ \delta x_+ &= (3.81 \pm 0.24) \cdot 10^{-3}, \\ \delta y_- &= (0.59 \pm 0.13) \cdot 10^{-3}, \\ \delta y_+ &= (0.13 \pm 0.12) \cdot 10^{-3}. \end{aligned} \tag{5.91}$$

The absolute value of these deviations is taken as the systematic uncertainties arising from the f_{TOS} ratio. They represent less than 1.5% of the statistical uncertainties.

5.8.4 Resolution on the Dalitz coordinates

The reconstruction of the squared invariant masses $m^2_\pm$ is not perfect. These Dalitz coordinates are measured with a given resolution, which produces a migration of the events in the Dalitz plane. The resolution on the Dalitz coordinates is determined from the $B^0 \to DK^{*0}$ simulated sample. The difference between the reconstructed and the true coordinates is measured, as well as their correlation. As illustrated in Fig. 5.91, the resolution is very small, of the order of $0.007\,\mathrm{GeV}^2$ and the variation of m^2_+ and m^2_- is anti-correlated.

To measure the effect of such a resolution on the Dalitz coordinates, a study is performed with pseudo-experiments. Around sixteen thousand pseudo-candidates are generated, including signal and background and become the nominal dataset. To simulate the migration effect, this nominal sample is then smeared randomly according to the two-dimensional distributions shown in Fig. 5.91. In this way, one thousand alternative data sample are generated. They differ only from the original sample by a variation on $m^2_\pm$ according to the resolution. These alternative data samples are fitted. The resulting distributions of the deviations of the cartesian parameters, compared to those obtained with the non smeared sample are shown in Fig. 5.92. Since there are non-negligible biases – nevertheless small compared to the statistical error on the cartesian

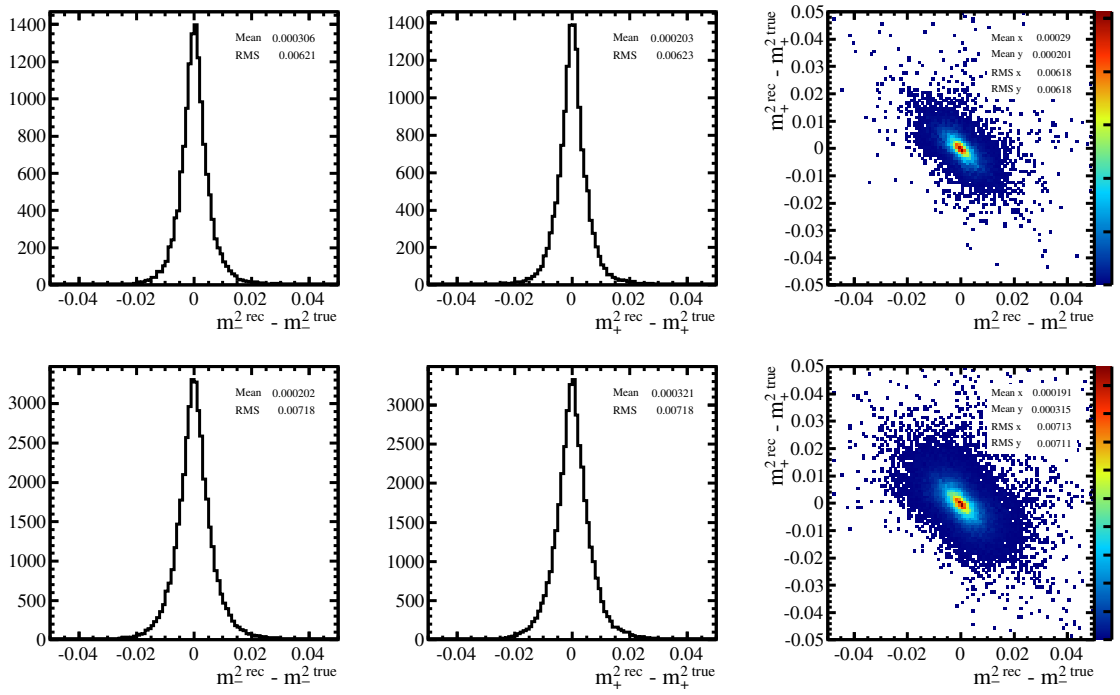

Figure 5.91 – Difference between the reconstructed and the true Dalitz coordinates m^2_- (left) and m^2_+ (middle), and their correlation (right). The top (bottom) plots correspond to $B^0 \to DK^{*0}$ LL (DD) candidates.

parameters – the systematic uncertainties arising from the migration across the Dalitz plane are taken as the quadratic sum of the mean and the width of the residuals:

$$\begin{aligned} |\delta x_-| &= 4.35 \cdot 10^{-3}, \\ |\delta x_+| &= 4.00 \cdot 10^{-3}, \\ |\delta y_-| &= 2.90 \cdot 10^{-3}, \\ |\delta y_+| &= 3.05 \cdot 10^{-3}. \end{aligned} \tag{5.92}$$

These systematic uncertainties are lower than 3.3% of the statistical uncertainties.

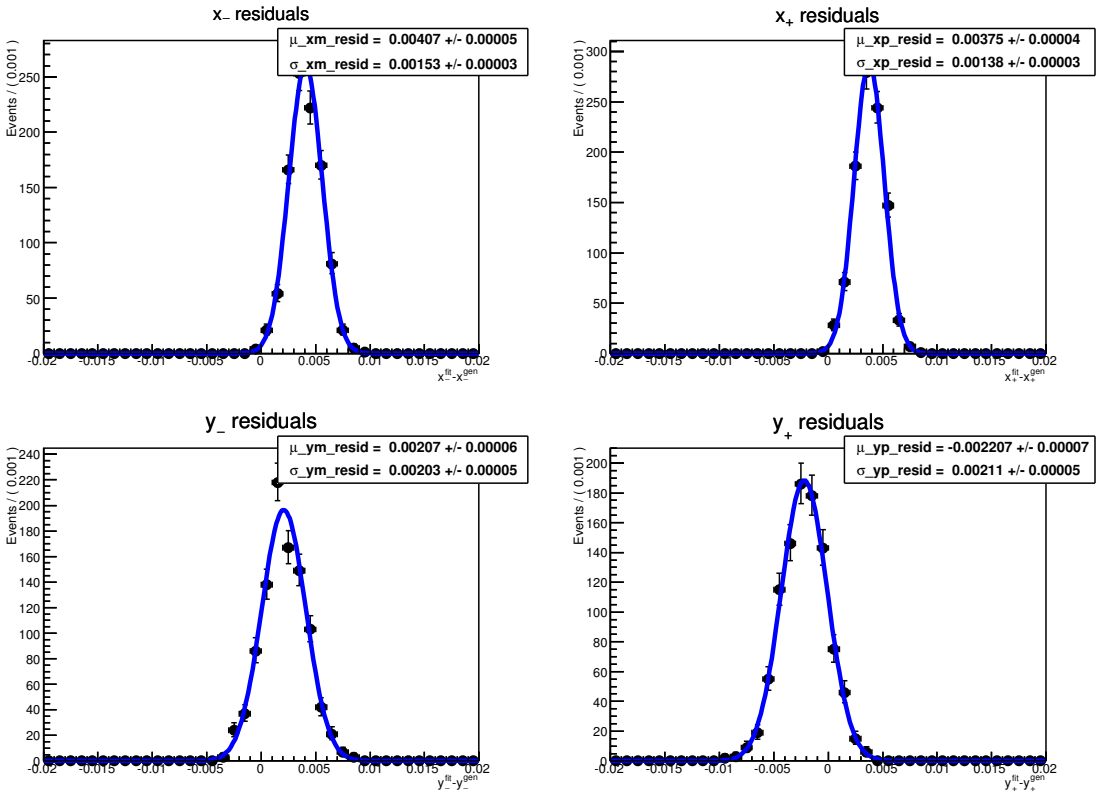

Figure 5.92 – Deviation of the cartesian parameters fitted on smeared toy samples compared to the result obtained with the non-smeared sample. The smearing corresponds to the resolution on the Dalitz plot coordinates.

5.8.5 Model related uncertainty

The model used to described the $D \to K^0_S\pi^+\pi^-$ decay, presented in Sec. 5.6, includes some uncertainties. A choice is made on the type of resonances used, and how they are expressed. Hence, a systematic uncertainty arising from the potential mis-modelling of the $D \to K^0_S\pi^+\pi^-$ decay is determined, following the same procedure as the LHCb $B^\pm \to DK^\pm$ model dependent GGSZ analysis [52]. Since this evaluation has not been performed by the author of this thesis, only a brief summary is presented. The systematic uncertainty evaluation consists in taking several alternative models and determining the deviations induced on the fitted cartesian parameters, with pseudo-experiments.

Alternative $D^0 \to K_S\pi^+\pi^-$ models considered

Compared to the nominal model, each alternative model is made with only one change; either in the parameterisation of a given component, or in the addition or suppression of one component. The different variations considered are:

- $\pi\pi$ S-wave: The nominal model uses one of the three possible solutions of the K-matrix, obtained from fits to scattering data. Two alternative models are defined to use the other two solutions.
- $\pi\pi$ S-wave: Remove the non-resonant term of the P-vector.
- $K\pi$ S-wave: Replace the generalised LASS parameterisation used in the nominal model to describe the $K^{0*}(1430)$ resonance with a relativistic Breit-Wigner propagator, with parameters taken from the E791 experiment.
- $\pi\pi$ P-wave: Replace the Gounaris-Sakurai propagator with a Breit-Wigner.
- $K\pi$ P-wave: Vary the mass and width parameters of the $K^*(1680)$ resonance by their quoted errors.
- $\pi\pi$ D-wave: Vary the mass and width parameters of the $f_2(1270)$ resonance by their quoted errors.
- $K\pi$ D-wave: Vary the mass and width parameters of the $K^*_2(1430)$ resonance by their quoted errors.
- Change the Blatt-Weisskopf centrifugal barrier radius to 0 and 3 GeV^{-1}.
- Add two extra resonances to the model - the $K^*(1410)$ and the $\rho(1450)$.
- Replace the Zemach formalism for the spin sum rules with the helicity formalism. This affects mostly D-waves.

One further alternative model is defined, containing several changes relative to the nominal model. This model contains the prominent K^*, ρ, ω and f^0 resonances, with an alternative parameterisation for the S-wave contributions (LASS/K-matrix).

Results of alternative model fits

From these alternative models, pseudo-experiments are generated and fitted, and the following deviations are computed

$$\delta x_{\pm}^{m} = x_{\pm}^{m} - x_{\pm}^{0}, \tag{5.93}$$

$$\delta y_{\pm}^{m} = y_{\pm}^{m} - y_{\pm}^{0}, \tag{5.94}$$

where $m = 0$ denotes the nominal model.

The different Cartesian parameters are assumed to be fully correlated or anti-correlated (according to the sign of the $\delta x_{\pm}^{m}$ and $\delta y_{\pm}^{m}$ deviations). Hence, the resulting covariance matrix has the form:

$$V^{m} = \begin{array}{c} \begin{matrix} x_{-}^{m} & y_{-}^{m} & x_{+}^{m} & y_{+}^{m} \end{matrix} \\ \begin{pmatrix} \delta x_{-}^{m}\delta x_{-}^{m} & \delta x_{-}^{m}\delta y_{-}^{m} & \delta x_{-}^{m}\delta x_{+}^{m} & \delta x_{-}^{m}\delta y_{+}^{m} \\ \delta y_{-}^{m}\delta x_{-}^{m} & \delta y_{-}^{m}\delta y_{-}^{m} & \delta y_{-}^{m}\delta x_{+}^{m} & \delta y_{-}^{m}\delta y_{+}^{m} \\ \delta x_{+}^{m}\delta x_{-}^{m} & \delta x_{+}^{m}\delta y_{-}^{m} & \delta x_{+}^{m}\delta x_{+}^{m} & \delta x_{+}^{m}\delta y_{+}^{m} \\ \delta y_{+}^{m}\delta x_{-}^{m} & \delta y_{+}^{m}\delta y_{-}^{m} & \delta y_{+}^{m}\delta x_{+}^{m} & \delta y_{+}^{m}\delta y_{+}^{m} \end{pmatrix} \end{array}, \tag{5.95}$$

for each alternative model m. Table 5.29 enumerates the model-related systematic uncertainties obtained for each alternative model considered.

The systematic uncertainties from different models are assumed to be independent. Therefore, the total covariance matrix is simply the sum of the covariances matrices from the separate models:

$$V_{\text{model}} = \sum_{m} V^{m} = \begin{array}{c} \begin{matrix} x_{-}^{m} & y_{-}^{m} & x_{+}^{m} & y_{+}^{m} \end{matrix} \\ \begin{pmatrix} 59.1 & -37.4 & 59.5 & 1.0 \\ -37.4 & 49.7 & -59.2 & 20.4 \\ 59.5 & -59.2 & 93.9 & -10.9 \\ 1.0 & 20.4 & -10.9 & 23.4 \end{pmatrix} \end{array} \cdot (10^{-6}). \tag{5.96}$$

Finally, the total systematic uncertainties on each cartesian coordinates are the square root of the diagonal matrix elements:

$$\begin{aligned} \delta x_{-} &= 7.7 \cdot (10^{-3}), \\ \delta y_{-} &= 7.1 \cdot (10^{-3}), \\ \delta x_{+} &= 9.7 \cdot (10^{-3}), \\ \delta y_{+} &= 4.8 \cdot (10^{-3}). \end{aligned}$$

They are of consistent with those found in the LHCb [52] and BaBar [160] $B^{\pm} \to DK^{\pm}$ model dependent GGSZ analyses.

Table 5.29 – Summary of model-related signed systematic uncertainties obtained for each alternative model considered.

Model description		$\delta x_-(\cdot 10^{-3})$	$\delta y_-(\cdot 10^{-3})$	$\delta x_+(\cdot 10^{-3})$	$\delta y_+(\cdot 10^{-3})$
K-matrix 1st solution		−1.7	0.9	1.9	1.2
K-matrix 2nd solution		0.3	0.3	0.0	−0.5
Remove non-res term of P-vector		−0.7	0.2	0.5	0.6
gLASS→RBW		1.7	3.0	−1.2	3.0
Gounaris-Sakurai→RBW		0.7	0.0	−0.1	0.8
$K^*(1680)$	$m+\delta m$	−0.0	0.6	0.1	0.5
	$m-\delta m$	−0.2	−0.5	0.2	−0.9
	$\Gamma+\delta\Gamma$	−0.2	0.2	0.0	−0.2
	$\Gamma-\delta\Gamma$	0.2	−0.1	0.5	−0.2
$f_2(1270)$	$m+\delta m$	−0.1	0.0	0.3	−0.2
	$m-\delta m$	−0.0	0.1	0.2	−0.2
	$\Gamma+\delta\Gamma$	−0.0	0.0	0.2	−0.2
	$\Gamma-\delta\Gamma$	−0.1	0.0	0.2	−0.2
$K_2^*(1430)$	$m+\delta m$	0.3	0.2	0.2	−0.2
	$m-\delta m$	−0.4	−0.2	0.3	−0.1
	$\Gamma+\delta\Gamma$	−0.2	0.2	0.1	−0.2
	$\Gamma-\delta\Gamma$	0.1	−0.1	0.3	−0.2
$r_{\rm BW} = 0.0\,{\rm GeV}^{-1}$		−1.8	0.7	−1.0	−0.3
$r_{\rm BW} = 3.0\,{\rm GeV}^{-1}$		4.2	−1.6	4.1	2.3
Add $K^*(1410)$ and $\rho(1450)$		−0.2	−0.2	0.3	−0.3
Zemach→helicity formalism		−5.5	6.0	−8.4	2.3

5.8.6 Summary of the systematic uncertainties

All the systematic uncertainties are summarised in Table 5.30. They are all quoted in absolute values. The main uncertainties come from the fake D background (yields and model), the mass fit floating parameters and the K^0_S flight distance cut. All have a partial statistical origin. With an increased data sample, they are expected to reduce. The following effects are ignored since they are expected to be negligible according to previous LHCb analyses [13, 52]: the D^0 mixing, the K^0_S mixing and CP violation effect and the pion charged asymmetries. Since they are relatively small and coming from independent effects, the systematic uncertainties are assumed to be uncorrelated.

Table 5.30 – Summary of the systematic uncertainties and their proportion compared to the statistical uncertainty.

Source of uncertainty	δx_- ($\cdot 10^{-3}$)	δx_+ ($\cdot 10^{-3}$)	δy_- ($\cdot 10^{-3}$)	δy_+ ($\cdot 10^{-3}$)
Mass fit induced				
Floating mass fit parameters	17.0 (13%)	6.6 (2.5%)	12.1 (8.1%)	39.2 (17%)
$B^0 \to \overline{D}^0\pi^+\pi^-$ contribution	0.98 (0.8%)	0.60 (0.2%)	0.43 (0.3%)	2.02 (0.9%)
B^0-B_s^0 mass difference	0.82 (0.6%)	0.50 (0.2%)	0.64 (0.5%)	2.33 (1.0%)
Mass PDF with BDTB	0.11 (0.1%)	0.17 (0.1%)	0.42 (0.3%)	1.22 (0.5%)
Signal PDF - CB parameters	0.39 (0.3%)	0.35 (0.1%)	0.35 (0.2%)	0.74 (0.3%)
Signal PDF - triple Gaussian	4.08 (3.1%)	1.87 (0.7%)	3.93 (2.6%)	9.92 (4.3%)
π^0/γ proportion	2.66 (2.0%)	2.07 (0.8%)	3.78 (2.5%)	14.49 (6.3%)
$B^0 \to D^{*0}K^{*0}$ effect	0.42 (0.3%)	0.32 (0.1%)	0.72 (0.5%)	2.34 (1.0%)
K_S^0 flight distance cut	70 (54%)	54 (21%)	5 (3.3%)	21 (9.1%)
Background description				
Fake D^0 background	47 (36%)	19 (7.3%)	22 (15%)	34 (15%)
Real D^0 background (D^0 asymmetry)	0.07 (0.1%)	0.16 (0.1%)	0.36 (0.2%)	1.05 (0.5%)
CP violation in $B_s^0 \to D^{*0}\overline{K}^{*0}$	2.46 (1.9%)	5.03 (1.9%)	0.75 (0.5%)	0.45 (0.2%)
$B^+ \to \overline{D}^0\pi^+\pi^+\pi^-$ contribution	1.22 (0.9%)	0.73 (0.3%)	0.97 (0.6%)	2.24 (1.0%)
$\Lambda_b^0 \to D^0 p\pi^-$ contribution	0.16 (0.1%)	0.28 (0.1%)	0.66 (0.4%)	1.77 (0.8%)
K^{*0} coherence factor (κ)	3.87 (3.0%)	2.66 (1.0%)	2.07 (1.4%)	0.96 (0.4%)
Efficiency on the Dalitz plane				
Efficiency variation	3.16 (2.4%)	5.4 (2.1%)	0.68 (0.5%)	0.40 (0.2%)
Efficiency with BDTB	0.24 (0.2%)	0.39 (0.1%)	0.06 (0.04%)	0.04 (0.02%)
HLT efficiency	3.62 (2.8%)	6.62 (2.5%)	0.88 (0.6%)	0.39 (0.2%)
BDT efficiency (Data/MC agreement)	0.68 (0.5%)	2.00 (0.8%)	0.29 (0.2%)	0.09 (0.04%)
Generator cuts efficiency	3.68 (2.8%)	5.82 (2.2%)	0.62 (0.4%)	0.50 (0.2%)
TOS/NotTOS proportion	1.91 (1.5%)	3.81 (1.5%)	0.59 (0.4%)	0.13 (0.1%)
Migration in the Dalitz plot	4.35 (3.3%)	4.00 (1.5%)	2.90 (1.9%)	3.05 (1.3%)
Fit bias	1. (0.8%)	8. (3.1%)	34. (23%)	38. (17%)
Total experimental	87 (67%)	60 (23%)	43 (29%)	70 (31%)
Total model related	8 (6%)	10 (4%)	7 (5%)	5 (2%)

5.9 Interpretation on γ

This section develops the interpretation of the results on the cartesian parameters in terms of the polar coordinates r_{B^0}, δ_{B^0} and γ. First, the evaluation of the K^{*0} coherence factor is explained, as well as the compatibility check of this analysis with the ADS/GLW one already published by LHCb.

5.9.1 K^{*0} coherence factor and compatibility with the ADS/GLW r_{B^0} value

The $B^0 \to DK^{*0}$ decay has already been studied in LHCb with an ADS/GLW analysis [59]. From the measured observables it is deduced that $r_{B^0} = 0.240^{+0.055}_{-0.048}$, in a $K\pi$ mass region of $\pm 50\,\text{MeV}$ around the K^{*0} mass and for an absolute value of the cosine of the K^{*0} helicity angle larger than 0.4 (corresponding to the variable `Kst_BKstarK_DecayAngle`, and noted $\cos\theta^*$ in the following). To improve the measurement of γ, the result of the ADS/GLW analysis and the present GGSZ analysis can be combined. Indeed, in addition to γ, the two analyses share the same nuisance parameters r_{B^0} and δ_{B^0}. However, as can be seen in its definition in Eq. (2.29), r_{B^0} depends on the K^{*0} region considered. That is why the same mass window of $\pm 50\,\text{MeV}$ and $\cos\theta^*$ cut are used in both analyses. But the choice of adding $\cos\theta^*$ in the BDT selection, instead of using a single rectangular cut at 0.4 in absolute value, might induce some difference between the r_{B^0} values measured by the ADS/GLW analysis and the GGSZ analysis. In general, any discrepancy in the selection efficiency across the B^0 Dalitz plane between the two analyses could make a difference on the measured r_{B^0}. If the efficiency ε, determined in Sec. 5.4, is taken into account Eq. (2.29) and (2.30) are transformed into:

$$r_{B^0}^2 \equiv \frac{\int_{\phi_{K^{*0}}} A_u^2(p)\varepsilon(p)\,\mathrm{d}p}{\int_{\phi_{K^{*0}}} A_c^2(p)\varepsilon(p)\,\mathrm{d}p}, \tag{5.97}$$

$$\kappa e^{i\delta_{B^0}} \equiv \frac{\int_{\phi_{K^{*0}}} A_c(p)A_u(p)e^{i[\delta_u(p)-\delta_c(p)]}\varepsilon(p)\,\mathrm{d}p}{\sqrt{\int_{\phi_{K^{*0}}} A_c^2(p)\varepsilon(p)\,\mathrm{d}p \int_{\phi_{K^{*0}}} A_u^2(p)\varepsilon(p)\,\mathrm{d}p}}. \tag{5.98}$$

As seen in Sec. 5.4.5, the efficiency variation across phase space is very similar in the ADS/GLW and the GGSZ analyses. Hence the two analyses are expected to measure the same r_{B^0} value. To check this, the method used to determine κ in the ADS/GLW analysis is carried out to determine:

- the κ coherence factor of the GGSZ analysis,
- the eventual correction factor to translate the ${r_{B^0}}^{ADS}$ value to the ${r_{B^0}}^{GGSZ}$ value.

Model of the $B^0 \to DK\pi$ decay

A realistic model is used for the $B^0 \to DK\pi$ decay. The $A_c(p)$ and $A_u(p)$ amplitudes are described by an isobar model (a sum of Breit-Wigner functions, BW, and a constant term representing the non-resonant contribution):

$$A(p) = A_{NR} + \sum_r a_r e^{i\phi_r} BW(p, M_r, \Gamma_r, J_r), \tag{5.99}$$

where a_r (ϕ_r) are the relative amplitudes (phases) of each resonances. The resonances considered are the following:

- $B^0 \to D^0 K^*(892)^0$ and $B^0 \to \overline{D}^0 K^*(892)^0$,

Table 5.31 – Parameters of the resonances used in the $B^0 \to DK\pi$ decay model.

Resonance	Mass (MeV) M	Width (MeV) Γ	Spin J
$K^*(892)^0$	895.81 ± 0.19	47.4 ± 0.6	1
$K^*(1410)^0$	1414 ± 15	232 ± 21	1
$K_0^*(1430)^0$	1425 ± 50	270 ± 80	0
$K_2^*(1430)^0$	1432.4 ± 1.3	109 ± 5	2
$K^*(1680)^0$	1717 ± 27	322 ± 110	1
$D_0^*(2400)^-$	2403 ± 38	283 ± 42	0
$D_2^*(2460)^-$	2462.6 ± 0.6	37 ± 6	2
$D_{s2}(2573)^+$	2571.9 ± 0.8	17 ± 4	2

- $B^0 \to D^0 K^*(1410)^0$ and $B^0 \to \overline{D}^0 K^*(1410)^0$,
- $B^0 \to D^0 K_0^*(1430)^0$ and $B^0 \to \overline{D}^0 K_0^*(1430)^0$,
- $B^0 \to D^0 K_2^*(1430)^0$ and $B^0 \to \overline{D}^0 K_2^*(1430)^0$,
- $B^0 \to D^0 K^*(1680)^0$ and $B^0 \to \overline{D}^0 K^*(1680)^0$,
- $B^0 \to D_0^*(2400)^- K^+$,
- $B^0 \to D_2^*(2460)^- K^+$,
- $B^0 \to D_{s2}(2573)^+ \pi^-$,
- Non resonant $B^0 \to D^0 K^+ \pi^-$ and $B^0 \to \overline{D}^0 K^+ \pi^-$.

The contribution from $B^0 \to D^*(2010)^- K^+$ is not included since it is a narrow resonance. All the resonance parameters are listed in Table 5.31.

The relative amplitudes between the resonances are deduced from the known branching ratio or their upper limit. The following values are used:

- $\mathscr{B}(B^0 \to \overline{D}^0 K^*(892)^0) \times \mathscr{B}(K^*(892)^0 \to K^+\pi^-) = (2.8 \pm 0.4) \times 10^{-5}$,
- $\mathscr{B}(B^0 \to D_2^*(2460)^- K^+) \times \mathscr{B}(D_2^*(2460)^- \to \overline{D}^0 \pi^-) = (1.8 \pm 0.5) \times 10^{-5}$,
- $\mathscr{B}(B^0 \to \overline{D}^0 K^+ \pi^-) < 3.7 \times 10^{-5}$ for the non resonant contribution,
- $\mathscr{B}(B^0 \to D^0 K^+ \pi^-) < 19 \times 10^{-6}$ [161] for the non resonant contribution,

To estimate the $B^0 \to D_0^*(2400)^- K^+$ branching fraction, the ratio

$$\frac{\mathscr{B}(B^0 \to D_0^*(2400)^- \pi^+) \times \mathscr{B}(D_0^*(2400)^- \to D^0 \pi^+)}{\mathscr{B}(B^0 \to D_2^*(2460)^- \pi^+) \times \mathscr{B}(D_2^*(2460)^- \to D^0 \pi^+)} = 0.28 \pm 0.14 \tag{5.100}$$

is applied to $\mathscr{B}(B^0 \to D_2^*(2460)^- K^+) \times \mathscr{B}(D_2^*(2460)^- \to \overline{D}^0 \pi^-)$. The K^* modes are assumed to have the same branching fraction as the $B^0 \to \overline{D}^0 K^*(892)^0$ transition, with the branching fractions to the $K\pi$ final state:

- $\mathscr{B}(K^*(1410)^0 \to K^+\pi^-) = 4.4\%$,
- $\mathscr{B}(K_0^*(1430)^0 \to K^+\pi^-) = 62\%$,
- $\mathscr{B}(K_2^*(1430)^0 \to K^+\pi^-) = 33.3\%$,
- $\mathscr{B}(K^*(1680)^0 \to K^+\pi^-) = 25.8\%$,

The relative uncertainties on these branching fractions are assumed to be of 30%. For the $B^0 \to D_{s2}(2573)^+\pi^-$ decay, the upper limit $\mathscr{B}(B^0 \to D_s^+\pi^-) < 2.26 \times 10^{-5}$ is used.

To take into account the uncertainty on the branching ratios a simulation is performed, generating the resonance fraction flat within the interval limits, when only a limit is known, or with a Gaussian when uncertainties are known. The relative phases between the resonances are generated flat between 0 and 2π. The amplitude of the $K^*(892)^0$ resonance is fixed to 1 for the favoured mode, as a reference. The suppressed amplitudes (a_{ub}) are mainly deduced from the favoured (a_{cb}), assuming a r_{B^0} value of 0.3. In summary:

- $|a_{cb}^{K^*(892)^0}|^2 = 1$
- $|a_{cb}^{K^*(1410)^0}|^2 \in [0.066 \times 0.7; 0.066 \times 1.3]$
- $|a_{cb}^{K_0^*(1430)^0}|^2 \in [0.92 \times 0.7; 0.92 \times 1.3]$
- $|a_{cb}^{K_2^*(1430)^0}|^2 \in [0.5 \times 0.7; 0.5 \times 1.3]$
- $|a_{cb}^{K_0^*(1680)^0}|^2 \in [0.38 \times 0.7; 0.38 \times 1.3]$
- $|a_{cb}^{D_0^*(2400)^-}|^2 = 0.18 \pm 0.12$
- $|a_{cb}^{D_2^*(2460)^-}|^2 = 0.64 \pm 0.21$
- $|a_{cb}^{NR}|^2 \in [0; 1.3]$
- $a_{ub}^{K^*(892)^0} = r_{B^0} a_{cb}^{K^*(892)^0}$
- $a_{ub}^{K^*(1410)^0} = r_{B^0} a_{cb}^{K^*(1410)^0}$
- $a_{ub}^{K_0^*(1430)^0} = r_{B^0} a_{cb}^{K_0^*(1430)^0}$
- $a_{ub}^{K_2^*(1430)^0} = r_{B^0} a_{cb}^{K_2^*(1430)^0}$
- $a_{ub}^{K_0^*(1680)^0} = r_{B^0} a_{cb}^{K_0^*(1680)^0}$
- $|a_{ub}^{D_{s2}(2460)^-}|^2 \in [0; 0.77]$
- $|a_{ub}^{NR}|^2 \in [0; 0.68]$

An example of a Dalitz plot obtained with this model is illustrated on Fig. 5.93. The projections on the squared invariant masses $m^2(D\pi)$ and $m^2(K\pi)$ are also drawn. The dashed lines represent the $m(K\pi)$ and $\cos\theta^*$ cuts, applied both in GGSZ and ADS/GLW analyses. On the $m^2(D\pi)$ projection, the lines correspond to a $\cos\theta^*$ cut at the value $\mathrm{m(K\pi) = m_{K^*(892)^0}}$.

Determination of κ and r_{B^0}

Using the present model, the integrals figuring in the equations (5.97) and (5.98) can be computed. Since the efficiency profile is known (see Sec. 5.4), the GGSZ κ coherence factor can be estimated. Furthermore, the ${r_{B^0}}^{ADS}$ value obtained with the ADS/GLW efficiency profile can be compared to the GGSZ one. A significant discrepancy is not expected, since the efficiency profile of the ADS/GLW and the GGSZ analyses are similar in the $|\cos\theta^*| > 0.4$ region (see Fig. 5.38).

Two thousand Dalitz plots are generated according to the $B^0 \to DK\pi$ toy model. The r_{B^0}, κ, and the fraction of non-$K^*(892)^0$ resonance contributions are computed using a MC integration (with 50000 points). The results obtained for the ADS/GLW and GGSZ efficiencies are illustrated in Fig. 5.94. The computed r_{B^0} values are equal to $r_{B^0} = 0.30 \pm 0.02$ for the two analyses (the

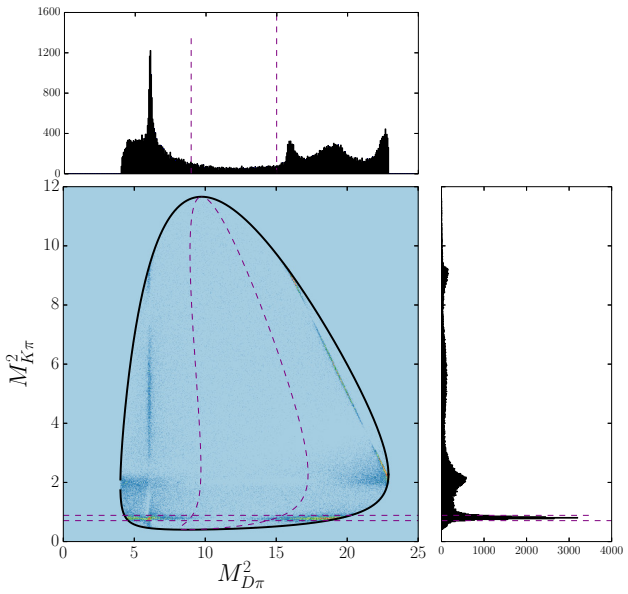

Figure 5.93 – Dalitz plot generated with the realistic model of $B^0 \to DK\pi$ decay. The dashed lines represent the $m(K\pi)$ and $\cos\theta^*$ cuts, applied both in GGSZ and ADS/GLW analyses. On the $m^2(D\pi)$ projection, the lines correspond to a $\cos\theta^*$ cut at the value $\mathrm{m(K}\pi) = \mathrm{m_{K^*(892)^0}}$

uncertainty arises from the fluctuation due to the model uncertainty). Therefore the r_{B^0} value is the same in the ADS/GLW and GGSZ analyses. The coherence factor is also identical and is

$$\kappa = 0.93 \pm 0.04. \tag{5.101}$$

As an illustration, the same parameters are computed taking into account the whole Dalitz plane (*i.e.* without a K^{*0} mass cut), with a flat efficiency. In this case the coherence factor severely decreases to a value of $\kappa = 0.29 \pm 0.14$ (see Fig. 5.95).

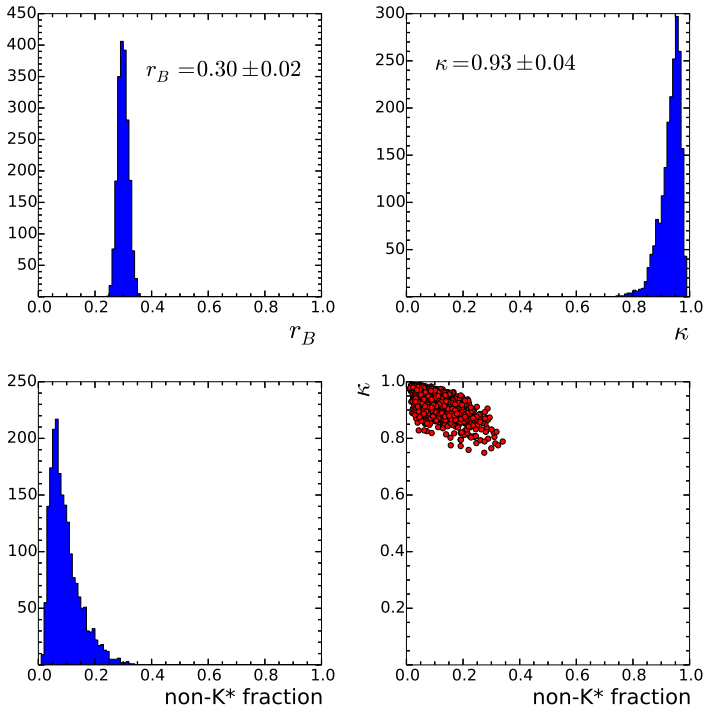

(a)

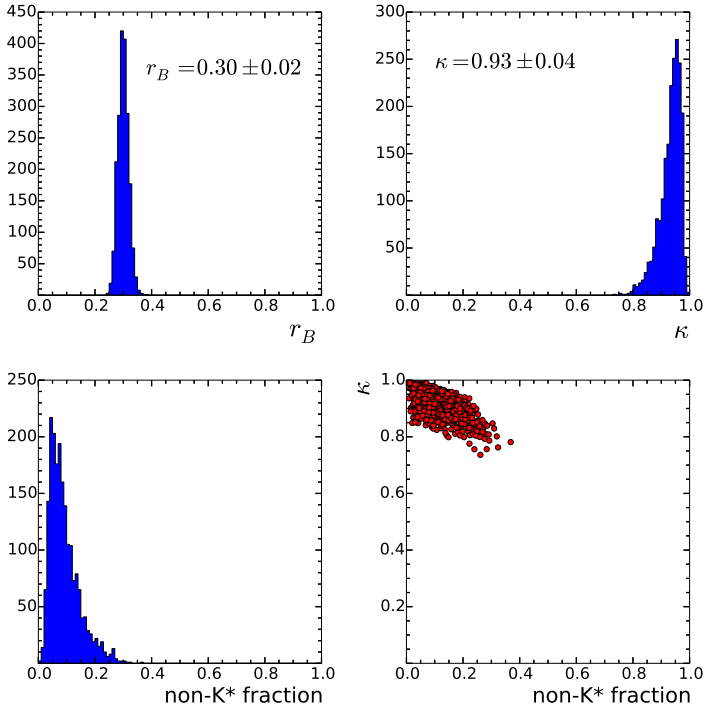

(b)

Figure 5.94 – r_{B^0}, κ and non $K^*(892)^0$ fraction computed with the $B^0 \to DK\pi$ model described in the text, for the ADS/GLW (a) and GGSZ (b) efficiency.

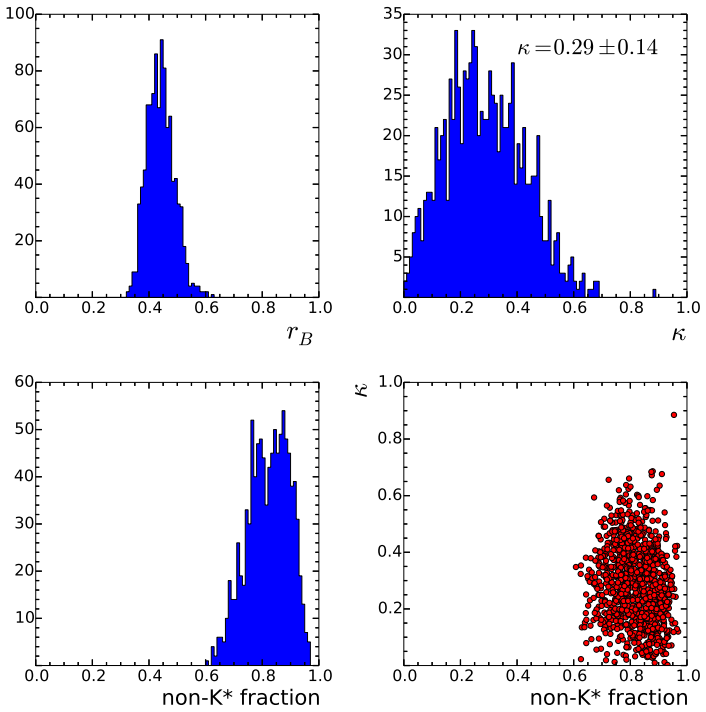

Figure 5.95 – r_{B^0}, κ and non $K^*(892)^0$ fraction computed with the $B^0 \to DK\pi$ model described in the text, with a flat efficiency and taking into account the whole Dalitz plane (no K^{*0} mass cut).

5.9.2 From the cartesian parameters to r_{B^0}, δ_{B^0} and γ

The final result on the cartesian parameters is

$$\begin{aligned} x_- &= -0.09^{+0.13}_{-0.13} \pm 0.09 \pm 0.01, \\ x_+ &= -0.10^{+0.27}_{-0.26} \pm 0.06 \pm 0.01, \\ y_- &= 0.23^{+0.15}_{-0.16} \pm 0.04 \pm 0.01, \\ y_+ &= -0.74^{+0.23}_{-0.26} \pm 0.07 \pm 0.01. \end{aligned} \tag{5.102}$$

The first uncertainty is statistical, the second is the experimental systematic and the third is the systematic due to the Dalitz model. To check that this evaluation does not suffer from multiple local minima, which could make the minimisation result inaccurate, a scan of the likelihood is done separately on the (x_-, y_-) and (x_+, y_+) spaces. Indeed, the "plus" and "minus" parameters are uncorrelated, they can be treated separately. The result of this scan is illustrated on Fig. 5.96. It shows the $\Delta\chi^2$ defined as the difference between the negative log-likelihood (defined in Eq. (5.51)) at the scan point and at the best fit values, as a function of the scan points. No secondary minimum is observed, therefore the minimisation is reliable. It can be noticed a small structure on the (x_+, y_+) scan around $(-0.1, 0.5)$, which could be at the origin of the few satellites observed in the residuals of the toys shown in Sec. 5.7.6.

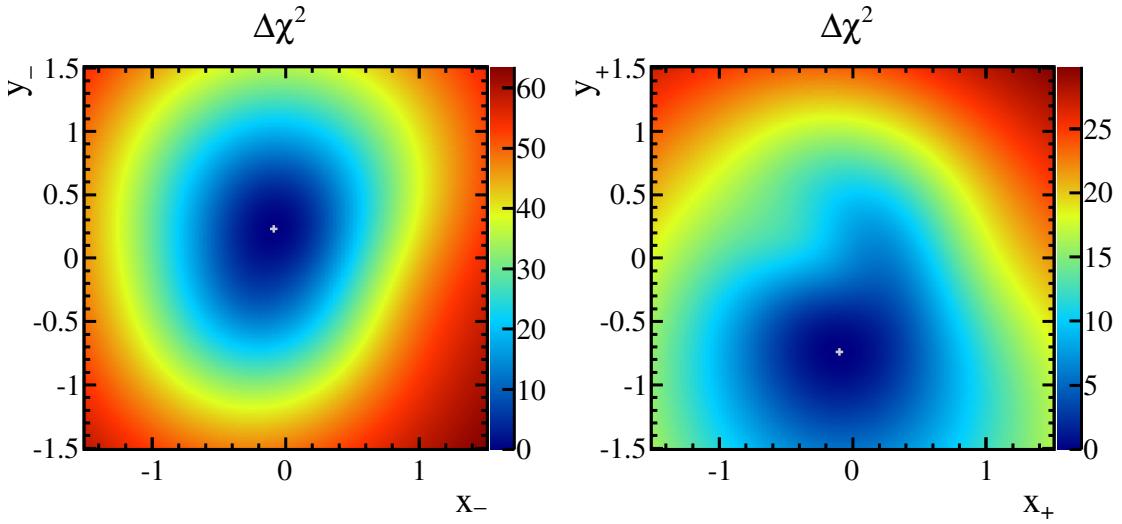

Figure 5.96 – Scan of likelihood of the Dalitz fit in the (x_-, y_-) (left) and (x_+, y_+) (right) planes. The best fit values are represented by the crosses (corresponding to $\Delta\chi^2 = 0$).

To interpret the result on $(x_\pm, y_\pm)$ in terms of the polar coordinates r_{B^0}, δ_{B^0} and γ, the relations

$$\begin{aligned} x_\pm &= r_{B^0} \cos(\delta_{B^0} \pm \gamma), \\ y_\pm &= r_{B^0} \sin(\delta_{B^0} \pm \gamma), \end{aligned} \tag{5.103}$$

must be inverted. This is done thanks to the `GammaCombo` package, developed for the LHCb γ combination [10, 87]. A global likelihood function is built from the probability density function of the cartesian observables

$$\mathscr{L}(x_-, x_+, y_-, y_+ | r_{B^0}, \delta_{B^0}, \gamma), \tag{5.104}$$

which gives the probability of observing a set of $(x_\pm, y_\pm)$ values given the true value $(r_{B^0}, \delta_{B^0}, \gamma)$. This likelihood provides an evaluation of the central values for $(r_{B^0}, \delta_{B^0}, \gamma)$, as well as the uncertainty on this evaluation by determining the confidence intervals. The central values are obtained by maximising the likelihood for the observed value $\vec{z}_{\rm obs} = (x_-, x_+, y_-, y_+)_{\rm obs}$. This implies a scan in the parameter space $(r_{B^0}, \delta_{B^0}, \gamma)$ to retain the values which maximise the function $\mathscr{L}(\vec{z}_{\rm obs}|r_{B^0}, \delta_{B^0}, \gamma)$. The confidence intervals are obtained either from a simple profile likelihood method or with a pseudo-experiment based method, described in the following sections.

The likelihood is taken to be a multivariate Gaussian of the form

$$\mathscr{L}(\vec{z}_{\rm obs}|r_{B^0}, \delta_{B^0}, \gamma) = \frac{1}{2\pi\sqrt{\det V}} \exp\left(-\frac{1}{2}(\vec{z}_{\rm obs} - \vec{z}_{\rm th})^T V^{-1} (\vec{z}_{\rm obs} - \vec{z}_{\rm th})\right), \tag{5.105}$$

where $\vec{z}_{\rm obs}$ is the vector of observed values and $\vec{z}_{\rm th} = (x_-, x_+, y_-, y_+)_{\rm th}$ is the vector of the theory parameters depending on the $(r_{B^0}, \delta_{B^0}, \gamma)$ values with the truth relations (5.103). V is the covariance matrix of the cartesian parameters.

Profile likelihood method

The profile likelihood method, also called "PROB" method, is based on the χ^2-function defined as

$$\chi^2(r_{B^0}, \delta_{B^0}, \gamma) = -2\ln \mathscr{L}(\vec{z}_{\rm obs}|r_{B^0}, \delta_{B^0}, \gamma). \tag{5.106}$$

The $(r_{B^0}, \delta_{B^0}, \gamma)$ central values correspond to the minimum $\chi^2_{\rm min}$. It is possible to have different values of $(r_{B^0}, \delta_{B^0}, \gamma)$ which give $\chi^2_{\rm min}$ (multiple solutions are found). A scan is performed in the $\vec{\alpha} \equiv (r_{B^0}, \delta_{B^0}, \gamma)$ space, and in each particular point $\vec{\alpha}'$, the χ^2 is minimised to get the value $\chi^2_{\rm min}(\vec{\alpha}')$. This value is compared to the best fit value $\chi^2_{\rm min}$ with the difference

$$\Delta\chi^2 = \chi^2_{\rm min}(\vec{\alpha}') - \chi^2_{\rm min}. \tag{5.107}$$

By definition, this $\Delta\chi^2$ is positive. With a Gaussian likelihood, the p value defined as $p \equiv 1 - CL$ is given by the probability that $\Delta\chi^2$ is exceeded according to a χ^2-distribution [20]. The confidence intervals are made by finding the points in the scan which intersect the levels $CL = 68\%$ or $CL = 95\%$. The PROB method is known to have a tendency to "undercover". This means that the intervals made with this method contain the true value in a lesser number of times than the claimed 68% or 95% frequency. The "PLUGIN" method, described in the next section, shows better coverage performance.

Pseudo-experiment based method

Instead of assuming that the $\Delta\chi^2$ test follows a χ^2-distribution, its distribution can be simulated using pseudo-experiments. The approach described here, called the "PLUGIN" method [162], is based on the Feldman and Cousins method [163] and introduces the concept of nuisance parameters. With the PLUGIN method, the nuisance parameters are always kept at there best fit values observed in the data.

The corresponding algorithm is [87, 162]:

1. $\Delta\chi^2 = \chi^2_{\rm min}(\vec{\alpha}') - \chi^2_{\rm min}$ is calculated as in the profile-likelihood method,
2. a pseudo result is generated leading to $\vec{z}_{\rm toy}$, by using the likelihood in Eq. (5.104) with the parameters fixed to $\vec{\alpha}'$,

3. the new $\Delta\chi^{2\,\prime}$ is computed by replacing $\vec{z}_{\text{obs}}$ with $\vec{z}_{\text{toy}}$,

4. finally the confidence level is calculated from the fraction of pseudo-experiment results which perform worse than the measured data:

$$1 - CL = N(\Delta\chi^2 < \Delta\chi^{2\,\prime})/N_{toy} \tag{5.108}$$

Results

The result of the pseudo-experiment method are illustrated on the 1− CL curves of Fig 5.97, 5.98a and 5.98b for γ, r_{B^0} and δ_{B^0} respectively. The two-dimensional contours in the (γ, r_{B^0}) and (γ, δ_{B^0}) are illustrated in Fig 5.99 and 5.100, respectively. Fig 5.97, shows that the profile-likelihood method slightly undercovers compared to the pseudo-experiment method. Therefore the confidence intervals retained are those made with the latter technique. In the 1− CL curve of δ_{B^0} (Fig. 5.98b), the 180° ambiguity is clearly seen. Only the solution corresponding to $\gamma \in [0, 180]^\circ$ is quoted in the following.

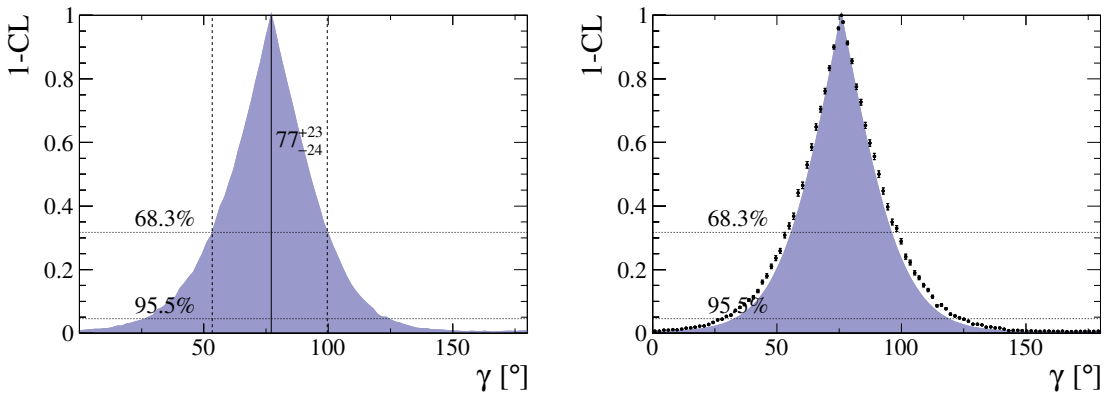

Figure 5.97 – 1-CL curves for the γ angle with the pseudo-experiment based method (a) and with the profile-likelihood (shaded region) and pseudo-experiment (points) superimposed (b). The profile-likelihood curve undercovers slightly.

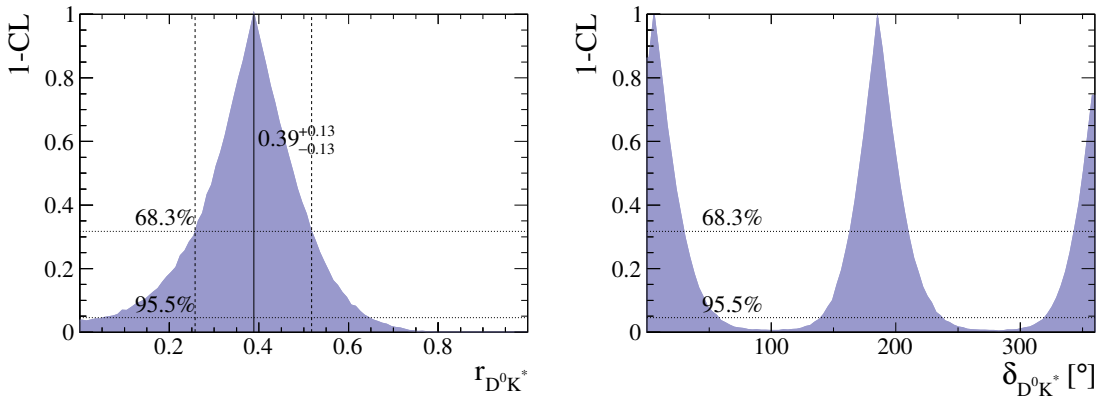

Figure 5.98 – 1-CL curves for r_{B^0} (a) and δ_{B^0} (b) with the pseudo-experiment method.

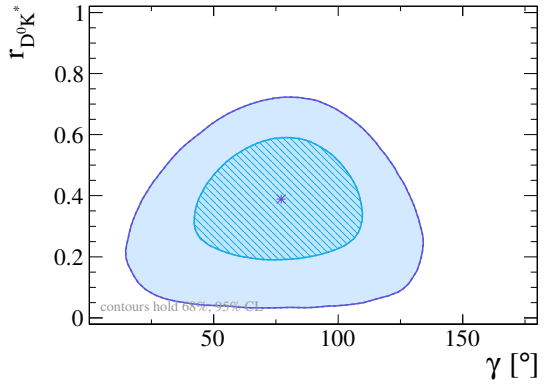

Figure 5.99 – Confidence level contour for r_{B^0} *vs.* γ, with the pseudo-experiments method. The contour corresponds to the two-dimensional 1σ and 2σ level, and the best fit value is represented by the star.

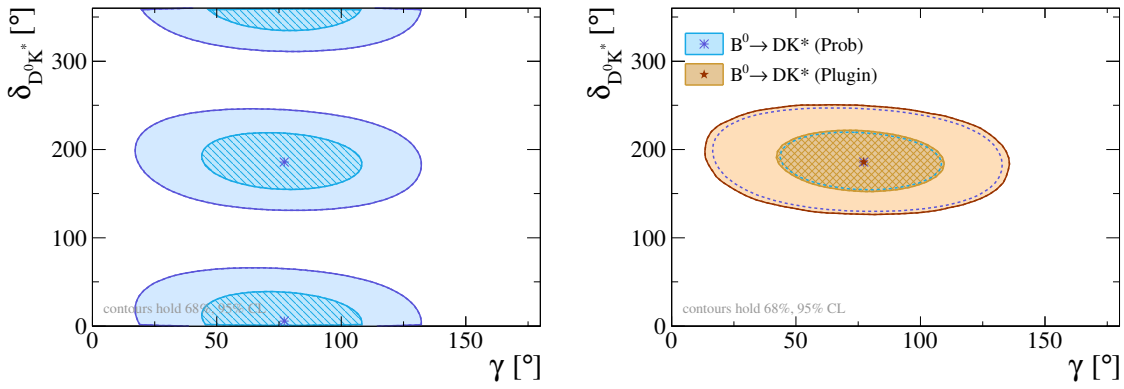

(a) (b)

Figure 5.100 – Profile likelihood contour of δ_{B^0} *vs.* γ (a) and comparison with the pseudo-experiment method (brown area), focusing only on the local minimum at $\delta_{B^0} = 186°$ (b). The contour corresponds to the two-dimensional 1σ and 2σ levels, and the best fit value is represented by the stars.

The interpretation of these curves gives at a confidence level of 68%:

$$\begin{aligned} r_{B^0} &= 0.39 \pm 0.13\,, \\ \delta_{B^0} &= \left(186^{+24}_{-23}\right)^\circ\,, \\ \gamma &= \left(77^{+23}_{-24}\right)^\circ\,. \end{aligned} \tag{5.109}$$

The central values, the 68% and 95% confidence intervals are summarised in Table 5.32. These results are in good agreement with the $B^0 \to DK^{*0}$ ADS/GLW analysis, which measured a value of $r_{B^0} = 0.240^{+0.055}_{-0.048}$ [59], as illustrated in Figure 5.101. Moreover, the measured γ value is also in good agreement with the current world averages [11, 12]. Fig. 5.102 shows the comparison of the result on γ reported in this thesis with the direct measurements of B-factories and LHCb, and with the world averages performed by the CKMfitter and UTFit collaborations.

Table 5.32 – Confidence intervals and central values obtained on the polar coordinates.

γ (°)	77
68% CL (°)	[53,100]
95% CL (°)	[27,124]
r_{B^0}	0.39
68% CL	[0.26,0.52]
95% CL	[0.06,0.64]
δ_{B^0} (°)	186
68% CL (°)	[163,210]
95% CL (°)	[140,236]

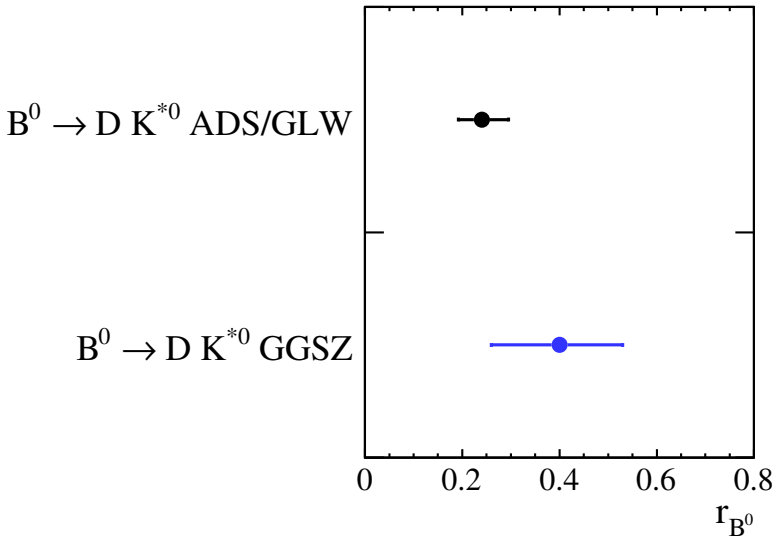

Figure 5.101 – Comparison of the reported result on r_{B^0} (in blue) with the $B^0 \to DK^{*0}$ ADS/GLW measurement performed by LHCb [59].

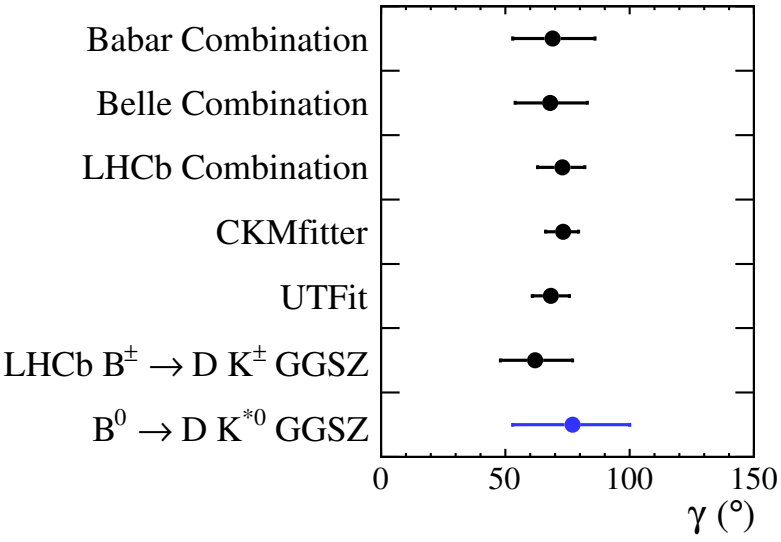

Figure 5.102 – Comparison of the reported result on γ (in blue) with the BaBar [8], Belle [9], LHCb [10] combinations of direct measurements, the averages performed by the CKMfitter [11] and UTFit [12] collaborations, and the present single most precise measurement obtained with $B^\pm \to DK^\pm$ decays [13].

Conclusion

The CKM angle γ is one of the standard model parameters still determined with a large uncertainty. Precise measurement of this quantity is needed to further constrain the Unitarity Triangle of the CKM matrix, and check the consistency of the theory. The measurement of this angle involves B meson decays to open charm final states, which are detected with good efficiency in the LHCb experiment. Thus, a precise measurement of γ is one of the main purposes of LHCb.

This thesis reports a measurement of γ with a Dalitz analysis of the $B^0 \to DK^{*0}$ channel where the D meson decays into $K^0_S\pi^+\pi^-$, based on the $3\,\text{fb}^{-1}$ of proton-proton collision data collected by LHCb during the LHC Run I, at the centre-of-mass energy of 7 and 8 TeV. The *CP* violation observables are measured to be

$$\begin{aligned} x_- &= -0.09^{+0.13}_{-0.13} \pm 0.09 \pm 0.01\,, \\ x_+ &= -0.10^{+0.27}_{-0.26} \pm 0.06 \pm 0.01\,, \\ y_- &= 0.23^{+0.15}_{-0.16} \pm 0.04 \pm 0.01\,, \\ y_+ &= -0.74^{+0.23}_{-0.26} \pm 0.07 \pm 0.01\,, \end{aligned}$$

where the first uncertainty is statistical, the second is the experimental systematic uncertainty and the third is the systematic uncertainty due to the Dalitz model. A frequentist interpretation of these observables leads to

$$r_{B^0} = \quad 0.39 \pm 0.13\,, \qquad \delta_{B^0} = \quad \left(186^{+24}_{-23}\right)^\circ\,, \qquad \gamma = \quad \left(77^{+23}_{-24}\right)^\circ\,.$$

This is the most precise measurement of γ with $B^0 \to DK^{*0}$ decays to date. This result will contribute to the next LHCb γ combination. Moreover, the perspectives for the γ measurement with the $B^0 \to DK^{*0}$ channel are promising. The present result is based on about one hundred signal events, and has a limited statistical accuracy. With the foreseen $8\,\text{fb}^{-1}$ of data collected at $\sqrt{s} = 13\,\text{TeV}$ during the Run II, the measurement will significantly improve. With the $50\,\text{fb}^{-1}$ of data expected after the LHCb experiment upgrade, the *CP* observables will be measured with a much reduced uncertainty, and lead to a precise direct measurement of γ.

The present thesis also reports on the optimisation of the photon reconstruction for the upgraded LHCb detector. After the LHCb upgrade, the instantaneous luminosity delivered by the LHC will be increased by one order of magnitude, above the LHCb design value. The occupancy of the detector will significantly grows reducing the performance of the photon measurement with the electromagnetic calorimeter. The study shows that reducing the cluster size used in the photon reconstruction limits the effect of the overlap between the showers, without inducing a significant energy leakage. With some dedicated corrections, the new cluster reconstruction improves the $B^0_s \to \phi\gamma$ mass resolution by 7 to 12%, depending on the calorimeter region. This new reconstruction will be tested with Run II data.

Appendix A

Generator level cuts

All the samples used in the analysis were simulated with loose generator level cuts in order to avoid generating too many events which would have been rejected at an early stage by the stripping selection. These cuts are listed in table A.1. Their possible bias over the Dalitz plane have been investigated with a specific sample without the cuts applied. Fig. A.1 shows the efficiency of these cuts along the three Dalitz coordinates on the truth matched signal after stripping. Since these distributions are flat, no bias is expected on the selection efficiency computation.

Table A.1 – Generator level cuts applied on the 2012 samples.

Particle	Variable	Cut value
K^{*0}	p	$> 12\,\text{GeV}$
	p_T	$> 800\,\text{MeV}$
	p of daughters	$> 2\,\text{GeV}$
	p_T of daughters	$> 98\,\text{MeV}$
D^0	p	$> 20\,\text{GeV}$
	p_T	$> 300\,\text{MeV}$
	p of $\pi^\pm$ direct daughters	$> 1\,\text{GeV}$
K^0_S	p	$> 6\,\text{GeV}$
	z position of the decay vertex	$< 2.4\,\text{m}$
	p of daughters	$> 2\,\text{GeV}$
B^0	p	$> 50\,\text{GeV}$
	p_T	$> 5\,\text{GeV}$
	τ_{B^0}	$> 0.35\,\text{ps}$

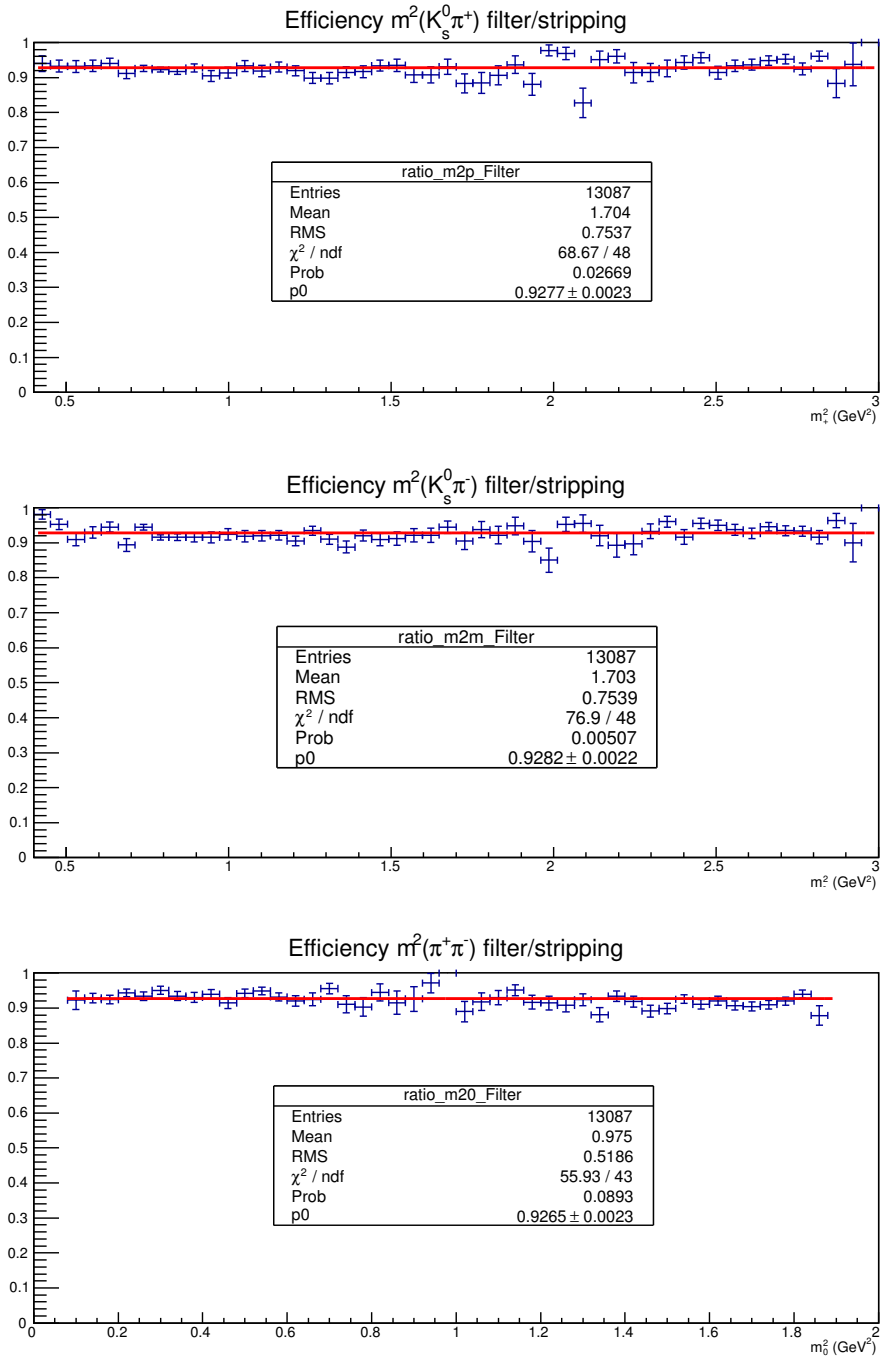

Figure A.1 – Efficiency distribution along the three Dalitz coordinates of the generator level cuts on the MC11a signal events after stripping.

Appendix B

Differences between 5.5 GeV and 5.8 GeV upper sidebands

Three regions of the data upper sideband, $m_{B^0} \in [5.5;5.6]$ GeV, $m_{B^0} \in [5.6;5.8]$ GeV and $m_{B^0} > 5.8$ GeV, were compared looking at the discriminating variables used in the BDT. In order to highlight any discrepancy, a high statistics is needed and therefore no preselection is applied. To check that the preselection applied before the training does not remove any difference, the distributions after PRESEL_BDT are also shown. The B^0 pointing angle, its impact parameter significance and its transverse momentum are the three variables with the most significant discrepancy between the [5.5;5.6] GeV range and the region above 5.8 GeV. Although the observed differences are limited, they are sizeable enough for a multivariate classifier to influence its selection performances.

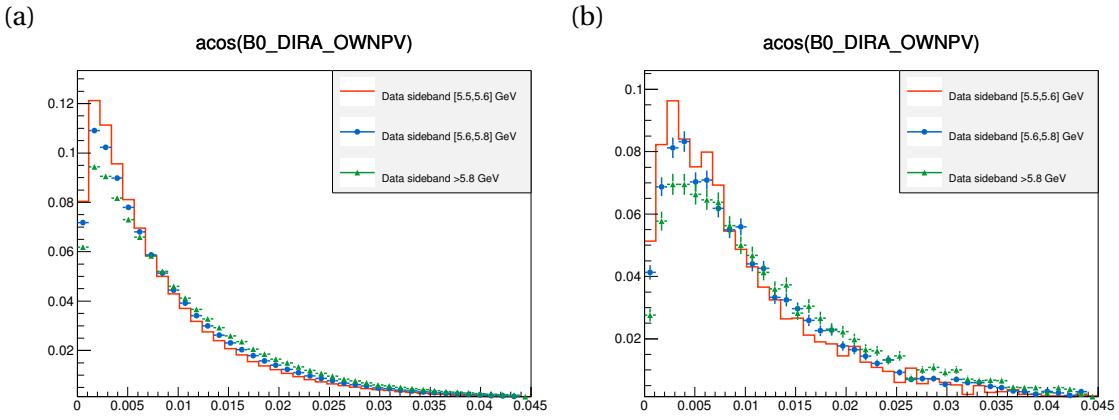

Figure B.1 – Distribution of the angle between the B^0 reconstructed momentum and the line made by the PV and the B^0 decay vertex (θ_{dira}). Three data upper sidebands are compared: $m_{B^0} \in [5.5;5.6]$ GeV (orange), $m_{B^0} \in [5.6;5.8]$ GeV (blue) and $m_{B^0} > 5.8$ GeV (green), without any preselection (a) and after PRESEL_BDT (b).

(a)

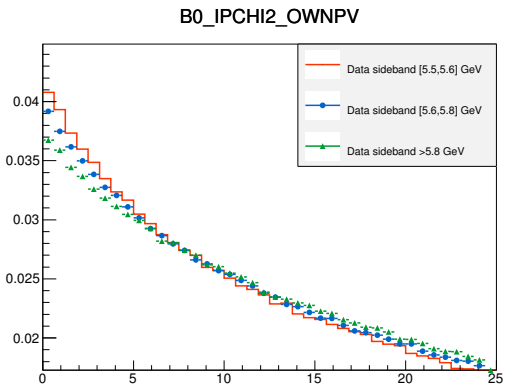

(b)

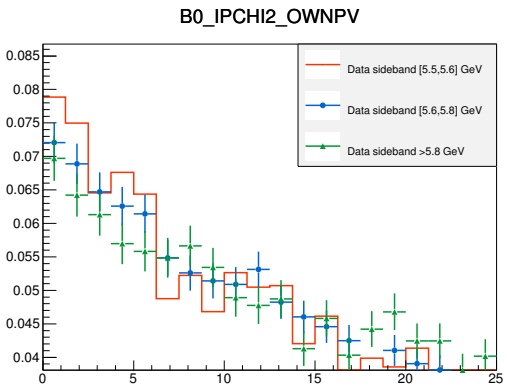

Figure B.2 – Distribution of the B^0 impact parameter significance with regards to the PV (χ^2_{IP}). Three data upper sidebands are compared: $m_{B^0} \in [5.5; 5.6]$ GeV (orange), $m_{B^0} \in [5.6; 5.8]$ GeV (blue) and $m_{B^0} > 5.8$ GeV (green), without any preselection (a) and after PRESEL_BDT (b).

(a)

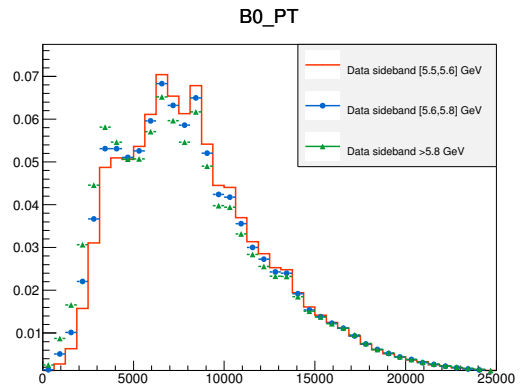

(b)

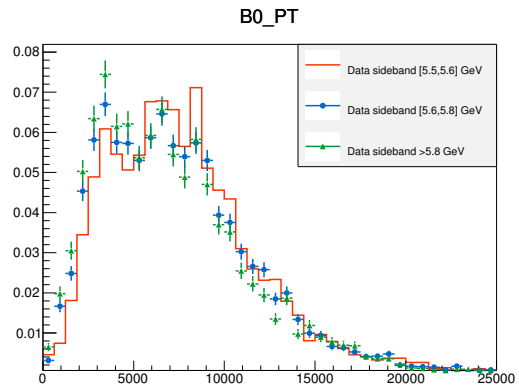

Figure B.3 – Distribution of the B^0 transverse momentum. Three data upper sidebands are compared: $m_{B^0} \in [5.5; 5.6]$ GeV (orange), $m_{B^0} \in [5.6; 5.8]$ GeV (blue) and $m_{B^0} > 5.8$ GeV (green), without any preselection (a) and after PRESEL_BDT (b).

Appendix C

Distributions of the variables used in the crossed BDT

The distributions of the sixteen discriminating variables used in the crossed BDT are shown. They are obtained from the signal and background samples used for the training (after PRESEL_BDT). LL and DD candidates are drawn apart, but the background distributions include both A and B data sidebands. It can be noticed that the signal and background distributions of the sum of the χ^2_{IP} with regards to the PV over the K^0_{S} daughters (`Sum2_IPS`), the K^0_{S} flight distance significance with regards to the PV (`Ks_FDCHI2_OWNPV`) and to the D^0 (`Ks_DKs_FDSig`) and the transverse momentum of the D^0 and the K^{*0} are different for LL and DD. Then the variable ranking given by TMVA is shown for the four classifiers BDTA_LL, BTDA_DD, BDTB_LL and BDTB_DD.

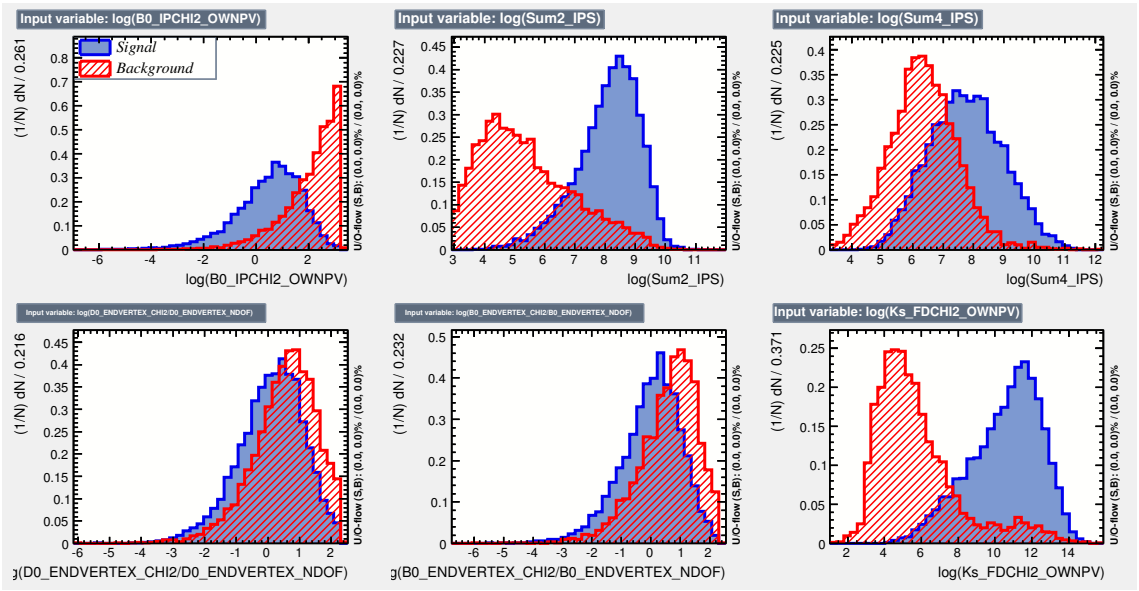

(a)

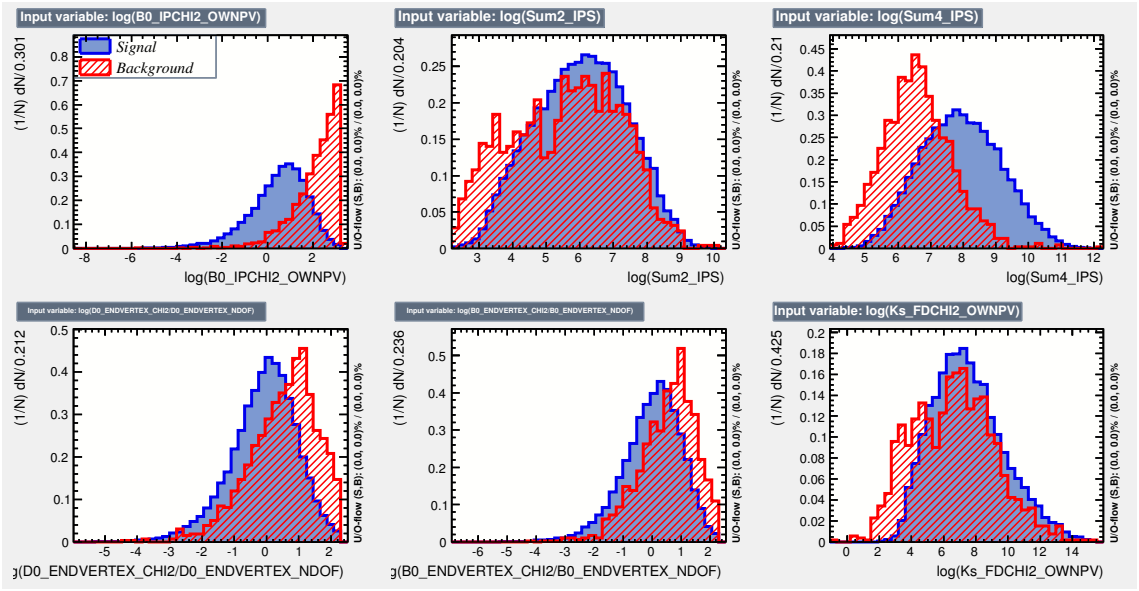

(b)

Figure C.1 – Distributions of the variables used by the BDT for LL (a) and DD (b) candidates, from the signal (blue) and background (red) training samples.

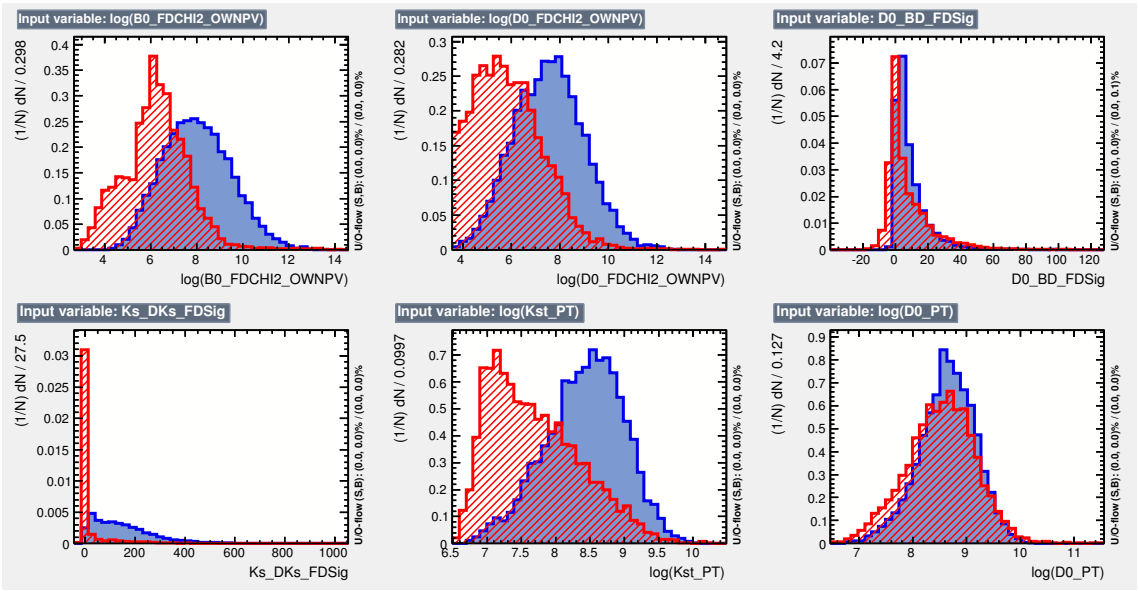

(a)

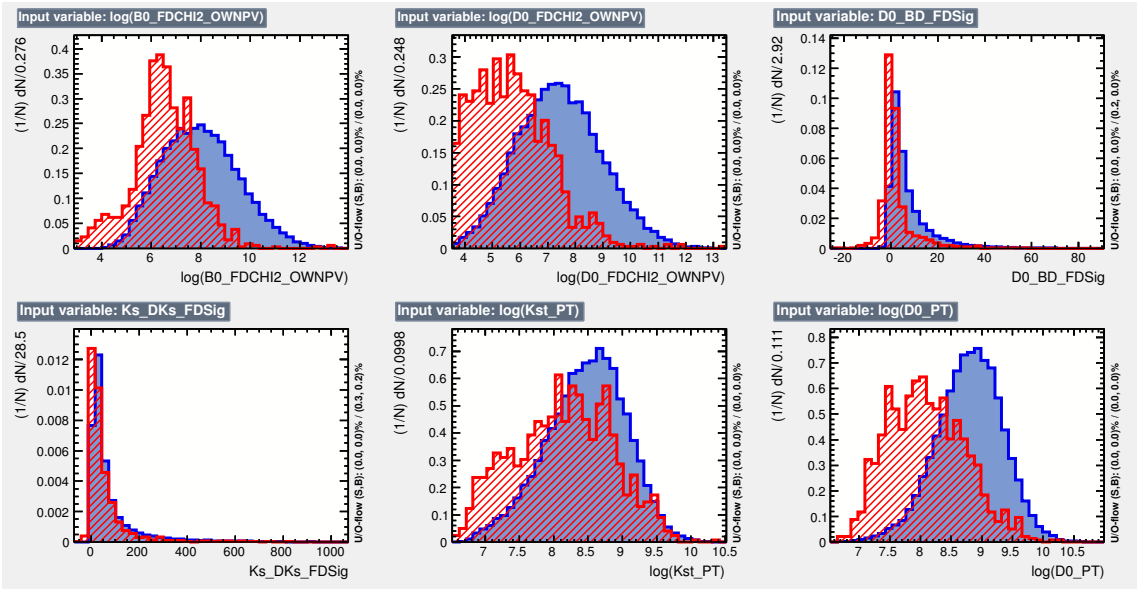

(b)

Figure C.2 – Distributions of the variables used by the BDT for LL (a) and DD (b) candidates, from the signal (blue) and background (red) training samples.

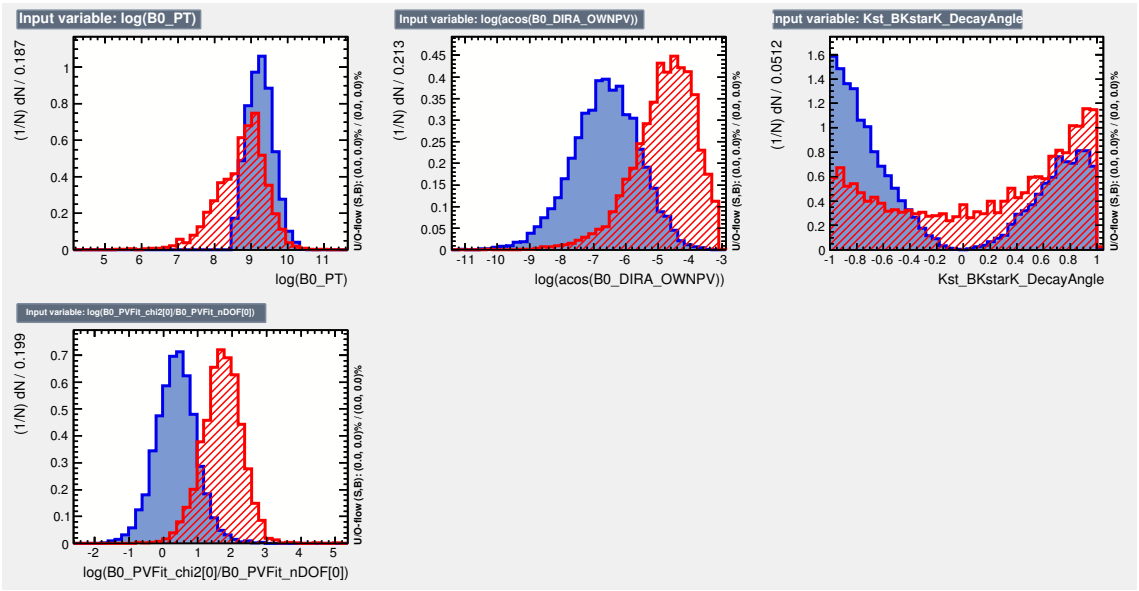

(a)

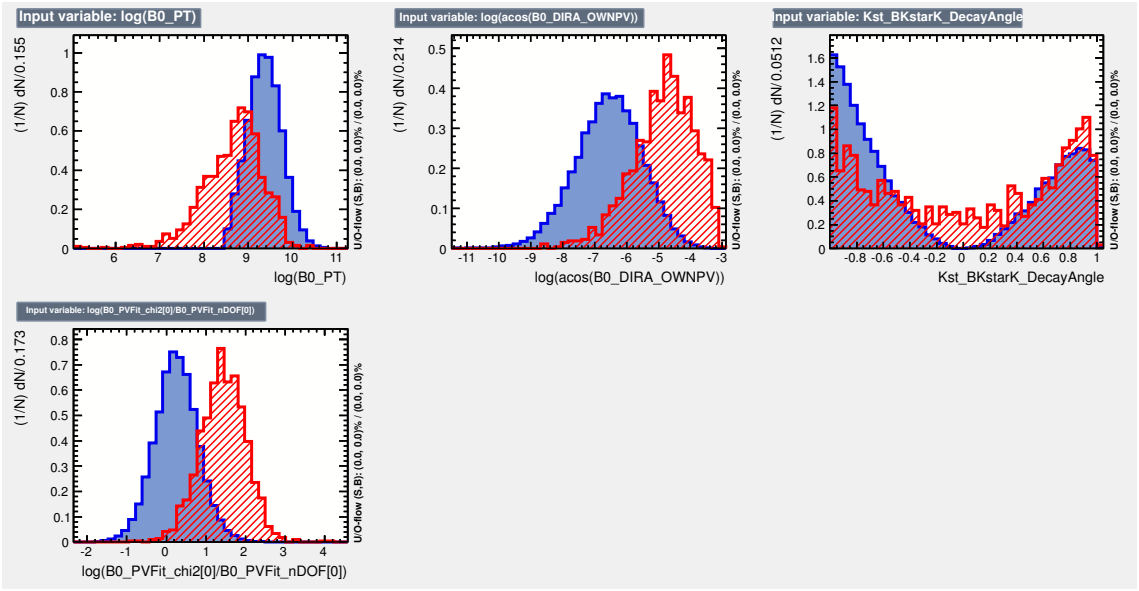

(b)

Figure C.3 – Distributions of the variables used by the BDT for LL (a) and DD (b) candidates, from the signal (blue) and background (red) training samples.

Variable ranking for BDTA_LL:

```
------------------------------------------------------------------------
Rank : Variable                                  : Variable Importance
------------------------------------------------------------------------
   1 : log(B0_PVFit_chi2[0]/B0_PVFit_nDOF[0])    : 1.243e-01
   2 : log(Ks_FDCHI2_OWNPV)                      : 1.005e-01
   3 : Ks_DKs_FDSig                              : 9.136e-02
   4 : log(B0_FDCHI2_OWNPV)                      : 8.221e-02
   5 : log(Kst_PT)                               : 7.515e-02
   6 : log(acos(B0_DIRA_OWNPV))                  : 6.895e-02
   7 : log(Sum2_IPS)                             : 6.842e-02
   8 : D0_BD_FDSig                               : 6.608e-02
   9 : log(D0_FDCHI2_OWNPV)                      : 6.354e-02
  10 : Kst_BKstarK_DecayAngle                    : 6.088e-02
  11 : log(D0_PT)                                : 5.445e-02
  12 : log(B0_PT)                                : 4.939e-02
  13 : log(B0_IPCHI2_OWNPV)                      : 3.787e-02
  14 : log(B0_ENDVERTEX_CHI2/B0_ENDVERTEX_NDOF)  : 3.348e-02
  15 : log(Sum4_IPS)                             : 1.657e-02
  16 : log(D0_ENDVERTEX_CHI2/D0_ENDVERTEX_NDOF)  : 6.791e-03
------------------------------------------------------------------------
```

Variable ranking for BDTA_DD:

```
------------------------------------------------------------------------
Rank : Variable                                  : Variable Importance
------------------------------------------------------------------------
   1 : log(B0_PVFit_chi2[0]/B0_PVFit_nDOF[0])    : 1.231e-01
   2 : log(Kst_PT)                               : 9.294e-02
   3 : log(B0_FDCHI2_OWNPV)                      : 9.118e-02
   4 : log(D0_PT)                                : 8.806e-02
   5 : D0_BD_FDSig                               : 8.224e-02
   6 : log(acos(B0_DIRA_OWNPV))                  : 7.653e-02
   7 : log(D0_FDCHI2_OWNPV)                      : 5.871e-02
   8 : log(Ks_FDCHI2_OWNPV)                      : 5.760e-02
   9 : log(B0_IPCHI2_OWNPV)                      : 5.627e-02
  10 : Kst_BKstarK_DecayAngle                    : 5.540e-02
  11 : Ks_DKs_FDSig                              : 5.355e-02
  12 : log(B0_PT)                                : 5.242e-02
  13 : log(Sum4_IPS)                             : 4.787e-02
  14 : log(B0_ENDVERTEX_CHI2/B0_ENDVERTEX_NDOF)  : 2.508e-02
  15 : log(D0_ENDVERTEX_CHI2/D0_ENDVERTEX_NDOF)  : 2.487e-02
  16 : log(Sum2_IPS)                             : 1.420e-02
------------------------------------------------------------------------
```

Variable ranking for BDTB_LL:

```
------------------------------------------------------------------------
Rank : Variable                                  : Variable Importance
------------------------------------------------------------------------
   1 : log(Ks_FDCHI2_OWNPV)                      : 9.670e-02
   2 : Ks_DKs_FDSig                              : 9.431e-02
   3 : log(B0_PVFit_chi2[0]/B0_PVFit_nDOF[0])    : 9.122e-02
   4 : log(B0_FDCHI2_OWNPV)                      : 7.431e-02
   5 : D0_BD_FDSig                               : 7.422e-02
   6 : log(Kst_PT)                               : 6.772e-02
   7 : log(acos(B0_DIRA_OWNPV))                  : 6.224e-02
   8 : log(D0_FDCHI2_OWNPV)                      : 6.207e-02
   9 : log(D0_PT)                                : 6.050e-02
  10 : Kst_BKstarK_DecayAngle                    : 5.948e-02
  11 : log(Sum2_IPS)                             : 5.525e-02
  12 : log(B0_PT)                                : 4.810e-02
  13 : log(B0_ENDVERTEX_CHI2/B0_ENDVERTEX_NDOF)  : 4.556e-02
  14 : log(B0_IPCHI2_OWNPV)                      : 4.217e-02
  15 : log(Sum4_IPS)                             : 3.538e-02
  16 : log(D0_ENDVERTEX_CHI2/D0_ENDVERTEX_NDOF)  : 3.076e-02
------------------------------------------------------------------------
```

Variable ranking for BDTB_DD:

```
------------------------------------------------------------------------
Rank : Variable                                  : Variable Importance
------------------------------------------------------------------------
   1 : log(B0_PVFit_chi2[0]/B0_PVFit_nDOF[0])    : 1.316e-01
   2 : log(Kst_PT)                               : 9.651e-02
   3 : log(D0_PT)                                : 8.948e-02
   4 : log(B0_FDCHI2_OWNPV)                      : 8.628e-02
   5 : D0_BD_FDSig                               : 8.301e-02
   6 : log(acos(B0_DIRA_OWNPV))                  : 8.169e-02
   7 : Kst_BKstarK_DecayAngle                    : 6.683e-02
   8 : log(B0_PT)                                : 6.439e-02
   9 : log(B0_IPCHI2_OWNPV)                      : 5.719e-02
  10 : log(D0_FDCHI2_OWNPV)                      : 5.625e-02
  11 : Ks_DKs_FDSig                              : 5.440e-02
  12 : log(B0_ENDVERTEX_CHI2/B0_ENDVERTEX_NDOF)  : 4.385e-02
  13 : log(Sum4_IPS)                             : 3.978e-02
  14 : log(Ks_FDCHI2_OWNPV)                      : 3.575e-02
  15 : log(Sum2_IPS)                             : 1.294e-02
  16 : log(D0_ENDVERTEX_CHI2/D0_ENDVERTEX_NDOF)  : 0.000e+00
------------------------------------------------------------------------
```

Remerciements

Voici donc venu le temps des remerciements, exercice dans lequel je suis loin d'exceller. Je m'excuse d'avance pour les oublis involontaires que je pourrais faire.

Tout d'abord je tiens à remercier le directeur Achille Stocchi, ainsi que le directeur adjoint Fabien Cavalier, de m'avoir permis de faire cette thèse au LAL. Merci également aux services administratifs du laboratoire, en particulier aux services missions et informatique, pour l'aide qu'ils m'ont apportée au cours de ces trois années.

Thanks to Guy Wilkinson and Fernando Martinez Vidal for accepting the heavy task of being my referees. I appreciate the effort you made to carefully read my thesis and allow my defence. Your comments were very useful. Thanks also to Jure Zupan for coming from Cincinnati to be a jury member. I hope you enjoy the thesis and your stay in Paris. Merci aussi à Isabelle Wingerter-Seez d'avoir accepté de faire partie du jury, j'espère que la lecture fut agréable et que je n'ai pas rendu la physique des saveurs trop indigeste.

Je tiens à remercier particulièrement Frédéric Machefert, mon Directeur de thèse. Pendant c'est trois années tu as toujours fait preuve d'écoute, de pédagogie et de bonne humeur. J'ai appris beaucoup de choses en travaillant avec toi et tu as toujours été disponible, même quand je venais te poser des questions bêtes. Merci pour tout le temps que tu m'as consacré. J'espère avoir été à la hauteur. Sans toi je n'aurais pas fait cette thèse et accessoirement le semi-marathon ;-)

Merci à toute l'équipe LHCb du LAL pour leur formidable accueil. J'ai passé trois années très agréables avec vous. Marie-Hélène, merci entre autre, pour ton aide toujours efficace, tes conseils bienveillants et ta franchise. Sergey je te suis redevable d'un bien rare au Laboratoire, la clé pour la machine à café ! Patrick, un jour j'arriverai à comprendre dans la seconde ton humour pince-sans-rire. Benoît, j'ai apprécié de t'avoir en co-bureau. Merci pour les pauses discussions politico-footballistiques, et tes histoires drôles du cesfo (mention spéciale à celle de l'Allemande coincée dans les toilettes d'un avion). Yasmine, merci pour tous ces conseils, ton soutien et pour transmettre ta bonne humeur. Je continuerai à suivre ppm assidûment. Guy j'espère que maintenant tu n'auras plus de mésaventures avec DaVinci, de toute façon j'arrivais à t'aider qu'une fois sur dix. Jacques, les discussions avec toi sont toujours enrichissantes, merci pour ta générosité et ton humilité. Bernard, merci encore pour les noix et pour avoir réparé la selle de mon vélo ! Je veux remercier également les étudiants du groupe Michelle, Sandra, Maksym, Olga, Claire, Martino, Renato et Victor. Je garde de très bons souvenirs des moments passés avec vous, que ce soit à la pause café, à Cracovie, aux jrjc et j'en passe et des meilleurs... Sandra je te remercie tout particulièrement de m'avoir mis sur de bon rails pour "BDKst" !

Je remercie également d'autre membre de LHCb pour leurs aides, leurs soutiens ou les discussions intéressantes que j'ai eues avec eux : Stéphane Monteil, Olivier Deschamps, Edwige Tournefier, Vava Gligorov, Francesco Polci. I am also grateful for the precious help of the B2OC conveners Anton Poluektov, Sneha Malde and I have a special thought to Moritz Karbach.

Stefania, thank you for chairing the BDK* microgroup. Jackson, thank you for the work done together. Jordi, many thanks for introducing us to cfit.

Merci aussi à tous les étudiants du LAL que j'ai pu côtoyer, en particulier à la team "Ultimate redactor". Grâce à vous mes chers Philippes ("venez ici que je vous butte !"), la fin de rédaction a été moins épique et les week-ends passés au clavier de l'ordinateur moins solitaires. Merci d'avoir toujours entretenu cette motivation collective. Je garderai toujours de bon souvenirs des ces moments si particuliers. Marta, merci pour ta joie de vivre et surtout pour les post-its ! Oublie pas de m'envoyer des photos de manchots (pas de pingouins !). Cyril, pense à pratiquer ton maniement du tube néon pour entrer au casting du prochain star wars. Camille, désolé pour toutes les fois où j'ai oublié de te prévenir qu'on allait manger. Et merci pour tout les services que tu m'as rendu. François, je te souhaite un joyeux ponycon !

Je remercie également mes amis hors du cercle de physique. Pierre-Yves et Nico, c'est cool de pouvoir vous retrouver autour d'une bière à Gre, prévue toujours à la dernière minute évidemment. Guillaume, j'ai hâte de refaire des sessions ski avec toi ! Sofiane et Aurélien, c'était super d'avoir fait le semi et le mud day ensemble !

Merci à ma Famille, et tout particulièrement à Papa et Maman. Comme dirait Pierre Perret, "merci de m'avoir fait si intelligent", ou du moins pas trop bête pour avoir pu faire cette thèse. Vous avez toujours été d'un soutient sans faille, tout au long de mes études. Merci d'avoir toujours éveillé ma curiosité. Merci aussi à mes grandes soeurs Aurélie et Claire, vous avez toujours pris soin de moi et vous êtes des exemples pour moi.
Merci également à Patrick, Marie et Mathilde pour m'avoir accueilli chaleureusement dans leur famille. Merci d'être venu à ma soutenance de physique subaquatique !

Enfin, merci Pauline. Après tous ces moments passés à tes cotés, je dois te remercier pour le formidable soutient que tu m'as apporté pendant cette thèse. Sans toi je n'aurais pas réussi, où alors pas de cette manière. Je ne te suis pas simplement redevable de 6 mois de vaisselles, pendant toute la thèse tu m'as remotivé dans les moments de doute, détendu dans les moments de stress, toujours avec tendresse, générosité et amour. C'était pas facile de supporter un thésard qui rentre à pas d'heure, où alors quasi-jamais à l'heure qu'il dit, qui pense encore à son chapitre où à son bout de code même rentré à la maison. Tu m'ouvres les yeux sur les choses qui comptent dans la vie et grâce à toi je suis une meilleure personne. Avec toi je suis heureux. Je t'aime.

Bibliography

[1] L. Wolfenstein, *Parametrization of the Kobayashi-Maskawa Matrix*, Phys. Rev. Lett. **51** (1983) 1945.

[2] M. Gronau and D. London, *How to determine all the angles of the unitarity triangle from $B^0_d \to DK_S$ and $B^0_s \to D\phi$*, Physics Letters B **253** (1991), no. 3–4 483 .

[3] M. Gronau and D. Wyler, *On determining a weak phase from charged b decay asymmetries*, Physics Letters B **265** (1991), no. 1–2 172 .

[4] D. Atwood, I. Dunietz, and A. Soni, *Enhanced CP Violation with $B \to KD^0(\bar{D}^0)$ Modes and Extraction of the Cabibbo-Kobayashi-Maskawa Angle γ*, Phys. Rev. Lett. **78** (1997) 3257.

[5] D. Atwood, I. Dunietz, and A. Soni, *Improved methods for observing* CP *violation in $B^\pm \to KD$ and measuring the CKM phase γ*, Phys. Rev. D **63** (2001) 036005.

[6] A. Giri, Y. Grossman, A. Soffer, and J. Zupan, *Determining γ using $B^\pm \to DK^\pm$ with multi-body D decays*, Phys. Rev. D **68** (2003) 054018.

[7] A. Bondar in *Proceedings of BINP special analysis meeting on Dalitz, unpublished*, 2002.

[8] BaBar collaboration, J. P. Lees *et al.*, *Observation of direct CP violation in the measurement of the Cabibbo-Kobayashi-Maskawa angle gamma with $B^\pm \to D^{(*)}K^{(*)\pm}$ decays*, Phys. Rev. **D87** (2013), no. 5 052015, arXiv:1301.1029.

[9] Belle collaboration, K. Trabelsi, *Study of direct CP in charmed B decays and measurement of the CKM angle gamma at Belle*, arXiv:1301.2033.

[10] LHCb collaboration, *Improved constraints on γ: CKM2014 update*, Sep, 2014. LHCb-CONF-2014-004.

[11] CKMfitter group, J. Charles *et al.*, *CP violation and the CKM matrix: assessing the impact of the asymmetric B factories*, Eur. Phys. J. **C41** (2005) 1, arXiv:hep-ph/0406184, updated results and plots available at: http://ckmfitter.in2p3.fr.

[12] UTfit collaboration, M. Bona *et al.*, *The 2004 UTfit collaboration report on the status of the unitarity triangle in the standard model*, JHEP **07** (2005) 028, arXiv:hep-ph/0501199, updated results and plots available at: http://www.utfit.org/UTfit/.

[13] LHCb collaboration, R. Aaij *et al.*, *Measurement of the CKM angle γ using $B^\pm \to DK^\pm$ with $D \to K^0_S\pi^+\pi^-$, $K^0_S K^+K^-$ decays*, JHEP **10** (2014) 097, arXiv:1408.2748.

[14] D. Griffiths, *Introduction to Elementary Particles*, John Wiley & Sons, New York, USA, 1987.

[15] M. D. Schwartz, *Quantum Field Theory and the Standard Model*, .

[16] I. I. Bigi and A. I. Sanda, *CP Violation*, Cambridge University Press, second ed., 2009. Cambridge Books Online.

[17] L. Boyle, *Standard model*, Wikipedia, `link`.

[18] LHCb collaboration, R. Aaij *et al.*, *Observation of the resonant character of the $Z(4430)^-$ state*, Phys. Rev. Lett. **112** (2014) 222002, `arXiv:1404.1903`.

[19] LHCb, R. Aaij *et al.*, *Observation of $J/\psi\, p$ Resonances Consistent with Pentaquark States in $Lb \to J/\psi\, K^- p$ Decays*, Phys. Rev. Lett. **115** (2015) 072001, `arXiv:1507.0341`.

[20] Particle Data Group, K. A. Olive *et al.*, *Review of particle physics*, Chin. Phys. **C38** (2014) 090001.

[21] E. Noether, *Invariant variation problems*, Transport Theory and Statistical Physics **1** (1971) 186, `arXiv:physics/0503066`.

[22] C. S. Wu *et al.*, *Experimental test of parity conservation in beta decay*, Phys. Rev. **105** (1957) 1413.

[23] BaBar, J. P. Lees *et al.*, *Observation of Time Reversal Violation in the B^0 Meson System*, Phys. Rev. Lett. **109** (2012) 211801, `arXiv:1207.5832`.

[24] J. H. Christenson, J. W. Cronin, V. L. Fitch, and R. Turlay, *Evidence for the 2π Decay of the K_2^0 Meson*, Phys. Rev. Lett. **13** (1964) 138.

[25] W. Pauli, L. Rosenfeld, and V. Weisskopf, *Niels Bohr and the development of physics*, Mc Graw-Hill, 1955.

[26] J. S. Schwinger, *The Theory of quantized fields. 1.*, Phys. Rev. **82** (1951) 914.

[27] G. Luders, *On the Equivalence of Invariance under Time Reversal and under Particle-Antiparticle Conjugation for Relativistic Field Theories*, Kong. Dan. Vid. Sel. Mat. Fys. Med. **28N5** (1954) 1.

[28] J. S. Bell, *Time reversal in field theory*, Proc. Roy. Soc. Lond. **A231** (1955) 479.

[29] H. Georgi and S. L. Glashow, *Unity of all elementary-particle forces*, Phys. Rev. Lett. **32** (1974) 438.

[30] F. Englert and R. Brout, *Broken symmetry and the mass of gauge vector mesons*, Phys. Rev. Lett. **13** (1964) 321.

[31] P. W. Higgs, *Broken symmetries, massless particles and gauge fields*, Physics Letters **12** (1964), no. 2 132 .

[32] P. W. Higgs, *Broken symmetries and the masses of gauge bosons*, Phys. Rev. Lett. **13** (1964) 508.

[33] G. S. Guralnik, C. R. Hagen, and T. W. B. Kibble, *Global conservation laws and massless particles*, Phys. Rev. Lett. **13** (1964) 585.

[34] ATLAS, G. Aad *et al.*, *Observation of a new particle in the search for the Standard Model Higgs boson with the ATLAS detector at the LHC*, Phys. Lett. **B716** (2012) 1, arXiv:1207.7214.

[35] CMS, S. Chatrchyan *et al.*, *Observation of a new boson at a mass of 125 GeV with the CMS experiment at the LHC*, Phys. Lett. **B716** (2012) 30, arXiv:1207.7235.

[36] B. Pontecorvo, *Mesonium and anti-mesonium*, Sov. Phys. JETP **6** (1957) 429.

[37] Z. Maki, M. Nakagawa, and S. Sakata, *Remarks on the unified model of elementary particles*, Prog. Theor. Phys. **28** (1962) 870.

[38] N. Cabibbo, *Unitary symmetry and leptonic decays*, Phys. Rev. Lett. **10** (1963) 531.

[39] M. Kobayashi and T. Maskawa, *CP Violation in the Renormalizable Theory of Weak Interaction*, Prog. Theor. Phys. **49** (1973) 652.

[40] S. L. Glashow, J. Iliopoulos, and L. Maiani, *Weak Interactions with Lepton-Hadron Symmetry*, Phys. Rev. **D2** (1970) 1285.

[41] CKMfitter Group, J. Charles *et al.*, *CP violation and the CKM matrix: Assessing the impact of the asymmetric B factories*, Eur. Phys. J. **C41** (2005) 1, arXiv:hep-ph/0406184.

[42] C. Jarlskog, *Commutator of the quark mass matrices in the standard electroweak model and a measure of maximal* CP *nonconservation*, Phys. Rev. Lett. **55** (1985) 1039.

[43] Planck, P. A. R. Ade *et al.*, *Planck 2013 results. I. Overview of products and scientific results*, Astron. Astrophys. **571** (2014) A1, arXiv:1303.5062.

[44] A. D. Sakharov, *Violation of CP Invariance, c Asymmetry, and Baryon Asymmetry of the Universe*, Pisma Zh. Eksp. Teor. Fiz. **5** (1967) 32.

[45] M. Ciuchini and A. Stocchi, *Physics Opportunities at the Next Generation of Precision Flavor Physics*, Ann. Rev. Nucl. Part. Sci. **61** (2011) 491, arXiv:1110.3920.

[46] J. Brod and J. Zupan, *The ultimate theoretical error on γ from $B \to DK$ decays*, JHEP **1401** (2014) 051, arXiv:1308.5663.

[47] Heavy Flavor Averaging Group, Y. Amhis *et al.*, *Averages of b-hadron, c-hadron, and τ-lepton properties as of summer 2014*, arXiv:1412.7515, updated results and plots available at http://www.slac.stanford.edu/xorg/hfag/.

[48] Y. Grossman, Z. Ligeti, and A. Soffer, *Measuring gamma in B+- —> K+- (KK*)(D) decays*, Phys. Rev. **D67** (2003) 071301, arXiv:hep-ph/0210433.

[49] LHCb collaboration, R. Aaij *et al.*, *A study of CP violation in $B^\pm \to DK^\pm$ and $B^\pm \to D\pi^\pm$ decays with $D \to K^0_S K^\pm \pi^\mp$ final states*, Phys. Lett. **B733** (2014) 36, arXiv:1402.2982.

[50] CLEO collaboration, J. Libby *et al.*, *Model-independent determination of the strong-phase difference between D^0 and $\bar{D}^0 \to K^0_{S,L} h^+ h^-$ ($h = \pi, K$) and its impact on the measurement of the CKM angle γ/ϕ_3*, Phys. Rev. **D82** (2010) 112006, arXiv:1010.2817.

[51] BaBar collaboration, P. del Amo Sanchez *et al.*, *Measurement of $D^0 - \bar{D}^0$ mixing parameters using $D^0 \to K^0_S \pi^+ \pi^-$ and $D^0 \to K^0_S K^+ K^-$ decays*, Phys. Rev. Lett. **105** (2010) 081803, arXiv:1004.5053.

[52] LHCb collaboration, R. Aaij *et al.*, *Measurement of CP violation and constraints on the CKM angle γ in $B^\pm \to DK^\pm$ with $D \to K^0_S\pi^+\pi^-$ decays*, Nucl. Phys. **B888** (2014) 169, arXiv:1407.6211.

[53] R. Aleksan, I. Dunietz, and B. Kayser, *Determining the CP violating phase gamma*, Z. Phys. **C54** (1992) 653.

[54] LHCb collaboration, R. Aaij *et al.*, *Measurement of CP violation and the B^0_s meson decay width difference with $B^0_s \to J/\psi K^+K^-$ and $B^0_s \to J/\psi\pi^+\pi^-$ decays*, Phys. Rev. **D87** (2013) 112010, arXiv:1304.2600.

[55] LHCb collaboration, R. Aaij *et al.*, *Measurement of CP asymmetry in $B^0_s \to D^\mp_s K^\pm$ decays*, JHEP **11** (2014) 060, arXiv:1407.6127.

[56] I. Dunietz, *Clean CKM information from $B^0(t) \to D^{(*)\mp}\pi^\pm$*, Physics Letters B **427** (1998), no. 1–2 179 .

[57] LHCb collaboration, R. Aaij *et al.*, *Observation of CP violation in $B^\pm \to DK^\pm$ decays*, Phys. Lett. **B712** (2012) 203, Erratum ibid. **B713** (2012) 351, arXiv:1203.3662.

[58] LHCb collaboration, R. Aaij *et al.*, *Observation of the suppressed ADS modes $B^\pm \to [\pi^\pm K^\mp\pi^+\pi^-]_D K^\pm$ and $B^\pm \to [\pi^\pm K^\mp\pi^+\pi^-]_D\pi^\pm$*, Phys. Lett. **B723** (2013) 44, arXiv:1303.4646.

[59] LHCb collaboration, R. Aaij *et al.*, *Measurement of CP violation parameters in $B^0 \to DK^{*0}$ decays*, Phys. Rev. **D90** (2014) 112002, arXiv:1407.8136.

[60] R. Fleischer, *New strategies to extract Beta and gamma from $B_d \to \pi^+\pi^-$ and $B_s \to K^+K^-$*, Phys. Lett. **B459** (1999) 306, arXiv:hep-ph/9903456.

[61] R. Fleischer, *$B_{s,d} \to \pi\pi, \pi K, KK$: Status and Prospects*, Eur. Phys. J. **C52** (2007) 267, arXiv:0705.1121.

[62] R. Fleischer and R. Knegjens, *In Pursuit of New Physics With $B^0_s \to K^+K^-$*, Eur. Phys. J. **C71** (2011) 1532, arXiv:1011.1096.

[63] M. Ciuchini, E. Franco, S. Mishima, and L. Silvestrini, *Testing the Standard Model and Searching for New Physics with $B_d \to \pi\pi$ and $B_s \to KK$ Decays*, JHEP **1210** (2012) 029, arXiv:1205.4948.

[64] M. Gronau and D. London, *Isospin analysis of CP asymmetries in B decays*, Phys. Rev. Lett. **65** (1990) 3381.

[65] LHCb Collaboration, B. Adeva *et al.*, *Road map for selected key measurements from LHCb*, Tech. Rep. LHCb-PUB-2009-029. CERN-LHCb-PUB-2009-029, CERN, Geneva, May, 2010.

[66] LHCb collaboration, R. Aaij *et al.*, *Determination of γ and $-2\beta_s$ from charmless two-body decays of beauty mesons*, Phys. Lett. **B739** (2014) 1, arXiv:1408.4368.

[67] M. Gronau, *Improving bounds on γ in $B^\pm \to DK^\pm$ and $B^{\pm,0} \to DX\_s^{\pm,0}$*, Phys. Lett. **B557** (2014) 198, arXiv:hep-ph/0211282.

[68] S. Pruvot, M. H. Schune, V. Sordini, and A. Stocchi, *Measuring γ with $B^0 \to DK^{*0}$ decays at Babar*, in *4th International Workshop on the CKM Unitarity Triangle (CKM 2006) Nagoya, Japan, December 12-16, 2006*, 2007. arXiv:hep-ph/0703292.

[69] BaBar, B. Aubert *et al.*, *Search for $b \to u$ transitions in $B^0 \to DK^{*0}$ decays*, Phys. Rev. **D80** (2009) 031102, arXiv:0904.2112.

[70] Belle, K. Negishi *et al.*, *Search for the decay $B^0 \to DK^{*0}$ followed by $D \to K^-\pi^+$*, Phys. Rev. **D86** (2012) 011101, arXiv:1205.0422.

[71] BaBar, B. Aubert *et al.*, *Constraints on the CKM angle gamma in $B^0 \to \overline{D}^0 K^{*0}$ and $B^0 \to D^0 K^{*0}$ with a Dalitz analysis of D^0 and $\overline{D}^0$ decays to $K^0_S\pi^+\pi^-$*, Phys. Rev. **D79** (2009) 072003, arXiv:0805.2001.

[72] LHCb collaboration, A. A. Alves Jr. *et al.*, *The LHCb detector at the LHC*, JINST **3** (2008) S08005.

[73] L. Forthomme, *Map of the cern accelerator complex*, Wikipedia, https://commons.wikimedia.org/wiki/File:Cern-accelerator-complex.svg.

[74] LHCb collaboration, R. Aaij *et al.*, *LHCb detector performance*, Int. J. Mod. Phys. **A30** (2015) 1530022, arXiv:1412.6352.

[75] LHCb collaboration, R. Aaij *et al.*, *Measurement of $\sigma(pp \to b\overline{b}X)$ at $\sqrt{s} = 7$ TeV in the forward region*, Phys. Lett. **B694** (2010) 209, arXiv:1009.2731.

[76] BaBar, D. Boutigny *et al.*, *The BABAR physics book: Physics at an asymmetric B factory*, .

[77] C.-W. Chiang *et al.*, *New Physics in $B^0_s \to J/\psi\,\phi$: A General Analysis*, JHEP **1004** (2010) 031, arXiv:0910.2929.

[78] C. Bobeth, T. Ewerth, F. Kruger, and J. Urban, *Enhancement of $\mathcal{B}(\overline{B}_d \to \mu^+\mu^-)$ / $\mathcal{B}(\overline{B}^0_s \to \mu^+\mu^-)$ in the MSSM with minimal flavor violation and large* $\tan\beta$, Phys. Rev. **D66** (2002) 074021, arXiv:hep-ph/0204225.

[79] F. Krüger and J. Matias, *Probing new physics via the transverse amplitudes of $B^0 \to K^{*0}(\to K^-\pi^+)l^+l^-$ at large recoil*, Phys. Rev. D **71** (2005) 094009.

[80] LHCb collaboration, R. Aaij *et al.*, *First evidence for the decay $B^0_s \to \mu^+\mu^-$*, Phys. Rev. Lett. **110** (2013) 021801, arXiv:1211.2674.

[81] LHCb collaboration, R. Aaij *et al.*, *Measurement of the $B^0_s \to \mu^+\mu^-$ branching fraction and search for $B^0 \to \mu^+\mu^-$ decays at the LHCb experiment*, Phys. Rev. Lett. **111** (2013) 101805, arXiv:1307.5024.

[82] LHCb collaboration, R. Aaij *et al.*, *Differential branching fraction and angular analysis of the decay $B^0 \to K^{*0}\mu^+\mu^-$*, JHEP **08** (2013) 131, arXiv:1304.6325.

[83] LHCb collaboration, R. Aaij *et al.*, *Measurement of form-factor-independent observables in the decay $B^0 \to K^{*0}\mu^+\mu^-$*, Phys. Rev. Lett. **111** (2013) 191801, arXiv:1308.1707.

[84] LHCb collaboration, *Angular analysis of the $B^0_d \to K^{*0}\mu^+\mu^-$ decay*, Mar, 2015. LHCb-CONF-2015-002.

[85] LHCb collaboration, R. Aaij *et al.*, *Measurement of the CP-violating phase ϕ_s in $\overline{B}^0_s \to J/\psi\pi^+\pi^-$ decays*, Phys. Lett. **B736** (2014) 186, arXiv:1405.4140.

[86] LHCb collaboration, R. Aaij *et al.*, *Precision measurement of CP violation in $B^0_s \to J/\psi K^+K^-$ decays*, Phys. Rev. Lett. **114** (2015) 041801, arXiv:1411.3104.

[87] LHCb collaboration, R. Aaij *et al.*, *A measurement of the CKM angle γ from a combination of $B^\pm \to Dh^\pm$ analyses*, Phys. Lett. **B726** (2013) 151, arXiv:1305.2050.

[88] LHCb collaboration, R. Aaij *et al.*, *Measurements of indirect CP asymmetries in $D^0 \to K^-K^+$ and $D^0 \to \pi^-\pi^+$ decays*, Phys. Rev. Lett. **112** (2014) 041801, arXiv:1310.7201.

[89] LHCb collaboration, R. Aaij *et al.*, *Inclusive W and Z production in the forward region at $\sqrt{s} = 7$ TeV*, JHEP **06** (2012) 058, arXiv:1204.1620.

[90] LHCb collaboration, R. Aaij *et al.*, *Measurement of the forward W boson production cross-section in pp collisions at $\sqrt{s} = 7$ TeV*, JHEP **12** (2014) 079, arXiv:1408.4354.

[91] LHCb collaboration, R. Aaij *et al.*, *Determination of the X(3872) meson quantum numbers*, Phys. Rev. Lett. **110** (2013) 222001, arXiv:1302.6269.

[92] LHCb collaboration, R. Aaij *et al.*, *Searches for Majorana neutrinos in B^- decays*, Phys. Rev. **D85** (2012) 112004, arXiv:1201.5600.

[93] LHCb collaboration, R. Aaij *et al.*, *Searches for violation of lepton flavour and baryon number in tau lepton decays at LHCb*, Phys. Lett. **B724** (2013) 36, arXiv:1304.4518.

[94] LHCb collaboration, R. Aaij *et al.*, *Study of J/ψ production and cold nuclear matter effects in pPb collisions at $\sqrt{s_{NN}} = 5$ TeV*, JHEP **02** (2014) 072, arXiv:1308.6729.

[95] LHCb collaboration, R. Aaij *et al.*, *Study of Υ production and cold nuclear effects in pPb collisions at $\sqrt{s_{NN}} = 5$ TeV*, JHEP **07** (2014) 094, arXiv:1405.5152.

[96] LHCb collaboration, R. Aaij *et al.*, *Precision measurement of the B_s^0–$\overline{B}_s^0$ oscillation frequency in the decay $B_s^0 \to D_s^-\pi^+$*, New J. Phys. **15** (2013) 053021, arXiv:1304.4741.

[97] A. Arefev *et al.*, *Beam Test Results of the LHCb Electromagnetic Calorimeter.*, Tech. Rep. LHCb-2007-149. CERN-LHCb-2007-149, CERN, Geneva, May, 2008. revised version submitted on 2008-05-15 09:09:53.

[98] LHCb collaboration, R. Aaij *et al.*, *Measurement of the ratio of branching fractions $\mathcal{B}(B^0 \to K^{*0}\gamma)/\mathcal{B}(B_s^0 \to \phi\gamma)$ and the direct CP asymmetry in $B^0 \to K^{*0}\gamma$*, Nucl. Phys. **B867** (2013) 1, arXiv:1209.0313.

[99] LHCb collaboration, R. Aaij *et al.*, *Absolute luminosity measurements with the LHCb detector at the LHC*, JINST **7** (2012) P01010, arXiv:1110.2866.

[100] A. Puig, *The LHCb trigger in 2011 and 2012*, LHCb-PUB-2014-046.

[101] V. V. Gligorov and M. Williams, *Efficient, reliable and fast high-level triggering using a bonsai boosted decision tree*, JINST **8** (2013) P02013, arXiv:1210.6861.

[102] M. Frank *et al.*, *Deferred high level trigger in lhcb: A boost to cpu resource utilization*, Journal of Physics: Conference Series **513** (2014), no. 1 012006.

[103] S. Tolk, J. Albrecht, F. Dettori, and A. Pellegrino, *Data driven trigger efficiency determination at LHCb*, Tech. Rep. LHCb-PUB-2014-039. CERN-LHCb-PUB-2014-039, CERN, Geneva, May, 2014.

[104] *The gaudi project*, http://proj-gaudi.web.cern.ch/proj-gaudi/.

[105] *Root data analysis framework*, https://root.cern.ch.

[106] M. Clemencic *et al.*, *The LHCb simulation application, Gauss: Design, evolution and experience*, J. Phys. Conf. Ser. **331** (2011) 032023.

[107] T. Sjöstrand, S. Mrenna, and P. Skands, *PYTHIA 6.4 physics and manual*, JHEP **05** (2006) 026, arXiv:hep-ph/0603175.

[108] T. Sjöstrand, S. Mrenna, and P. Skands, *A brief introduction to PYTHIA 8.1*, Comput. Phys. Commun. **178** (2008) 852, arXiv:0710.3820.

[109] D. J. Lange, *The EvtGen particle decay simulation package*, Nucl. Instrum. Meth. **A462** (2001) 152.

[110] Geant4 collaboration, S. Agostinelli *et al.*, *Geant4: A simulation toolkit*, Nucl. Instrum. Meth. **A506** (2003) 250.

[111] Geant4 collaboration, J. Allison *et al.*, *Geant4 developments and applications*, IEEE Trans. Nucl. Sci. **53** (2006) 270.

[112] *Letter of Intent for the LHCb Upgrade*, Tech. Rep. CERN-LHCC-2011-001. LHCC-I-018, CERN, Geneva, Mar, 2011.

[113] LHCb collaboration, *Framework TDR for the LHCb Upgrade: Technical Design Report*, CERN-LHCC-2012-007. LHCb-TDR-012.

[114] V. V. Gligorov, *Performance and upgrade plans of the LHCb trigger system*, Nuclear Instruments and Methods in Physics Research Section A: Accelerators, Spectrometers, Detectors and Associated Equipment **718** (2013), no. 0 26 , Proceedings of the 12th Pisa Meeting on Advanced Detectors La Biodola, Isola dÉlba, Italy, May 20–26, 2012.

[115] LHCb collaboration, *LHCb VELO Upgrade Technical Design Report*, CERN-LHCC-2013-021. LHCb-TDR-013.

[116] LHCb collaboration, *LHCb PID Upgrade Technical Design Report*, CERN-LHCC-2013-022. LHCb-TDR-014.

[117] LHCb collaboration, R. Aaij *et al.* , and A. Bharucha *et al.*, *Implications of LHCb measurements and future prospects*, Eur. Phys. J. **C73** (2013) 2373, arXiv:1208.3355.

[118] LHCb collaboration, *Tagged time-dependent angular analysis of $B_s^0 \to J/\psi\phi$ decays at LHCb*, LHCb-CONF-2012-002.

[119] LHCb collaboration, R. Aaij *et al.*, *Measurement of the CP-violating phase ϕ_s in $\overline{B}_s^0 \to J/\psi\pi^+\pi^-$ decays*, Phys. Lett. **B713** (2012) 378, arXiv:1204.5675.

[120] LHCb collaboration, *Differential branching fraction and angular analysis of the $B^0 \to K^{*0}\mu^+\mu^-$ decay*, LHCb-CONF-2012-008.

[121] LHCb collaboration, R. Aaij *et al.*, *Measurement of the isospin asymmetry in $B \to K^{(*)}\mu^+\mu^-$ decays*, JHEP **07** (2012) 133, arXiv:1205.3422.

[122] LHCb collaboration, R. Aaij *et al.*, *First observation of the decay $B^+ \to \pi^+\mu^+\mu^-$* , JHEP **12** (2012) 125, arXiv:1210.2645.

[123] LHCb collaboration, R. Aaij *et al.*, *Strong constraints on the rare decays $B_s^0 \to \mu^+\mu^-$ and $B^0 \to \mu^+\mu^-$*, Phys. Rev. Lett. **108** (2012) 231801, arXiv:1203.4493.

[124] LHCb collaboration, R. Aaij *et al.*, *Evidence for CP violation in time-integrated $D^0 \to h^-h^+$ decay rates*, Phys. Rev. Lett. **108** (2012) 111602, arXiv:1112.0938.

[125] LHCb collaboration, R. Aaij *et al.*, *A study of CP violation in $B^\mp \to Dh^\mp$ ($h = K, \pi$) with the modes $D \to K^\mp\pi^\pm\pi^0$, $D \to \pi^+\pi^-\pi^0$ and $D \to K^+K^-\pi^0$*, arXiv:1504.0544, submitted to Phys. Rev. D.

[126] E. Longo and I. Sestili, *Monte Carlo Calculation of Photon Initiated Electromagnetic Showers in Lead Glass*, Nucl. Instrum. Meth. **128** (1975) 283.

[127] B. Rossi, *High Energy Particles*, Prentice-Hall New York, 1952.

[128] W. R. Nelson, T. M. Jenkins, R. C. McCall, and J. K. Cobb, *Electron-Induced Cascade Showers in Copper and Lead at 1 GeV*, Phys. Rev. **149** (1966) 201.

[129] G. Bathow *et al.*, *Measurements of the longitudinal and lateral development of electromagnetic cascades in lead, copper and aluminum at 6 GeV*, Nuclear Physics B **20** (1970), no. 3 592 .

[130] G. A. Akopdjanov *et al.*, *Determination of photon coordinates in a hodoscope cherenkov spectrometer*, Nuclear Instruments and Methods **140** (1977), no. 3 441 .

[131] G. Ferri *et al.*, *The Structure of Lateral Electromagnetic Shower Development in Si / W and Si / U Calorimeters*, Nucl. Instrum. Meth. **A273** (1988) 123.

[132] G. Abshire *et al.*, *Measurement of Electron and Pion Cascades in a Lead / Acrylic Scintillator Shower Detector*, Nucl. Instrum. Meth. **164** (1979) 67.

[133] SICAPO, E. Borchi *et al.*, *Systematic investigation of the local hardening effect and lateral electromagnetic shower development*, Nucl. Phys. Proc. Suppl. **23A** (1991) 119.

[134] G. Grindhammer, M. Rudowicz, and S. Peters, *The Fast Simulation of Electromagnetic and Hadronic Showers*, Nucl. Instrum. Meth. **A290** (1990) 469.

[135] G. Grindhammer and S. Peters, *The Parameterized simulation of electromagnetic showers in homogeneous and sampling calorimeters*, arXiv:hep-ex/0001020.

[136] A. Martens, *Towards a measurement of the angle γ of the Unitarity Triangle with the LHCb detector at the LHC (CERN): calibration of the calorimeters using an energy flow technique and first observation of the $B_s^0 \to \overline{D}^0\overline{K}^{*0}$ decay*, .

[137] LHCb, I. Belyaev, D. Savrina, R. Graciani, and A. Puig, *Kali: The framework for fine calibration of the LHCb electromagnetic calorimeter*, J. Phys. Conf. Ser. **331** (2011) 032050.

[138] O. Deschamps *et al.*, *Photon and neutral pion reconstruction*, .

[139] T. Skwarnicki, *A study of the radiative cascade transitions between the Upsilon-prime and Upsilon resonances*, PhD thesis, Institute of Nuclear Physics, Krakow, 1986, DESY-F31-86-02.

[140] W. D. Hulsbergen, *Decay chain fitting with a Kalman filter*, Nucl. Instrum. Meth. **A552** (2005) 566, arXiv:physics/0503191.

[141] L. Breiman, J. H. Friedman, R. A. Olshen, and C. J. Stone, *Classification and regression trees*, Wadsworth international group, Belmont, California, USA, 1984.

[142] B. P. Roe *et al.*, *Boosted decision trees as an alternative to artificial neural networks for particle identification*, Nucl. Instrum. Meth. **A543** (2005) 577, arXiv:physics/0408124.

[143] A. Hocker *et al.*, *TMVA - Toolkit for Multivariate Data Analysis*, PoS **ACAT** (2007) 040, arXiv:physics/0703039.

[144] LHCb collaboration, R. Aaij *et al.*, *Study of $B^0_{(s)} \to K^0_S h^+ h'^-$ decays with first observation of $B^0_s \to K^0_S K^\pm \pi^\mp$ and $B^0_s \to K^0_S \pi^+ \pi^-$*, JHEP **10** (2013) 143, arXiv:1307.7648.

[145] Particle Data Group, J. Beringer *et al.*, *Review of particle physics*, Phys. Rev. **D86** (2012) 010001, and 2013 partial update for the 2014 edition.

[146] A. Martin Sanchez, P. Robbe, and M.-H. Schune, *Performances of the LHCb L0 Calorimeter Trigger*, LHCb-PUB-2011-026.

[147] A. Martin Sanchez and P. Robbe, *CP violation studies on the $B^0 \to DK^{*0}$ decays and hadronic trigger performance with the LHCb detector at CERN*, PhD thesis, Orsay, 2013, presented 25 Jun 2013.

[148] K. S. Cranmer, *Kernel estimation in high-energy physics*, Comput. Phys. Commun. **136** (2001) 198, arXiv:hep-ex/0011057.

[149] M. Jacob and G. C. Wick, *On the general theory of collisions for particles with spin*, Annals of Physics **7** (1959), no. 4 404 .

[150] J. D. Richman, *An experimenter's guide to the helicity formalism*, Tech. Rep. CALT-68-1148, Calif. Inst. Technol., Pasadena, CA, Jun, 1984.

[151] F. James and M. Winkler, *MINUIT User's Guide*, , www.cern.ch/minuit.

[152] D. Asner, *Charm Dalitz plot analysis formalism and results: Expanded RPP-2004 version*, arXiv:hep-ex/0410014.

[153] G. J. Gounaris and J. J. Sakurai, *Finite-Width Corrections to the Vector-Meson-Dominance Prediction for $\rho \to e^+ e^-$*, Phys. Rev. Lett. **21** (1968) 244.

[154] V. V. Anisovich and A. V. Sarantsev, *K-matrix analysis of the ($IJPC = 00++$)-wave in the mass region below 1900 MeV*, The European Physical Journal A - Hadrons and Nuclei **16** (2003), no. 2 229.

[155] D. Aston *et al.*, *A study of $k^-\pi^+$ scattering in the reaction $kp \to k^-\pi^+ n$ at 11 gev/c*, Nuclear Physics B **296** (1988), no. 3 493 .

[156] LHCb collaboration, R. Aaij *et al.*, *Dalitz plot analysis of $B^0 \to \overline{D}^0 \pi^+ \pi^-$ decays*, LHCb-PAPER-2014-070, in preparation.

[157] M. Pivk and F. R. Le Diberder, *sPlot: A statistical tool to unfold data distributions*, Nucl. Instrum. Meth. **A555** (2005) 356, arXiv:physics/0402083.

[158] LHCb collaboration, R. Aaij *et al.*, *Measurement of the $D^{\pm}$ production asymmetry in 7 TeV pp collisions*, Phys. Lett. **B718** (2013) 902, arXiv:1210.4112.

[159] A. Bondar and T. Gershon, *On ϕ_3 measurements using $B^- \to D^* K^-$ decays*, Phys. Rev. D **70** (2004) 091503.

[160] BaBar collaboration, P. del Amo Sanchez and other, *Evidence for direct CP violation in the measurement of the Cabibbo-Kobayashi-Maskawa angle gamma with $B^{\pm} \to D^{(*)} K^{(*)\pm}$ decays*, Phys. Rev. Lett. **105** (2010) 121801, arXiv:1005.1096.

[161] BaBar collaboration, B. Aubert *et al.*, *Measurement of Branching Fractions and Resonance Contributions for $B^0 \to \overline{D}^0 K^+ \pi^-$ and Search for $B^0 \to D^0 K^+ \pi^-$ Decays*, Phys. Rev. Lett. **96** (2006) 011803.

[162] S. Bodhisattva, M. Walker, and M. Woodroofe, *On the Unified Method with Nuisance Parameters*, Statist. Sinica **19** (2009) 301.

[163] G. J. Feldman and R. D. Cousins, *A Unified approach to the classical statistical analysis of small signals*, Phys. Rev. **D57** (1998) 3873, arXiv:physics/9711021.